University of Southampton

Faculty of Engineering and the Environment
Institute of Sound and Vibration Research

Acoustic detection of seabed gas leaks, with application to Carbon Capture and Storage (CCS), and leak prevention for the oil and gas industry

by
Benoît Jean Pierre Bergès

Thesis for the degree of Doctor of Philosophy

April 2015

To my parents

Contents

List of Figures

List of Tables

Author's declaration

I, Benoît Jean Pierre Bergès declare that this thesis and the work presented in it are my own and has been generated by me as the result of my own original research.

I confirm that:

1. This work was done wholly or mainly while in candidature for a research degree at this University;
2. Where any part of this thesis has previously been submitted for a degree or any other qualification at this University or any other institution, this has been clearly stated;
3. Where I have consulted the published work of others, this is always clearly attributed;
4. Where I have quoted from the work of others, the source is always given. With the exception of such quotations, this thesis is entirely my own work;
5. I have acknowledged all main sources of help;
6. Where the thesis is based on work done by myself jointly with others, I have made clear exactly what was done by others and what I have contributed myself;
7. Either none of this work has been published before submission, or parts of this work have been published (see below).

Signed:

Date:

Acknowledgments

This work was carried out under a full-time PhD studentship funded by the University of Southampton and Statoil Ltd. and to them I express my gratitude for their support and funding. I am thankful to Trond Erland Bustnes for providing guidance on industrial practicalities and requirements. I feel extremely lucky to have been involved into the fascinating area of research.

I am very thankful to my PhD supervisors, Professor Tim Leighton and Professor Paul White. They have given me the opportunity to undertake the research presented in this thesis. Their patient guidance, encouragement and excellent advice throughout this study enabled me to develop an understanding of the subject. It amazed me that despite their very tight schedules they always devoted countless, enthusiastic and fun times to help me in my research. I feel extremely fortunate to have been supervised by such scientists and their rigorous scientific approach, attention to details and creativity are truly inspirational. Their enthusiasm for their science is contagious and they certainly raised motivation for me to pursue an academic career.

I am thankful to my PhD examiners Dr. Paul Lepper and Victor Humphrey for their insightful reviews and comments. I am also particularly thankful to Professor Viktor Humphrey for discussions about sonar calibration and sound fields in test tanks (chapter 7, Appendix A). I thankful to Professor Phillip Joseph for useful discussions and comments on Appendix A.

I am thankful to Michal Tomczyk for providing multiple research opportunities and equipment to me. During the research cruise JR253, I worked with Michal on the collection of acoustical data presented in chapter 7. Here began a true friendship. After the research cruise JR253, Michal visited the ISVR for a few months. During this period, he helped me to collect the data presented in chapter 4 and provided me part of the equipment for the experiments presented in this chapter. We also undertook collaborative research related to chapter 6 and chapter 7. These few

months constituted the most enjoyable time of my PhD research. Michal gave me the opportunity to participate to the research cruise HE387 during which we worked together on the collection of the data presented in chapter 7.

I am thankful to Dr. Jeremy Blackford, Professor Jonathan Bull and Dr. Henrik Stahl for giving me the opportunity to be involved in the QICS project (chapter 5). During the experimental period, Dr. Henrik Stahl and Pete Taylor provided vital assistance. The quality of the data presented in chapter 5 is a consequence of their devotion to manage the hydrophone recorders on the field when I was away. I am thankful to Professor Jonathan Bull for support and fruitful comments on my research. I am thankful to Melis Cevatoglu who helped me to deal with the ArcGIS software for producing Fig. 5.5. I am thankful to Jun Kita for providing the data presented in Fig. 5.2(c). I am thankful to Jon Howe who provided tidal height data (INIS Hydro projet) presented in Fig. 5.2(b). I am thankful to the crew members of R/V Seol Mara that helped me deploying hydrophone recorders during the QICS project.

I am thankful to Professor Ian Wright, Dr. Rachel James and Dr. Doug Connelly for giving me the opportunity to be involved in the research cruise JR253. I am thankful to Carla Scalabrin and Laurent Berger for fruitful discussions and for providing resources (documentation, software from the ifremer) related to the active acoustic inversion (chapter 6, chapter 7). I am thankful to the crew members of R/V James Clark Ross for the help in the data collection during the research cruise JR253.

I am thankful to Heiko Sahling for giving me the opportunity to be involved in the research cruise HE387. I was genuinely impressed by the strong team spirit and cruise management that was built during the research cruise HE387 by Heiko Sahling. I am thankful to the crew members of R/V Heincke for the help with the data collection during the research cruise HE387.

I am thankful to Dezhang Chu and Timothy Stanton for providing me with help and MATLAB resources for the computation of the acoustic scattering from rigid spheres. I am thankful to Charles Greenlaw for very open and fruitful discussions and countless MATLAB resources related to the inversion presented in chapter 6 and chapter 7. I am thankful to Grant Deane for providing data presented in Fig. 3.3. This data set was vital for the computation of the uncertainties of the inverse method presented in chapter 4 and chapter 5.

With the large experimental testing, the technical staff at the ISVR was of tremendous help. They provided me time and technical support to the construction of my various (sometimes not very successful) experiments. Of particular relevance, I would like to thank Phil Oxborrow and Anthony Wood.

I am thankful to Professor Phillip Joseph, Dr. Jeff Priest, Alessandra Tesei, Alberto Figoli, Jian Ming Peng and Frederica Pace who with I worked through various projects at the ISVR aside from the research presented in this thesis.

I am thankful to the fellows of room 2037. They brought a good atmosphere on a daily basis at the office and this was much needed! I feel fortunate to have been part of such a nice working environment. I had the chance to build solid friendship with Gim Hwa Chua, Symeon Mattes and Hessam Alavi.

The best outcome of these years of study is meeting my best friend and partner. I feel lucky to have crossed the way of such a truthful, resourceful and joyful person.

Finally, I would like to thank my parents who provided me unconditional support for so many years.

Publications

Journal articles

- **Bergès, B. J. P.**, Leighton, T. G., White, P. R. (2015). “*Passive acoustic quantification of gas fluxes during controlled gas release experiments,*” International Journal of Greenhouse Gas Control, Special Issue: CCS in the marine environment, in press, doi:10.1016/j.ijggc.2015.02.008
- Blackford, J. C., Stahl, H., Bull, J. M., **Bergès, B. J. P.**, Cevatoglu, M., Lichtschlag, A., Connelly, D., James, R. H., Kita, J., Long, D., Naylor, M., Kiminori, S., Smith, D., Taylor, P., Wright, I., Akhurst, M., Chen, B., Gernon, T. M., Hauton, C., Hayashi, M., Kaieda, H., Leighton, T. G., Sato, T., Sayer, M. D., J. Suzumura, M., Tait, K., Vardy, M. E., White, P. R., Widdicombe, S. (2014). “*Detection and impacts of leakage from sub-seafloor deep geological Carbon Dioxide Storage,*” Nature Climate Change, 4, doi:1011-1016, 10.1038/nclimate2381
- Sahling, H., Römer, M., Pape, T., **Bergès, B.**, dos Santos Fereirra, C., Boelmann, J., Geprägs, P., Tomczyk, M., Nowald, N., Dimmler,W., Schroedter, L., Glockzin, M., Bohrmann, G. (2014). “*Gas emissions at the continental margin west off Svalbard: mapping, sampling, and quantification,*” Biogeosciences Discussion, 11, 7189–7234. doi:10.5194/bgd-11-7189-2014.
- Wright, I. C., James, R. H., Minshull, T. A., Westbrook, G. K., Graves, C. A., Connelly, D. P., Alker, B., Le Bas, T. P., **Bergès, B. J.P.**, Cole, C., Czerski, H., Ferré, B., Hühnerbach, V., Leifer, I., Leighton, T. G., Lowry, D., Ogor, A., Scalabrin, C., Thomas, Y., Tomczyk, M., Vardy, M. E. and White, P. R. (n.d.) “*Methane venting to the atmosphere from the seabed of the Arctic continental shelf, offshore Svalbard,*”.

Conference articles

- Sahling, H., Römer, M., Pape, T., dos Santos Fereirra, C., Bohrmann, G., and **Bergès, B. J. P.** (2014). "*Quantification of Gas Emissions at the Continental Margin West of Svalbard,*" 12th Int. Conf. Gas Mar. Sediment, Taipei, Taiwan, 7–8.
- **Bergès, B. J. P.**, Leighton, T. G., White, P. R., and Tomczyk, M. (2014). "*Passive acoustic quantification of gas release,*" Proceedings of the 2nd International Conference and Exhibition on Underwater Acoustics (Rhodes, 22– 27 June, 2014), pp. 177-184.
- **Bergès, B. J. P.**, Leighton, T. G., White, P. R., Tomczyk, M., and Wright, I. C. (2012). "*Acoustic detection of seabed gas leaks, with application to carbon capture and storage (CCS), and leak prevention for the oil and gas industry: preliminary assessment of use of active and passive acoustic inversion for the quantification of underwater gas,*" Proceedings of the 11th European Conference on Underwater Acoustics, (ECUA2012), Edinburgh, UK, 2-6 July 2012, 146-152.
- Tomczyk, M., Bohrmann, G., **Bergès, B. J. P.**, White, P. R., Leighton, T. G., and Wright, I. C. (2012). "*Detection, localization and quantification of the emissions of gas from the seabed in fieldwork and experimental studies using active sonar systems,*" Proceedings of the 11th European Conference on Underwater Acoustics, (ECUA2012), Edinburgh, UK, 2-6 July 2012, 605-612.

Reports

- Sahling, H., **Bergès, B. J. P.**, Boelmann, J., Dimmler, W., Geprägs, P., Glockzin, M., Kaboth, S., Nowald, N., Pape, T., Römer, M., dos Santos Fereirra, C., Schroedter, L., Tomczyk, M. (2012). "*R/V Heincke cruise report HE-387, Gas emissions at the Svalbard continental margin. Longyearbyen - Bremerhaven, 20 August - 16 September 2012,*" Berichte, MARUM – Zentrum für Marine Umweltwissenschaften, Fachbereich Geowissenschaften, Universität Bremen, No. 291, p. 170.

Abstract

The acoustic remote sensing of subsea gas leakage, applied to the monitoring of underwater gas discharges from anthropogenic and natural sources, is becoming increasingly important. First, as the oil and gas industry is facing increasing regulation, there is a need to put more control in the industrial process and to assess the impact on the marine environment. The applications are diverse, including: early warnings of "blow-out" from offshore installations, detection of leaks from underwater gas pipelines, gas leakage detection from Carbon and Capture and Storage facilities (a process aimed at mitigating the release of large quantities of CO2 in the atmosphere), and seabed monitoring. Second, this technology has a role to play in oceanography for a better understanding of natural occurrences of gas release from the sea floor such as methane seeps. This is of major importance for the assessment of the exchange of gas between the ocean and the atmosphere with application to global warming. All those phenomena involve the formation and release of bubbles of different sizes. These are strong sources and scatterers of sound. Within this context, this thesis draws on a two part study.

The first part experimentally addresses the accuracy of a passive acoustic inversion method for the quantification of gas release. Such a technique offers the advantage of lower power requirements for long term monitoring. It is common practice for researchers to identify single bubble injection events from time histories or time frequency representations of hydrophone data, and infer bubble sizes from the centre frequency of the emission. This is well suited for gas release at a low flow rate, involving solitary bubble release. However, for larger events, with overlapping of bubble acoustic emissions, the inability to discriminate each individual bubble injection events makes this approach inappropriate. Using an inverse method based on the spectrum of the acoustic emissions allows quantification of such releases with good accuracy. The inverse scheme is tested using data collected in a large test tank and data collected at sea during the QICS (Quantifying Impacts of Carbon Storage) project.

The second part of the thesis addresses the problem of quantifying gas releases using active acoustics. Single beam echosounders are commonly used instruments in fisheries acoustics. When investigating gas release from the seafloor, they are frequently employed to study the spatial distribution of the gas releases. However, few studies make use of these data to quantify the amount of gas being released. Here, using the common multi-frequency ability of these systems, an inverse method aimed at determining gas volumes is developed. This is tested against simulated data and the method shows good performances in scenarios with limited data sets (data collected at limited number of frequencies). Then, using data collected at sea from methane seeps to the west of Svalbard (from two research cruises), the method is applied and compared to independent measurements of gas fluxes.

Nomenclature

α	regularization factor for Tikhonov method
α_{w}	sound absorption in water
$\bar{\epsilon}$	% error relative to reference volume
β_0	bubble damping factor accounting for non acoustic mechanisms
β_{ac}	bubble damping factor accounting for acoustic mechanisms
β_{th}	bubble damping factor accounting for thermal losses
β_{tot}	bubble total damping factor
β_{vis}	bubble damping factor accounting for viscous losses
$\boldsymbol{\sigma}_{\mathrm{bs}}$	backscattering cross section matrix
δ_{ac}	bubble dimensionless damping factor accounting for acoustic mechanisms
δ_{th}	bubble dimensionless damping factor accounting for thermal losses
δ_{tot}	bubble dimensionless total damping factor
δ_{vis}	bubble dimensionless damping factor accounting for viscous losses
ϵ	quantity associated with the derivation of σ_{bs} (backscattering cross section)
η_{s}	shear viscosity
η_{th}	thermal viscosity

η_l	Coefficient associated with the derivation of the form function of a rigid sphere
$\forall_{1,2}$	coefficients associated with the derivation of β_{th}
Γ	gamma function
γ	ratio of specific heats
$\Gamma_{1,2}$	coefficients associated with Prosperetti's thermal damping derivation
γ_d	sound pressure level decay rate associated with the calculation of reverberation times T_{60}
$\hat{\mathbf{A}}$	kernel matrix of the system associated with Levenberg-Marquardt least squares
$\hat{\mathbf{b}}$	measurements matrix of the system associated with Levenberg-Marquardt least squares
$\hat{\rho}$	$\hat{\rho} = \log\rho$
$\hat{\xi}$	$\hat{\xi} = \log\xi$
$\hat{C}$	curvature function in log-log space for L-curve criterion (Tikhonov and Levenberg-Marquardt methods)
κ	polytropic index
Λ	parameter for Levenberg-Marquardt least squares
$\Lambda_{1,2}$	coefficients associated with the derivation of β_{th}
λ_g	gas thermal conductivity
λ_l	liquid thermal conductivity
$\mathbf{A}$	system's kernel matrix (associated with the description of inverse problems)
$\mathbf{b}$	vector containing outputs of the system (associated with the description of inverse problems)

$\mathbf{e}$	error vector in $\mathbf{b}$
$\mathbf{g}$	vector associated with derivation of Levenberg-Marquardt L-curve criterion
$\mathbf{I}_n$	identity matrix of size $n \times n$
$\mathbf{M}$	singular values matrix (SVD of $\mathbf{A}$)
$\mathbf{N}$	bubble size distribution (BSD) matrix
$\mathbf{s}_{\mathrm{v}_{\mathrm{exact}}}$	exact volume backscattering coefficient vector
$\mathbf{s}_{\mathrm{v}}$	volume backscattering coefficient vector (including measurement errors)
$\mathbf{S}$	spectrum matrix containing the elements of S
$\mathbf{U}$	matrix containing left singular vectors u_i (SVD of $\mathbf{A}$)
$\mathbf{u}_l$	l^{th} left singular vector (SVD of $\mathbf{A}$)
$\mathbf{V}$	matrix containing right singular vectors v_i (SVD of $\mathbf{A}$)
$\mathbf{v}_l$	l^{th} right singular vector (SVD of $\mathbf{A}$)
$\mathbf{x}$	vector containing inputs of the system (associated with the description of inverse problems)
$\mathbf{x}_{\alpha/\Lambda}$	vector containing inputs of the system solved through Tikhonov regularization (α parameter) or Levenberg-Marquardt least squares (Λ parameter)
$\mathcal{L}$	target acoustic length
TS	Target strength
UND	under-determination parameter
x	input of the system (associated with the description of inverse problems)
μ_X	mean of the random variable $\ln(X)$

ν	variable associated with the description of inverse problems
ω	angular frequency
$\omega_{0_{\mathrm{ac}}}$	acoustic contribution to bubble angular resonance frequency
$\omega_{0_{\mathrm{phys}}}$	bubble angular resonnance frequency excluding acoustic contribution
ω_0	bubble angular resonnance frequency
ω_{d}	driving angular frequency
ϕ	phase of the pulse of bubble passive acoustic emission
Ψ	bubble generation rates matrix containing the elements of ψ
ψ	bubble generation rates in radius bins
ψ_{A}	bubble generation rates per unit bubble radius, per unit area, per second
ρ	square of residual norm $\rho = \left\| \mathbf{A}\mathbf{x}_{\alpha/\Lambda} - \mathbf{b} \right\|^2$
ρ_{gA}	density of free gas at sea level
ρ_{g}	density of gas medium
ρ_{l}	density of liquid medium
ρ_{s}	density of solid medium
σ	liquid surface tension
σ_l	l^{th} singular value (SVD of $\mathbf{A}$)
σ_{bs}	backscattering cross section
σ_{sp}	spherical scattering cross section
σ_X	variance of the random variable $\ln(X)$
$\theta_{-3\mathrm{dB}}$	echosounder beam angle
θ_{chi}	parameter of Chi distribution

Υ	GCV function associated with Tikhonov regularization
$\varphi_l^{[\alpha]}$	l^{th} filter factor associated with Tikhonov regularization (parameter α)
ξ	square of solution norm $\xi = \left\Vert \mathbf{x}_{\alpha/\Lambda} \right\Vert^2$
ζ_j	quadrature factors (associated with the description of inverse problems)
A	kernel function associated with the description of inverse problems
a	spherical target radius
$A_{-3\text{dB}}$	echosounder footpring area
$A_{1,2}$	Coefficients associated with the derivation of the form function of a rigid sphere
a_{chi}	parameter of Chi distribution
A_{s}	Sabine coefficient
b	output of the system (associated with the description of inverse problems), including measurement errors
$B_{1,2}$	Coefficients associated with the derivation of the form function of a rigid sphere
b_{exact}	exact output of the system (associated with the description of inverse problems), without measurement errors
C	curvature function for L-curve criterion (Tikhonov and Levenberg-Marquardt methods)
$C_{1,2}$	Coefficients associated with the derivation of the form function of a rigid sphere
c_{g}	speed of sound in gas medium
c_{l}	speed of sound in liquid medium

$C_{\mathrm{p,g}}$	gas specific heat capacity at constant pressure
$C_{\mathrm{p,l}}$	liquid heat capacity at constant pressure
$c_{\mathrm{s_l}}$	compressional wave speed in solid medium
$c_{\mathrm{s_t}}$	shear wave speed in solid medium
$C_{\mathrm{v,g}}$	gas specific heat capacity at constant volume
D	bubble emission size distribution
D_l	quantity associated with the derivation of the modal solution for $\mathcal{L}$
$D_{-3\mathrm{dB}}$	echosounder footprint diameter
D_{g}	gas thermal diffusivity
D_{l}	liquid thermal diffusivity
E	relative noise level
f	frequency
f_∞	form function
$f_{0_{\mathrm{ac}}}$	acoustic contribution to bubble natural frequency
f_0	bubble resonant frequency
f_{d}	driving frequency
F_{gm}	volume gas flux per unit area
F_{g}	flow rate
f_{min}	Schroeder frequency
g_l	l^{th} components of $\mathbf{g}$ vector associated with derivation of Levenberg-Marquardt L-curve criterion
$G_{1,2,3,4,5}$	coefficients associated with Prosperetti's thermal damping derivation
g_ρ	density ratio $g_\rho = \rho_{\mathrm{g}}/\rho_{\mathrm{l}}$

G_l	relative gas flux of l^{th} bubble stream
H	Heaviside step function
h_l	spherical Hankel function of the first kind of order l
h_{c}	sound speed ratio $h_{\mathrm{c}} = c_{\mathrm{g}}/c_{\mathrm{l}}$
i	imaginary number
I_{bs}	intensity of the backscattered wave
I_{i}	intensity of the transmitted wave at the target
j_l	spherical Bessel function of the first kind of order l
$J_{l+1/2}$	Bessel function of the first kind or order $l+1/2$
k	wavenumber in liquid
k_{g}	wavenumber in gas medium
l_{ac}	bubble acoustic length scale
l_{th}	bubble thermal length scale
l_{vis}	bubble viscous length scale
$N(R_0)$	abundance density function
N_0	bubble abundance
N_R	number of radius bins
N_{b}	number of bubbles in the sampled volume
N_{S}	total number of bubble streams
N_ω	number of frequency bins
p_0	ambient pressure
p_{b0}	amplitude of the pulse of bubble passive acoustic emission

p_{b}	acoustic pressure emitted from a single bubble
p_{d}	direct field rms pressure
$P_{\mathrm{Leifer\,major}}$	Leifer major probability density function
$P_{\mathrm{Leifer\,minor\,1}}$	Leifer minor 1 probability density function
$P_{\mathrm{Leifer\,minor\,2}}$	Leifer minor 2 probability density function
$P_{\mathrm{Leifer\,mixed}}$	Leifer mixed probability density function
$P_{\mathrm{lognormal}}$	lognormal probability density function
p_{r}	reverberant field rms pressure
p_{t}	total rms pressure
p_{v}	vapour pressure
$q_{1,2}$	Coefficients associated with the derivation of the form function of a rigid sphere
Q_{θ}	directivity factor
r	range
$R_{0_{\mathrm{d}}}$	dominant equivalent bubble radius
$R_{\epsilon 0i}$	initial displacement amplitude of bubble wall
R_0	equilibrium bubble radius
r_0	reverberant radius
r_{eff}	effective range
R_{Laplace}	Laplace radius
R_{mode}	mode of the probability density function. Value of R_0 for which the probability density function is largest
r_l	range between sensor and l^{th} bubble stream

S	power spectral density
s	variable associated with the description of inverse problems
S_l	liquid salinity
S_o	source output
S_v	$S_\mathrm{v} = 10\log(s_\mathrm{v})$
s_v	volume backscattering coefficient
T	quantity associated with the derivation of X_b
t	time
t_0	formation time of the pulse of bubble passive acoustic emission
T_{60}	reverberation time
T_l	liquid temperature
V	volume of enclosure
v	bubble rise speed
V_0	sampled volume of sonar beam
V_est	estimated volume of simulated volumes
V_ref	reference volume of simulated volumes
W	acoustic source power
X	random variable
X_b	spectrum of a single bubble emission
$Y_{l+1/2}$	Bessel function of the second kind of order $l + 1/2$
y_l	Spherical Bessel function of the second kind of order l

z	depth
CCS	Carbon Capture and Storage
GCV	Generalized Cross Validation
HE387	HE387 research cruise
IPCC	Intergovernmental Panel on Climate Change
JR253	JR253 research cruise
pdf	probability density function
QICS	QICS project (Quantifying Impacts of Carbon Storage)
SNR	Signal to Noise Ratio
SVD	Singular Value Decomposition

1. Introduction

1.1. Background

The monitoring of subsea gas leaks from anthropogenic and natural sources is becoming increasingly important. This applies not only to the detection of gas emissions (e.g. in order to alert pipeline users to a leak) but also in terms of quantification in order to assess gas fluxes (e.g. in order to assess the growth rate of a leak and inform judgement of when to deploy costly intervention). From the seafloor, gas escaping underwater originates from the migration of gas through the sediments and diffuses in the water column either as dissolved gas or as a free gas. In the later, this takes the form of bubbles that, on release into the water column, generate specific acoustic pressure fluctuations [1] and can scatter sound very efficiently [1–3]. The size and structure of those releases vary from small bubble streams to larger bubble clouds. Depending on the flow rate regime (i.e. the size of the leak), various factors contribute to the acoustic emission or the response to a sound wave. In this study, the sound emission or response to sound is assumed to be due to the contribution of gas bubbles generated by the leak. If the flow rate of a leak is sufficiently high, other sources (e.g. jetting noise) are likely to dominate over the acoustic contribution from the bubbles. There is two main reasons for studying such releases. First, there is a need to better characterise gas release mechanisms and amplitudes from natural sources. Second, monitoring requirements for underwater leaks from industrial facilities is increasing.

As the oil and gas industry is facing increasing regulation with respect to marine environmental pollution, there is a need for increased monitoring and control in the industrial processes [4]. In the context of global warming, the control of greenhouse gas emissions to the atmosphere and the ocean is likewise a high priority. Recently, the IPCC working group I (Intergovernmental Panel on Climate Change, working group reporting on the physical science basis of climate change) reported with more than 95% confidence that observed global warming is induced by anthropogenic activities [5–7]. Consequently, the development and maturing of technologies that allow mitigation of the release of greenhouse gases in the atmosphere has become key over the past decade [8] and the need for the development of monitoring technologies and strategies for these mitigation processes has increased. With greenhouse gas mitigation facilities involving undersea operations, gas leaks are a real possibility (i.e. release of gas bubbles) and monitoring using acoustic technologies could be a powerful tool as gas bubbles are found to be strong sources and scatterers of sound [1].

Various technological options to reduce net emissions of CO_2 have been identified [9, 10] and Carbon Capture and Storage (CCS) is to date a promising technology. A complete end-to-end CCS system captures CO_2 from large stationary point sources, transports and injects the compressed CO_2 into a suitably deep (typically more than 800 m below the surface) geologic structure. During or after the injection has stopped, Measurement, Monitoring and Verification (MMV) operations are performed to control the safety, efficacy and permanence of the reservoir. There is a body of literature that is growing about strategies for MMV operations associated with large-scale deployment of CCS because it is important to develop the CCS technology to a stage where the confidence is high. This is important in order to control the industrial process but also to achieve public acceptance [11, 12]. Although there are five large end-to-end commercial CCS facilities in operation around the world to date, in 2013 CCS facilities were not deployed at a large scale [9]. In the UK, there are plans to deploy CCS on a large scale in the 2020s [13].

For CCS facilities, potential gas escapes are of primary concern because this represents a key parameter of the long-term integrity of the CO_2 storage site. Therefore, technologies are needed in order to detect gas leaks of different sizes. This implies methods able to quantify uncontrolled release of gas accurately [14]. In this study, two methods using acoustics are described and their potential application for CCS monitoring is examined. In addition, the method using passive acoustics is deployed during a large scale at sea experiment mimicking gas leakage from a CCS facility. From these data, the accuracy and workability of the passive acoustic method is addressed.

Natural occurrences of gas release are relevant for various reasons. Examples include earthquakes that can be preceded by significant bubble release from the sea floor, which has been proposed as an indicator of such events [15–17]; the melting of growlers in Arctic regions in the form of gas bubbles [18, 19]; and methane seeps from methane hydrate dissociation [20, 21]. In this study, it is methane seeps that are of interest. This has raised interest among oceanographers because of concerns regarding climate change. There is therefore collective researchers that endeavoured to better understand hydrocarbon gas releases as they play an important role in the carbon cycle [20, 21]. Following several decades of interest in gas flux from the atmosphere into the upper ocean layer, and vice versa [22, 23], in recent years there has been growing interest in the climate importance of gas flux into the ocean from the sediment. Such natural gas releases are believed to contribute as a positive feedback for global warming [24, 25]. An increase of ocean temperature due to global warming would cause gas hydrate dissociation and then release of methane gas from the sea floor [24, 25]. This increased release of methane in the water column is of concern for amplified global warming but also for ocean acidification [26]. Recently, the IPCC identified that seabed emissions of CH_4 are poorly understood and requires further investigation [6]. Such gas release results in subsequent emissions to the atmosphere in the form of CO_2 due to oxidation in the water column [7, 27]. Robust and reliable methods able to provide order of magnitude estimates at a low cost are needed and would help furthering the current understanding on the role these natural occurrences have on global warming.

For both anthropogenic and natural gas releases, temporal variability is of importance. The rate of the leakage can change because of increased gas injection from the reservoir or because of environmental parameters. For example, tidal heights can influence the rate at which the gas is being released by several orders of magnitude [28–35]. Berndt et al. [36] recently suggested that long term monitoring of methane seepage to the west of Svalbard is needed in order to assess methane hydrate dissociation in this region because of potential large changes in flow rates over time due to various environmental effects.

Within this context, this study investigates two methods for the monitoring of gas releases in the form of bubbles: a method using active acoustics; a method using passive acoustics. Both methods use established numerical methods for solving inverse problems in order to determine gas fluxes. Gas fluxes are the quantities that are sought. In order to better characterize gas leaks, there is a need to combine different techniques that can work locally and at a larger scale for long and short term monitoring. Here, the active and passive acoustic methods described are shown to be a complementary mean of performing these different types of monitoring.

Active acoustic techniques have frequently been used to locate and produce sonar images of, for example, methane plumes [20]. Because bubbles scatter sound efficiently [1], these systems are powerful tools to locate gas releases in the form of bubbles. In addition, active sonar holds the potential to produce quantitative estimates of these releases [28, 37–42]. Here, data from single beam echosounder instruments firstly designed for fisheries acoustics applications [43, 44], are used. From these data, a novel inverse scheme inspired from fisheries acoustics is described and is aimed to provide assessment of gas fluxes from sonar images of plumes.

Usually, quantification from sonar images of gas plumes only provide a snapshot in time and the temporal variability of the gas release is not determined [28, 37, 38, 40, 41]. Though active acoustic sonars can be used to monitor gas leaks over time [45, 46], the feasibility of these systems is compromised by their high electric power requirements and they are consequently only deployed over limited periods of time. For example, in the case of methane seeps, the study of the temporal variability has only been sparsely measured [34, 36]. Passive emission of gas releases are dominated by the sound of bubbles and this can be acquired at low power cost with relative operational ease using hydrophones. Based on such data set, an inverse method is described here in order to convert the acoustic emissions into quantitative assessments of flow rates, allowing ones to track changes in flow rate in real time over long periods of time.

In this study, data collected during laboratory experiments are presented together with data collected at sea over three research expeditions. These were:

- Research cruise JR253 [47]: research cruise to the west of Svalbard from 26th July to 25thAugust 2011.
- Research cruise HE387 [48, 49]: research cruise to the west of Svalbard from 20th August to 10thSeptember 2012.
- Project QICS (Quantifying Impacts of Carbon Storage) [50]: project that consisted on controlled CO_2 gas release from the seabed. This was aimed at evaluating the impact of potential leaks from CCS (Carbon Capture and Storage) facilities. The gas release phase was conducted from 17th May to 22nd June 2012 near Oban (Scotland).

1.2. Thesis outline

This thesis is divided into eight chapters. The first chapter provides a literature review that highlights the relevance of this study in the context of gas leak monitoring to date (chapter 1). Because inverse methods are used throughout this study, chapter 2 is dedicated to describe the methods that are used in this thesis in order to solve the various numerical inverse problems. This includes theoretical considerations of inverse problems with the need for regularization to mitigate ill-conditioness issues. Two formulations of inverse problems including parametrization of the solution are drawn out (Tikhonov regularization [51] and Levenberg-Marquardt least squares [52]). Then, two methods for optimizing the parametrization of the two inverse methods are outlined (Generalized Cross Validation and L-curve [51, 53]). In chapter 3, theory of bubbles related to acoustics is introduced and constitutes the theoretical basis for the following chapters. First, bubble size regimes will be described in order to clarify various assumptions made throughout this thesis. Then, equations for damping and natural frequencies of spherical gas bubbles are provided, followed by threads discussing passive acoustic emissions and scattering strength from single bubbles. These two last items are the basis of the active and passive acoustic inversions performed within chapters 4, 5, 6 and 7.

Following the theoretical background (chapters 2 and 3), chapter 4 describes an inverse problem based on the passive acoustic emissions of gas bubbles. This inverse scheme is used to estimate gas flow rates. First, theoretical developments are given. Then, results from a laboratory experiment are presented. This outlines the process whereby amounts of gas are injected in a large water tank using two different injection systems and the acoustic emissions are recorded. The comparison of flow rates inferred from acoustics with direct measurements of the amount of injected gas addresses the accuracy of the method. This laboratory trial constitutes a validation exercise for the deployment of hydrophones in the framework of the QICS project (aimed at investigating the potential impact of gas leaks from CCS facilities). During this project, over a period of 7 days, acoustic emissions of gas leaks were recorded. Using the passive acoustic inversion, gas flow rates are estimated. Procedures and results of this trial are reported in chapter 5.

Primary data set of gas leaks from the seabed usually consists of single beam echosounder data. In particular, calibrated acoustic systems with multiple frequency channels are of interest here. These are useful for detection but are only sparsely used to give quantitative assessments of gas volumes. In chapter 6, an inverse scheme based on the backscattering from gas bubbles at multiple frequencies is described. Drawing on simulated data from different bubbles size distributions from the literature [54, 55], the accuracy of the method is examined. More specifically, the efficiency of the method for a limited number of frequency channels is investigated. The three frequencies inversion case is the most limited but is found to give accurate estimates depending on the bubble size distribution. Also, a two frequency scheme is described and tested. Then, using data from 2 research cruises (JR253, HE387), these active acoustic inverse methods are applied. Procedures and results are presented in chapter 7. This chapter shows the potential use of these methods, i.e. the ability to track changes in flow rates in the water column or to give order of magnitude of gas fluxes along with their spatial variability.

Finally, conclusions are drawn in chapter 8 on the use of the passive and active acoustic techniques described in this thesis, summarizing their individual advantages and disadvantages. Discussion on how the research undertaken in this thesis could be furthered is provided as concluding remarks.

2. The inverse problem

2.1. Introduction

So called inverse problems are those that use direct measurements to determine indirectly information on a system (whether the input of the system or the system itself, Figure 2.1). This is largely applied in physics and applications are various, spanning domains such as remote sensing of the atmosphere [56] or reconstruction of blurred images [51]. Applied to underwater acoustics, this has applications to e.g. acoustic tomography or localization [57, 58]. In this study, gas quantification is attempted using two inverse approaches: based on the acoustic emissions of gas bubbles (chapters 4 and 5); based on measurements of the acoustic backscattering from gas bubbles (chapters 6 and 7). The subject of solving inverse problems is, for example, covered extensively by Hansen [51, 59] or Doicu [56]. This study will use two established methods. In this chapter, theoretical development will be outlined in order to provide background for the calculations presented in the following chapters.

A problem dependent on 2 variables s and ν is considered (known as a Fredholm integral of the first kind) and defined as:

$$\int A\left(s,\nu\right)\mathrm{x}\left(\nu\right)d\nu = b\left(s\right), \tag{2.1}$$

with $b\left(s\right)$ representing the measurable quantity and $\mathrm{x}\left(\nu\right)$ the input of the system (the sought quantity). The quantity $A\left(s,\nu\right)$ is the kernel of the problem, i.e. where the modelling of the physical process is incorporated. Equation 2.1 defines the continuous forward problem and to assist with solving it, a discretized form is sought. Defining the variables at discrete points $\nu_j\ j = 1,\ldots,n$ and $s_j\ j = 1,\ldots,m$, the problem can be approximated as a system of linear equations:

$$\mathbf{Ax} = \mathbf{b}, \tag{2.2}$$

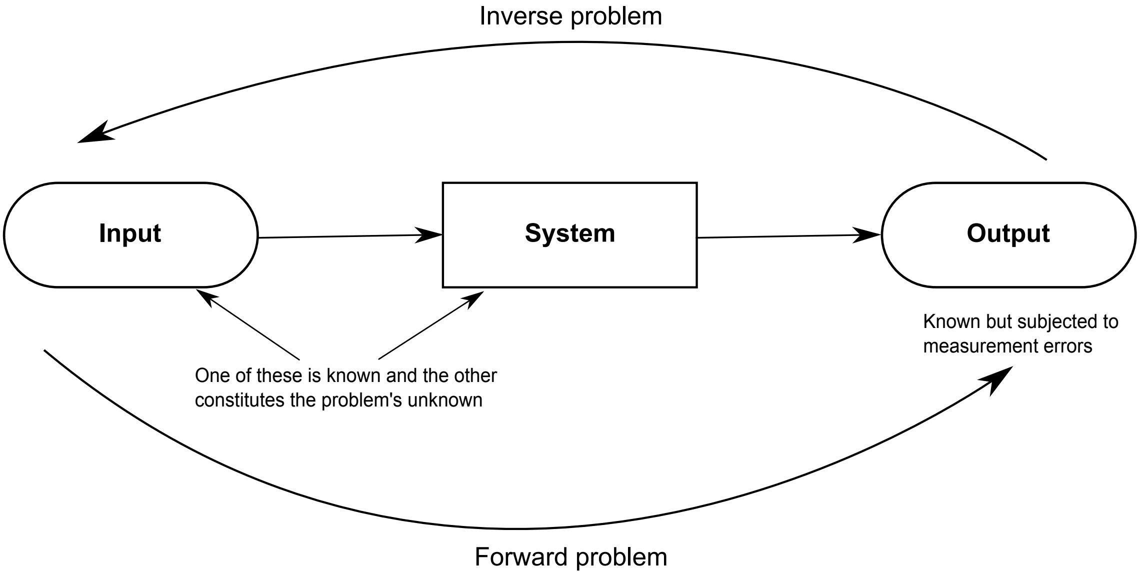

Figure 2.1.: Diagram exemplifying inverse problems. An input to a system produces an output, this is the forward problem. The output represents the measurements that are collected with inevitable errors. Solving the inverse problem consists on determining either the system or the input. In this thesis, input quantities are sought and the system is where modelling is involved.

with $\mathbf{b}$ the vector containing the measurements, the kernel matrix $\mathbf{A}_{jl} = \zeta_l A\left(s_j, \nu_l\right)$ and $\mathbf{x} = \mathrm{x}\left(\nu_j\right)$ the discrete values of the input of the system (sought quantity). When constructing the discretized kernel matrix $\mathbf{A}_{jl}$, ζ_l is the quadrature factor that is used to approximate the continuous problem to a discrete form. For easiness of use, the midpoint rule is used here, $\zeta_l = \frac{\nu_{\max} - \nu_{\min}}{n}$ and represents the spacing between each ν linearly spaced bins. Other approaches for discretization exist and are extensively described by Hansen [51, chapter 3] or Doicu [56, chapter 2]. Three cases arise when approximating the problem at discrete points:

- $m > n$: in this case, the problem is under-determined with less measurements than discrete bins for $\mathbf{x}$.
- $m < n$: in this case, the problem is over-determined with more measurements than discrete bins for $\mathbf{x}$.
- $m = n$: in this case, the problem is square with an equal number of measurements and discrete bins for $\mathbf{x}$.

Square and under-determined problems are of interest later in this thesis. Square inverse problems are constructed for the passive acoustic inversion in chapter 4 and chapter 5. In chapter 6 and chapter 7 (active acoustic inversion), because of the limited number of measurements for each inversion process, the inverse problem is considered as squared and under-determined.

The level of noise in the measurements depends on the problem considered [51] and the measurement vector can be expressed as $\mathbf{b} = \mathbf{b}_{\text{exact}} + \mathbf{e} = b\left(s_j\right)$ with $\mathbf{e}$ a vector that represents errors in the measurement vector $\mathbf{b}$. When solving inverse problems, because small perturbations in $\mathbf{b}$ (e.g. due to measurement errors and ill-condition of the kernel matrix $\mathbf{A}$) produce high perturbations in $\mathbf{x}$, the naive solution $\mathbf{x} = \mathbf{A}^{-1}\mathbf{b}$ does not solve the problem accurately and formulations that lessen the sensitivity of the computed solution are needed [51]. Various solution methods exist in the literature [51, 56, 60] and their performances are dependant upon the formulated problem [51]. Throughout this study, two solution methods are used: Tikhonov regularization and Levenberg-Marquadt least squares. Leighton and White [61] found that Tikhonov regularization is suitable to solve the passive acoustic inversion described in chapter 4 and chapter 5 (square problem). Levenberg-Marquardt least squares is shown to be efficient at solving the active acoustic inversion [60, 62] described in chapter 6 and chapter 7 (square/over-determined problem). The two solution methods are expended on in the following sections.

2.2. Solution methods

Tikhonov regularization The Tikhonov regularization (or ridge regression) allows one to compute $\mathbf{x}$, enforcing regularity of the solution through the regularization factor α. This quantity controls the balance between the norm of the solution $\|\mathbf{x}\|$ and the norm of the residual $\|\mathbf{Ax} - \mathbf{b}\|$. The problem in matrix form is commonly expressed as [51]:

$$\mathbf{x}_\alpha = \left(\mathbf{A}^t\mathbf{A} + \alpha^2\mathbf{I}_n\right)^{-1}\mathbf{A}^t\mathbf{b} \tag{2.3}$$

with $\mathbf{I}_n$ the identity matrix of size $n \times n$ and $\mathbf{x}_\alpha$ the solution vector obtained with the regularization factor α. The choice of the regularization parameter α takes different forms [51, chapter 5].

The passive acoustic inverse problem described by Leighton and White [61] (of interest in chapter 4 and chapter 5) is used to illustrate the effect of different

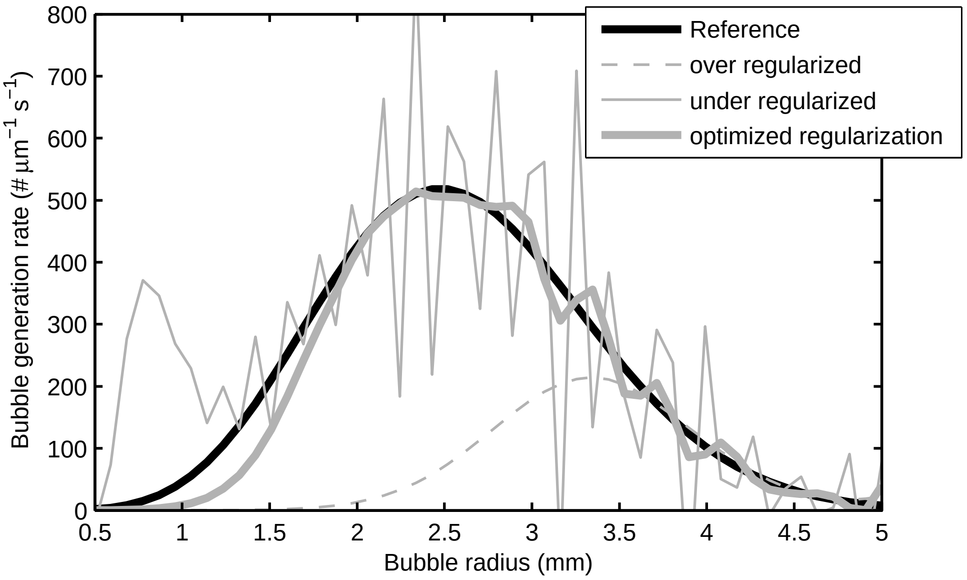

Figure 2.2.: Comparison of solutions computed with different amount of regularization for the inverse problem described by Leighton and White [61] and recalled in chapter 4. The results are computed using Tikhonov regularization with α being: over regularized (dashed grey line); under regularized (solid grey line); optimally regularized (using GCV criterion, thick solid grey line). The thick solid black line is the reference distribution.

levels of regularization in Figure 2.2. The data that are inverted are simulated with a moderate amount of noise. The inverse scheme used to obtain the solution is extensively described in chapter 4. In this particular problem, the solution vector $\mathbf{x}_\alpha$ represents the rate of generation of bubbles of different sizes. With the reference distribution represented as the thick solid black line, Figure 2.2 shows the regularized solution computed when α is too small (thin solid grey line) or too large (thin dashed grey line). Using an optimal amount of regularization through the Generalized Cross Validation criterion (GCV, section 2.3), the initial distribution is recovered with good accuracy (thick solid grey line). With decreasing α, the solution $\mathbf{x}_\alpha$ tends to the solution $\mathbf{x} = \mathbf{A}^{-1}\boldsymbol{b}$ ($\alpha = 0$) where small perturbations in $\mathbf{b}$ lead to large perturbations in the solution. This is observable in Figure 2.2 where the low regularization case exemplifies large spikes and high frequency oscillations. With large α, the solution is smooth but scaled down compared to the reference distribution. It can be noted that a constraint on the positivity of the solution $\mathbf{x}_\alpha$ can be added when optimizing the regularization parameter α.

Levenberg-Marquardt A second approach for solving the inverse problem (Equation 2.2) is described here with the Levenberg-Marquardt least squares [52, 60, 62]. This method is used in chapter 6 and chapter 7. Extended theoretical developments are addressed for example by Lawson and Hanson [52, Chap. 25] or by Greenlaw and Johnson [60]. This technique offers advantages for solving under-determined problems and has for example been applied for the determination of zooplankton populations from echosounder data [43, 60, 62–64]. The inverse problem as in Equation 2.2 is modified to include the Levenberg-Marquardt parameter Λ:

$$\begin{bmatrix} \hat{\mathbf{b}} \\ \mathbf{0} \end{bmatrix} = \begin{bmatrix} \hat{\mathbf{A}} \\ \Lambda \left\| \hat{\mathbf{A}} \right\| \mathbf{I}_n \end{bmatrix} \mathbf{x}_{\Lambda}, \tag{2.4}$$

with the modified kernel matrix $\hat{\mathbf{A}} = \mathbf{A}_{jl}/\mathbf{b}_j$ and the new measurement vector $\hat{\mathbf{b}} = \mathbf{b}_j/\mathbf{b}_j$. In Equation 2.4, the solution vector $\mathbf{x}_{\Lambda}$ is dependent upon the Levenberg-Marquardt parameter Λ that controls its stability. In an expanded and more explicit form, Equation 2.4 is:

$$\begin{array}{r} m\left\{\vphantom{\begin{matrix}1\\ \vdots\\ 1\end{matrix}}\right. \\ n\left\{\vphantom{\begin{matrix}0\\ \vdots\\ 0\end{matrix}}\right. \end{array} \begin{bmatrix} 1 \\ \vdots \\ 1 \\ 0 \\ \vdots \\ 0 \end{bmatrix} = \begin{array}{r} m\left\{\vphantom{\begin{matrix}1\\ \vdots\\ 1\end{matrix}}\right. \\ n\left\{\vphantom{\begin{matrix}0\\ \vdots\\ 0\end{matrix}}\right. \end{array} \underbrace{\begin{bmatrix} \zeta_1 A\left(s_1, \nu_1\right)/b\left(s_1\right) & \cdots & \zeta_n A\left(s_1, \nu_n\right)/b\left(s_1\right) \\ \vdots & \ddots & \vdots \\ \zeta_1 A\left(s_m, \nu_1\right)/b\left(s_m\right) & \cdots & \zeta_n A\left(s_m, \nu_n\right)/b\left(s_m\right) \\ \Lambda \left\| \hat{\mathbf{A}} \right\| & \cdots & 0 \\ \vdots & \ddots & \vdots \\ 0 & \cdots & \Lambda \left\| \hat{\mathbf{A}} \right\| \end{bmatrix}}_{n} \mathbf{x}_{\boldsymbol{\Lambda}} . \tag{2.5}$$

Solutions to this problem can be computed using least squares algorithms. In chapter 6 and chapter 7, a positivity constraint is needed when solving the inverse problem and this issue is addressed by using the non negative least squares algorithm (NNLS) as described by Lawson and Hansen [52, chapter 23].

The Levenberg-Marquardt formulation in Equation 2.5 leads to a non-squared problem. This is a consequence of adding zeros to the measurement vector, making it of size $(m+n) \times 1$ and the component $\Lambda \left\| \hat{\mathbf{A}} \right\| \mathbf{I}_n$ to the kernel matrix, making it of size $(m+n) \times n$. This formulation gives robustness against under-determination of the problem [52, 62]. The level of under-determination is introduced with the under-determination parameter UND. Defining, $n = \mathrm{UND} \times m$, UND controls the number of discretized size bins for ν, having it equal of greater than the number of measurement points. Then, by increasing UND, it artificially enhances the resolution of the solution $\mathbf{x}_{\mathbf{\Lambda}}$ but as UND increases, the stability of $\mathbf{x}_{\mathbf{\Lambda}}$ decreases [52, 60, 62]. The optimized amount of under-determination is specific to each inverse problem [52]. For example, in the case of biovolume zooplankton estimations from single beam echosounder data, Lebourges-Dhaussy and Ballé-Béganton [62] find an optimal value of UND = 4.

2.3. Choosing the regularization parameter

Methods described in section 2.2 are formulations of Equation 2.2 that allow one to control the behaviour of the computed solution with a parameter: α for Tikhonov regularization; Λ for Levenberg-Marquardt least squares. Two methods for computing these parameters are described here: the L-curve criterion; the GCV criterion. While the L-curve can be used for both Tikhonov regularization and Levenberg-Marquardt least squares, the formulation for the GCV criterion given here only applies to the Tikhonov regularization.

L-curve The L-curve criterion consists of minimizing the solution norm $\|\mathbf{x}\|$ together with the residual norm $\|\mathbf{Ax} - \mathbf{b}\|$. This commonly used technique is referred as the L-curve criterion because when plotted in a log-log space, this consists on finding the corner of the curve that forms an “L” shape [53]. Figure 2.3(a) shows the L-curve criterion as used to compute the optimized solution in Figure 2.2. It can be observed that the optimized α is found at the corner of the curve. From a mathematical perspective, finding the corner of the curve corresponds to finding the maximum curvature of $\left(\log \left\|\mathbf{x}_{\alpha/\Lambda}\right\|, \log \left\|\mathbf{A}\mathbf{x}_{\alpha/\Lambda} - \mathbf{b}\right\|\right)$. Defining $\xi = \left\|\mathbf{x}_{\alpha/\Lambda}\right\|^2$ and $\rho = \left\|\mathbf{A}\mathbf{x}_{\alpha/\Lambda} - \mathbf{b}\right\|^2$ the curvature function C is given by:

$$C(\alpha) = \frac{\rho^{'}\xi^{''} - \rho^{''}\xi^{'}}{\left((\rho^{'})^2 + (\xi^{'})^2\right)^{3/2}}, \tag{2.6}$$

with the symbols $'$ and $''$ denoting derivation with respect to the parameter α or Λ. Introducing $\hat{\xi} = \log\xi$ and $\hat{\rho} = \log\rho$, the first and second derivatives of these quantities are then:

$$\begin{aligned} \hat{\xi}' &= \frac{\xi'}{\xi} \quad , \quad \hat{\xi}'' = \frac{\xi''\xi - \left(\xi'\right)^2}{\xi^2} \\ & \qquad\qquad\qquad\qquad\qquad\qquad , \\ \hat{\rho}' &= \frac{\rho'}{\rho} \quad , \quad \hat{\rho}'' = \frac{\rho''\rho - \left(\rho'\right)^2}{\rho^2} \end{aligned} \tag{2.7}$$

and from Equation 2.6 the corresponding curvature function $\hat{C}$ in log-log space is:

$$\hat{C} = 2 \times \frac{\hat{\rho}'\hat{\xi}'' - \hat{\rho}''\hat{\xi}'}{\left(\left(\hat{\rho}'\right)^2 + \left(\hat{\xi}'\right)^2\right)^{3/2}}. \tag{2.8}$$

The optimization of parameters α and Λ is computed from the calculation of the terms ρ', ρ'', ξ', ξ'' for the case of Tikhonov regularization and Levenberg-Marquardt methods. As a function of α and Λ, these terms are derived in Appendix B. The curvature function of the curve shown in Figure 2.3(a) is displayed in Figure 2.3(b). This shows the optimized value of α as the maximum of $\hat{C}$.

Generalized Cross Validation (GCV) The GCV is a statistical technique for the optimization of the regularization factor α. Separating the measurement vector $\mathbf{b}$ into two sets of data, one is used to compute a solution which is then used to predict the elements in the other set. Such process is repeated, separating $\mathbf{b}$ differently each time. The resulting α is the one that optimizes best all the combinations. In the specific case of Tikhonov regularization the GCV criterion can be reduced to a function of α [51]:

$$\Upsilon(\alpha) = \frac{\left\|\mathbf{A}\mathbf{x}_\alpha - \mathbf{b}\right\|^2}{\left(m - \operatorname{tr}\left(\mathbf{A}\left(\mathbf{A}^t\mathbf{A} + \alpha^2\mathbf{I}_n\right)^{-1}\mathbf{A}^t\right)\right)^2}. \tag{2.9}$$

The optimization of α through the GCV criterion for the problem shown in Figure 2.2 is displayed in Figure 2.4 with the optimal α found at the minimum of $\Upsilon(\alpha)$. In the case of the example in Figure 2.2, the L-curve and GCV criteria both give the same optimized regularization factor. In the case of Tikhonov regularization, a positivity constraint can be implemented by enforcing each element in $\mathbf{x}_\alpha$to be positive when computing $\Upsilon(\alpha)$ or $\hat{C}(\alpha)$. This constraint is implemented when solving the inverse problems throughout this thesis because the final result of the

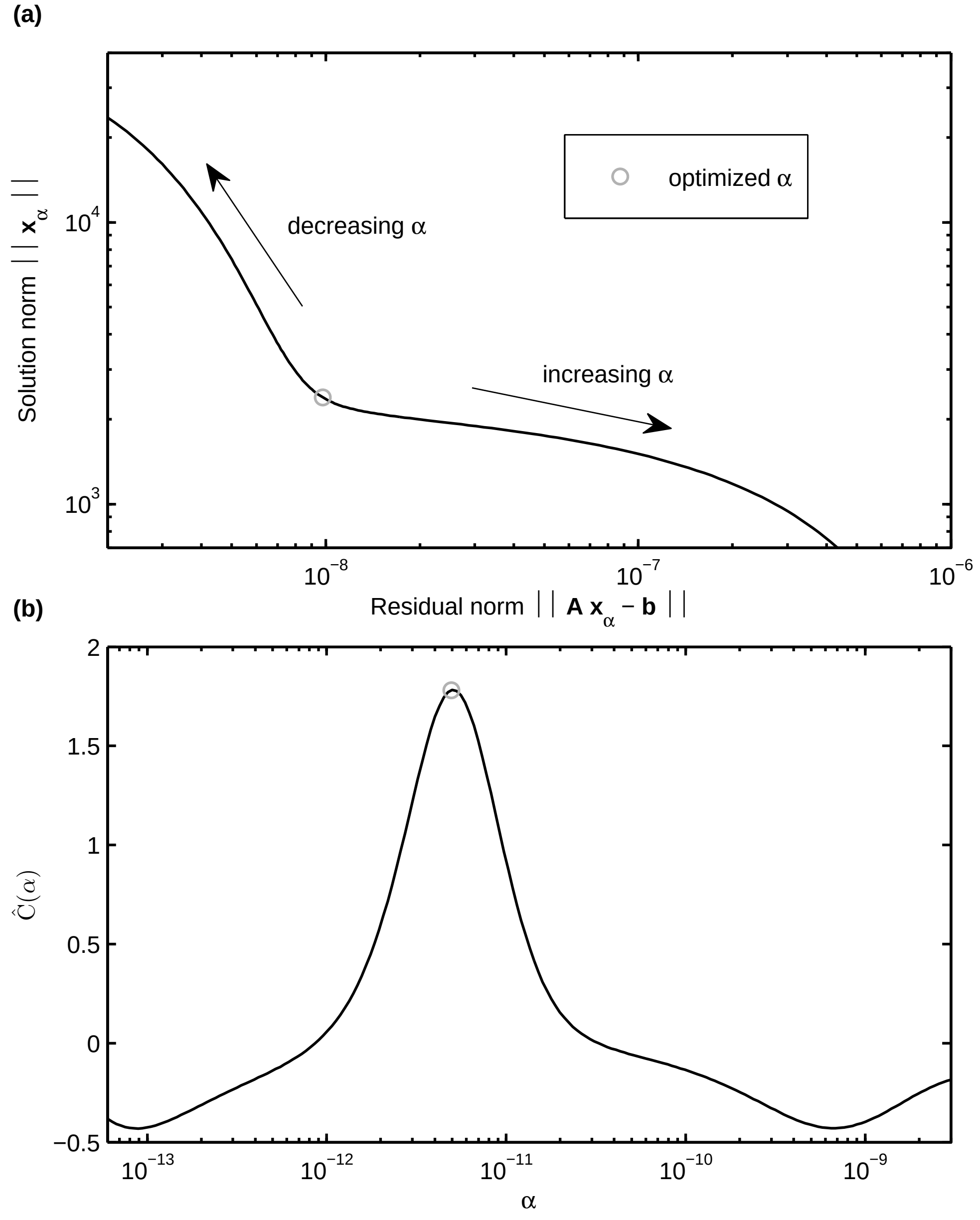

Figure 2.3.: Example of optimization of the regularization parameter α using the L-curve criterion. (a): Solution norm $\|\mathbf{x}_\alpha\|$ versus residual norm $\|\mathbf{A}\mathbf{x}_\alpha - \mathbf{b}\|$. The optimized α is found at the corner of the plotted curve. (b): Curvature function $\hat{C}(\alpha)$ of the curve plotted in (a) versus α. The optimized α is found at the maximum of the curvature function.

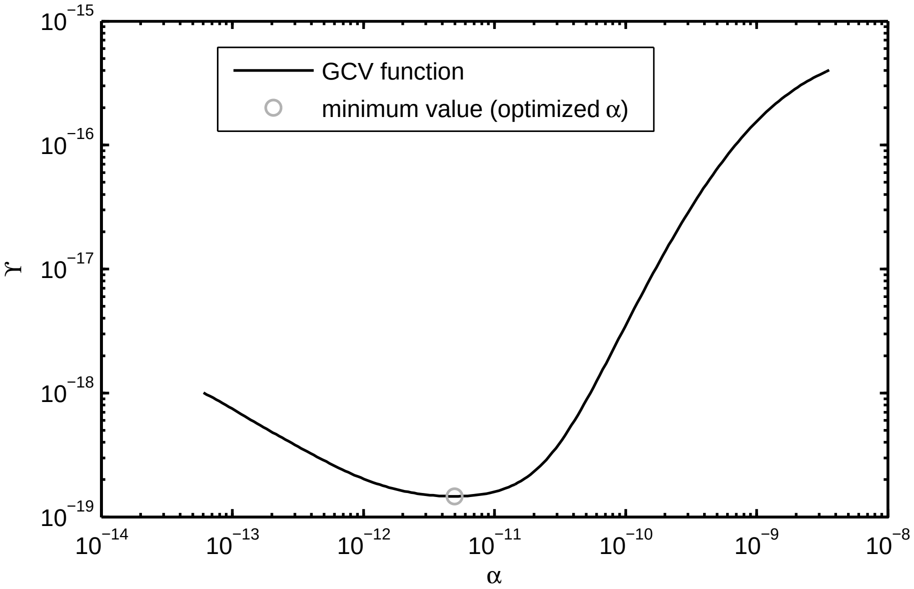

Figure 2.4.: Example of optimization of the regularization parameter α using the GCV criterion. With the GCV function $\Upsilon(\alpha)$ plotted against α, the optimized value for α is found at the minimum of $\Upsilon(\alpha)$.

inverse methods consists on distributions of bubble sizes. As negative distributions are not physically representative, the solutions are taken to be positive or equal to 0.

2.4. Summary

In this chapter, two methods for solving inverse problems are presented: Tikhonov regularization; Levenberg-Marquardt least squares. Each method is controlled by a parameter (α, Λ) that defines the stability of the solution and two methods are given to optimize these parameters: the GCV criterion; the L-curve criterion. Futher in this thesis, the GCV criterion is used to optimize α when solving Tikhonov regularization because of its computing efficiency and easiness of implementation. For Levenberg-Marquardt, the L-curve criterion is used to compute Λ. The main difference between regularization and least squares methods for solving the inverse problem is that regularization methods assume a smooth solution [51]. It is known that the performance of a solving method is dependent upon the inverse problem considered [51, 59] because each method offers benefits at the cost of drawbacks. Choosing between the different solving schemes can contain a certain degree of subjectivity. While Tikhonov regularization is shown to be efficient at solving the passive acoustic inverse problem (chapter 4) [61], Levenberg-Marquardt has been used for year for solving the active acoustic inverse problem considered here (chapter 6) [60, 62, 65–68]. These solution methods are used as follows throughout this thesis:

- chapter 4 and chapter 5: use of Tikhonov regularization (with GCV criterion).
- chapter 6: Tikhonov regularization (with GCV criterion) and Levenberg-Marquardt least squares (with L-curve criterion) methods are compared in this chapter. Because Levenberg-Marquardt least squares are shown to perform better, it is used throughout for solving the active acoustic inverse problem.
- chapter 7: use of Levenberg-Marquardt least squares (with L-curve criterion).

In chapter 3, theoretical developments are given for the models used to build the kernel matrices for the inverse problems considered later in this thesis.

3. A review of the acoustics of gas bubbles

3.1. Introduction

The subject of this thesis is the study of gas release in the form of bubbles, aiming at quantifying them using active and passive acoustics. Gas releases often take the form of bubbles and their interaction with acoustic fields is of interest in this section. Theoretical basis is given here and is used in the following chapters. First, bubble size regimes are described, helping giving consistency in assumptions being made when relating bubbles with the acoustic field. Then, expressions for the natural frequency and damping of a spherical gas bubbles are given. Using these, the spectrum of the acoustic emission of a single gas bubble is derived and forms the basis for the inversion method presented in chapter 4 and chapter 5. Lastly, models for the scattering cross section of a gas bubbles are given together with discussion about their limitations. This is of importance for chapter 6 and chapter 7. Throughout this section, parameters used to produce the various figures are listed in Appendix E and are chosen as typical for sea water (surrounding medium) and air (gas in the bubble). The speed of sound in water c_l is calculated using Lovett equations [69] and density ρ_l, vapour pressure p_v, shear viscosity η_s and surface tension σ are calculated using formulas given by Siedler and Peters [70]. These make use of the following parameters: salinity S_l; temperature T_l; depth z.

3.2. Bubble size regimes

When discussing acoustic interaction with bubbles, many assumptions are usually undertaken by for example considering “small” or “large” bubbles relative to different aspect. Recently, Ainslie and Leighton [3] clarified these assumptions by proposing quantities for the bubble size in the acoustical, thermal, viscous and Laplace pressure senses. This are expressed as specific length scales that are the following:

- The acoustic length scale l_{ac} corresponds to the acoustic wavelength and is expressed in terms of the driving angular frequency $\omega_{\mathrm{d}} = 2\pi f_{\mathrm{d}}$ (f_{d} being the driving frequency of the acoustic field) and the speed of sound in the surrounding liquid c_{l} as:
$$l_{\mathrm{ac}}\left(\omega_{\mathrm{d}}\right) = \frac{2\pi c_{\mathrm{l}}}{\omega_{\mathrm{d}}}. \tag{3.1}$$
- The viscous length scale l_{vis}, in terms of the shear viscosity η_{s}, the surrounding medium density ρ_{l} and the driving frequency ω_{d} is:
$$l_{\mathrm{vis}}\left(\omega_{\mathrm{d}}\right) = \sqrt{\frac{2\eta_{\mathrm{s}}}{\rho_{\mathrm{l}}\omega_{\mathrm{d}}}}. \tag{3.2}$$
- The thermal length scale l_{th} or thermal diffusion length is given by:
$$l_{\mathrm{th}}(\omega_{\mathrm{d}}, R_0) = \sqrt{\frac{D_{\mathrm{g}}\left(R_0\right)}{2\omega_{\mathrm{d}}}}, \tag{3.3}$$

with D_{g} being the thermal diffusivity of the gas inside the bubble that can be expressed in terms of the specific heat capacity at constant pressure $C_{\mathrm{p,g}}$, the thermal conductivity of the gas λ_{g} and the gas density inside the bubble ρ_{g}:

$$D_{\mathrm{g}}\left(R_0\right) = \frac{\lambda_{\mathrm{g}}}{\rho_{\mathrm{g}}\left(R_0\right) C_{\mathrm{p,g}}}. \tag{3.4}$$

According to Clay and Medwin [71, (A6.1.24)]:

$$\rho_{\mathrm{g}}\left(R_0\right) = \rho_{\mathrm{gA}}\left(1 + \frac{2\sigma}{p_0 R_0}\right)\left(1 + 0.1z\right), \tag{3.5}$$

with ρ_{gA} the density of free gas at sea level, p_0 the ambient pressure, σ the liquid surface tension and z the depth.

- The Laplace radius R_{Laplace} (the equilibrium bubble radius at which the Laplace pressure is equal to the equilibrium surrounding medium pressure) is:
$$R_{\mathrm{Laplace}} = \frac{2\sigma}{p_0}. \tag{3.6}$$

3.3. Natural frequency

As a bubble is released into the water column, it undergoes fluctuations in its volume which efficiently radiates sound [1]. These oscillations decay with time and so the detectable acoustic emission has a finite duration. The bubbles will be assumed to be spherical and these volume changes result from oscillations of the bubble radius R about the equilibrium radius R_0. The natural frequency relates to the radius R_0 which has been used for decades to count and size bubbles in laboratories, and even in the natural world for studies of waterfalls [72], wave-breaking and rain at sea [73, 74], and methane seeps [75].

A theory for the bubble natural frequency f_0 was first proposed by Minnaert [76] as a function of the equilibrium radius R_0, assuming a spherical bubble in a liquid undergoing low amplitude simple harmonic motion. Adding the assumptions that the gas inside the bubble behaves adiabatically and that bubbles are acoustically small, $R_0 \ll l_{\mathrm{ac}}$ (commonly stated as $kR_0 \ll 1$, with $k = \omega_{\mathrm{d}}/c_{\mathrm{l}}$ the wavenumber), the "Minnaert resonance frequency" is given by:

$$f_0\left(R_0\right) = \frac{1}{2\pi R_0}\sqrt{\frac{3\gamma p_0}{\rho_{\mathrm{l}}}}, \tag{3.7}$$

with $\gamma = C_{\mathrm{p,g}}/C_{\mathrm{v,g}}$ the ratio of specific heats of the gas inside the bubble ($C_{\mathrm{v,g}}$ being the specific heat capacity at constant volume and $C_{\mathrm{p,g}}$ the specific heat capacity at constant pressure). Equation 3.7 approximates f_0 and was later adapted by Leighton [1, equation (4.86)]:

$$f_0\left(R_0\right) = \frac{1}{2\pi R_0\sqrt{\rho_{\mathrm{l}}}}\sqrt{3\kappa\left(p_0 - p_{\mathrm{v}} + \frac{2\sigma}{R_0}\right) - \frac{2\sigma}{R_0} + p_{\mathrm{v}} - \frac{\eta_{\mathrm{s}}^2}{\rho_{\mathrm{l}} R_0^2}}. \tag{3.8}$$

This expression accounts for the effect of vapour pressure p_{v}, surface tension σ, and shear viscosity η_{s} in the surrounding medium. The polytropic index κ accounts for the behaviour of the gas (varying from adiabatic behaviour $\kappa = \gamma$, to isothermal behaviour $\kappa = 1$). Furthermore, when the bubble is subjected to an acoustic field at frequency ω_{d}, the driving acoustic field contributes to f_0 as:

$$\omega_0^2 = \omega_{0_{\mathrm{phys}}}^2 + \omega_{0_{\mathrm{ac}}}^2, \tag{3.9}$$

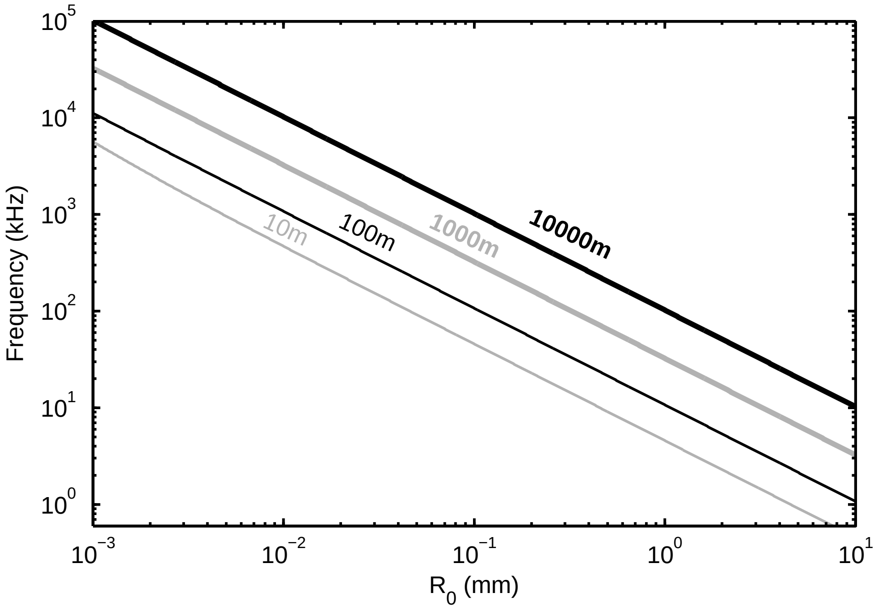

Figure 3.1.: Resonance frequency f_0 of a gas bubbles in water versus bubble sizes at different depths: $z = 10$m (thin grey line); $z = 100$m (thin black line); $z = 1000$m (thick grey line); $z = 10000$m (tick black line).

with ω_0, $\omega_{0_{\text{phys}}}$, and $\omega_{0_{\text{ac}}}$ the angular frequencies: $\omega_0 = 2\pi f_0$. The quantify $f_{0_{\text{ac}}}$ is given by [77]:

$$f_{0_{\text{ac}}} = \frac{1}{2\pi}\sqrt{(\omega_{\text{d}} R_0/c_{\text{l}})^2 \left[1 + (\omega_{\text{d}} R_0/c)^2\right]^{-1} \omega_{\text{d}}^2}. \tag{3.10}$$

The contribution of the driving acoustic field is usually disregarded as its effects are of importance only for large bubbles in acoustic fields presenting high frequencies [77]. The natural frequency against bubble radii R_0 is shown in Figure 3.1 at different depths. With increasing depth, the natural frequency increases. Throughout this thesis, depths of interest range from ≈ 5 m to ≈ 400 m.

3.4. Damping

The total damping factor β_{tot} of a gas bubble in a liquid is a combination of thermal damping β_{th}, viscous damping β_{vis} and acoustic damping β_{ac}:

$$\beta_{\text{tot}} = \underbrace{\beta_{\text{th}} + \beta_{\text{vis}}}_{\beta_0} + \beta_{\text{ac}}, \tag{3.11}$$

with β_0 the contribution of non acoustic mechanisms. In the literature, damping is given as factors with dimensions of s^{-1} (β_{tot}, β_{th}, β_{vis}, β_{ac}) [77] or dimensionless damping factors (δ_{tot}, δ_{vis},δ_{th},δ_{ac}) [71, 78, 79]. Recently, Ainslie and Leighton [2, 3] reviewed the theory and clarified these notations. The relation between the two type of damping factors is:

$$\beta_{\mathrm{i}} = \frac{\delta_{\mathrm{i}}\omega_{\mathrm{d}}}{2} \qquad \mathrm{i} = \mathrm{tot, th, vis, ac}. \tag{3.12}$$

The linear theory for the calculation of damping factor was extensively described for example by Clay and Medwin [71], Medwin [78, 80], Prosperetti [77] or Leighton [1]. The theory by Medwin has been widely used but a discrepancy for the acoustic damping is reported and resolved by Ainslie and Leighton [2, 3] in the framework of the derivation of spherical gas bubble scattering cross sections. In a correct form, it is expressed as:

$$\beta_{\mathrm{ac}} = \frac{\omega_{\mathrm{d}} R_0/c_{\mathrm{l}}}{1 + (\omega_{\mathrm{d}} R_0/c_{\mathrm{l}})^2} \frac{\omega_{\mathrm{d}}}{2}. \tag{3.13}$$

The theory by Prosperetti [77] can be used to determined the damping constants β_{th}, and β_{vis}. Those quantities are defined as [77]:

$$\beta_{\mathrm{vis}} = \frac{2\eta_{\mathrm{s}}}{\rho_{\mathrm{l}}} R_0^2, \tag{3.14}$$

$$\beta_{\mathrm{th}} = \frac{\eta_{\mathrm{th}}}{\rho_{\mathrm{l}}} R_0^2, \tag{3.15}$$

with η_{th} the thermal viscosity. The calculation of this quantity based on the clarified derivation of Prosperetti [77] by Leighton [1] and Zhang and Li [81] is presented below.

Thermal viscosity and polytropic index calculation In order to determine the thermal viscosity η_{th} and the polytropic index κ, the dimensionless parameters G_1, G_2, G_3 and G_4 are defined for the calculation of the general term G_5. The term G_1 is the square of the ratio of the thermal diffusion l_{th} length to the gas acoustic wavelength while G_2 and G_3 represent the thermal diffusion in the liquid and the gas respectively. The quantities G_1, G_2 and G_3 are given by:

$$G_1 = \left(\frac{l_{\mathrm{th}}}{c_{\mathrm{g}}/\omega_{\mathrm{d}}}\right)^2, \tag{3.16}$$

$$G_2 = \frac{1}{2}\left(\frac{R_0}{l_{\mathrm{th}}}\right)^2, \tag{3.17}$$

$$G_3 = \frac{\omega_{\mathrm{d}} R_0^2}{D_{\mathrm{l}}}, \tag{3.18}$$

where c_{g} is the speed of sound of the gas inside the bubble and D_{l} is the thermal diffusivity of the liquid defined as:

$$D_{\mathrm{l}} = \frac{\lambda_{\mathrm{l}}}{\rho_{\mathrm{l}} C_{\mathrm{p,l}}}. \tag{3.19}$$

The quantities λ_{l}, ρ_{l} and $C_{\mathrm{p,l}}$ are respectively the thermal conductivity, the density and the heat capacity at constant pressure of the surrounding liquid. Other quantities that are used for the calculation of G_5 are:

$$\left\{\begin{array}{c} G_4 = \dfrac{k}{k_{\mathrm{g}}}\left(1 + (1+i)\sqrt{\dfrac{G_3}{2}}\right) \\ \\ \Gamma_{1,2} = i + G_1 \pm \sqrt{(i - G_1)^2 + \dfrac{4i\mathrm{G}_1}{\gamma}} \\ \\ \forall_{1,2} = \sqrt{\dfrac{\gamma G_2}{2}\left(i - G_1 \pm \sqrt{(i - \mathrm{G}_1)^2 + \dfrac{4i\mathrm{G}_1}{\gamma}}\right)} \\ \\ \Lambda_1 = \forall_1 \coth(\forall_1) - 1 \\ \\ \Lambda_2 = \forall_2 \coth(\forall_2) - 1 \end{array}\right. . \tag{3.20}$$

The general term G_5 is finally given by:

$$G_5 = \frac{G_4(\Gamma_2 - \Gamma_1) + \Lambda_2\Gamma_2 - \Lambda_1\Gamma_1}{G_4(\Lambda_2\Gamma_1 - \Lambda_1\Gamma_2) - \Lambda_2\Lambda_1(\Gamma_2 - \Gamma_1)}, \tag{3.21}$$

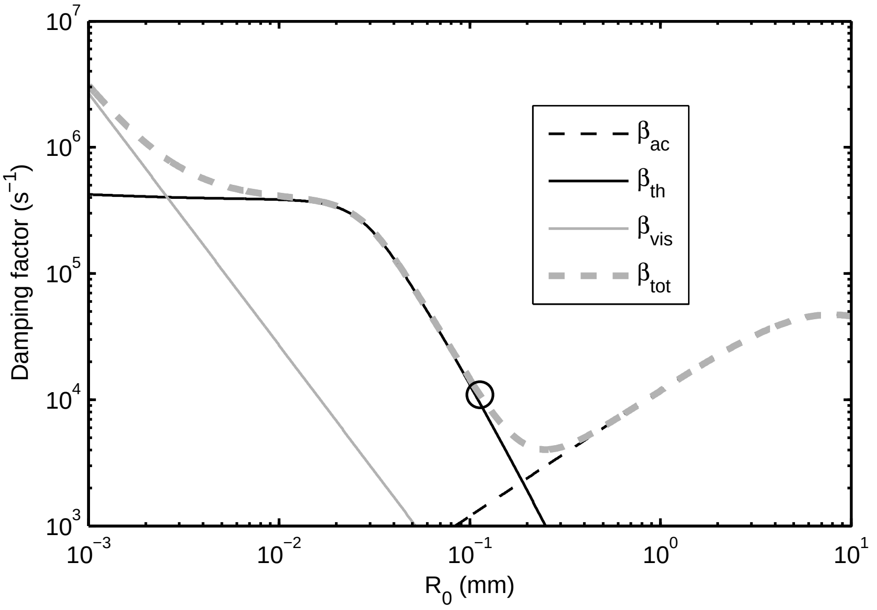

Figure 3.2.: Damping coefficients versus bubble size R_0 within an acoustic field driven at $f_\mathrm{d} = 30$ kHz at a depth $z = 10$ m. The solid black line is β_th, the solid grey line is β_vis, the dashed black line is β_ac and β_tot is represented by the thick dashed grey line. For different R_0, β_tot is dominated by different damping mechanisms (thermal, viscous, acoustic).

and the thermal viscosity η_th is:

$$\eta_\mathrm{th} = \frac{\omega_\mathrm{d}\rho_\mathrm{g}R_0^2}{4}\mathrm{Im}\left(\mathrm{G}_5\right), \tag{3.22}$$

with the polytropic index κ expressed as:

$$\kappa = \frac{\omega_\mathrm{d}^2\rho_\mathrm{g}R_0^2}{3\left(\frac{2\sigma}{R_0} + p_0\right)}\mathrm{Re}\left(G_5\right). \tag{3.23}$$

The different components of bubble damping are shown in Figure 3.2, exemplifying the asymptotic behaviours at different bubble sizes. For large bubble radii, β_tot is dominated by β_ac while at $R_0 \to 0$, viscous damping dominates. In the transition, the thermal damping has the most significant contribution.

3.5. Passive acoustic emission

The oscillations of the acoustic emission from a gas bubble occur close to the natural frequency f_0 of the bubble and decay exponentially. This can be ideally described as a damped sinusoid [1, 82]:

$$p_{\mathrm{b}}\left(t, R_0\right) = p_{\mathrm{b}0}\cos\left(\omega_0\left(t-t_0\right)+\phi\right)e^{-\omega_0\delta_{\mathrm{tot}}\left(t-t_0\right)/2}H\left(t-t_0\right), \tag{3.24}$$

with t_0 the bubble formation time, ϕ the pulse phase and $H\left(t-t_0\right)$ the Heaviside step function at time t_0. The quantity $p_{\mathrm{b}0}$ is the pulse amplitude and can be expressed as a function of the initial displacement amplitude of the bubble wall $R_{\epsilon0i}$ and the range r (distance between the observation point and the bubble) [82]:

$$p_{\mathrm{b}0} = R_{\epsilon0i} \times \frac{3\kappa p_0}{r}. \tag{3.25}$$

Using Minnaert expression (Equation 3.7, neglecting the effects of vapour pressure, surface tension and shear viscosity), the polytropic index can be expressed as $\kappa = \frac{\omega_0^2 R_0^2 \rho_{\mathrm{l}}}{3p_0}$ and $p_{\mathrm{b}0}$ can further be given by:

$$p_{\mathrm{b}0} = R_{\epsilon0i} \times \frac{\omega_0^2 R_0^2 \rho_{\mathrm{l}}}{r} = \frac{R_{\epsilon0i}}{R_0} \times \frac{\omega_0^2 R_0^3 \rho_{\mathrm{l}}}{r}. \tag{3.26}$$

Assuming a pulse phase $\phi = 0$ and applying the Fourier transform to equation Equation 3.24 gives:

$$X_{\mathrm{b}}\left(\omega, R_0\right) = \int_{-\infty}^{+\infty} p_{\mathrm{b}0}\cos\left(\omega_0\left(t-t_0\right)\right)e^{-\omega_0\delta_{\mathrm{tot}}\left(t-t_0\right)/2}H\left(t-t_0\right)e^{-it\omega}dt, \tag{3.27}$$

with the angular frequency $\omega = 2\pi f$. Expanding Equation 3.27 yields:

$$X_{\mathrm{b}}\left(\omega,R_0\right)= p_{\mathrm{b}0}\left[\int\limits_{t_0}^{+\infty}\cos\left(\omega_0\left(t-t_0\right)\right)e^{-\omega_0\delta_{\mathrm{tot}}(t-t_0)/2}H\left(t-t_0\right)e^{-it\omega}dt+\right.$$
$$\left.\int\limits_{-\infty}^{t_0}\cos\left(\omega_0\left(t-t_0\right)\right)e^{-\omega_0\delta_{\mathrm{tot}}(t-t_0)/2}H\left(t-t_0\right)e^{-it\omega}dt\right].$$

With the Heaviside step function being equal to 0 on the interval $]-\infty,0]$ and 1 on the interval $[0,+\infty[$:

$$X_{\mathrm{b}}\left(\omega,R_0\right)=p_{\mathrm{b}0}\int\limits_{t_0}^{+\infty}\cos\left(\omega_0\left(t-t_0\right)\right)e^{-\omega_0\delta_{\mathrm{tot}}(t-t_0)/2}e^{-it\omega}dt.$$

Using variable $T=t-t_0$:

$$X_{\mathrm{b}}\left(\omega,R_0\right)=p_{\mathrm{b}0}e^{-i\omega t_0}\int\limits_{0}^{+\infty}\cos\left(\omega_0 T\right)e^{-T[\omega_0\delta_{\mathrm{tot}}/2+i\omega]}dT,$$

and recalling that $\int e^{bx}\cos\left(ax\right)dx=\dfrac{e^{bx}\left(a\sin\left(ax\right)+b\cos\left(ax\right)\right)}{a^2+b^2}$ leads to:

$$X_{\mathrm{b}}\left(\omega,R_0\right)=-p_{\mathrm{b}0}e^{-i\omega t_0}\frac{\omega_0\delta_{\mathrm{tot}}/2+i\omega}{\left(\omega_0\delta_{\mathrm{tot}}/2+i\omega\right)^2+\omega_0^2}. \tag{3.28}$$

The square magnitude of X_{b} is then:

$$\left|X_{\mathrm{b}}\left(\omega,R_0\right)\right|^2=p_{\mathrm{b}0}^2\times\frac{4\left[\left(\omega_0\delta_{\mathrm{tot}}\right)^2+4\omega^2\right]}{\left[\left(\delta_{\mathrm{tot}}\omega_0\right)^2+4\left(\omega_0-\omega\right)^2\right]\left[\left(\delta_{\mathrm{tot}}\omega_0\right)^2+4\left(\omega_0+\omega\right)^2\right]}. \tag{3.29}$$

This model assumes that each bubble is excited only once [87], generating an initial amplitude of bubble wall pulsation for the breathing mode ($R_{\epsilon 0\mathrm{i}}$ for want of further information [61]), a quantity that could be treated as being broadly invariant with depth and the nature of the gas-emitting orifice, an assumption that this study examines experimentally in chapter 4 and chapter 5. Assumptions about the correct

Reference	Bubble radius (mm)	$R_{\epsilon 0i}/R_0$	Comments
Leighton and Walton [72]	≈ 1	$\approx 10^{-4}$	Laboratory experiment, nozzle injection. Analysis from Leighton [1]
Pumphrey and Walton [83]	≈ 0.44	$\approx 7.5 \times 10^{-5}$	Laboratory experiment, water drop. Extracted from Leighton and White [61].
Medwin and Beaky [84]	≈ 0.312	$\approx 1.5 \times 10^{-2}$	Laboratory experiment, bubbles from breaking waves.
Pumphrey and Crum [85]	≈ 0.43	$\approx 7.5 \times 10^{-3}$	Laboratory experiment, water drop.
Deane and Stokes [82, 86]	[0.065 2.6]	$[5.4 \times 10^{-6}, 0.02]$	Laboratory study, bubble fragmenting in sheared flow.

Table 3.1.: Table summarizing current knowledge on the $R_{\epsilon 0i}/R_0$ factor.

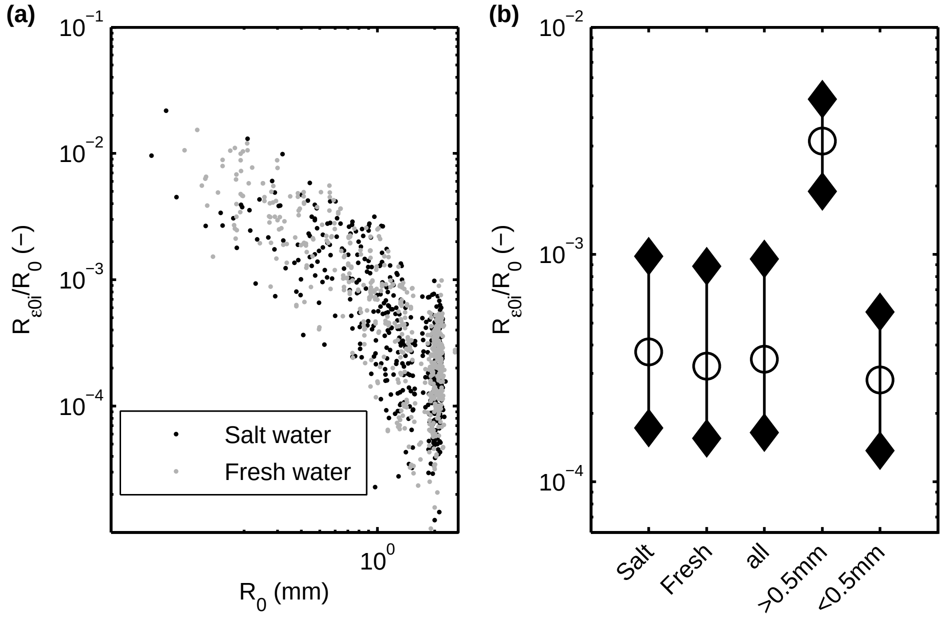

Figure 3.3.: Measures of $R_{\epsilon 0\mathrm{i}}/R_0$ for bubbles fragmented in sheared flow in fresh and salt water. Data were kindly provided by Grant Deane and are published in [82]. (a): $R_{\epsilon 0\mathrm{i}}/R_0$ versus R_0 for salt (black dots) and fresh water (grey dots). (b): Mean values (circle markers), 75th and 25th percentiles (diamond markers) of $R_{\epsilon 0\mathrm{i}}/R_0$ for: Salt water; fresh water; combining all data points; combining all data points with $R_0 < 0.5\,\mathrm{mm}$; combining all data points with $R_0 > 0.5\,\mathrm{mm}$.

value of $R_{\epsilon 0\mathrm{i}}$ to use constitutes the main source of uncertainty for the model and the estimated flow rates in chapter 4 and chapter 5. The parameter that characterises this effect in the model is the dimensionless ratio $R_{\epsilon 0\mathrm{i}}/R_0$ (taken as a constant value) in Equation 3.26. In order to better predict this factor for different bubble sizes and nozzle types, more experimental and theoretical work is needed and here, constant values are used to help solving the inverse problem because this reduces the number of unknown [88]. Through the literature, $R_{\epsilon 0\mathrm{i}}/R_0$ has been evaluated only few times within different applications on the field and in laboratory experiments: nozzle injections [1, 72]; water drop on water surface [83–85]; bubble fragmenting in sheared flow [86, 89]. The values for each reference are summarized in Table 3.1. It can be observed that $R_{\epsilon 0\mathrm{i}}/R_0$ can vary significantly between the studies, especially because the range of bubbles sizes and bubble generation processes considered are various. When describing their inverse scheme, Leighton and White [90] use the constant value of $R_{\epsilon 0i}/R_0 = 3.7 \times 10^{-4}$, inferred from Deane and Stokes [82, 86]. Here, data kindly provided by Grant Deane [82] are examined and used to determine uncertainties in the acoustic estimates of gas fluxes.

For now, the most recent and complete estimate of this ratio comes from Deane and Stokes [82], who calculated $R_{\epsilon 0\mathrm{i}}/R_0$ for fragmented bubbles in sheared flow. This data set consists on the acoustic emission of 1010 fragmented bubbles in a 15 m deep test tank, 2 m away from the water surface. A nozzle releases bubbles that are fragmented by a sheared flow approximately 20 cm above the bubble injection point. From each fragmented bubble signature, using Equation 3.24, the following parameters are estimated: t_0, ϕ, ω_0, $p_{\mathrm{b}0}$, δ_{tot}. Furthermore, from the measurements of $p_{\mathrm{b}0}$, using Equation 3.26, the quantity $R_{\epsilon 0\mathrm{i}}/R_0$ can be determined and results are shown in [82, Figure 7]. A scatter plot is shown in Figure 3.3(a), reproducing this data set. Most data points relate to bubbles of radius greater than 1 mm and $R_{\epsilon 0\mathrm{i}}/R_0$ increases with decreasing bubble size for $R_0 < 1\,\mathrm{mm}$ while above $R_0 = 1\,\mathrm{mm}$, $R_{\epsilon 0\mathrm{i}}/R_0$ levels off. In Figure 3.3(b), statistics (mean value, 75th and 25th percentiles) are shown for different cases: in salt water; in fresh water; combining all data points; combining all data points with $R_0 < 0.5\,\mathrm{mm}$; combining all data points with $R_0 > 0.5\,\mathrm{mm}$. The value of 0.5 mm is chosen because this corresponds to the lowest bubble sizes considered in chapter 4 and chapter 5. The quantity $R_{\epsilon 0\mathrm{i}}/R_0$ seems to be invariant with salinity. However, a significant difference is noticeable between large ($R_0 > 0.5$ mm) and small bubbles ($R_0 < 0.5$ mm), suggesting a dependence of $R_{\epsilon 0\mathrm{i}}/R_0$ at low bubble sizes. In the regime $R_0 > 0.5\,\mathrm{mm}$, employing the assumption that $R_{\epsilon 0\mathrm{i}}/R_0$ is invariant with depth and bubble size, a confidence interval is determined for $R_{\epsilon 0\mathrm{i}}/R_0$ based on the 25th and 75th percentiles. This is used in chapter 4 and chapter 5. Respectively, this corresponds to $R_{\epsilon 0\mathrm{i}}/R_0 = 1.37 \times 10^{-4}$ and $R_{\epsilon 0\mathrm{i}}/R_0 = 5.58 \times 10^{-4}$ (the fixed value of 3.7×10^{-4} used by Leighton and White [61] lies within this range).

3.6. Scattering cross section

The ability of an object to scatter sound is defined by its acoustic scattering cross section. If a sound transmitter and a sound receiver are separate (bistatic sonar), the differential scattering cross section is used [91], quantity that is function of the direction of the receiver relative to the transmitter. In this study, the case where transmitter and receiver are co-located (monostatic sonar) is of interest and the acoustic backscattering cross section σ_{bs} (which measures the acoustic energy scattered in the direction opposite to the direction of the incident wave) is considered. For a target of size a, with I_{i} the intensity of the transmitted wave at the target and I_{bs} the intensity of the backscattered wave, σ_{bs} is defined as:

$$\sigma_{\mathrm{bs}} = \frac{r^2 I_{\mathrm{bs}}\left(a,r\right) 10^{\alpha_{\mathrm{w}}/10}}{I_{\mathrm{i}}}, \tag{3.30}$$

with α_{w} the sound absorption in water and σ_{bs} is often expressed on a logarithmic scale as the “target strength” TS $= 10\log\left(\sigma_{\mathrm{bs}}\right)$. In Figure 3.4 the backscattering cross section is plotted versus ka for the case of a gas bubble and a tungsten carbide sphere (rigid sphere, theory presented in Appendix D). In the case of the gas bubble, the target size a is equivalent to the equivalent radius R_0. The results for σ_{bs} are shown as divided by πa^2 (equal to πR_0^2 in the case of the gas bubble) [92]. The graph exemplifies two ka regimes:

- $ka \ll 1$: for the sphere and the gas bubble, Rayleigh scattering occurs at low ka where σ_{bs} increases linearly with ka. In the case of the gas bubble, resonance scattering follows from Rayleigh scattering with a sharp peak at the bubble natural frequency f_0.
- $ka \gg 1$: this is the scattering regime where the geometry of the target is mostly accountable for the acoustic scattering. In this regime, the response is the consequence of the interaction of various modes. This causes the scattering to be very spiky.

Urick [93, chapter 9] gives approximations of σ_{bs} for rigid spheres corresponding to the rigid high frequency limits of objects of different geometries. For a large sphere, $\sigma_{\mathrm{bs}} = a^2/4$. In Figure 3.4, this is plotted as the horizontal dashed black line and can be observed to be the line around which σ_{bs} for the gas bubble and tungsten carbide sphere converge for large ka. For the gas bubble, depending on the regime, σ_{bs} can be modelled with different accuracies and two models are described in the following sections: the breathing mode solution, limited to $kR_0 \ll 1$ (subsection 3.6.1); the modal solution that is valid for all kR_0 but imprecise for $kR_0 \ll 1$ (because it does not account for damping effects, subsection 3.6.2).

3.6.1. Breathing mode solution

In the case of a spherical gas bubble, models have been developed, accounting for the omnidirectional breathing mode resonance [71, 80, 91]. Theory has been recently reviewed by Ainslie and Leighton [2, 3], clarifying discrepancies that existed about

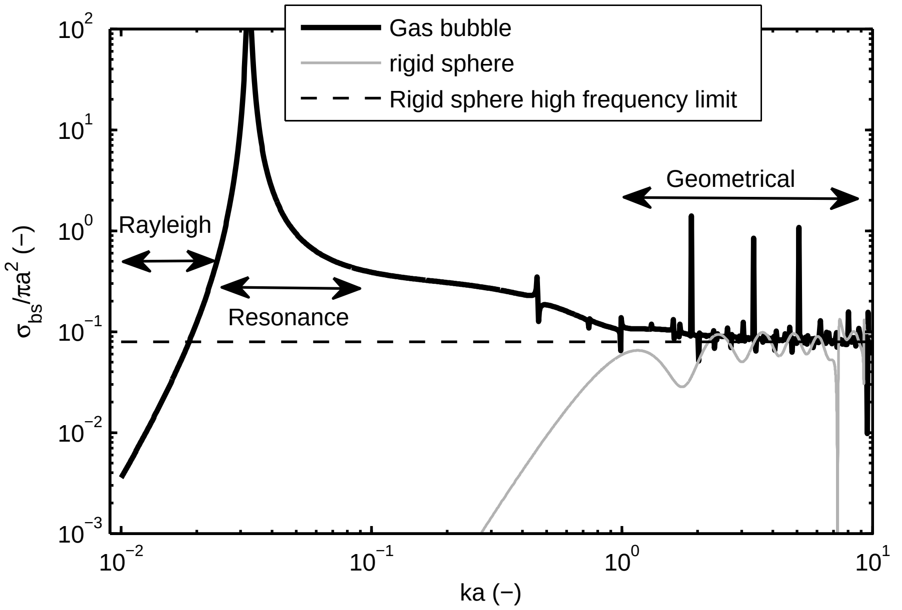

Figure 3.4.: comparison of backscattering cross sections σ_{bs} for gas bubbles, tungsten carbide spheres [94, 95] and for large spheres when neglecting constituents of the object [93, chapter 9] ($\sigma_{\mathrm{bs}} = a^2/4$, rigid sphere high frequency limit). This plot exemplifies two regimes: $ka \ll 1$ with resonance (for the gas bubble only) and Rayleigh scattering; $ka \gg 1$ with geometrical scattering.

these calculations. This models the backscattering of a gas bubble within the regime $kR_0 \ll 1$ (i.e. assuming that the bubble is acoustically small, $R_0 \ll l_{\mathrm{ac}}$). In an acoustic field driven at a frequency ω_{d}, σ_{bs} is [2, 3]:

$$\begin{cases} \sigma_{\mathrm{bs}}\left(R_0, \omega_{\mathrm{d}}\right) = \dfrac{R_0^2}{\left(\frac{\omega_0^2}{\omega_{\mathrm{d}}^2} - 1 - 2\frac{\beta_0}{\omega_{\mathrm{d}}}\epsilon\right)\left(2\frac{\beta_0}{\omega_{\mathrm{d}}} + \frac{\omega_0^2}{\omega_{\mathrm{d}}}\epsilon\right)} \\ \\ \epsilon = \omega_{\mathrm{d}}\dfrac{R_0}{c_{\mathrm{l}}} \end{cases}. \tag{3.31}$$

A solution accounting for the contribution of the breathing mode overcoming the limitation $kR_0 \ll 1$ (i.e. valid for all kR_0) is proposed by Thuraisingham [96] :

$$\sigma_{\mathrm{bs}}\left(R_0, \omega\right) = \frac{R_0^2}{\left(\dfrac{\omega_0^2}{\omega_{\mathrm{d}}} - 1 - 2\dfrac{\beta_0}{\omega_{\mathrm{d}}}\epsilon\right)\left(2\dfrac{\beta_0}{\omega_{\mathrm{d}}} + \dfrac{\omega_0^2}{\omega}\epsilon\right)} \times \frac{\left(\sin\left(kR_0\right)/kR_0\right)^2}{1 + \left(kR_0\right)^2}. \tag{3.32}$$

In the regime, $kR_0 \ll 1$ Equation 3.31 is an adequate approximation for σ_{bs} because in this regime, the acoustic scattering is dominated by the contribution of the breathing mode. With increasing kR_0, the contribution of the breathing mode is lessened. Following Equation 3.32, the decay of the contribution of the breathing mode is given by the term $\left(\sin\left(kR_0\right)/kR_0\right)^2/1 + \left(kR_0\right)^2$. With increasing R_0, the contribution of the breathing mode decreases, so that the contribution of other modes becomes more significant. A comparison between models in Equation 3.32 and Equation 3.31 is shown in Figure 3.5(a). It can be observed that as kR_0 increases, entering the transition region ($kR_0 \approx 1$) and in the geometrical scattering regime ($kR_0 \gg 1$), σ_{bs} for the breathing mode decreases by several order of magnitude. In the geometrical regime ($kR_0 \gg 1$), the modal solution better models σ_{bs} and is described in subsection 3.6.2 (Equation 3.34). Furthermore, Figure 3.5(b) shows that with increasing depth, the breathing mode resonance of σ_{bs} is shifted toward larger kR_0.

3.6.2. Modal solution

This section describes the scattering from a spherical bubble by the mean of a modal solution. This solution does not include bubble damping effects due to viscous and

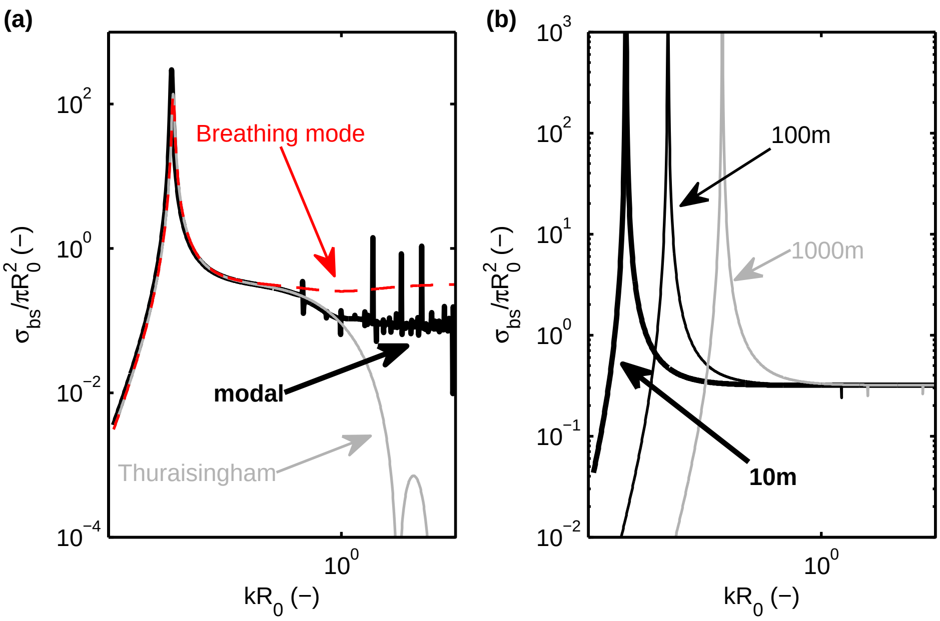

Figure 3.5.: (a): Comparison of different models for σ_{bs}: breathing mode solution (thin dashed red line, Equation 3.31); Thuraisingham model (thin grey line, Equation 3.32); modal solution (thick black line, Equation 3.34). The breathing mode solution is only valid at $kR_0 \ll 1$ (key assumption of the analytical expressions in Equation 3.31). At $kR_0 \ll 1$, Equation 3.31 models σ_{bs} accurately because the contribution of the breathing mode dominates other the contribution of other modes. However, Thuraisingham model shows that the contribution of the breathing mode is decreasing significantly with increasing kR_0. At $kR_0 \gg 1$, the modal solution (Equation 3.34) estimates best σ_{bs} because it sums the contribution of all modes. However, Equation 3.34 does not account for damping effects (section 3.4) that are important for the modelling of σ_{bs} around the resonance. (b): Comparison of σ_{bs} (computed using Equation 3.31) for different depths: 10 m (thick black line); 100 m (thin black line); 1000 m (thin grey line). The resonance scattering shifts toward larger kR_0 for larger depths.

thermal losses [77] (section 3.4). These effects have a significant contribution for the scattering around the resonance but is of lessened importance when considering geometrical scattering. In addition to the drawback of not accounting for bubble damping effects, the main disadvantage of the modal solution is the computation time required as this can be significant if summing over many modes. For processing efficiency, approximations are given for example by Stanton [92] or Johnson [97]. Because the accuracy of the modal solution is lessened in the $kR_0 \ll 1$ regime, it is recommended to use formulations that are modelling more precisely the contribution of the breathing mode (e.g. subsection 3.6.1). Figure 3.5(a) shows the need for a solution including both the breathing mode and higher order modes to model σ_{bs} in the regimes $kR_0 \approx 1$ and $kR_0 \gg 1$. For example at $kR_0 \gg 1$ the decrease and level off in σ_{bs} is not modelled by the breathing mode solution (comparing dashed red line and thick black line in Figure 3.5(a)). Equation 3.31 is best used when modelling scattering around the resonance because σ_{bs} is dominated by the contribution of the breathing mode and damping effects are important. Although Equation 3.31 assumes that $kR_0 \ll 1$, Thuraisingham's analytical solution (Equation 3.32) [96] overcomes this assumption. However, as it can be observed in Figure 3.5(a) (Thuraisingham solution, grey line), the contribution of the breathing mode is decreasing by several orders of magnitude with increasing kR_0. For $kR_0 \approx 1$ and $kR_0 \gg 1$, it is clear that a solution accounting for the various modes in addition to the breathing mode is needed and the modal solution (Equation 3.34) is therefore best suited for the modelling of σ_{bs} in this regime.

The modal solution of spheres is described in the early work of Faran [98] and is extended to the limiting case of fluid-filled spheres by Anderson [99]. Anderson's solution has often been revisited [95, 97, 100, 101] and been tried to be simplified for computation efficiency [92, 97]. The formulation of σ_{bs} by Feuillade and Clay [100] is used here and is shown as the thick black line in Figure 3.5(a). In the acoustic far field ($kr \gg 1$), the backscattering cross section in terms of the acoustic length $\mathcal{L}$ is given by:

$$\sigma_{\mathrm{bs}}\left(R_0, \omega_{\mathrm{d}}\right) = \left|\mathcal{L}\right|^2, \tag{3.33}$$

and for a gas bubble, $\mathcal{L}$ is as:

$$\begin{aligned}\mathcal{L} &= \frac{iR_0}{kR_0}\sum_{l=0}^{\infty}(-1)^l(2l+1)\,D_l \\ D_l &= \frac{j_l'(k_\mathrm{g}R_0)\,j_l(kR_0) - g_\rho h_\mathrm{c}\times j_l(k_\mathrm{g}R_0)\,j_l'(kR_0)}{j_l'(k_\mathrm{g}R_0)\,h_l(kR_0) - g_\rho h_\mathrm{c}\times j_l(k_\mathrm{g}R_0)\,h_l'(kR_0)}\end{aligned}, \tag{3.34}$$

where $g_\rho = \rho_\mathrm{g}/\rho_\mathrm{l}$ and $h_\mathrm{c} = c_\mathrm{g}/c_\mathrm{l}$ are the ratios of densities and sound speed respectively and $k_\mathrm{g} = \omega_\mathrm{d}/c_\mathrm{g}$ is the wavenumber in the gas bubble. The quantities j_l and h_l are respectively the spherical Bessel function and spherical Hankel functions of the first kind, with the symbol $'$ denoting derivation with respect to the quantity inside the brackets. The depth z can approximately be accounted for by scaling the density ratio: $g_\rho(z) = \rho_\mathrm{g}/\rho_\mathrm{l}\times(1+0.1z)$ [92].

3.6.3. Irregular shapes and changing incidence

Models described in subsection 3.6.1 and subsection 3.6.2 assume spherical bubbles. For small bubbles, the assumption that bubbles are spherical holds. However, as bubbles get larger, their shape tends to be more irregular [102] and it becomes important to take this effect into account when modelling σ_bs. Larger bubbles imply larger kR_0, tending to lie in the $kR_0 \gg 1$ region (best modelled by the modal solution). Furthermore, in this regime, a change of geometry leads to significant discrepancies in σ_bs [62, 65].

For fisheries acoustics, scattering from gas filled objects of different shapes are of interest in order to model acoustic scattering traces from fishes presenting swimbladers. Stanton [92, 95] gives calculations of σ_bs through modal solutions for regular and irregular spheres, prolate spheroids, straight cylinder and bent cylinder with different shell types. Deviations from these simple shapes constitute the irregular factor in the models. In the case of a gas bubble [92, figure 3], the irregularity in the shape is found to have a significant impact at $kR_0 \gg 1$. In the low kR_0 regime ($kR_0 \ll 1$), Ye [103, 104] derives analytical expressions for the sound scattering from prolate spheroids with different aspect ratios. This shows a reduction in the height of the resonance peak together with its shift toward higher kR_0 [104, figure 1]. Similar results are found by Feuillade [105, figure 2].

Furthermore, with a spherical bubble, the scattering can be assumed to be omnidirectional at low frequencies, but with increasing size and irregularities in the shape, the directivity pattern becomes more directional and complex [91]. In short, the incidence angle of the sound wave on the gas bubble becomes more important when working in the geometrical regime $kR_0 \gg 1$. This is shown by Okumura [106, figure 1-d] where a 90° incidence angle produces a drop in target strength of up to 30 dB in the geometric regime (increased discrepancy for larger kR_0).

In chapter 6 and chapter 7, the modal solution (assuming spherical bubbles) described in subsection 3.6.2 is used. However, because large bubbles are considered (bubbles from 1 mm to 10 mm, see chapter 6 and chapter 7), irregularities in the bubble shapes are likely and the effect of the deviation from sphericity combined to varying incidence angles are potential sources of error. Chapter 6 and chapter 7 discuss a preliminary assessment of an active acoustic inverse method (subsection 6.4.2) for simulated and field data assuming spherical bubbles.

3.7. Summary

In this chapter, theoretical background used in the following chapters is given. In this thesis, acoustic inversions are based on the spectrum from passive emissions of gas bubbles (chapter 4 and chapter 5, theory in section 3.5) and on the backscattering strength of gas bubbles (chapter 6 and chapter 7, theory in section 3.6). The models used to form the kernel matrix of the system in both of these problems are given in final form by Equation 3.29 (passive acoustic inversion) and Equation 3.34 (active acoustic inversion).

First, an expression that predicts the spectrum of a bubble of size R_0 at a given frequency f is derived. A key parameter in this model is the initial amplitude of bubble wall pulsation for the breathing mode ($R_{\epsilon 0\mathrm{i}}$). This quantity, expressed as a dimensionless ratio $R_{\epsilon 0\mathrm{i}}/R_0$ can vary depending for example on the bubble size or the type of bubble injection. This factor is the main source of error and a data set from Deane and Stokes [82, 86] is used to construct confidence intervals that are used to determine uncertainties for the acoustic estimates in chapter 4 and chapter 5.

Second, gas bubble backscattering cross section models are given and discussed. Depending on the kR_0 regimes considered, the models in section 3.6 apply with various accuracies. At $kR_0 \ll 1$, the breathing mode solution is a better predictor while at $kR_0 \gg 1$ where other modes start to dominate, the modal solution is more suited. In this study, because kR_0 ranges from 0.16 to 8.38, the modal solution is used (Equation 3.34). This model assumes spherical bubbles and deviation from sphericity and irregularities in geometries are potentially source of errors as large bubbles tend to present more irregular shapes.

In the next chapter, a passive acoustic inversion method is used to estimate gas fluxes from experimental data collected in laboratory conditions. The passive acoustic emissions from gas bubbles constitute the starting point and using the model in Equation 3.29, the distributions of bubbles sizes are determined. From these, flow rates can be calculated. Using data collected in a large water tank, the method is tested for different nozzle types and flow rate regimes.

4. Passive acoustic quantification of gas releases

4.1. Introduction

In the 1980s it was established that bubbles size distributions and gas fluxes associated with natural processes could be quantified by identifying the natural frequency emitted by each bubble upon entrainment in the natural world [72], and this has subsequently been tested as a means for studying methane seeps [75, 107–109]. However this technique can only be applied at flow rates that are sufficiently low to identify the acoustic “signature”of each injection event. When flow rate is high, the acoustic emissions of bubbles overlap and one is unable to distinguish individual bubble injection events [87]. Whilst signal processing methods (such as the Gabor transform [74, 110]) can be helpful to isolate individual acoustic emissions from each bubble, they do not provide a complete solution. An alternative approach is needed to quantify high volumes of natural and industrial gas emissions. In industrial applications these are usually the releases which it is most imperative to correct, since they represent gas losses so great that they can lead to structural failure, as well as potential major economic and pollutionary impacts.

The use of passive acoustic systems to monitor gas releases offer the advantage of lower power requirements monitoring (e.g. in comparison with active acoustic monitoring) as performed using for example a minimal setting with a single hydrophone. Also, such a deployment can usually be performed at low cost. An important benefit from such systems is that they are able to resolve the time variability of flow rates and are then able to resolve the impact of time dependent environmental factors (e.g. tidal height) or the deterioration of a leak. In the past, few studies have made use of this mean to quantify oceanographic gas escapes [75, 82, 86, 107, 109]. However, these models only work at low flow rate regimes.

Recently Leighton and White [61] described a scheme for quantifying the gas flux and bubble generation rates injected into liquid from high volume gas releases, using the passive acoustic emissions. They considered example applications of leaks from undersea gas pipelines, carbon capture and storage facilities, and natural methane seeps. They tested their method with simulated data. This inverse scheme is used throughout this chapter and in chapter 5. This chapter reports on a validation exercise for this method using data from a laboratory experiments while chapter 5 applies the scheme to data collected at sea during the release phase of the QICS project. First, the procedure for the passive acoustic inversion is recalled. Following description of experimental procedures, results from the laboratory trials are presented and discussed. Last, concluding remarks are given, including potential further research that would improve the method.

4.2. Inverse problem

The method used in this chapter is aimed at determining bubble generation rate distributions from sound emissions from bubble plumes as proposed by Leighton and White [61]. Part of this theory will be outlined in this section in order to provide the background for the calculations that are presented in this chapter and chapter 5.

The starting point is the acoustic waveform received on a calibrated sensor which is close enough to a cloud of bubbles (whilst remaining in the acoustic far field) to record its emissions at an acceptable SNR (signal to noise ratio). The output of the inversion process is the bubble generation rates from which the gas flow rate (the experimental quantity measured here) is estimated.

As described in section 3.5, bubble sizes can be inferred using, for example, Equation 3.8 that relates R_0 to the natural frequency f_0. However, this requires one to discriminate each lone bubble emission and when rapid gas releases occur, this approach is not suited. In this case, the bubble signatures overlap and the size distribution of the bubbles being produced can be characterized by the spectrum of the acoustic signal [88]. If it is assumed that the acoustic emissions of each bubble are uncorrelated, the power spectral density $S(\omega)$ of the the acoustic signature of the leak is given by:

$$S(\omega) = \int_0^\infty D(R_0) \left| X_\mathrm{b}(\omega, R_0) \right|^2 dR_0, \tag{4.1}$$

with $D(R_0)$ the rate at which bubbles of radius R_0 are generated. Equation 4.1 defines a Fredholm integral equation of the first kind that can be approximated at discrete frequencies ω_l, $l = 1, \ldots, N_\omega$ and bubble radii R_n, $n = 1, \ldots, N_R$:

$$S(\omega_l) \approx \sum_{n=1}^{N_R} \psi(R_n) \left| X_\mathrm{b}(\omega_l, R_n) \right|^2 \Delta R_n, \tag{4.2}$$

with ΔR_n the bin width for the n^th radius bin. Here, the centre of the radius bins are taken to be equally spaced and the bin width is therefore constant, $\Delta R_n = \Delta R_0$. The quantity $\psi(R_n)$ is the bubble generation rates within a radius bin R_n in number of bubbles $\mu\mathrm{m}^{-1}\mathrm{s}^{-1}$ (where the $\mu\mathrm{m}^{-1}$ represents the fact that a bubble generation rate is determined for each bubble radius size bin, which by convention is of one micron width). For the set of frequencies and bubble radii, Equation 4.2 can be expressed in matrix form:

$$\mathbf{S} = \Sigma \Psi, \tag{4.3}$$

with $\mathbf{S}$ and Ψ the column vectors containing respectively the elements $S(\omega_l)$ and $\psi(n)$. The spectral matrix Σ is constructed at each ω_l and R_n using Equation 3.29, $\Sigma_{l,n} = \left| X_\mathrm{b}(\omega_l, R_n) \right|^2 \Delta R_0$ and is of size $N_R \times N_\omega$. In Equation 4.3, Ψ is resolved by solving the inverse problem $\Psi = \Sigma^{-1}\mathbf{S}$. Techniques to solve problems in this form [51, 56, 59] are described in chapter 2. If the number of radius bins N_R and the number of frequencies N_ω are chosen to be equal, the spectral matrix Σ is square, which mitigates against potential over- or under-determination of the problem. The problem tends to be ill-conditioned and the inevitable measurement errors in $\mathbf{S}$ lead to large errors in the estimated bubble generation rates. To mitigate this, it is prudent to include some form of regularization and Tikhonov regularization is used here (section 2.2, Equation 2.3). For the choice of the regularization factor α, the Generalized Cross Validation (GCV) criterion function $\Upsilon(\alpha)$ is computed, including a positivity constraint (section 2.3, Equation 2.9). From the solution $\Psi(R_0)$, assuming spherical bubbles, the flow rate is estimated using:

$$F_\mathrm{g} = \frac{4\pi}{3} \sum_{n=1}^{N_R} \psi(R_n) R_n^3 \Delta R_0, \tag{4.4}$$

Leighton and White [61] outline key simplifications that they note require further research, such as the assumption that each bubble rings only once (when of course subsequent fragmentation of that bubble would cause subsequent emissions) and that the excitation $R_{\epsilon 0\mathrm{i}}/R_0$ (section 3.5) is simplified to an expression which ignores details of the way the gas is released (through nozzle, pipe rupture, seabed seepage etc.) and the mechanisms of excitation [89, 111, 112], when even reshaping or reorientation of a given nozzle can in some circumstances change the acoustic emission. Therefore it was important to undertake a validation exercise to investigate to what extent the inversion scheme described here allows useful gas flux estimates to be made before the developing theoretical basis for bubble excitation mechanics can progress to a level to use in this model. The results are given as a range of acoustic estimates using a confidence interval for $R_{\epsilon 0\mathrm{i}}/R_0$ based on the data from Deane and Stokes (section 3.5, Figure 3.3) [82, 86].

4.3. Experimental procedure

Measurements of passive acoustic emissions of bubble clouds were conducted in a 8 m x 8 m x 5 m (i.e. of volume $V = 320\,\mathrm{m}^3$) deep test tank containing fresh water at $10\,^\circ\mathrm{C}$ (Figure 4.1). A schematic of the experimental procedure is presented in Figure 4.1(a). Two bubble generation systems were used: a commercial bubbling stone designed for aquarium use (Figure 4.1(b)); and a needle array consisting of six needles with a nozzle inner diameter of 1 mm arranged in circle with a spacing of approximately 3 cm on a flat platform (Figure 4.1(c)). A nitrogen gas cylinder was used to produce the gas for generating the bubbles. The outflow of the bottle was connected to a mass flow meter (Bronkhorst high-tech in-flow F-111BI) to adjust the gas flux along with a data acquisition unit. One or other of the two bubble generation systems were then connected to the end of the gas line and deployed at the bottom of the test tank. Acoustic pressure was recorded using a calibrated hydrophone. First, 30 seconds of continuous acoustic measurements of bubble emissions at different regimes (flow rate was kept steady for 30 seconds, 15 regimes from $0.11\,\mathrm{kg\,d^{-1}}$ to $3.01\,\mathrm{kg\,d^{-1}}$) were performed at a sample rate of 48 kHz. Then, as a second test, gas flow rate was varied manually and monitored (approximately from $0.09\,\mathrm{kg\,d^{-1}}$ to $3.8\,\mathrm{kg\,d^{-1}}$) for 200 seconds. The acoustic signals were acquired at a sample rate of 48 kHz. This test was also conducted for both bubble generation systems. In addition, measurements of the ambient noise were performed in order to study its

	Metered (kg d^{-1})	Needle array (kg d^{-1}) high bound	Needle array (kg d^{-1}) low bound	Best fit $R_{\epsilon 0\mathrm{i}}/R_0(-)$ for needle array	Bubbling stone (kg d^{-1}) high bound	Bubbling stone (kg d^{-1}) low bound	Best fit $R_{\epsilon 0\mathrm{i}}/R_0(-)$ for bubbling stone
15	3.01	14.68	0.89	3.02×10^{-4}	5.46	0.33	1.85×10^{-4}
14	2.79	11.98	0.72	2.83×10^{-4}	4.6	0.28	1.76×10^{-4}
13	2.58	10.28	0.62	2.74×10^{-4}	4.18	0.25	1.74×10^{-4}
12	2.36	8.9	0.54	2.66×10^{-4}	3.11	0.19	1.57×10^{-4}
11	2.15	7.66	0.46	2.59×10^{-4}	2.64	0.16	1.52×10^{-4}
10	1.93	6.23	0.38	2.46×10^{-4}	2.71	0.16	1.62×10^{-4}
9	1.72	3.67	0.22	2×10^{-4}	2.34	0.14	1.59×10^{-4}
8	1.5	4.17	0.25	2.28×10^{-4}	1.68	0.1	1.45×10^{-4}
7	1.29	3.14	0.19	2.14×10^{-4}	1.51	0.09	1.48×10^{-4}
6	1.07	3.86	0.23	2.59×10^{-4}	1.6	0.1	1.67×10^{-4}
5	0.86	4.95	0.3	3.29×10^{-4}	1.57	0.09	1.85×10^{-4}
4	0.64	4.71	0.28	3.7×10^{-4}	1.72	0.1	2.24×10^{-4}
3	0.43	2.98	0.18	3.61×10^{-4}	1.85	0.11	2.84×10^{-4}
2	0.22	2.97	0.18	5.09×10^{-4}	1.21	0.07	3.25×10^{-4}
1	0.11	1.29	0.08	4.75×10^{-4}	0.03	0.003	0.92×10^{-4}

Table 4.1.: Summary of results from the experiment described in section 4.3 for steady flow rates. Acoustic estimates are given using the 75th and 25th percentiles from statistical analysis of measured values of $R_{\epsilon 0\mathrm{i}}/R_0$ by Deane and Stokes[82] (section 4.2, section 3.5, $R_{\epsilon 0\mathrm{i}}/R_0 = 1.37 \times 10^{-4}$ and $R_{\epsilon 0\mathrm{i}}/R_0 = 5.58 \times 10^{-4}$). If instead the appropriate value of $R_{\epsilon 0\mathrm{i}}/R_0$ to use for this type of injection is inferred by finding the value that allows the acoustically-inferred gas flux to equal the metered flow, then that enables calculation of best fit values of $R_{\epsilon 0\mathrm{i}}/R_0$, which are shown in the table.

impact on the estimated gas fluxes.

For the acquisition of the acoustic signals, a wildlife acoustic SM2M+ recorder was used. This consists of a buoyant body containing an acquisition board powered by internal battery connected to a calibrated hydrophone. The unit was loaded on the bottom of the test tank. Whilst use of a hydrophone array would have produced benefits in terms of gain and directionality [61], this experiment was designed to test the lowest cost (single hydrophone) option, and was appropriate for this short range tank test. Also, this allowed the testing of the experimental set-up used for field measurements (chapter 5).

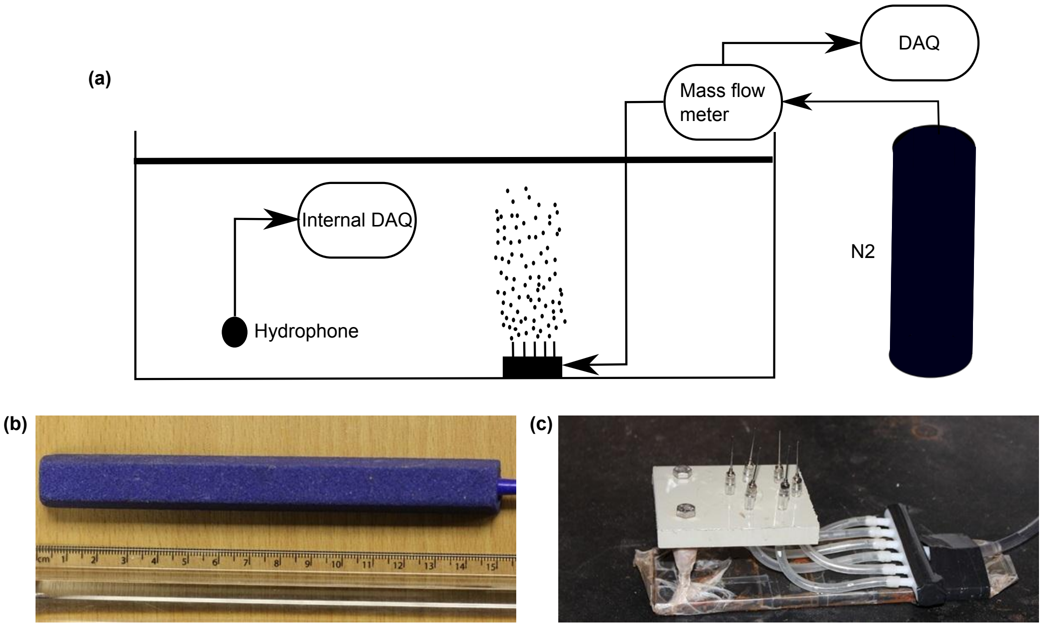

Figure 4.1.: (a): schematic of the experimental set up. Acoustic emissions of gas bubbles were recorded using a calibrated hydrophone with an internal data acquisition unit. Bubbles were released using a nitrogen gas bottle and the bubble generation systems: a bubbling stone (b) and an array of needles (c). The flow rates were acquired using a mass flow meter.

In order to collect measurements relating to the free field, it was important to take into account the effect reverberation has on the recorded signals. For this purpose, care was given to position the hydrophone close to the bubble release, where the direct field dominates over the reverberant field. Theoretical and experimental considerations are given more extensively in Appendix A. In order to evaluate the effect of the reverberant field, the radius of reverberation r_0 is introduced. This is defined as the distance from the source where the direct and reverberant fields have equal contribution [113, 114] $r_0 = \sqrt{A_\mathrm{s} Q_\theta / 16\pi}$ (Equation A.3) with $A_\mathrm{s} = 55.3 \times \dfrac{V}{T_{60} c_\mathrm{l}}$ (Equation A.2) the Sabine coefficient being dependent on the volume of the enclosure V, the speed of sound in the medium c_l and the reverberation time T_{60} of the enclosure. The quantity Q_θ is the directivity factor, equal to 2 for an omnidirectional source sitting on a reflective flat surface [113]. For the enclosure used in this experiment, $T_{60} = 181\,\mathrm{ms}$ between 0.8 kHz and 8 kHz, giving $r_0 = 1.62\,\mathrm{m}$ (measurement procedures are given in Appendix A). For different steady flow rates (15 regimes, Table 4.1), for the two bubble generation systems, measurements at 10 distances were repeated. The Sound Pressure Levels (SPL) were determined. These are defined as: $\mathrm{SPL} = 10\log(p_\mathrm{rms}^2 / p_\mathrm{ref}^2)$ with $p_\mathrm{ref} = 1\ \mu\mathrm{Pa}$ and $p_\mathrm{rms} = \sqrt{\bar{p^2}}$ ($\bar{p^2}$ is the time average of the square of the sampled acoustic pressure). These 10 data points at each regime are plotted against the distance from the source and a fitting based on Equation A.1 is performed. This is shown in Figure 4.2 for regimes 10 and 15 for the needle array (Figure 4.2(a)) and the bubbling stone (Figure 4.2(b)). The direct field decay can be observed at short ranges while the contribution of the reverberant field is noticeable at largest r (SPL levelling off). For the bubbling stone and the needle array, it can be observed that the fitting does not level off because of the lack of data points measurements (10 data points). In order to obtain a more precise fitting, measurements are more numerous distances would be needed. Because of technical difficulties, measurements were performed only at 10 distances. However, Appendix A presents results from a similar experiment using two different underwater loudspeakers in a smaller enclosure. Using 26 data points, the fitting from Equation A.1 is more effective. Because it is needed to apply the inversion to data in free field, it is important to account for the effect of the reverberation field. To that purpose, the measurements at the shortest range (1 m) are used because at this distance, the direct field dominates over the reverberant field. At this range, the total acoustic field is 5.6 dB higher than the reverberant field and the direct field is determined within 1.4 dB.

Another important limitation on the measurement in a reverberant enclosure is the mode mixing, i.e. working at frequencies where there is enough modal overlap to give an acoustic field that is isotropic and homogeneous. This condition is fulfilled by working at frequencies higher than the Schroeder frequency [113] $f_\mathrm{min} = c_\mathrm{l} \times \sqrt{6/A_\mathrm{s}}$ (Equation A.5). In this study this gives $f_\mathrm{min} = 447$ Hz which is well below the minimum frequency of interest (796.8 Hz, corresponding to the highest bubble size considered). Also, care was given at placing the bubble injection site (after the

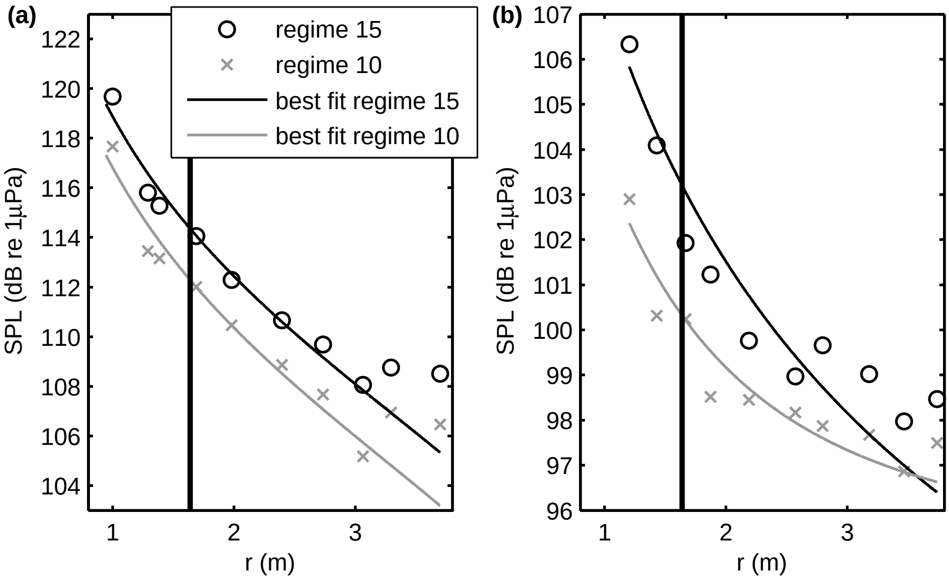

Figure 4.2.: Sound pressure levels from acoustic emissions from bubbles at different regimes (Table 4.1) recorded at 10 different distances. Black circle markers (regime 15) and grey cross markers (regime 10) are the measurements. Black lines (regime 15) and grey lines (regime 10) are the best fits of the measurements using Equation A.1. (a): Needle array. (b): Bubbling stone.

method of Leighton et al. [115]) in order to reduce the driving effect of the bubble emissions on the bubble itself, after reflection from the tank walls, to a level that did not significantly change the bubble natural frequency [116] and damping [115] within the experimental uncertainty, and so no corrections were necessary for these effects (quantitative assessments of these corrections should be considered when taking such data in reverberant test tanks).

In order to determine gas flow rates, the model described in section 4.2 is applied to the hydrophone measurements through Equation 2.3 with the range $r = 1$ m and the regularization factor α determined through Equation 2.9. This results in bubble generation rate distributions Ψ that are further converted into volumetric flow rates (Equation 4.4). Volumetric to mass flow rate conversion is performed based on the ideal gas law. Bubble sizes are chosen to be from $R_0 = 0.5$ mm to $R_0 = 5$ mm, with 50 linearly spaced bins. The choice of the bubble radius range is dictated by the need to have Ψ decreasing at the largest bubble radii. For each radius bin R_n is associated a natural frequency ω_0, calculated using Equation 3.8. At $R_n = 0.5$ mm and $R_n = 5$ mm, $\omega_0 = 796.8$Hz and $\omega_0 = 7973.3$Hz respectively. In this frequency range, the spectrum $\mathbf{S}$ is first computed from the time series in 154 linearly spaced frequency bins. Interpolation of $\mathbf{S}$ at the 50 frequencies ω_0 is then performed prior to the inversion process. Furthermore, because the model is dependent upon the factor $R_{\epsilon 0\mathrm{i}}/R_0$ that remains a source of uncertainty, a confidence interval is given based on the data from Deane and Stokes [82] (section 3.5, Figure 3.3). This factor is taken to be invariant with depth and bubble radius, and in the bubble range of interest, a statistical analysis of these data (871 bubble emissions of bubbles from 0.5 mm to 2.6 mm, section 3.5) gives $R_{\epsilon 0\mathrm{i}}/R_0 = 5.58 \times 10^{-4}$ for the 75th percentile and $R_{\epsilon 0\mathrm{i}}/R_0 = 1.37 \times 10^{-4}$ for the 25th percentile. Because the model is scaled by the quantity $\left(\omega_0 R_0^3 \frac{\rho_\mathrm{l} R_{\epsilon 0\mathrm{i}}}{r R_0}\right)^2$ ($p_{\mathrm{b}0}^2$ in Equation 3.29) and Ψ is obtained from the inverse of the spectral matrix Σ, the low solution bounds correspond to the 75th percentile while the high bounds of the estimates are computed using the 25th percentile.

For the case of steady flow rates, power spectral densities are calculated from the 30 second acoustic traces for each regime. Prior to inversion the spectrum of the recorded ambient noise is subtracted to isolate the contribution of the bubbles. The SNR is computed by forming the ratio of a bubble sound spectrum to the ambient noise spectrum. For the processing of the 200 second varying flow rates, a spectrum is computed each second. For each spectrum, the inversion scheme is applied and the released gas volume can be estimated and the fluctuations tracked.

4.4. Results and discussion

The first aim of this study is to test the accuracy of the flow rates predicted by the technique proposed by Leighton and White [61]. A number of factors need to be taken into account when addressing the potential usefulness of this technique. The detection of fluxes of this scale is at least two orders of magnitude more sensitive than current industry methods for leak detection from long, deep sea pipelines [61]. Whilst photography and direct gas collection could be more sensitive, those are strictly local methods: if resources allow use of an array of hydrophones [61], passive acoustics can be implemented at some range providing greater coverage.

In addition to sensitivity, accuracy is a key consideration (the two being linked when one compares the requirement to produce absolute estimates of a leak flux, with comparative measures of the changes in an existing leak, or monitoring for the start of a leak). Accuracy is particularly an issue because inversions can lack robustness to the presence of noise. Here cross-comparison with direct flow measurements are possible, but if such measurements were available over the whole region of seabed of interest, then the passive acoustic technique would not be needed. The simulations of real world gas releases indicated accuracies for this approach of around $4-40\%$, depending on the circumstances and assumptions made [61]. Confirmation here of such levels of accuracy would be seen as useful given that practitioners would realistically cite experimentally measured void fractions of uncontrolled bubble populations to 2 significant figures, if that [117].

4.4.1. Inversion process considerations

Under laboratory conditions, the experimental assessment of the model is performed by comparing the flow rates inferred from acoustics to the measurements from the mass flow meter. This is repeated for 30 different scenarios, specifically 15 flow regimes (mass flow rates from $0.11\,\mathrm{kg\,d^{-1}}$ to $3.01\,\mathrm{kg\,d^{-1}}$, as shown in Table 4.1), for each of the two bubble injection systems. Scenarios with varying flow rates over a 200 seconds time period are also carried out.

The passive inversion process described in section 4.2 is based on the spectrum of the signals emitted from bubbles as measured by a calibrated hydrophone in the tank. The signals consist of 30 seconds of data at a constant flow rate. Examination of the time series are shown in Figure 4.3(a) and Figure 4.3(b) and reveals single bubble signatures are indistinguishable because the signals from different bubbles are heavily overlapped. Also, an increase in acoustic pressure amplitude with increasing flow rates can be observed. Figure 4.3(c) presents the power spectral densities from signals recorded at a range of 1 m, distance where the direct field is dominant (section 4.3). Spectra for the ambient noise and the signals emitted by the two bubbling systems in regime 15 (which has the highest flow rate - Table 4.1) are presented. For the inversions, the radius range used is 0.5 to 5 mm which, using the inverse of Equation 3.8, corresponds to the frequency band 0.8 to 8 kHz, fulfilling the condition for the minimum frequency to be used in the enclosure $f_{\mathrm{min}} = 447$ Hz (section 4.3, Appendix A). In this band, the noise floor presents a spectral level equivalent to an acoustic noise between $55.5\,\mathrm{dB\,re\,1\mu Pa^2\,Hz^{-1}}$ at 0.9 kHz and $45.6\,\mathrm{dB\,re\,1\mu Pa^2\,Hz^{-1}}$ at 7.2 kHz. The sound associated with bubble generation is from 3 dB at the highest frequency of interest to 18 dB (at lower frequencies) greater than the ambient noise. The noise spectrum is subtracted from

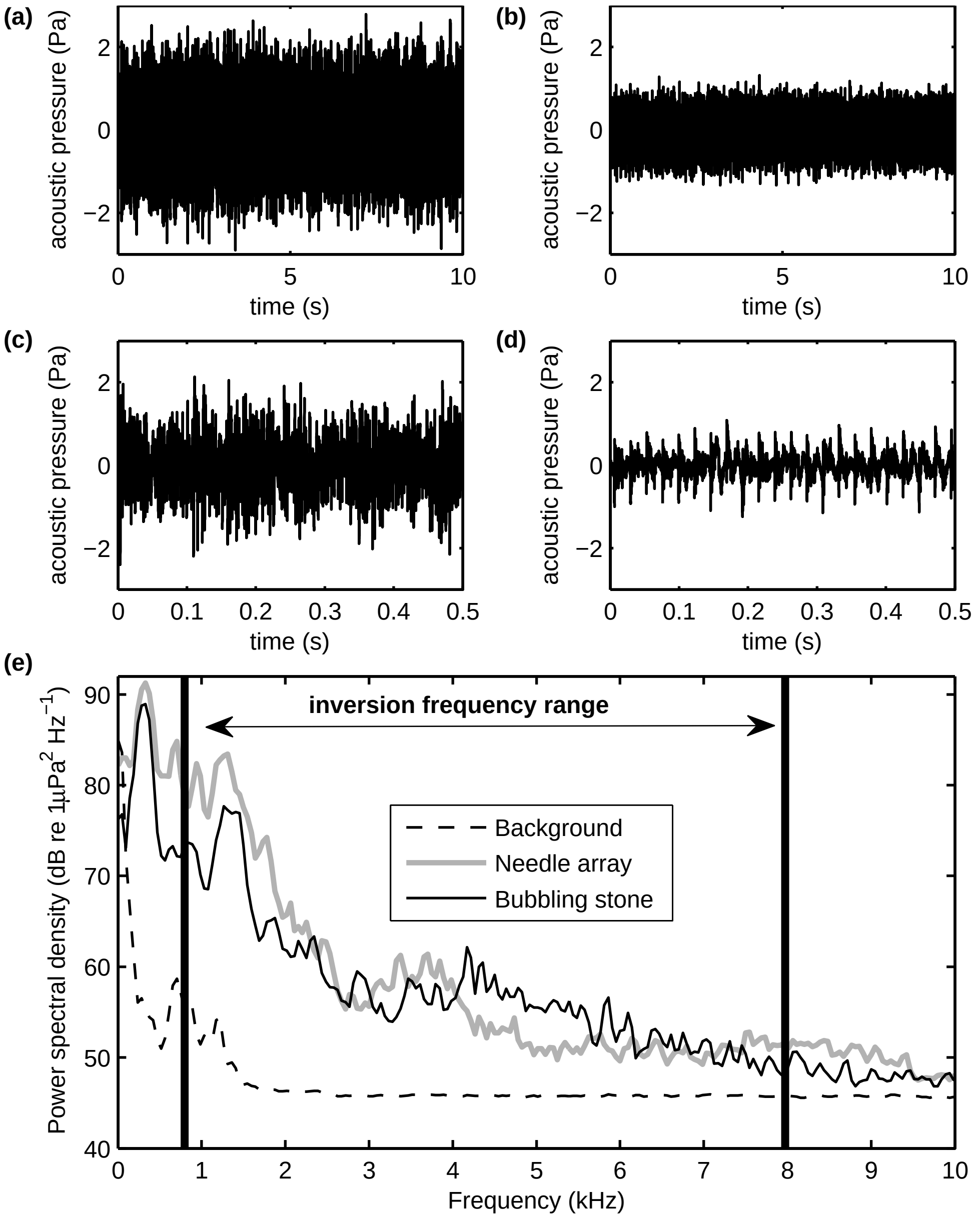

Figure 4.3.: (e): comparison of spectra in a frequency band including the one used for the computation of the inversion (0.8 kHz to 7.9 kHz) for ambient noise (dashed black line) and signals emitted from the needles array (thick solid grey line) and the bubbling stone (solid black line). The flow rate for these measurements was of 3.01 $\mathrm{kg\,d^{-1}}$ (regime 15). (a) and (c): 10 seconds (figure (a)) and 0.5 seconds (figure (c)) of the signal emitted by the bubble plume generated with the needle array at a flow rate of 3.01 $\mathrm{kg\,d^{-1}}$ (regime 15). The rms level of the signal is of 116.2 dB re 1 µPa. (b) and (d): 10 seconds (figure (b)) and 0.5 seconds (figure (d)) of the signal emitted by the bubble plume generated with the needle array at a flow rate of 0.22 $\mathrm{kg\,d^{-1}}$. The rms level of the signal is of 108.2 dB re 1 µPa. (regime 2).

the signal spectrum to avoid the artificial enhancement of the bubble count [118] even though within the analysis band, the signal from the bubble generation process remains much greater than the noise floor. In cases where the measured spectrum is close to the noise spectrum, limited information about the bubble generation is available. The processing methodology adopted here is based on a fixed bandwidth and the band where noise dominates are assumed to have zero contribution from the bubble generation process. Such an assumption is inconsistent with any solution for a strictly positive bubble generation rate, since bubbles of any size make some contribution to all frequencies, as $|X_{\mathrm{b}}(\omega, R_0)|^2 > 0$ for nearly all combinations of ω and R_0. This potentially problematic theoretical issue is mitigated by the use of regularisation. However as the flow rate is reduced the frequency bands where the noise dominates become more prevalent, so the accuracy of the estimation reduces as the need for regularization increases.

Figure 4.4 depicts the rate of generation of bubbles, per micron radius increment Ψ calculated using Equation 2.3 (Figure 4.4(a)) with help of the GCV function $\Upsilon(\alpha)$ (Equation 2.9, Figure 4.4(b)). The low frequency components are greater for the arrangement of needles (Figure 4.3(c), f <2 kHz), this translates to a higher bubble count at large bubble radii. Whereas the greater energy in the high frequency band of the bubbling stone spectrum (Figure 4.3(c), 4 kHz to 6 kHz) results in Ψ exhibiting larger levels at low bubble radii (e.g. at $R_0 < 1$ mm in Figure 4.4(a)). Trends in bubble size distributions can be inferred from the inversion results, and those from all the regimes (e.g. by fitting power laws to the various regimes and bubblers) but rather than doing so it would be better to question first the reliability of perceived details and differences from such an inversion.

For each given flow regime, the acoustically-estimated bubble generation rate is integrated across all bubble sizes to obtain the estimated flow rate (Equation 4.4). This is then compared with the metered value (Table 4.1). Thus, since each regime/bubbler combination gives a single data point, all these combinations can be plotted and compared (Figure 4.5(a) and (b), left axis). Signal to noise ratio is also presented (Figure 4.5(a) and (b), right axis) and it can be observed that the accuracy of the model is dependent on the regime. The error bars represent the uncertainty in the estimated gas flux from statistical analysis on the data from Deane and Stokes [82] as described in section 4.2. Although the confidence interval inferred this way spans 12.2 dB, this will reduce as theoretical and experimental studies on the initial amplitude of bubble wall pulsation for the breathing mode ($R_{\epsilon 0 \mathrm{i}}$) develop.

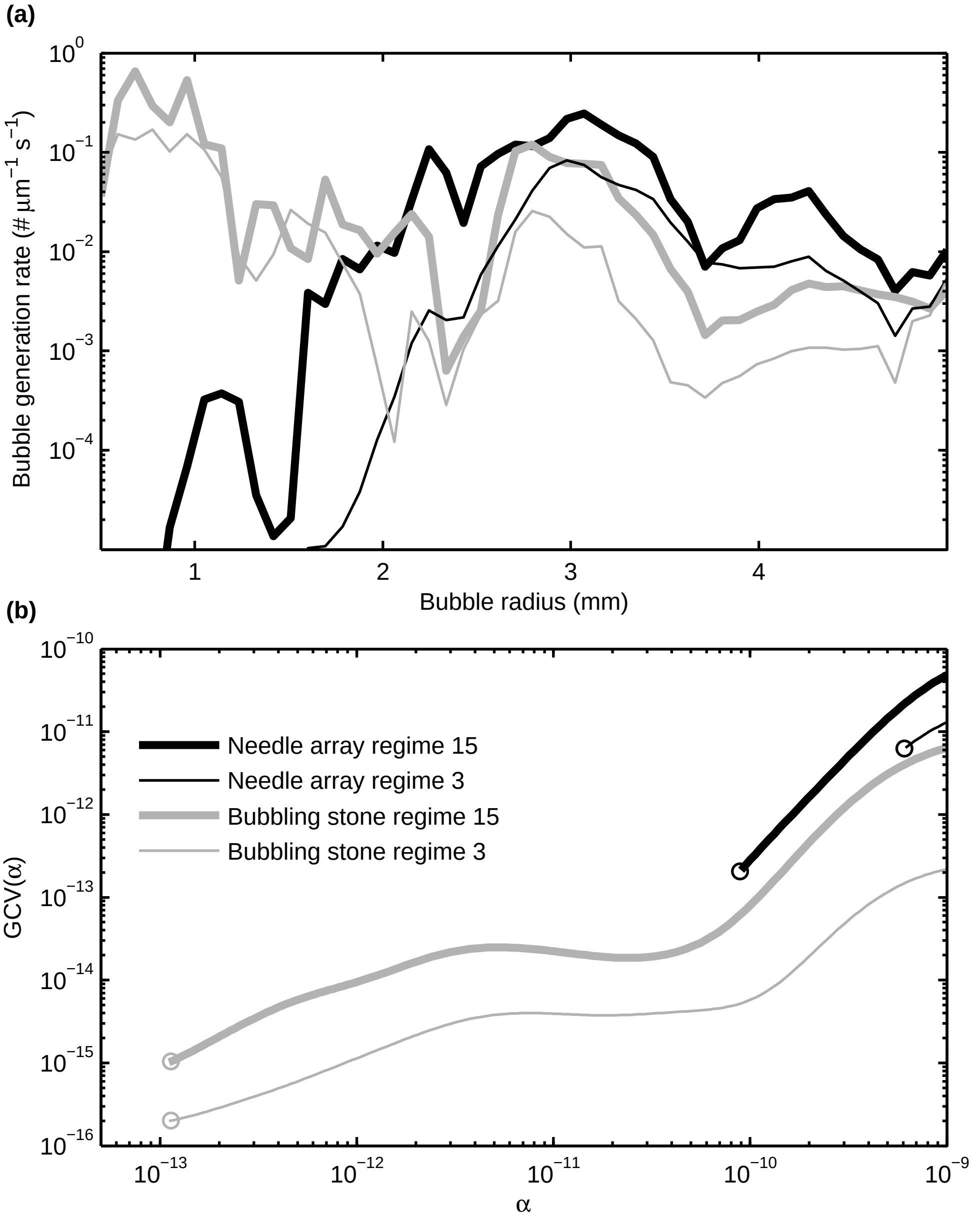

Figure 4.4.: (a): Plot of the bubble generation rates Ψ obtained from the inversion of the acoustic emission versus bubble radius. (b): GCV functions $\Upsilon(\alpha)$ used for the determination of the regularization factor α. In both graphs, the results from the needle array is plotted at regime 15 (thick solid black line) and regime 3 (thin solid black line). At the same regimes, results from the bubbling stone are represented by the thick solid grey line (regime 15) and the thin solid grey line (regime 3). The circle markers are the points corresponding to the values of α used for the inversion.

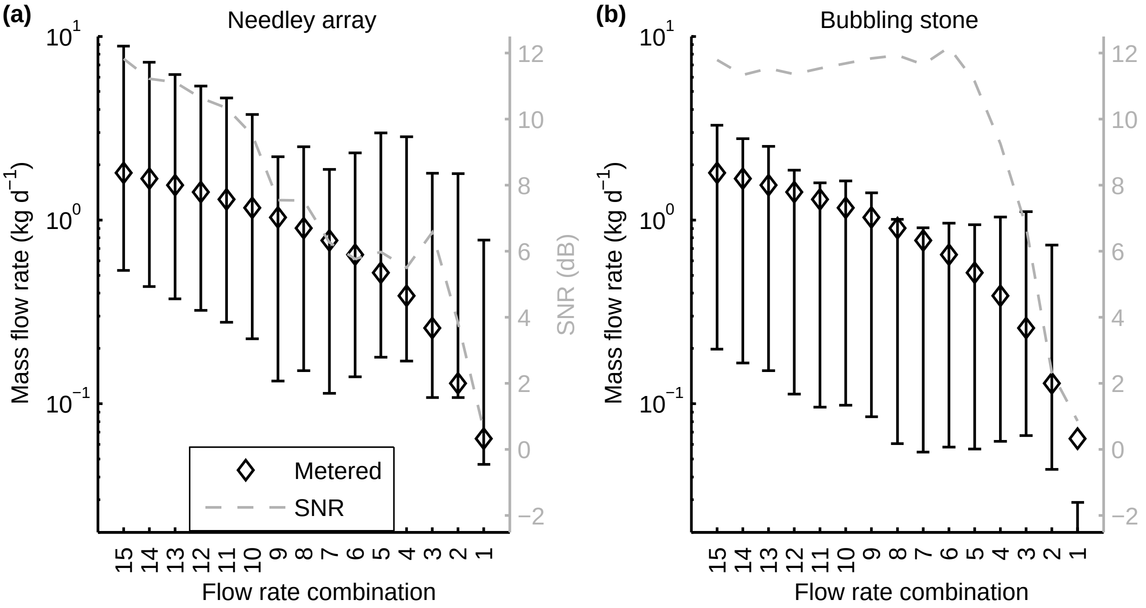

Figure 4.5.: Comparison of different steady flow rates (left axis) inferred from acoustics (solid black line error bars) and direct flow rate measurements (diamond markers) at different regimes. SNR levels of acoustic signals monitored are also presented (right vertical axis, dashed grey lines). The error bars represent the uncertainty from $R_{\epsilon 0\mathrm{i}}/R_0$, calculated using the 75th and 25th percentiles from statistical analysis of measured values by Deane and Stokes [82] (section 4.2, section 3.5, $R_{\epsilon 0\mathrm{i}}/R_0 = 1.37 \times 10^{-4}$ and $R_{\epsilon 0\mathrm{i}}/R_0 = 5.58 \times 10^{-4}$). (a): needle array. (b): bubbling stone.

Here, the relative change in flow rate compared to metered gas volumes is of interest. This would demonstrate the ability of the inversion technique to accurately predict temporal changes in flow rates.

4.4.2. Estimates of steady state gas releases

From Figure 4.5(a) and (b), the relative change in flow rate for the highest regimes is predicted with good agreement from the acoustics, this for both bubble generation systems. The change in flow rate is then resolved without significant impact from the factor $R_{\epsilon 0\mathrm{i}}/R_0$ at the highest flow rates (15 to 5). However, at the smallest flow rates (5 to 1), when the SNR is weaker (Figure 4.5, right axis), the acoustic inversion fails to follow the metered reduction in flow rate, as expected because here the noise significantly corrupts the measurements and lessen the ability to infer flow rate. The model considered is able to monitor temporal variable in gas volume released with a good precision, given the signal to noise ratio is sufficient. At lower flow rates, the error becomes significant and sizing each bubble from the natural frequency [75, 107] might be more suited if single bubble signatures can be identified. It should be added that a single hydrophone is used in this study and the SNR could be increased with the use of an array of sensors.

This analysis assumes $R_{\epsilon 0\mathrm{i}}/R_0$ is constant, this quantity affects the accuracy of the estimates for each regime. By matching the acoustic estimates on the mass flow meter measurements allows to evaluate $R_{\epsilon 0\mathrm{i}}/R_0$ for the different nozzle type and regimes (Table 4.1). The needle array results in values of $R_{\epsilon 0\mathrm{i}}/R_0$ between 2×10^{-4} and 3.02×10^{-4} for regimes 15 to 5 (range of regimes where the SNR is best). In these regimes, the bubbling stone estimates results in values of $R_{\epsilon 0\mathrm{i}}/R_0$ between 1.48×10^{-4} and 1.85×10^{-4}. These values all lie within the 25^{th} and 75^{th} percentiles of the considered data set [82] (section 3.5, Figure 3.3) for $R_{\epsilon 0\mathrm{i}}/R_0$.

4.4.3. Estimates of time varying gas releases

In order to assess further the applicability of the technique, it is tested with a flow rate varying over a period of 200 seconds for both the needle array and bubbling stone. Direct comparison of the computed flow rates from acoustics is given through a confidence interval based on the uncertainty on $R_{\epsilon 0\mathrm{i}}/R_0$ (section 3.5, section 4.2). The results are shown in Figure 4.6(a) and (b). In both figures, the metered flow

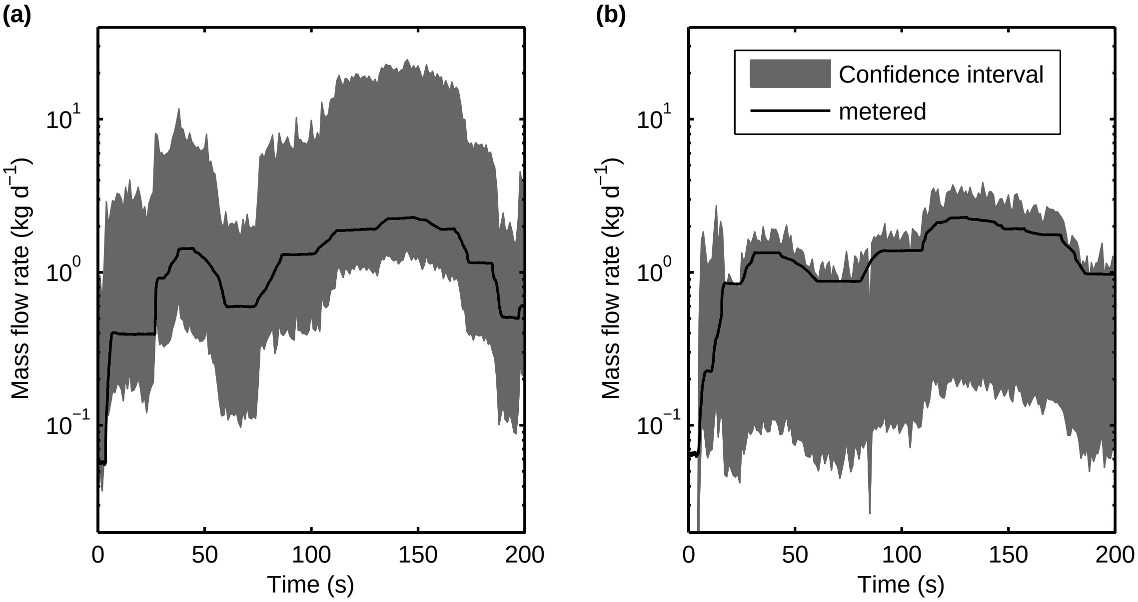

Figure 4.6.: Comparison between metered (solid black line) and estimates inferred from acoustics (grey area) of fluctuant gas release over 200 seconds. The confidence interval represents the uncertainty on $R_{\epsilon 0\mathrm{i}}/R_0$. (a): needle array. (b): bubbling stone.

rates lie within the confidence interval. In addition, the changes in gas injection is accurately tracked by the acoustically inferred flow rates. Also, it can be observed that the estimates can fluctuate locally due to the influence of noise. This issue can be mitigated with the use of a filter to smooth the final results.

The different calculation stages for the inversion scheme applied to these data are presented in Figure 4.7. Each step for the varying flow rate over a period of 200 seconds is shown for the case of the needle array (Figure 4.7(a), (c), (e)) and the bubbling stone (Figure 4.7(b), (d), (f)). This includes the spectrogram of the data to be inverted (Figure 4.7(a), (b)), the resulting bubble generation rate distributions Ψ (Figure 4.7(c), (d)) and finally the mass flow rates (Figure 4.7(e), (f)). Just as was done for the steady flow rate data of the preceding section, $R_{\epsilon 0\mathrm{i}}/R_0$ are estimated and presented in Figure 4.7(e) and (f) (right axis). An optimized value is then used to compute an estimate that best fits the metered flow rates. This gives $R_{\epsilon 0\mathrm{i}}/R_0 = 3.5 \times 10^{-4}$ for the needle array and $R_{\epsilon 0\mathrm{i}}/R_0 = 1.6 \times 10^{-4}$ for the bubbling stone. The optimized flow rates solution is obtained by averaging the $R_{\epsilon 0\mathrm{i}}/R_0$, and presented in Figure 4.7(e) and (f) (left axis). When comparing the spectrum with Ψ, correlation can be observed with dominant spectrum level at

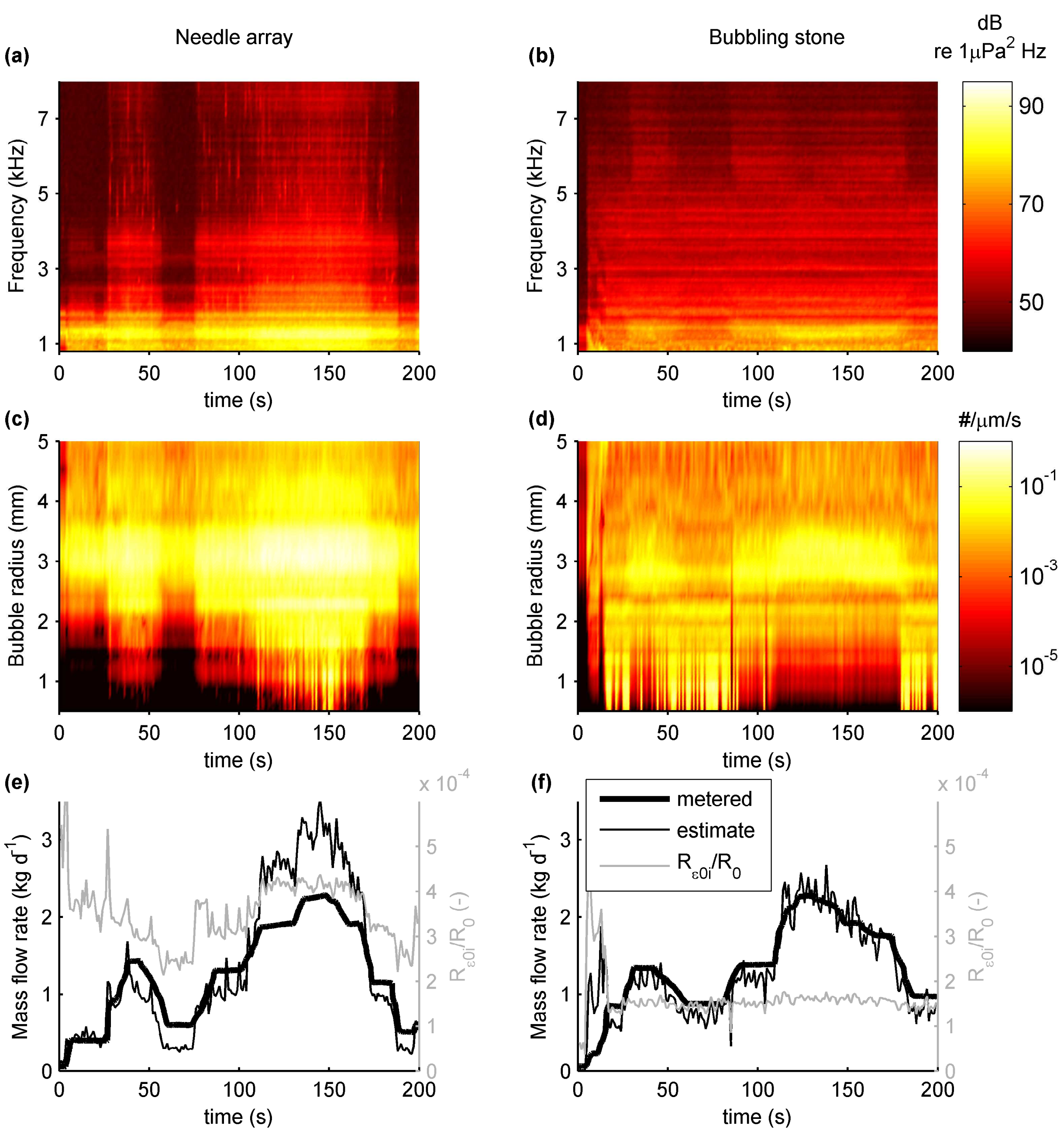

Figure 4.7.: Passive acoustic inversion calculation steps in the case of gas release varying over 200 seconds. Results are given for injected gas using the needle array (graphs on the left) and the bubbling stone (graphs on the right). (a) and (b): spectrogram from the bubble emissions. (c) and (d): resulting bubble generation rates Ψ from the inversion. (e) and (d): mass flow rates and corresponding $R_{\epsilon 0\mathrm{i}}/R_0$. The left axis relate to the mass flow rates that are metered (solid thick black line) and estimated from acoustics (solid thin black line) with an optimized $R_{\epsilon 0\mathrm{i}}/R_0$. The right axis are for the quantities $R_{\epsilon 0\mathrm{i}}/R_0$ that would be required to have mass flow rate measurements matching the direct measurements.

low frequencies resulting in a high bubble count at large bubble radius. Moreover, the largest bubbles contribute most to the computed flow rates. For the scenario presented in Figure 4.7(e) (needle array), 4.76×10^{-3} kg of nitrogen is released over 200 seconds and the acoustic inversion estimates 5.23×10^{-3} kg, overestimating the metered amount by 9.9%. In the case of the bubbling stone (Figure 4.7(f)), the estimation of 4.96×10^{-3} kg is to be compared to 5.14×10^{-3} kg measured from the mass flow meter, giving an underestimation of 3.5%.

Results from both trials clearly show that the inversion scheme can detect temporal changes and demonstrate the ability of the technique to characterize gas leaks precisely. In practical uses for today's industrial leaks (in order to assess of gas leaks levels for oil and gas facilities) or high volume methane seeps (to investigate temporal variability over long periods of time), estimates of gas flux to within an order of magnitude are usually useful. Better characterization of emission mechanisms [82, 89, 111] will improve the accuracy of the method in line with the deployment of new methods for increasingly accurate estimates of the void fraction of gas bubbles beneath the seabed [119–121].

4.5. Summary

The accuracy of a passive acoustic inversion model for the quantification of gas leaks proposed by Leighton and White [61] is studied and presented in this chapter. Passive acoustic measurements of gas release in the form of bubbles were performed under laboratory conditions in a large test tank. Two different systems producing different bubble sizes are used and the rate of gas released considered is relatively high, including regimes where emissions from each bubble overlap. The inversion of these experimental results allows calculations of flow rates that are compared to direct measurements from a mass flow meter. The results of this study exhibit an agreement at a practically useful level for high flow rates. As expected, at lower flow rates the reduction of SNR decreases the accuracy of the estimate and at these flow rates it would be better to obtain gas flux estimates from the detection of single bubble signatures. However, the method employed here is designed for the high gas volume regime where the detection of individual bubble signatures is not feasible.

The accuracy of the inverse scheme is found to rely mostly upon the initial amplitude of bubble wall pulsation for the breathing mode. Using two different types of nozzle for bubble releases, estimates for this quantity are different. However, in both cases, the relative change in flow rate is measured accurately from the acoustic emissions and if optimized values are used for this parameter, the gas volumes that are released are estimated with good accuracy.

This chapter consists of a validation exercise for chapter 5 which reports results from the deployment of an hydrophone recorder at sea for the monitoring of a gas release (QICS project). The passive acoustic inversion is used to determine flow rates from gas escaping from the seabed over a period of 7 days.

5. Passive acoustic quantification of an at sea CO_2 gas release

5.1. Introduction

Following chapter 4, this chapter applies the passive acoustic inversion (section 4.2) to data collected at sea. In chapter 4, under laboratory conditions, good agreement is observed between gas flow rates inferred from acoustic emissions and independent measures of injected gas. It is found that the factor $R_{\epsilon 0\mathrm{i}}/R_0$ is a key parameter that vary depending on the mean of generating bubbles. Because this technique has not yet been demonstrated in the field, it was challenging to assess its applicability. Together with the $R_{\epsilon 0\mathrm{i}}/R_0$ factor, the range at which the signal to noise ratio is good enough to perform the inversion was of interest. Results in this chapter explore these two aspects. The data collected consist of acoustic signature of gas bubbles generated from the seabed during the final phase of the QICS project (Quantifying and Monitoring Potential Ecosystem Impacts of Geological Carbon Storage) [50, 122]. This consisted in a controlled CO_2 release in the sediment layer leading to gas leaks from the seabed.

The QICS project was funded by the Natural Environment Research Council of the UK and involved the collaboration of 14 UK and Japanese institutes. Its purpose is to improve understanding of the sensitivities of the UK marine environment to a potential leak from CCS facilities. The gas release phase took place in Ardmucknish bay near Oban in Scotland (Figure 5.1(a)) and the experimental procedures were led by the Scottish Association for Marine Science (SAMS, Scotland). A schematic of the experiment is shown in Figure 5.1(b). From a container on the shore, using a bore hole drilled through the bedrock to the sediment layer, CO_2 gas was injected, mimicking potential gas release from a CCS facility reservoir. The migration of the gas in the sediments and in the water column, together with the environmental

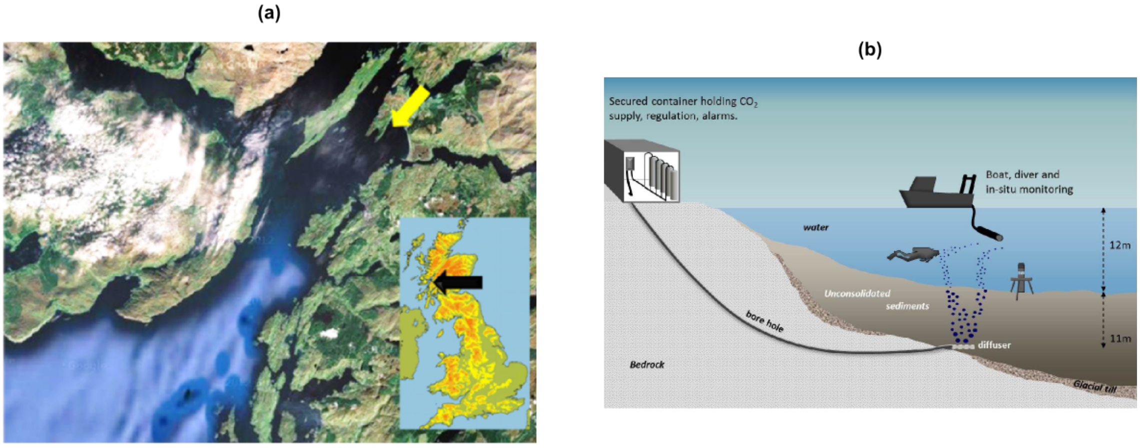

Figure 5.1.: (a): Map showing the location of the release phase of the QICS project. It was conducted in Ardmucknish bay in Scotland, near the town of Oban. (b): Schematic of the release phase of the QICS project.

impact was investigated over 37 days with different level of injection rates. For this experiment, it was important to monitor the amount of gas released from the seabed in order to compare it to the injected amount. To this purpose, different flow rate measurements were performed: divers measurements using a graduated cylinder; measurements using video recordings; measurements using passive acoustic measurements (of interest in this chapter).

This chapter reports on the collection of the acoustic data during the gas release period, giving details on the experimental procedures and the difficulties encountered at treating environmental noise. Considerations for the applicability of the passive acoustic inversion with a single hydrophone configuration are given. This includes uncertainties on the location and intensity of each bubble streams. Estimates of flow rates are computed and results are presented and discussed.

5.2. Experimental procedure

The release phase of the QICS project [50, 123] was conducted from 17th of May to 22nd June 2012. Throughout this period of 37 days, CO2 gas was released from a diffuser under the seabed at a controlled rate. Taylor et al. [124] describe the set-up of this large scale experiment and outcomes of this project are discussed by Blackford et al. [123]. The measurement of the injected gas is shown in Figure 5.2(a). Gas injection started on 17th May 10.00 am, and the gas flux was stabilized to 20 kg/d until 18th May 03.30 pm where flow rate was stepped up over 2 days to 90 kg/d (20th May 09.00 pm). The injection rate was increased over 3 days, from 5th June 04.00 pm to 8th June 02.20 am to a level of 160 kg/d. Level was kept stable until 17th June 11.40 am with a disturbance between 15th June 04.00 pm and 15th June 10.00 pm due to a technical problem in the injection system. The injection rate was finally increased to 220 kg/d on 17th June 11.00 pm. Between 20th June 11.30 pm and 21st June 11.00 am, a significant decrease can be observed, corresponding to the time where gas cylinders had to be replaced. Injection was stopped on 22nd June 04.00 pm.

Over the experimental period, tidal levels fluctuated between 1 m and 3.5 m. These are shown in Figure 5.2(b). The tide is shaped with a long cycle period and a more local tidal height change over 14 hours. This is of importance because hydrostatic pressure (and then tidal heights) influences significantly the amount of gas released from a point source [28–35]: high hydrostatic pressure is associated with lower gas release; low hydrostatic pressure is associated with higher gas release. Such correlation of flow rates with tide was observed from video observations from 4th to 18th June. This is shown in Figure 5.2(c) (data kindly provided by Jun Kita) where various intensities of bubble emissions were observed. Also, gas was observed to stop promptly after cessation of gas injection. This is shown in Figure 5.2(d) and Figure 5.2(e). Photographs show intensive bubble release one hour prior to cessation of gas injection and no bubble release 30 minutes after the cessation of gas injection.

Here, gas escaping the seafloor that took the form of bubbles in the water column is of interest acoustically. On 13rd June, a SM2M+ hydrophone recorder (wildlife acoustics) was deployed using a mooring and was positioned approximately 1 m above the seafloor. The unit was moved on 15th June by divers into the region where bubble releases occurred. The depth of the region where the bubbles escaped varied with tide and was of 10-12 m. The gas injection was stopped on 22rd June, thus there was a period of 7 days during which acoustic signals were acquired and gas was being injected. The hydrophone unit was recovered on 29th June. The recorder measured continuously during this period at a sample rate of 48 kHz. The inversion scheme is to be applied to the data, following the method described in section 4.2.

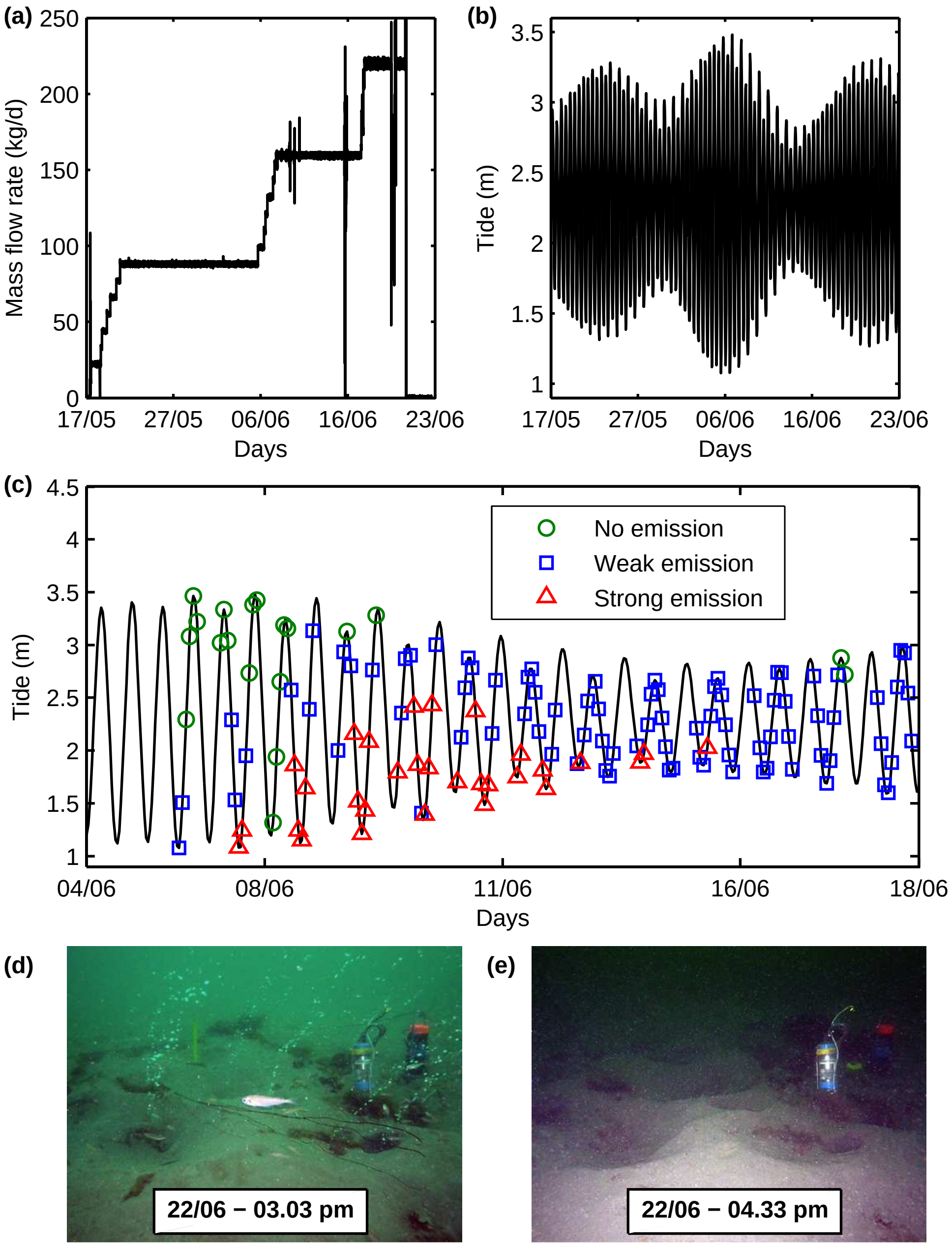

Figure 5.2.: Various results from the release phase of the QICS project. (a): Gas injection rate over the experimental period. (b): Tidal heights over the experimental period. (c): Tidal heights plotted with video observation of bubble releases at the seabed from 4th June to 18th June. Data were kindly provided by Jun Kita (RITE, Kyoto, Japan). (d): Photograph of the seabed on 22nd June 03.03 pm (Shortly before cessation of gas injection). (e): Photograph of the seabed on 22nd June 04.33 pm (Shortly after cessation of gas injection).

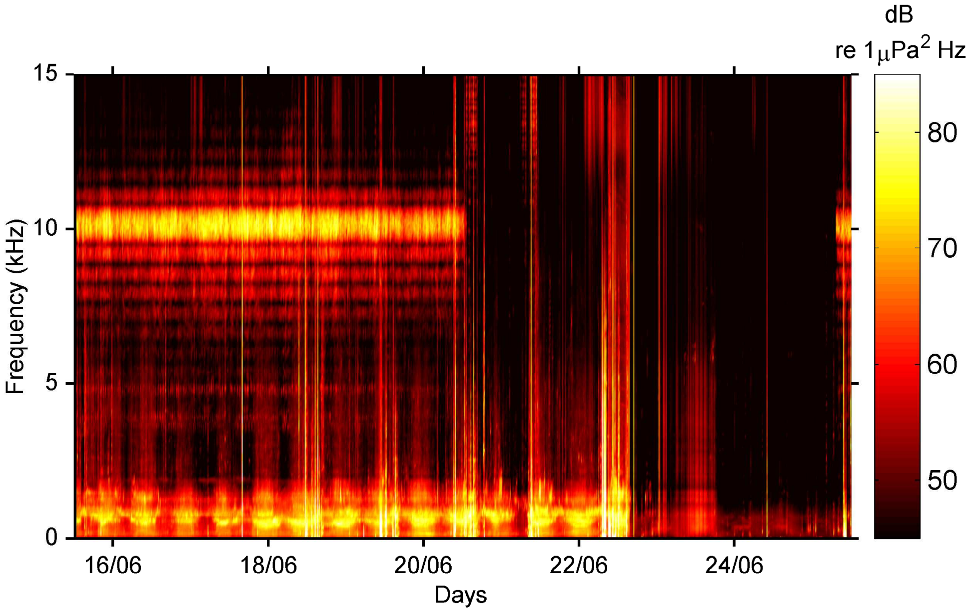

Figure 5.3.: Spectrogram of acoustic signal measured between the 15th and the 26th of June 2012. The gas was stopped being injected on the 22nd at 17:07.

From the 14 days acoustic time series, a spectrum **S** for each 10 second segment of data is computed and constitutes the input to the inversion. A spectrogram of the data from 15th to 26th June is presented in Figure 5.3, with periods with (15th to the end of 22nd June) and without (end 22nd to 26th June) bubble emissions. Also, acoustic energy from three seal deterrent devices (sdd) can be observed from 15th to the end of 20th June. These are identified as Airmar dB Plus II sited at 2 fish farms $\approx$ 5 km and $\approx$ 6.5 km from the gas release site and emitted continuously until 20th June where they were turned off for 5 days. A closer analysis of the acoustic signature is presented in Figure 5.4(a) (spectrogram over 60 seconds). It shows the combination of the three sea deterrent devices with the continuous emission of sound pulses. Most of the acoustic energy is concentrated around 10 kHz frequency. This is consistent with the results from Gordon and Northridge [125], showing that this device highly affects a frequency range between 5 kHz and 15 kHz. Figure 5.4(b) illustrates this by comparing the ambient noise spectrum with and without the devices on. The signals analysed here are those measured after the gas injection was stopped and they do not contain the acoustic emission of bubbles. Whilst at low frequencies ($<$ 2kHz) the two spectra are close, whereas at higher frequencies they diverge with a maximum difference of approximately 32 dB at 10 kHz. The passive acoustic inversion should be applied on the spectral contribution only from the bubbles (otherwise, the bubble

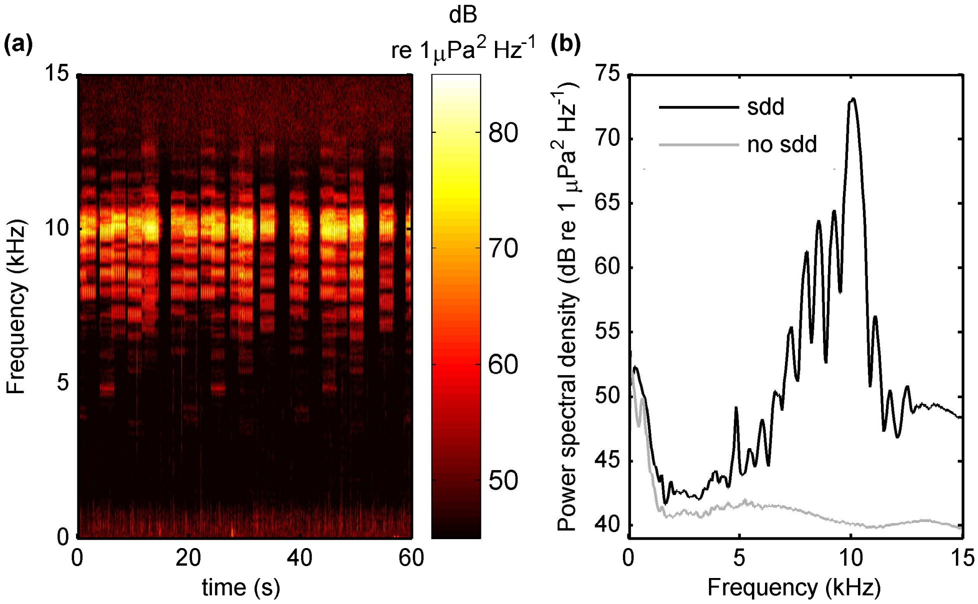

Figure 5.4.: Impact of seal deterrent devices (sdd) used by fish farms that corrupted the collection of acoustic data during the release phase of the QICS project. (a): Spectrogram for a duration of 60 seconds on 25th June (gas injection stopped, no acoustic emission from gas bubbles). (b): Spectrum comparison of signal corrupted by seal deterrent (solid black line) devices with a clean signal (solid grey line).

count can be artificially inflated). To that purpose, two steady noise floor spectra when there were no acoustic emissions from bubbles are computed from 3 minutes of data collected on 24th June (no noise from seal deterrent device) and on 25th June (seal deterrent devices turned on). As in chapter 4 (section 4.3), these spectra are then used to subtract steady ambient noise.

The ambient noise level varies during the experiment as a function of time. This was in part the result of the passage of vessels near the site and activity associated with the experiment. To reduce the impact of transient noise events and to smooth the results somewhat, the results from each 10 s sequence were combined using a 1 hour rolling median filter. Noise sources which persisted for more than 30 minutes would inevitably corrupt the bubble estimates artificially by inflating the bubble count. Such an event happened at the time at which the divers measured the gas flux or toward the end of the experiment, and the implications of this will be discussed in section 5.3.

For the inversion, 50 bubble radius bins linearly spaced from 0.5 mm to 10 mm are chosen in order to have Ψ decreasing at the largest bubble radii. The spectra $\mathbf{S}$

are first interpolated at the corresponding frequencies (from 451 Hz to 9034 Hz) using Equation 3.8. The inversion is carried out as described in section 4.2. However, because there were multiple bubble streams (contrary to the test tank experiment where bubbles were release from a single location), a critical variable to evaluate is the range r because Equation 3.29 is proportional to $1/r^2$. For the need of the inversion, an 'effective' range r_{eff} is determined by taking the average of the inverse distances squared of every bubble streams:

$$1/r_{\mathrm{eff}}^2 = \left(\sum_{l=1}^{N_{\mathrm{s}}} G_l \right)^{-1} \times \sum_{l=1}^{N_{\mathrm{s}}} G_l / r_l^2 \tag{5.1}$$

with N_{s} the total number of bubble streams and r_l the distances from the sensor to the bubble streams. The quantity G_l is the relative gas flux and accounts for the differences of intensity at different bubble releases. With the use of a suitable sensor array, the use of an effective range could be overcome. However, in the experimental set up described here, a single hydrophone was used and it was not possible to identify each G_l factors. In addition, in the absence of dedicated resource to provide estimates, the position taken here is to assume $G_l = 1$. Each location r_l was determined from pockmarks revealed by multi-beam echosounder mapping on the morning of 20th June (corresponding to low tide). This is shown in Figure 5.5 with the location of the pockmarks, the diffuser and the hydrophone. This only constitutes a snapshot at a specific point in time, evaluating the range r_{eff} from this image does not take into account potential appearance or disappearance of bubble streams throughout the measurement period. While ideally one would determine the location and appearance of each release, the position taken here of assuming a single effective range is constrained by technical limitations. This issue could be mitigated by the use of an array of hydrophones instead of a single sensor in order to locate and monitor each stream of bubbles. Alternatively, if resources allowed it, a dedicated camera or active sonar systems could be used to identify where and when the gas releases occurred in order to provide these data as input for the passive acoustic study. Using the map presented in Figure 5.5, 57 pockmarks are identified and from the location of the hydrophone, it is found that distances from bubble streams to the acoustic sensor vary from 0.8 m to 6.5 m. The resulting effective range is $r_{\mathrm{eff}} = 2.4$ m to input in Equation 3.29. Similarly to section 4.3, results are given in the form of a confidence interval based on the data from Deane and Stokes [82] (Figure 3.3).

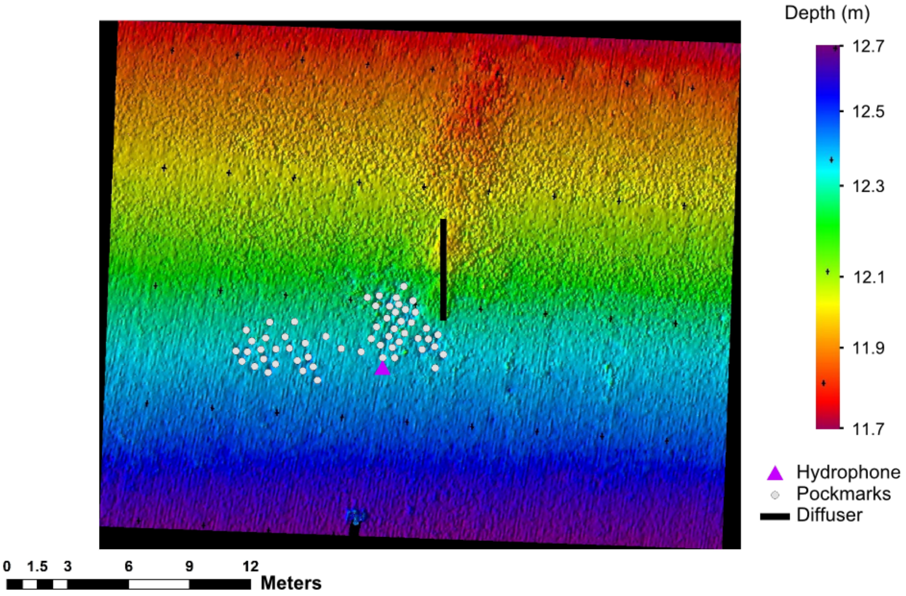

Figure 5.5.: Topography of the site where the release phase of the QICS project took place in May/June 2012. The gas diffuser is represented by a black line while the pink triangle marker is the position of the hydrophone unit. The white circle markers are the estimated location of each bubble stream inferred from the pockmarks, inferred from multi-beam mapping.

5.3. Results and discussion

5.3.1. General considerations

Preliminary validation tests were conducted in a water-filled tank (chapter 4), as a precursor to the at sea measurements in the framework of the QICS project (Figure 5.6-Figure 5.9). Before discussing the results from the inversion, it is useful to understand where these tests are leading, as this explains the accuracy, uncertainty, and advantages of the passive acoustic technique. Consider the lower plot in Figure 5.7, which shows the mass flux at QICS as inferred from the passive acoustic emissions. Plot shows a shaded region, its upper and lower borders denoting the 25th and 75th percentile of $R_{\epsilon 0\mathrm{i}}/R_0$ (section 4.2, section 3.5), defining the spread in acoustic estimates. This uncertainty derives almost wholly from the single factor $R_{\epsilon 0\mathrm{i}}/R_0$ which dominates the error estimation. In chapter 4 and in this chapter, that estimation comes from analysis of the data presented by Deane and Stokes [82, 86] (Figure 3.3), who measured the range of excitations as a function of bubble size in laboratory tests. Previously, Leighton and White [61] used a fixed value, that lies close to the middle of the range observed by Deane and Stokes [82]. In future, the developing theoretical basis should allow the amplitude of the initial excitation, and how this varies with the type of injection (from a needle, a leaking gas pipe, or the seabed), to be calculated, which may well reduced the uncertainty associated with the method used in this paper.

Half way through 19th June, a single cross overlies the lower curve in Figure 5.7(c). This is the gas flux measurements made at a single point in time by divers on each visible bubble stream using an inverse funnel. It lies well within the borders of the acoustically-inferred gas flux, adding confidence to the latter. However, as explained in section 5.2, the acoustic signal here is contaminated by noise from the boat and divers, and so a more realistic comparison is to compare the diver-generated flux estimate with the acoustically-inferred fluxes at similar points in the tidal cycle either side of the diver measurement. One further point from the comparison of diver- and acoustically-generated fluxes is this: it illustrates the power of the passive acoustical method. Whilst the divers, at considerable expense and effort, managed to obtain only one data point for the gas flux, the passive acoustic method monitors the gas flux in real time, continuously, over 7 days. For example, over the whole bubble release field, it details the temporal correlation of the gas flux with the tidal cycle

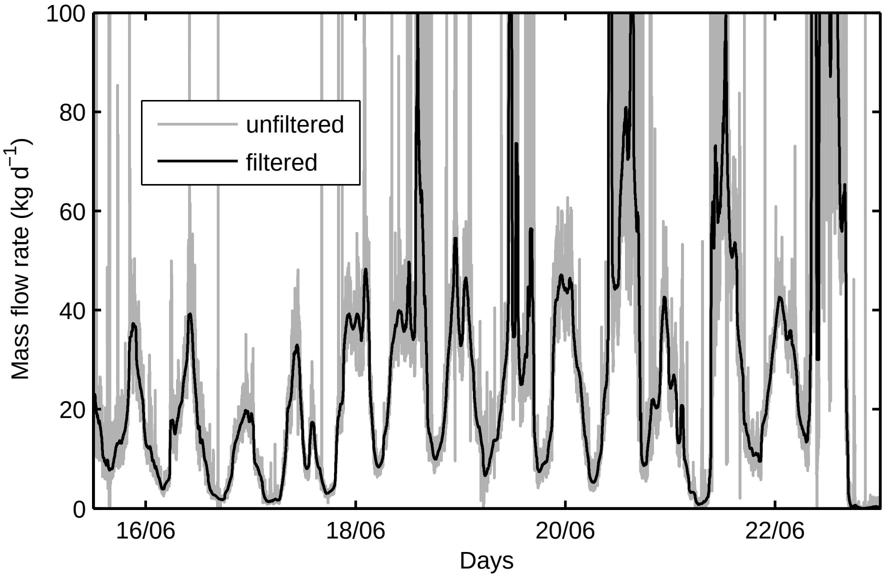

Figure 5.6.: Mass flow rates estimated from acoustic measurements during the release phase of the QICS project with (solid black line) and without (solid grey line) the application of a 1 hour median filter.

(as shown on Figure 5.7 to 5.9).

Having therefore provided perspective to the data to be presented in this section, the results from data collected at sea during the QICS experiment are presented and discussed.

5.3.2. Correlation with tide and injection rate

Through the release phase of the QICS experiment, passive acoustic emissions from a bubble release was recorded for 7 days, from 15th to 22nd June. Using the inversion scheme gas flow rates are estimated (section 4.2). Results are investigated in order to determine the applicability of the passive acoustic inversion method in an at sea environment. The procedure is similar to the one used for the test tank experiments with varying flow rates (chapter 4). Spectra that are determined for every 10 seconds of signals constitute the input of the model. Inversion is applied similarly. As observed in section 4.4, the inversion scheme is sensitive to noise, especially for the set-up considered here with a single hydrophone. Various sources of noise disturbed the measurements and contribution of noise sources such as seal scrammers could be mitigated (Figure 5.4) by subtracting its contribution to the inverted spectrum. However, noise events such as those arising from boat activities could not be accounted for, resulting in mass flow rates varying significantly. This is observable in Figure 5.6 (solid grey line) where occasional large spikes in the estimated flow rate are evident. In order to reduce the effect of these random noise events, a 1 hour median filter is applied, resulting in a smoothed curve (Figure 5.6, solid black line), reducing the local fluctuations.

The resulting flow rates are presented in the form of a confidence interval (section 3.5 and section 4.3) and are to be compared with injected flow rates. The results (from 15^{th} to 23^{rd} June) are presented in Figure 5.7 with bubble generation rate distributions Ψ (Figure 5.7(a)), tide levels (Figure 5.7(b)), injected and acoustically inferred flow rates (Figure 5.7(c)). Even though a median filter is applied to the data as in Figure 5.6, strong fluctuations in flow rates can be observed on 20^{th}, 21^{st} and 22^{nd} June after mid-day. This corresponds to increased boat activity related to the end of the experimental period and results in artificially increased bubble count (thus producing overestimated mass flow rates). This cannot be corrected by the median filter.

A strong correlation of the estimates from the acoustic measurements with the tidal height can be seen in Figure 5.7, a correlation also noted in the time lapse photography and pCO_2 (partial pressure of carbon dioxide) data [123]. This variability with tidal height is noteworthy and diverse for marine seeps [28–35]. Here the variability with tidal height is noticeable in the bubble generation rate distributions Ψ (Figure 5.7(a)) and in estimated flow rates (Figure 5.7(c)). Using a 12 hour hamming window with 50% overlap, the cross power spectral density between the upper bound of the estimated flow rates and tidal heights is computed (Figure 5.8(a)). This exemplifies peaks at diurnal (24 hour period) and semi-diurnal cycles (12 hour period). Here, the tidal height is dominated by semi-diurnal cycles. Fourier transforms of the tidal heights and the flow rates over windows of 12 hours with 50% overlap from 14th 05:30 pm to 22nd 02.00 pm, phase delays for the semi-diurnal cycle at different times are calculated. The histogram of these estimates is plotted in Figure 5.8(b) and it exemplifies a delay of $174° \pm 23°$ (5.8 ± 0.8 hours) between tidal heights and flow rates. The point where the release of gas is highest is then located just before the lowest level of tide and low hydrostatic pressure corresponds to high levels of gas release while high pressure corresponds to low flow rates. It has been suggested that such a relation between tidal heights and flow rates is mostly accountable for the activation/deactivation of individual vents [34].

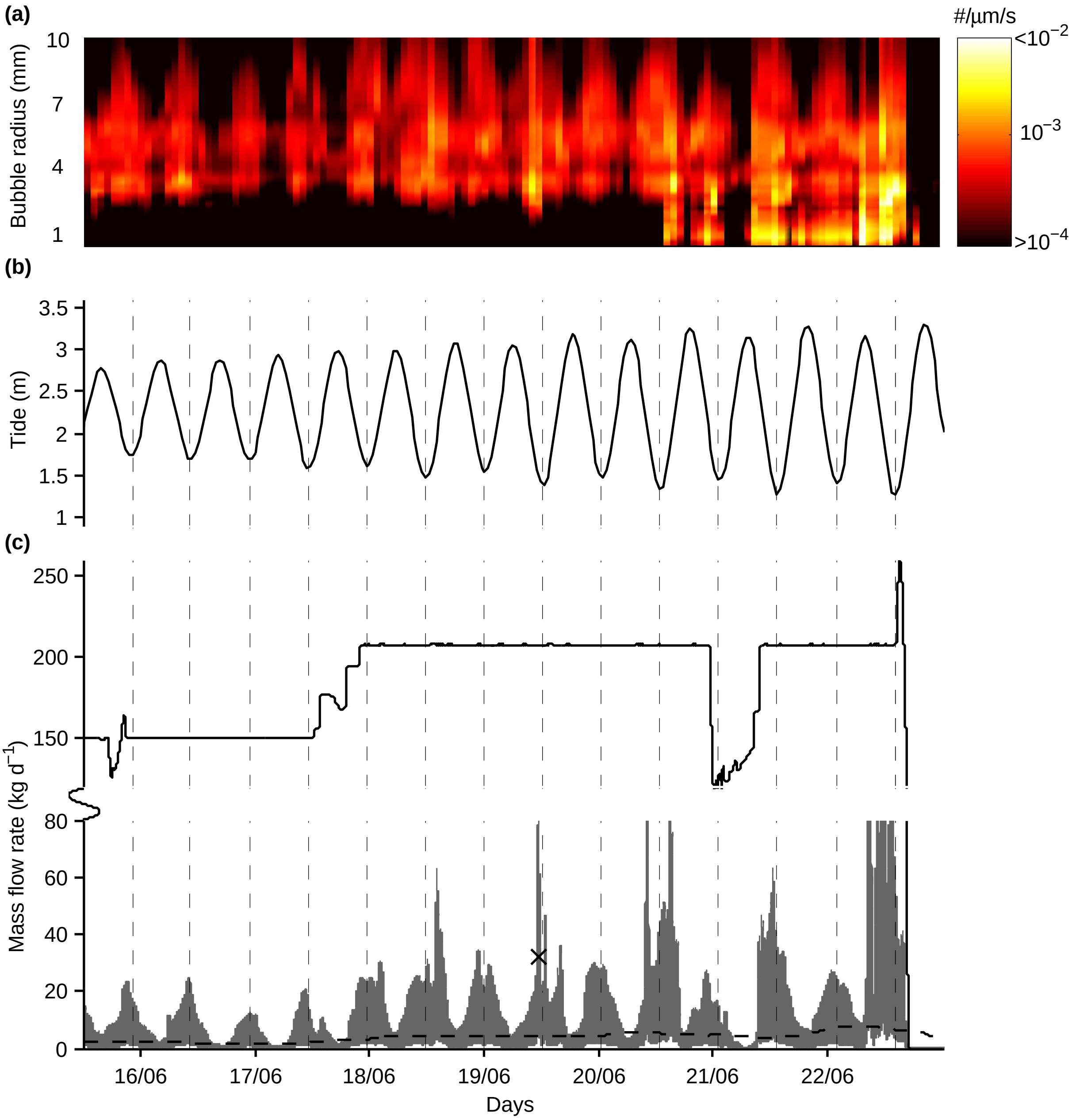

Figure 5.7.: Various results from the release phase of the QICS project. (a): Bubble generation rate Ψ versus days. (b) Tide versus days. (c) injected (solid black line) and acoustically inferred (grey area) mass flow rates. The acoustic estimates are computed as a confidence interval based on uncertainties on $R_{\epsilon 0\mathrm{i}}/R_0$ from the 25th and 75th percentiles of the data from Deane and Stokes [82] (section 3.5). The black cross marker represents the diver flow rate measurements on each individual bubble stream. The dashed black line is the 1h moving averaged gas flow rate acoustic estimate showing the general increase after 18th June.

Using an active sonar, Schneider von Deimling [28] reported a 90° phase delay and suggest this is associated with the diffusion of gas in the sediments [29]. In order to further characterise the relation between the tide and the ebullition rate, Figure 5.9 presents tide plotted against the upper bound of the estimated flow rates. Tidal height is sampled every 43 minutes and flow rates are averaged between two data points. The tidal effect is investigated from 14th 05:30 pm to 18th 02.00 pm, period during which the noise is limited. Figure 5.9(a) shows results for each tidal height data point together with a linear regression with a regression coefficient of $R^2 = 0.7$. Refining the focus to peak tide changes with flow rates averaged over 86 minutes around tidal height peaks and dips gives a linear regression to the subsequent 13 data points with a regression coefficient of $R^2 = 0.9$. This increased correlation between tidal height and flow rate suggests that the change in flow rates is more closely related when the tidal cycle is at its local maximum or minimum [34]. Results suggest a decrease of 15.1 kg d^{-1} for each meter increase in tide around tidal height peaks.

When comparing the injected flow rate levels with the acoustically estimated gas volume released in the form of bubbles, correlation can be observed. First, the increase of gas injection occurring on 17^{th} June from 150 kg d^{-1} to 210 kg d^{-1} produces an increase in gas release from the seafloor as seen in Figure 5.7(c) by the dashed black line (increase during 18^{th} of June). This dashed line represents the 24 hour rolling average based on the upper bound of the confidence interval (grey area) of which this tracks intensity changes in flow rates over a day period. From the 15^{th} at 12.00 am to the 17^{th} at 00.00 am, the average flow rate of the upper bound is of 9.2 kg d^{-1} and from the 18^{th} 02.00 pm to the 20^{th} 02.00 am, estimates are of 15.5 kg d^{-1}. These two periods of time were chosen because the effect of boat noise seems to be limited. This gives an increase of 83.2% when including the difference in tidal levels. This responds to a 40% increase in gas injection. Further, the gas injection drops on 21^{st} June and shows direct effect on the gas escape from the seafloor as shown by the sharper decrease at this time in Figure 5.7(c). Finally, the estimates reduce dramatically when the gas injection is stopped, correlating with photographic observations that also showed that the bubble emissions stop shortly after the end of the gas injection (Figure 5.2(e) and (d)).

On 19^{th} June at 11.00 am, diver measurements of each individual bubble stream were performed using an inverse funnel. The gas collection was performed over 49 minutes at high tide and measured 31.8 kg d^{-1} with the mass flow rates from streams

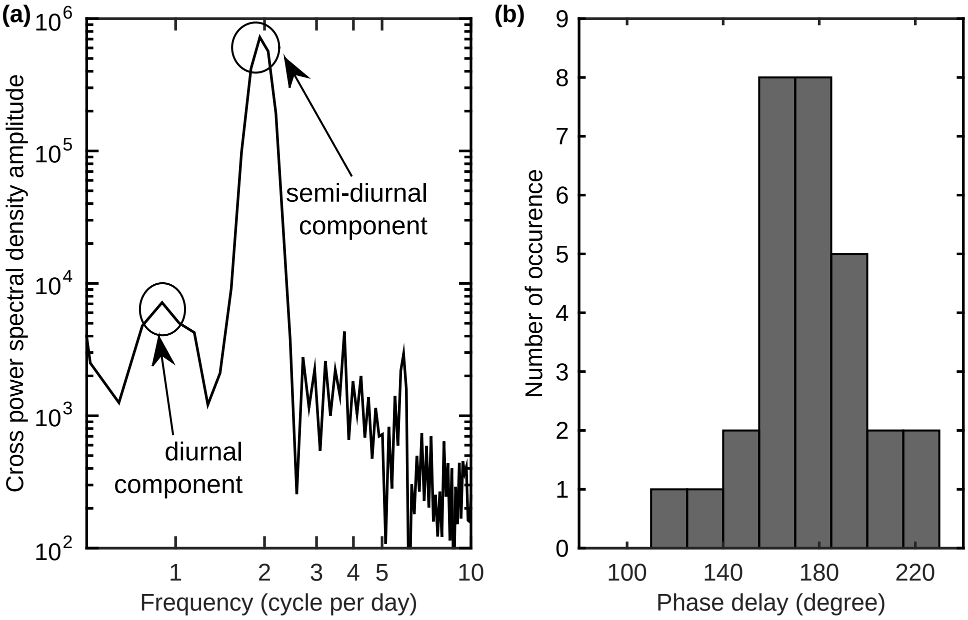

Figure 5.8.: Correlation between tidal height (Figure 5.7(b)) and flow rates inferred from acoustics (Figure 5.7(c), grey area). (a): Cross power spectral density amplitude versus frequency in cycles per day. The cross power spectral density is computed using a 12 hours hamming window with 50% overlap. The graph shows high correlation at the semi-diurnal component (~12 h cycle). A peak is also noticeable at diurnal components (~24 h cycle). (b): Distribution of phase delay between tidal heights and flow rate estimates for the semi-diurnal cycle. This gives a phase estimate of 174° ± 23° (5.8 ± 0.8 hours).

spanning 0.1 $\mathrm{kg\,d^{-1}}$ to 2.4 $\mathrm{kg\,d^{-1}}$. This measure is represented by a black cross marker inFigure 5.7(c) and represents $\approx 15\%$ of the injected CO_2 at the time. The estimates from the inversion averaged over the measurement period, using $R_{\epsilon 0\mathrm{i}}/R_0 = 2.8\times10^{-4}$ (mean value) is 15.9 $\mathrm{kg\,d^{-1}}$, 7.5% of the injected gas. The initial amplitude of bubble wall pulsation for the breathing mode required to match the measurements from the divers is $R_{\epsilon 0\mathrm{i}}/R_0 = 2 \times 10^{-4}$. As explained in section 5.2, on 19th June at the time of diver measurements (11.00 am to 11.49 am), the inferred gas flow rates from the hydrophone are contaminated by noise. Comparison of the diver-generated flux estimate with the acoustically-inferred fluxes at similar points in the tidal cycle at the same conditions of gas injection rate where the impact of noise is minimized allows refinement of the estimate of flow rate and $R_{\epsilon 0\mathrm{i}}/R_0$. These are computed over four periods. On 19th June between 11.00 pm and 11.49 pm, averaged flow rate of 6.6 $\mathrm{kg\,d^{-1}}$, $R_{\epsilon 0\mathrm{i}}/R_0 = 1.3 \times 10^{-4}$. On 18th June between 11.00 pm and 11.49 pm, averaged flow rate of 6.2 $\mathrm{kg\,d^{-1}}$, $R_{\epsilon 0\mathrm{i}}/R_0 = 1.2 \times 10^{-4}$.

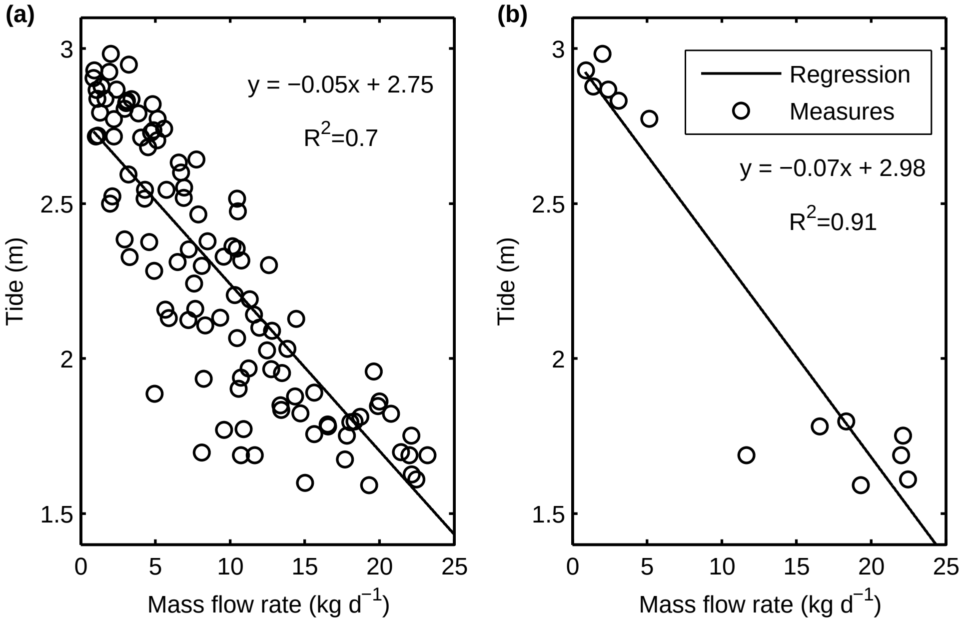

Figure 5.9.: Tidal levels against mass flow rates inferred from acoustics. In both graphs, circle markers are the measurements at various times and the solid black lines are the linear regression of these data points. (a): data points are the average over 43 minutes periods from 14th June 05:30 pm to 18th June 02.00 pm. (b): data points are the average over 86 minutes periods at peak tidal heights from 14th June 05:30 pm to 18th June 02.00 pm.

On 18th June between 11.00 am and 11.49 am, averaged flow rate of 5.3 kg d^{-1}, $R_{\epsilon 0\mathrm{i}}/R_0 = 1.1 \times 10^{-4}$. On 17th June between 11.00 pm and 11.49 pm, averaged flow rate of 5.3 kg d^{-1}, $R_{\epsilon 0\mathrm{i}}/R_0 = 1.1 \times 10^{-4}$. This refines the estimated flow rates at the time of the diver measurements to 5.9 ± 0.7 kg d^{-1} and the estimation for $R_{\epsilon 0\mathrm{i}}/R_0$ to $R_{\epsilon 0\mathrm{i}}/R_0 = 1.2 \times 10^{-4} \pm 6.8 \times 10^{-6}$.

The quantitative assessments of CO_2 released as free gas (by the divers and using passive acoustics) is only a fraction of the injected CO_2 ($\approx$ 15%) and the remaining ($\approx$ 85%) was retained in the sediments during the limited time of the observation. Although free gas trapped within the sediment layers could be observed using seismic reflection surveying[126], Blackford et al. [123] suggest that a large part of the injected gas was dissolved in sediment pore waters. It is likely that sediments in general can build up reservoirs of free and dissolved gas, both of which may become released from sediments at a later time.

In summary, even when using only a single hydrophone, the passive acoustic technique managed to obtain real time continuous data over 7 days of the gas flux from the QICS experiment, in agreement with the single data point provided by divers who directly collected gas. The source of uncertainty in the acoustically-induced gas flux is well characterized and the route to reducing it is well-understood. Furthermore, the technique also provides real time and continuous monitoring of the bubble size distribution.

5.4. Summary

In the framework of the QICS project, the passive acoustic inversion described by Leighton and White [61] (section 4.2) is used on data collected at sea. During this experiment, CO_2 gas was released at different rates and passive acoustic recordings provided continuous monitoring for 7 days. It is observed that the estimates inferred from the acoustic data correlate well with the different changes in flow rates, exemplifying good accuracy of the method in a limited set up (one hydrophone deployment). The tide is found to have a dominant effect on the flow rate. High tide is associated with low gas release and low tide with high gas release. This correlates with photographic observations. A decrease of 15.1 kg d^{-1} in flow rate for each meter of tide increase is estimated. These changes in flow rates are mostly occurring when the tidal cycle is at its local maximum or minimum [34].

When addressing the potential use of the passive acoustic inversion scheme described in this study, it can be noted that gas release detection can be performed efficiently using hull mounted sonar systems on vessels (e.g. scientific echosounders) [20, 28, 38]. These systems can also be used to estimate the amount of gas released [40, 41, 127]. However, these measures only constitute snapshots at a specific point in time and do not usually provide coverage of the development of a leak. Local techniques can provide such insights [33, 42, 45, 46] but the power requirements are significant. In that respect, the use of passive acoustic sensors presents a low cost and low power consumption alternative.

Though, hull mounted echosounders are very efficient at detecting gas leaks because gas bubbles scatter sound very efficiently. These systems produce a large amount of data over areas typically surveyed by vessels. Using echosounders, a vessel can survey vast areas acoustically, resulting in data sets that can further be used to provide order of magnitude estimate for the amount of gas released over the area covered [28, 37, 38, 40, 41, 127]. This is complementary to the deployment of passive acoustic sensors. Based on echosounder data at multiple frequencies, an inversion method based on the backscattering of gas bubbles and inspired from fisheries acoustics is described in chapter 6. The method is tested against simulated data and accuracy and precision in various scenarios are studied.

6. Multi-frequency acoustical estimation of gas release

6.1. Introduction

Estimations of gas fluxes of leaks from the seabed using direct, local sampling methods (such as use of sample collection bottles [129] in the water column or tubes [130] in the sediment) would be significantly complemented by a remote quantification method, such as active sonar might provide. Low frequency methods for remotely assessing the gas flux of the seabed have been proposed [119, 120]. In the oceanic water column, high frequency active sonar is known to scatter strongly from bubble seeps [131] and these are instruments scientists frequently rely on to preliminarily assess seeping areas [28, 37, 38, 40, 41, 127]. These tools are active sonar units that image the water column below the vessel (Figure 6.1(a) and (b)) [20, 132]. These can also be part of systems lying on the seafloor in order to image gas releases over extended periods of time [33, 42, 45, 46]. This consists of data collected from a single broad acoustic beam (single beam echosounder) or across multiple narrow acoustic beams (multi-beam echosounder). Multi-beam systems have long been used to measure bathymetry [43]. However, they can also provide a cross sectional image of the water column (using the data collected from each individual beams), offering high resolution capability for the water column. conversely, a single beam echosounder only returns single data stream corresponding to the acoustic strength in its insonified volume. Thus, with a broad acoustic beam, large volumes are covered but at the cost of reduced resolution. This offers a simple method to detect flares because bubbles scatter sound very efficiently and produce clear traces (e.g. Figure 6.1(c)). For this reason, single beam echosounders are frequently used to provide preliminary assessments of gas escapes. In addition, while robust calibration procedures are established for single beam echosounders [133], calibration of multi-beam echo-

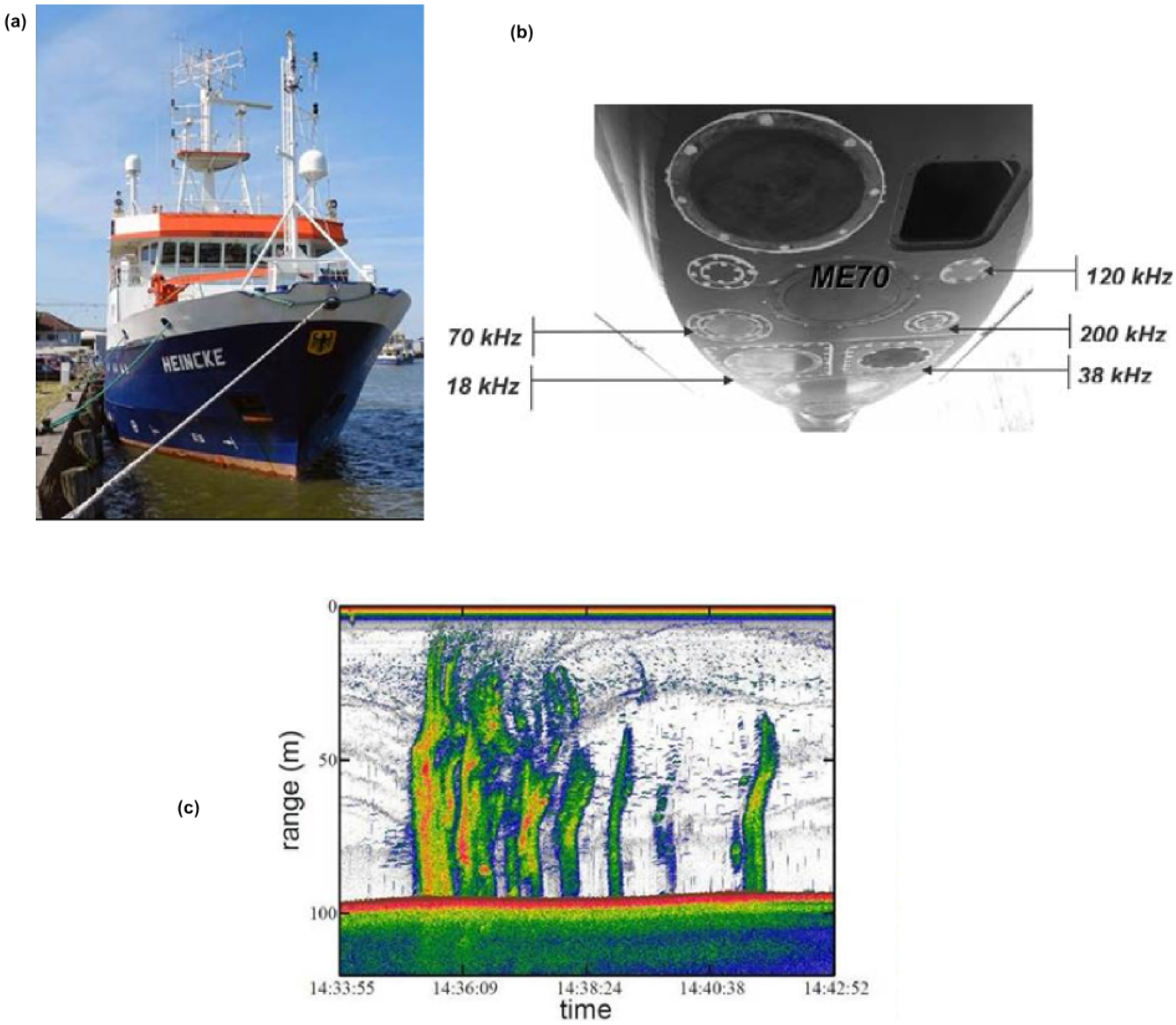

Figure 6.1.: (a): Photograph of the vessel Heincke. (b): Photograph of an EK60 echosounder (from the vessel Thalassa, ifremer, extracted from Berger et al. [128]). This shows each unit of the EK60 (for each frequency channel, 18 kHz, 38 kHz, 70 kHz, 120 kHz and 200 kHz). The ME70 instrument is a multibeam system. (c): EK60 echogram from a research cruise (JR253) to the seas off Svalbard [47] showing gas escaping from the seabed (~100 m). These acoustic flares are usually the combination of several bubbles streams populating the insonified volume.

sounders remains topical [134, 135]. In this chapter, an inverse method based on calibrated single beam echosounder data is described. This method is aimed at estimating gas flow rates utilizing an inversion based on the backscattering of gas bubbles section 3.6.

Furthermore, single beam sonars (Figure 6.2(a)) have the ability to be embedded on ROVs (Remote Operated Vehicles) in order to provide assessments of the surroundings of the vehicle [48, 49]. At a local level, this detects individual bubble streams (Figure 6.2(b)). While the use of optics can be challenging underwater, the use of a sonar unit provides benefits when detecting gas bubbles. For example, Figure 6.2(c) shows a sonar scan (with a range of 20 m) where three bubble stream are detected around the ROV. The detection of each bubble streams allows the ROV to close up, allowing local operations to be performed (gas sampling, seafloor sampling, video observation etc.). In addition, this gives precise mapping of individual bubble streams that can further be correlated to the acoustic scattering recorded by the echosounders from the vessel. These systems are usually not calibrated as their main focus is to provide acoustic imaging of the surroundings. Though, if such a system is able to produce absolute acoustic scattering measurements, quantitative assessment of each bubble stream can be achieved using the inversion scheme described in this chapter.

Single beam sonars return the acoustic strength in the insonified volume that contains either a single target or multiple targets. Data processing strategies differ in each case and a summary of the processing strategies are well established for fisheries acoustics [43, 64]. Similar decision flow charts are applicable when considering the scattering from gas bubbles. The diagram from Horne and Jech [64, Figure 1] is recalled in Figure 6.3. With a single scatterer in the insonified volume, individual targets can be inferred (echocounting) and abundances are determined by analysing the response from each single target. However, with overlapping echoes, two cases arise depending on the type of data set: single frequency data; multi-frequency data. With a single frequency approach, assumptions that limit the range of applicability of the techniques are necessary (e.g. assuming the population present a strongly dominant size). Earlier single-frequency sonar imagery of bubble populations under breaking waves could be interpreted to estimate the bubble size distribution present, as was done in the pioneering work of Thorpe [136] for bubbles generated by breaking waves on Loch Ness. However quantitative estimates of the bubble population from single-frequency data require the assumption that only resonant bubbles scatter the

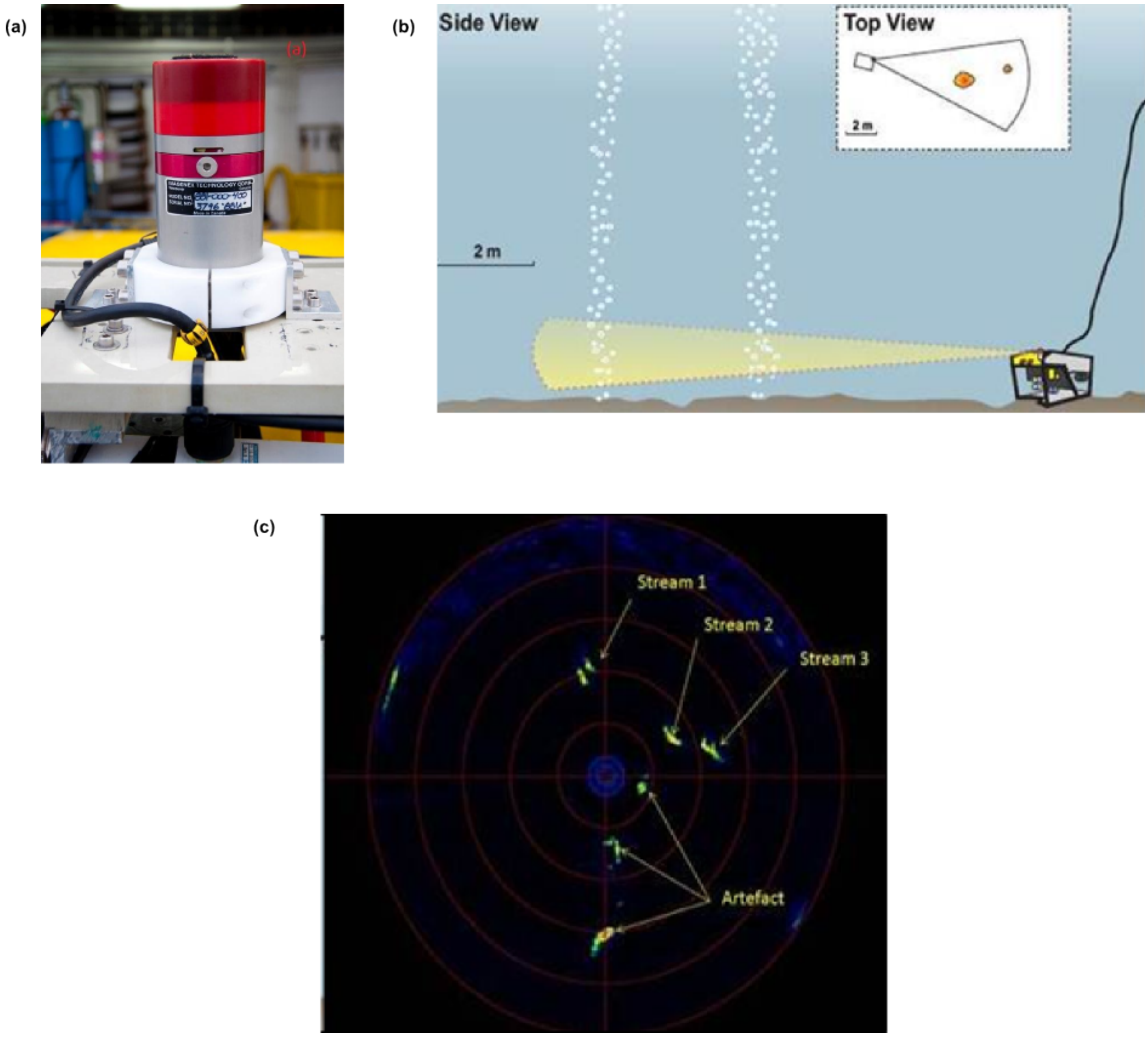

Figure 6.2.: (a): Photograph of the Imaginex 881A sonar that was mounted on the ROV during a research cruise (HE387) to the seas off Svalbard. (b): Schematic of the use of an imaging sonar mounted on an ROV for the detection of gas leaks. Acoustic surveys performed with a vessel provide approximate locations of gas releases. Then, ROV operations are undertaken in order to determine more precisely the spatial and temporal characteristics of each gas stream. (c): Imaginex 881A sonar scan (20 m range) from the ROV landed on the seafloor. This shows imaging of three streams of bubbles. Artefact reflections from cables appear at the rear of the ROV.

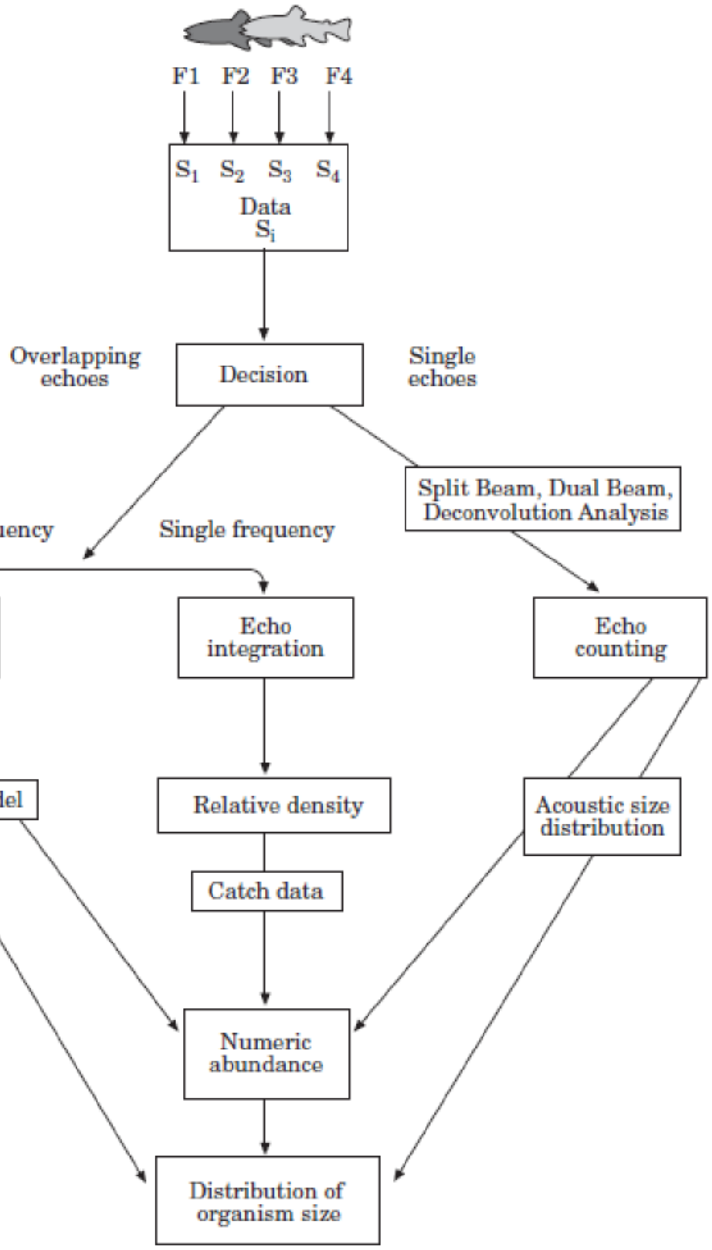

Figure 6.3.: Diagram of acoustic data processing for assessment of fish abundances given different type of echosounder data sets. The methodology described in the following sections is inspired from the multi-frequency approach (with scattering from bubbles instead of fishes). The figure is extracted from Horne and Jech [64]

sound. As abilities for bubble modelling developed, the inherent ambiguity between large bubbles and resonant bubbles (both of which can scatter strongly) placed a fundamental limitation on the accuracy of estimations using single frequencies [137]. If a wide range of frequencies are used (ideally spanning the resonances of all bubbles present), then matrix inversion methods can be used to estimate the number of bubbles present, and their sizes, although this has tended to be through measurement of attenuation rather than backscatter [117, 138–140]. In principle the bubble-induced perturbation of the sound speed can also be inverted to estimate the bubble size distribution, but unless all the bubbles are much smaller than the bubble size that would be resonant with the sound field [119, 141–143], then the precision required in the phase calibration of the receivers can make inversion by sound speed imprecise [144].

In this chapter, theoretical consideration for two inverse approaches based on the backscattering strength from bubbles plumes are presented. They are inspired and adapted from methods used to estimate biovolumes for zookplankton [60, 62, 63, 65, 67, 145] and various fish types [43, 44, 146, 147]. Using theoretical developments on the backscattering cross section of single gas bubbles described in section 3.6, two inverse approaches are developed, based on: a two frequency data set; a three and more numerous frequency data sets. In order to examine the accuracy of each method, a test problem is constructed. This simulates data to be the inputs for the inversion. Scenarios are considered with:

- Various size distributions
- Various number of frequencies
- Different number of scatterers in the sampled volume
- Different levels of noise

First, theoretical development is given on the different inverse methods. Then, procedures for constructing and solving the test problem are detailed. Afterwards, results of the inversion on the simulated data are presented and discussed. These address the accuracy and the precision of the methods.

6.2. Inverse approach

In this study, the case of a calibrated monostatic single beam sonar [133] is considered with a scenario where targets of different sizes and of the same type are insonified. If targets are sufficiently separated in range so that single echoes can be resolved, one can perform echo counting to determine the size of each target from their distinctive echo trace. However, in the case that multiple targets are insonified simultaneously, they cannot be distinguished individually and they combine to form a more complicated signal. An inverse approach is required to determine the distribution of sizes. In this situation, a commonly used unit is the backscattering coefficient per unit volume s_v ($S_\mathrm{v} = 10\log_{10}(s_\mathrm{v})$), expressed in m^{-1} [148]. This consists of the measurements that are intended to be inverted in this study. It represents a measure of the absolute backscattered intensity corrected for spreading, absorption losses and normalized to a volume of 1 m^3. Within a sampled volume V_0, this is defined as [43, 60]:

$$s_\mathrm{v} = \frac{\sum \sigma_\mathrm{bs}}{V_0}. \tag{6.1}$$

This quantity can be measured at different frequencies [128, 149, 150]. The information at each frequency is used to input the inverse problem and the multi-frequency ability of the echosounder is employed here. The volume backscattering strength $s_\mathrm{v}^{f_l}$ can also be expressed in terms of the the abundance density as function of bubble sizes $N(R_0)$:

$$s_\mathrm{v}^{f_l} = \int_0^\infty N(R_0)\sigma_\mathrm{bs}(R_0, f_l)dR_0. \tag{6.2}$$

Before applying the inversion, it is important to meet certain conditions as described by Holliday and Pieper [63], Greenlaw and Lawson [60] or Lebourges-Dhaussy [65]. The basic assumption is that the echo from a volume containing scatterers is considered as the sum of echoes from each individual scatterers. This implies the following:

- Incoherent scattering between scatterers
- Shadowing effects are negligible (absorption of the acoustic wave through the bubble layer)

- The distribution of the scatterers is homogeneous through the sampled volume

Also, it is important to note that the quality of the information inferred from the measurements depends on the accuracy of the calibration of the acoustic system [133, 151].

6.2.1. Choosing the appropriate scattering model

Before expanding on theoretical consideration of the inversion process, it is important to clarify the choice for the modelling of the physics. Here, the kernel matrix of the inverse problem (chapter 2) is based on the backscattering cross section σ_{bs} for a single gas bubble. This acoustic quantity is discussed in section 3.6. Depending on the kR_0 regime considered, the different models for σ_{bs} apply with various accuracies:

- $kR_0 \ll 1$: the analytical breathing mode solution (Equation 3.31) works best in this regime because it describes the resonance behaviour precisely by including damping effects. While the modal solution (Equation 3.34) also predicts the response at the bubble resonance frequency f_0, the accuracy is less than for the analytical solution because damping effects are not accounted for.
- $kR_0 \gg 1$: one of the assumptions for the analytical breathing mode solution (Equation 3.31) is that $kR_0 \ll 1$ (i.e. the acoustical wavelength is very much longer than the bubble radius), thus making this model inappropriate in the $kR_0 \gg 1$ regime. Although the range of applicability of Equation 3.31 can be expanded to all kR_0 through the solution derived by Thuraisingham (Equation 3.32) [96], this only models the contribution of the breathing mode. At $kR_0 \approx 1$ and $kR_0 \gg 1$, the contribution of the breathing mode is predicted to be very small and it is needed to account for other modes (Figure 3.5). The modal solution is then best suited to predict σ_{bs} in these regimes.

Almost all attempts to quantify gas releases from single sonars [28, 37, 42, 152, 153] assume that $kR_0 \ll 1$, using the analytical breathing mode solution for the modelling of σ_{bs}. Application of formulations which assume this, in situations that this assumption does not hold, will lead to significant errors [2, 3] (and furthermore may not deal with several important errors that have become embedded in the literature of the acoustic scattering cross-section). Table 6.1 summarizes studies that make use of models that assume $kR_0 \ll 1$ while working at $kR_0 \gg 1$. This situation has probably arisen for two reasons. First, even if the assumptions in the physics do not match the prevailing conditions under which the measurement was taken, the inversion algorithm can always be constrained to produce an answer, even if the answer is incorrect. The result from an inversion should be constrained to be physical (e.g. the bubble size distributions should be positives but their accuracy can not be confirmed without independent ground truthing). Second, inversions based on bubble physics that assumes that $kR_0 \ll 1$ have for years been successfully and accurately completed to estimate the bubble size distribution in the upper ocean, under breaking waves [79]. However here buoyancy tends to remove large bubbles rapidly from the water column, such that the bubble population is dominated by bubbles of roughly tens of microns in radius, with relatively few of millimetre radius [154]. In contrast, when gas is released from the seabed, all bubbles that are injected into the water column travel upwards, and there is not a balance between the downwards components of ocean turbulence and circulation, and the upwards effects of buoyancy, that filters out the larger bubbles at the upper sea surface [136]. As a result of this, and the tendency of bubbles to coalesce upon injection [87, 155], bubbles released from seeps tend [54, 55, 61] to be several millimetres in radius. In this chapter and chapter 7, insonifying frequencies considered span from 38 kHz to 200 kHz (range of frequencies typical of the EK60 instrument that produced data analysed in chapter 7). Considering bubbles sizes ranging from 1 mm to 10 mm, this gives kR_0 between 0.16 and 8.4, enforcing the use of the modal solution in order to compute σ_{bs} .

Whilst models of the evolution of a gas plume in the sediment [54, 158] and in the water column [155, 159–161] (and beyond that into the atmosphere [54]) have been developed (and may yet need further development, for example to include variability in gas flux and composition [162]), modelling of the acoustical scattering by bubbles has relied heavily on formulations that assume $R_0 \ll \lambda$. In using high frequencies with large bubbles, some authors state that they are avoiding the complications that the bubble resonance would introduce, but do not take account of the fact that the algorithm linking scattering cross-section to bubble size becomes multi-valued outside of the $kR_0 \ll 1$ limit. Hornafius et al. [37] used 50 kHz sonar scatter off bubbles with a mean radius of 6 mm ($kR_0 \approx 1.3$) and a maximum of 15 mm ($kR_0 \approx 3.1$). Muyakshin and Sauter [153] estimated the gas flux from 38 kHz sonar scattering of bubbles having up to 12 mm radius ($kR_0 \approx 1.9$); whilst Nikolovska et al. [152] made similar quantifications using 675 kHz on a bubble population whose

Study	Sonar frequency (kHz)	Maximum bubble size (mm)	Corresponding value of kR_0
Hornafius et al. [37]	50	6 (mean radius)	~1.3
Hornafius et al. [37]	50	15 (maximum radius)	~3.1
Muyakshina and Sauter [153]	38	12	~1.9
Nikolovska et al. [152]	675	2-5 mm (mean radius)	~5.7-14.1
Granin et al. [156]	28	5.2	~0.6
Artemov et al. [157]	38	18.3	~2.9
Artemov et al. [157]	120	18.3	~9.2

Table 6.1.: Non-exhaustive list of studies using an analytical breathing mode model for σ_{bs}. The maximum values of kR_0 at which these studies are working break the basic assumption of the breathing mode formulations, $kR_0 \ll 1$ (i.e. the wavelength is long compared to the size of the bubble).

average radius was 2-5 mm ($kR_0 \approx 5.7 - 14.1$). Granin et al. [156] used 28 kHz sonar to study bubbles with radii as large as 5.2 mm ($kR_0 \approx 0.6$). Artemov et al. [157] exposed bubble radii up to 18.3 mm with 38 kHz ($kR_0 \approx 2.9$) and 120 kHz ($kR_0 \approx 9.2$) sonar. Nikolovska and Schanze [38] also used a 675 kHz sonar, but with an opaque algorithm that does not depend on the size of the bubbles present, but only the overall void fraction and the size of the cloud they occur in. Ostrovsky et al. [40] used 120 kHz sonar on bubbles at least as large as 10 mm radius ($kR_0 \approx 5$), although they follow the long-wavelength formulations, they relied upon empirical relationships between target strengths for freshwater bubbles. Schneider von Deimling and Papenberg [163] also worked outside of this ‘long wavelength’ regime, with bubble radii as large as 20 mm scattering 50 kHz ultrasound ($kR_0 \approx 4.1$), though in fairness they focused on acoustic Particle Imaging Velocimetry rather than the quantification of the gas flux from the strength of the acoustic scattering. Salomatin and Yusupov [164] were cogniscent of the need to account for the violation of the long wavelength assumption, and also (like Ostrovsky et al. [40]) account for the departure of the shape of the rising bubble from the sphere.

One approach [62] has been to take formulations [92, 165, 166] developed for zooplankton (modelled as simplified idealized shapes) and employ these well-known inversions to bubble data. Whilst the zooplankton formulations were not developed with the assumption that $kR_0 \ll 1$, there is however a fundamental problem with the approach that relies on this. The inversion for zooplankton abundance is based on well-known formulations [92, 165, 166] for calculating the frequency-dependent scattering on the dimensions of the sphere, the cylinder or the ellipsoid that has a volume that is equivalent to that of the organism in question. The problem with applying this to bubbles is that the mechanism of scattering is different, as explained by Leighton [1].

Some authors [156] comment that the results of the acoustically-derived gas flux are not in keeping with their expectations and with independent measurements, if those exist. Whilst not the sole source of discrepancy, note should be taken of the possibility of errors that could accrue through use of an inappropriate algorithm to convert rise speed to bubble size, and the use of formulae that assume $kR_0 \ll 1$ and/or a monotonic relationship between scattering cross section and bubble size, and the possible errors in quoting historical expressions for the scattering cross-section of a bubble [2, 3].

In this thesis, the formulation of Feuillade and Clay [100] of the Anderson fluid sphere scattering model [99] is utilized through two approaches:

- a two frequency inversion
- an inverse approach based on 3 or more frequencies using Levenberg-Marquardt least squares method [52, chap. 25] (section 2.2).

6.2.2. Single frequency approach

If it is assumed the insonified volume V_0 contains bubbles of one size only R_0, through the assumption that s_v is the result of the sum of echoes from each individual scatterers (linearity assumption), s_v measured at frequency f is as:

$$s_\mathrm{v}^f = N_0 \times \sigma_\mathrm{bs}\left(f, R_0\right), \tag{6.3}$$

with N_0 representing the total number of bubbles. Thus, by using an appropriate model for σ_{bs}, the number of bubbles can be inferred given R_0 is known. However, assuming only one bubble size is present is unrealistic and in practice, distribution of bubbles span a spread of bubble sizes. This approach is then imprecise and is only able to perform efficiently if the bubble size distribution is dominated by a single size $R_{0_{\mathrm{d}}}$ (e.g. bubble size distribution in Leifer and Culling [54, Figure 6]). Though, if the bubble size distribution is spread across a large range of bubble radii, this can partially be taken into account by using an average value $\bar{\sigma}_{\mathrm{bs}}$ for σ_{bs} in order to determine the abundance N_0:

$$s_{\mathrm{v}} = N_0 \bar{\sigma}_{\mathrm{bs}} = N_0 \sum F_l \sigma_{\mathrm{bs}} \left(f, R_l\right), \tag{6.4}$$

with F_l the fraction of bubbles in the radius bin R_l to the total number of bubbles N_0. However, the spread in scatterer size needs to be determined experimentally prior to invert the data. In the case of gas bubbles, this can be performed by using for example optics. In the case of fisheries acoustics, prior knowledge is given from organism samples from capture using fish nets. Gas volumes are further obtained through:

$$V_{\mathrm{est}} = \frac{4\pi}{3} N_0 \sum F_l R_l^3. \tag{6.5}$$

The main drawback of this technique is the prior knowledge required about the bubble population. This implies measurement of bubble sizes prior to quantification which is frequently impractical: local methods to determine bubble size distributions are costly and only sample few individual bubble streams specimen. In the case of methane seeps, it has been shown that bubble releases span different types of bubble size distributions [54] and in many cases it is clearly impractical to obtain prior knowledge before collecting acoustic data. In addition, the bubble size distribution can change with time [34]. It is then very beneficial to be able to determine the bubble size distributions directly from sonar data. This way, gas volumes could be inferred solely based on acoustical data.

6.2.3. Two frequency approach

Description of two frequency techniques is given for example in Lebourges-Dhaussy [65] or Mitson et al. [167]. Similarly to the single frequency approach, bubbles contained in the insonified volume V_0 are assumed to be concentrated about a single size R_{0_d}. If a sonar system provides measurement of s_v at two frequencies f_1 and f_2, these approximately relate to the abundance N_0 as:

$$\begin{aligned} s_\mathrm{v}^{f_1} &= N_0 \sigma_\mathrm{bs}\left(f_1, R_{0_\mathrm{d}}\right) \\ s_\mathrm{v}^{f_2} &= N_0 \sigma_\mathrm{bs}\left(f_2, R_{0_\mathrm{d}}\right) \end{aligned}. \tag{6.6}$$

This provides a system of two equations with two unknowns, R_{0_d} and N_0. Using an appropriate model for σ_bs, it is possible to estimate the dominant size R_{0_d} through:

$$\frac{s_\mathrm{v}^{f_1}}{s_\mathrm{v}^{f_2}} = \frac{\sigma_\mathrm{bs}\left(f_1, R_{0_\mathrm{d}}\right)}{\sigma_\mathrm{bs}\left(f_2, R_{0_\mathrm{d}}\right)}. \tag{6.7}$$

If a simplified model is available, it is possible to determine the dominant size analytically (e.g. in the case of Rayleigh scattering). Otherwise, this can be solved numerical. It is important to note that analytically, the ratio $s_\mathrm{v}^{f_1}/s_\mathrm{v}^{f_2}$ is:

$$\frac{s_\mathrm{v}^{f_1}}{s_\mathrm{v}^{f_2}} = \frac{\int\limits_0^\infty N(R_0)\sigma_\mathrm{bs}(R_0, f_1)dR_0}{\int\limits_0^\infty N(R_0)\sigma_\mathrm{bs}(R_0, f_2)dR_0}. \tag{6.8}$$

Assuming a single bubble radius distribution $R_{0_\mathrm{d}}$with a single valued abundance N_0 is an approximation of Equation 6.8. As a result, the system of equation presented in Equation 6.6 does not have a single solution but two solutions for a single value of R_{0_d}. The first step of the two frequency algorithm is to find the quantity R_{0_d} through numerical optimization of Equation 6.7. Then, N_0 can be calculated from Equation 6.6 that provide 2 different solutions. The behaviour of the method, especially the closeness between the two solutions will be discussed further in this chapter. From the dominant bubble radius R_{0_d} and the two solution abundances N_0, Volumes are estimated through:

$$V_{\mathrm{est}} = \frac{4\pi}{3} R_{0_{\mathrm{d}}}^{3} N_0 \tag{6.9}$$

Single and two frequency systems can provide order of magnitudes for gas release from acoustic measurements but assume a strongly dominant bubble size $R_{0_{\mathrm{d}}}$. This assumption holds if the release of bubbles produces a size distribution that is narrowly concentrated around $R_{0_{\mathrm{d}}}$. However, most gas release span a large spectrum of bubbles sizes [54, 55]. In order to produce results that account for varying bubble size distributions, it is necessary to have a technique able to discriminate bubbles sizes well enough, i.e. able to be sensitive to significant spreading in the bubble size distribution. This is the aim of the multi-frequency approach (subsection 6.4.2) that is based on three or more frequencies.

6.2.4. Multi-frequency approach

In order to determine more unknowns than for the single and two frequency system, it is necessary to have measurements at a greater number of frequencies (three or more). From a multi-frequency data set, inversion can be performed, allowing one to determine abundances versus bubble sizes. Practically, systems need to cover specific frequencies that are convenient for the inversion process in order to avoid linear regions in σ_{bs} (e.g. Rayleigh scattering regime). Examples of systems using this approach are the Multi-frequency Acoustic Profiler System (MAPS, 21 frequencies from 100 kHz to 10 MHz) [63, 145, 168] or the Tracor Acoustic Profiling System (TAPS, TAPS6 and TAPS8) [68]. In the case of a multi-frequency approach, no assumption on the bubble size distribution is required prior to the inversion (contrary to a single or two frequency approach where the bubble size distribution is assumed to be concentrated about a single size $R_{0_{\mathrm{d}}}$). With a system collecting data at frequencies f_l, $l = 1, 2, 3 \ldots N_\omega$ Equation 6.2 can be approximated at discrete bubbles of radii R_n, $n = 1, 2, 3 \ldots N_R$:

$$s_{\mathrm{v}}^{f_l} = \sum_{n=1}^{N_R} N_n \sigma_{\mathrm{bs}} \left(R_n, f_l\right), \tag{6.10}$$

with N_n the number of bubbles in the radius bin R_n. Expressed in an expanded form:

$$\begin{aligned} s_{\mathrm{v}}^{f_1} &= N_1\sigma_{\mathrm{bs}}\left(R_1, f_1\right) + N_2\sigma_{\mathrm{bs}}\left(R_2, f_1\right) + \ldots + N_{N_R}\sigma_{\mathrm{bs}}\left(R_{N_R}, f_1\right) \\ s_{\mathrm{v}}^{f_2} &= N_1\sigma_{\mathrm{bs}}\left(R_1, f_2\right) + N_2\sigma_{\mathrm{bs}}\left(R_2, f_2\right) + \ldots + N_{N_R}\sigma_{\mathrm{bs}}\left(R_{N_R}, f_2\right) \\ &\vdots \\ s_{\mathrm{v}}^{f_{n_f}} &= N_1\sigma_{\mathrm{bs}}\left(R_1, f_{N_\omega}\right) + N_2\sigma_{\mathrm{bs}}\left(R_2, f_{N_\omega}\right) + \ldots + N_{N_R}\sigma_{\mathrm{bs}}\left(R_{N_R}, f_{N_\omega}\right) \end{aligned} \quad . \tag{6.11}$$

In matrix form [51, 79]:

$$\mathbf{s}_{\mathrm{v}}=\boldsymbol{\sigma}_{\mathrm{bs}}\mathbf{N}, \tag{6.12}$$

with $\boldsymbol{\sigma}_{\mathrm{bs}}$ the kernel matrix containing the quantities $\sigma_{\mathrm{bs}}\left(R_m, f_l\right)$ and $\mathbf{N}$ the vector of abundances containing the quantities N_n. This inverse problem can be solved using the Levenberg-Marquardt least squares or Tikhonov regularization methods (section 2.2). The solution is the vector of abundances $\mathbf{N}$ and is relative to 1 m^3 of water. This represents the abundance of bubbles in different radius bin and it is expressed in $\sharp$/m^3. The level of $\mathbf{N}$ is relative to its bubble radius increment ΔR_0 and in order to provide cross comparison between the different results, it is important to harmonize $\mathbf{N}$ and express them in conventionally defined radius bin increments. By convention the radius bin increment is taken as 1 µm and abundances are then of dimension $\sharp$/m^3/µm. The discrete abundance vectors are converted into $\sharp$/m^3/µm by scaling $\mathbf{N}$ as $\mathbf{N}/\Delta R_0 \times 10^{-6}$ and the quantities then relates to the abundance density as function of bubble sizes $N\left(R_0\right)$. Gas volumes in 1 m^3 of water are estimated by assuming spherical bubbles:

$$V_{\mathrm{est}} = \frac{4\pi}{3}\sum_{l=1}^{N_R} N_l R_l^3 \tag{6.13}$$

6.3. Test problem

6.3.1. Simulation procedure

In the following sections, the inverse approach (inversion based on three or more frequencies, subsection 6.2.4) and the two frequency approach (subsection 6.2.3) are tested against simulated data. The efficiency of the two methods is first assessed in terms of the determination of the dominant bubble size recovery (for the two frequency approach) and the bubble size distribution (for the inverse approach). Then, the accuracy and precision of each technique is assessed through their ability to estimate gas volume. Environmental conditions used for the simulation are: 80 m water depth; 10°C temperature; fresh water ($S_l = 0$); air bubbles (gas parameters listed in Appendix E).

A simulation trial consists of 500 or 100 individual bubble sizes R_0 randomly generated using a probability density function P. Within one simulation, all bubble sizes are assumed to be contained within a volume $V_0 = 1\,\mathrm{m}^3$ and spread across this sampling volume homogeneously. Six cases for P are considered:

- A lognormal distribution, generic probability density function and convenient mathematical model chosen so that a large lobe appears at $R_0 \approx 3$ mm (Equation C.2, Figure 6.4(a), grey line). Bubble sizes range from $R_0 = 1$ mm to $R_0 = 10$ mm.
- A chi distribution, generic probability density function and convenient mathematical model chosen so that a large lobe appears at $R_0 \approx 5.5$ mm (Equation C.1, Figure 6.4(a), black line). Bubble sizes range from $R_0 = 1$mm to $R_0 = 10$mm. This is representative of what is observed by Sauter et al. [55].
- Distributions from Leifer and Culling [54] (methane seepage):
    - A bubble size distribution from a minor seep [54, Figure 5(a)], called "Leifer minor 1" in this study (Equation C.3, Figure 6.4(b), solid grey line). Bubble sizes range from $R_0 = 1$ mm to $R_0 = 5$ mm.
    - A bubble size distribution from a major seep [54, Figure 5(b)], called "Leifer major" in this study (Equation C.6, Figure 6.4(b), solid black line). Bubble sizes range from $R_0 = 1$ mm to $R_0 = 5$ mm.
    - A bubble size distribution from a minor seep [54, Figure 6(a)] called "Leifer minor 2" in this study (Equation C.4, Figure 6.4(b), dashed black line). Bubble sizes range from $R_0 = 1$ mm to $R_0 = 5$ mm.
    - A bubble size distribution from a mixed seep [54, Figure 7(a)], called "Leifer mixed" in this study (Equation C.5, Figure 6.4(b), dashed grey line). Bubble sizes range from $R_0 = 1$ mm to $R_0 = 5$ mm.

The formulation for each individual probability density function together with their characteristics are given in Appendix C. A simulation case is then defined by its

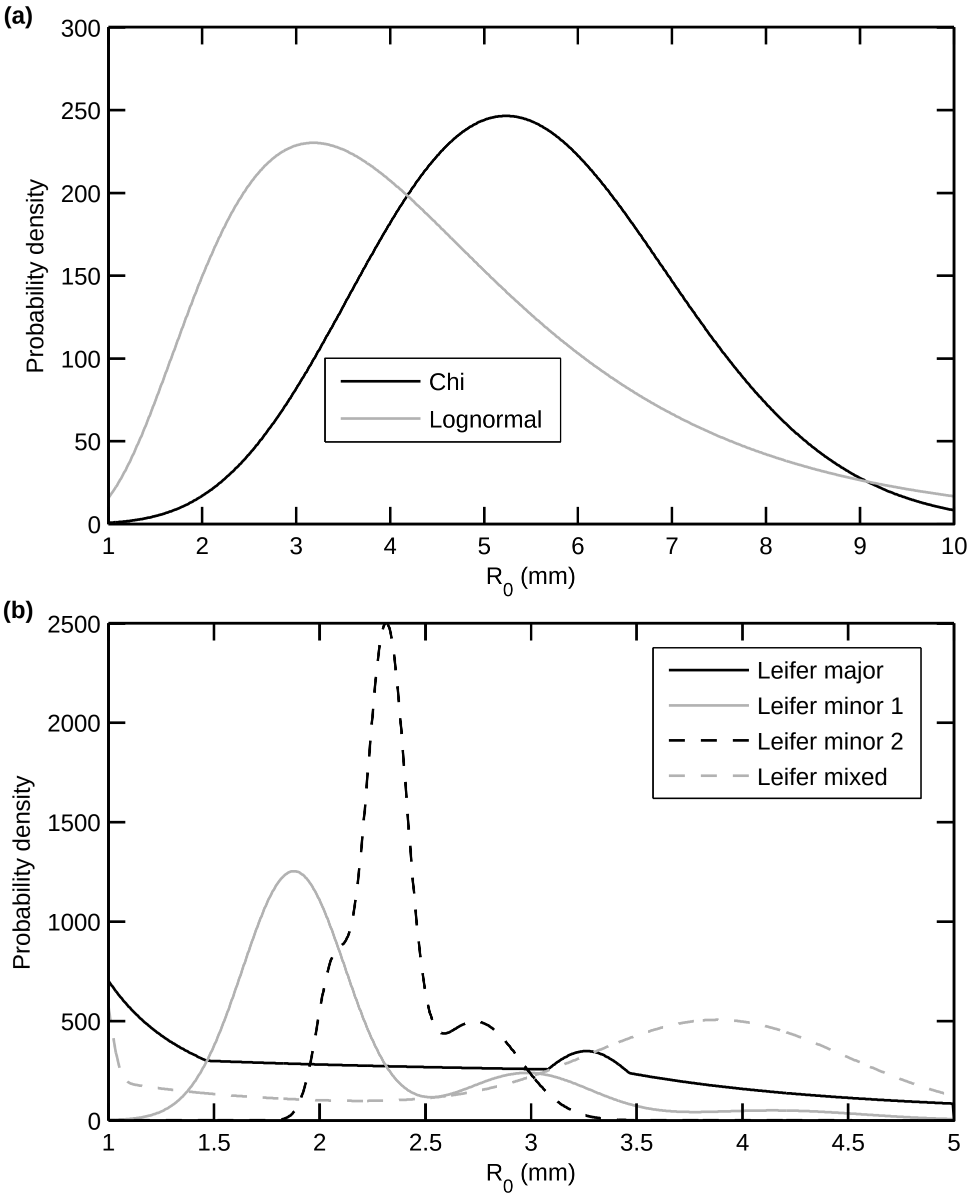

Figure 6.4.: Probability density functions used to randomly generate bubble radii. (a): Two probability density functions are considered with a spread in bubble sizes between $R_0 = 0$ mm and $R_0 = 10$ mm: chi distribution (solid black line); lognormal distribution (solid grey line). (b): Four probability density functions [54] are considered with a spread in bubble sizes between $R_0 = 0$ mm and $R_0 = 5$ mm: Leifer major (solid black line); Leifer minor (solid grey line); Leifer minor 2 (dashed black line); Leifer mixed (dashed grey line).

probability density function and the number of bubbles within the sampling volume N_{b} ($N_{\mathrm{b}} = 500, 100$). For each scenario, 100 different simulations are computed and for each trial a reference volume V_{ref} is calculated as:

$$V_{\mathrm{ref}} = \frac{4\pi}{3} \sum_{l=1}^{N_{\mathrm{b}}} R_l, \qquad N_{\mathrm{b}} = 100, 500. \tag{6.14}$$

This constitutes the quantity that is sought through the inverse or two frequency approach. Further in this chapter, the performances in terms of volume estimates are computed by compiling the results from each 100 simulation as:

$$\bar{\epsilon} = \frac{1}{100} \sum_{l=1}^{100} \frac{|V_{\mathrm{est}_l} - V_{\mathrm{ref}_l}|}{V_{\mathrm{ref}_l}}. \tag{6.15}$$

The quantity $\bar{\epsilon}$ is expressed in % error of the reference volume. For each of the six probability density function with one of the two population size N_{b}, bubble radii are randomly generated, thus producing a given bubble population within V_0. Using Equation 6.1, measurements s_{v} are simulated at different frequencies. For each bubble in a given trial, $\sigma_{\mathrm{bs}}(R_n, f)$ is determined at frequency f through Equation 3.34. For each bubble population, the acoustic backscattering quantity s_v at frequency f is then calculated by adding linearly each σ_{bs} and dividing by V_0 (Equation 6.1). Data sets with various number of frequencies are considered:

- 2 frequencies: 38 kHz; 120 kHz
- 3 frequencies: 38 kHz; 70 kHz; 120 kHz
- 4 frequencies: 38 kHz; 70 kHz; 120 kHz; 200 kHz
- 5, 6, 7, 8, 9, 10, 20, 30, 40 and 50 linearly spaced frequencies from 38 kHz to 200 kHz

The 2, 3 and 4 frequencies cases are representative of the EK60 echosounder instrument (single beam sonar). This system was used to collect data presented in chapter 7 and is commonly used on vessel for various applications (e.g. methane seeps [46, 49], fisheries acoustics [43, 44]). At these frequencies, considering bubble radii from $R_0 = 1$mm to $R_0 = 10$mm, kR_0 lies in the range 0.16 to 8.38. As explained in subsection 6.2.1, σ_{bs} is calculated using the modal solution (subsection 3.6.2, Equation 3.34) and σ_{bs} is plotted in Figure 6.5(a). Figure 6.5(b) shows σ_{bs} in the

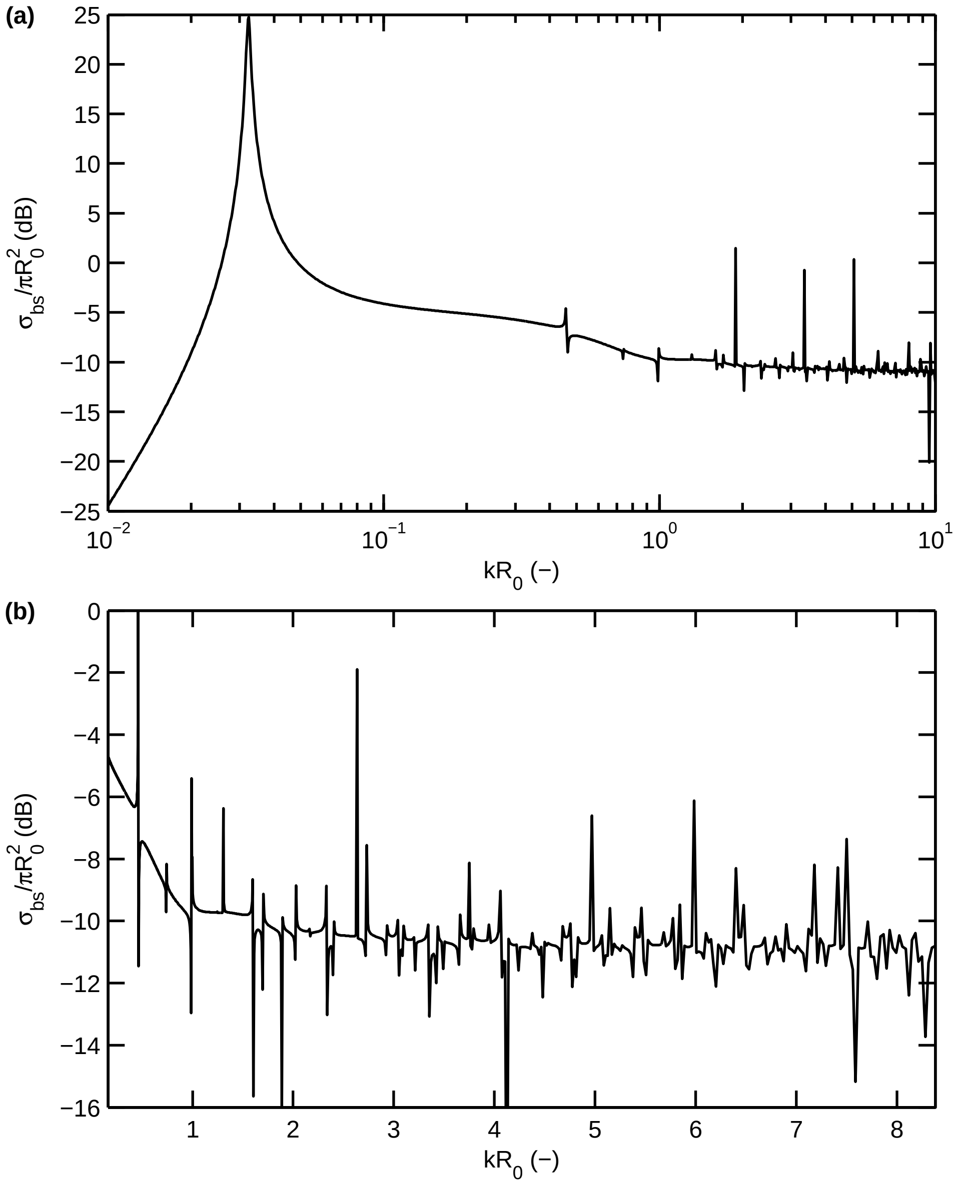

Figure 6.5.: Model for σ_{bs} (modal solution, Equation 3.34) used for simulating data and solving the inverse problem. (a): σ_{bs} (normalized by πR_0^2) versus kR_0. (b): Zoom on the kR_0 regime of interest in this chapter and chapter 7. This includes the transition region and the geometrical scattering regime ($kR_0 << 1$).

range of kR_0 of interest. This spans the transition region ($kR_0 \approx 1$) and the geometrical regime ($kR_0 \gg 1$). For each set of simulated bubble population, measurement vectors $\mathbf{s}_{\mathrm{v}_{\mathrm{exact}}}$ are determined at different frequencies. White noise is introduced by adding an error vector $\mathbf{e}$ (representing errors in the measurement) to $\mathbf{s}_{\mathrm{v}_{\mathrm{exact}}}$, $\mathbf{s}_{\mathrm{v}} = \mathbf{s}_{\mathrm{v}_{\mathrm{exact}}} + \mathbf{e}$. The level of the noise in $\mathbf{e}$ is controlled by the quantity E (relative noise level):

$$E = \frac{\|\mathbf{e}\|}{\|\mathbf{s}_{\mathrm{v}_{\mathrm{exact}}}\|}. \tag{6.16}$$

The quantity E relates to the Signal to Noise level Ratio as $\mathrm{SNR} = 20\log(1/E)$. Noise is added to the data for the case of the two frequency inversion and the multi-frequency inversion with three and ten frequencies. In each case, noise is introduced with a relative noise level from 0% to 50%. From the resulting measurement vectors $\mathbf{s}_{\mathrm{v}}$ (with various amount of noise), V_{est} is computed through the multi-frequency inversion (subsection 6.2.4) and the two frequency inversion (subsection 6.2.3).

6.3.2. Solution procedure

From the procedure described in subsection 6.3.2, the computed measurement vectors $\mathbf{s}_{\mathrm{v}}$ are determined at different frequencies with: different number of bubbles in the sampling volume; different bubble size distribution. In addition, various amounts of noise are added to $\mathbf{s}_{\mathrm{v}}$ to simulate measurement errors. Each simulation then stands a reference volume V_{ref} that is sought to be estimated (V_{est}) through:

- A two frequency approach.
- An inverse approach based on 3, 4, 5, 6, 7, 8, 9, 10, 20, 30, 40, 50 frequencies.

Two frequency approach Following the theoretical development for the two frequency approach described in subsection 6.2.3, V_{est} is calculated by computing the dominant bubble size $R_{0_{\mathrm{d}}}$. Then, the abundance of $R_{0_{\mathrm{d}}}$ (N_0) can be inferred. With the constraint that the dominant radius $R_{0_{\mathrm{d}}}$ lies between $R_0 = 1$ mm and $R_0 = 5, 10$ mm (input ranges of bubble sizes are different depending on the probability density function, subsection 6.3.1), Equation 6.7 is first solved numerically, resulting in a solution for $R_{0_{\mathrm{d}}}$. Using $R_{0_{\mathrm{d}}}$, the abundance N_0 is computed from Equation 6.6. It is important to note that because data are simulated from a range of bubble sizes (and not one bubble size only), assuming that bubbles are of size R_{0_d} is wrong based on the definition of the problem. As a result, the problem does not possess an exact solution and solving Equation 6.6 then produces two different solutions for N_0. Thus, for each simulation, two volumes V_est are resulting from Equation 6.9. The two solutions are labelled “solution 1” and “solution 2” in the following sections. The degree of discrepancy between these two solutions and the level of accuracy and precision to which they estimate V_ref are investigated.

Inverse approach When applying a two frequency scheme, the assumption is made that the bubble size distribution is of one size only and approximated by a dominant bubble radius R_{0_d}. While employing a multi-frequency inversion requires more frequencies in order to provide acceptable performance [65], this allows one to determine characteristics of the bubble size distribution and then estimate more precisely gas volumes, especially those of a complex form. The procedure used here follows theory given in subsection 6.2.4.

The vector $\mathbf{s}_\mathrm{v}$ containing the measurements s_v^f at different frequencies (of size $N_\omega \times 1$) is the starting point of the inverse problem. A range of bubble radius bins is chosen, consisting of linearly spaced bins between the chosen bubble radii R_1 and R_{N_R}, the smallest and largest bubble size bins. The number of bubble size bins is $N_R = N_\omega \times \mathrm{UND}$, with UND the under-determination factor (section 2.2). With $\mathrm{UND} = 1$, the constructed problem is square while if $\mathrm{UND} > 1$, additional rows are added to the least squares problem, leading to an under-determined problem. While building an under-determined problem ($\mathrm{UND} > 1$) can increase the degree to which the problem is ill-conditioned, it presents benefits when the number of measurements are limited [62, 169] because the resolution of the bubble size distribution $N(R_0)$ is increased. In the specific case of the active inversion considered in this study, because of technical and cost limitations, the number of frequency channels is often reduced, giving limited data set (see chapter 7). The first and last bubble radius bins R_1 and R_{N_R} are chosen as the same than those chosen when constructing the probability density functions for generating discrete bubble radii: $R_1 = 1\,\mathrm{mm}$ and $R_{N_R} = 10\,\mathrm{mm}$ (chi and lognormal probability density functions); $R_1 = 1\,\mathrm{mm}$ and $R_{N_R} = 5\,\mathrm{mm}$ (Leifer minor 1, Leifer minor 2, Leifer mixed and Leifer major probability density functions). For each bubble radius R_m, $m = 1, 2, 3 \ldots N_R$ and frequency f_l, $l = 1, 2, 3 \ldots N_\omega$, the matrix $\boldsymbol{\sigma}_{\mathrm{bs}_{l,m}} = \sigma_\mathrm{bs}\left(R_m, f_l\right)$ (Equation 3.34) is constructed.

For each simulation and for each frequency setting, $\boldsymbol{\sigma}_{\mathrm{bs}}$ and $\mathbf{s}_{\mathrm{v}}$ are the kernel and the measurement matrices of the forward problem in Equation 6.12. Through the inversion of this equation, the vector of abundances $\mathbf{N}$ is sought. This is computed using:

- A Tikhonov regularization (section 2.2, Equation 2.3) with the regularization factor α determined using the GCV criterion (section 2.3, Equation 2.9).
- Levenberg-Marquardt least squares (section 2.2, Equation 2.4) with the parameter Λ determined using the L-curve criterion (section 2.3, Equation 2.8).

Using these two methods, abundance vectors $\mathbf{N}$ are calculated for each simulation and V_{est} are determined through Equation 6.13.

6.4. Results and discussion

In this chapter, methods to solve the active acoustic inverse problem described in section 6.2 are tested against simulated data (subsection 6.3.1). This section is divided into two subsections, discussing each of the two techniques: the two frequency approach (subsection 6.2.3); the multi-frequency approach (using three or more frequencies, subsection 6.2.4). From active acoustic measurements in the form of volume backscattering strength coefficients s_{v}^{f} at frequency f, the methods described in section 6.2 aim to estimate gas volumes V_{ref} (Equation 6.14). For both approaches, the way by which the estimated volume V_{est} is obtained relies on the multi-frequency ability of the data set.

With a one or two frequency data set the basic assumption is that the bubble size distribution are of one size only. A reasonable approximation is to considerer distribution with a dominant size $R_{0_{\mathrm{d}}}$. This way, the problem is reduced to two unknowns: the dominant size $R_{0_{\mathrm{d}}}$; the abundance N_0 of bubbles of size $R_{0_{\mathrm{d}}}$. The one frequency case provides a single equation that can be used to determine either N_0 or $R_{0_{\mathrm{d}}}$ given a prior knowledge of one of these two quantities. If s_{v} is measured at two frequencies, both $R_{0_{\mathrm{d}}}$ and N_0 can be solved without prior knowledge. The use of a separate method to obtain prior knowledge of the bubble size distributions is often infeasible. Techniques that provide quantification without prior knowledge are then very advantageous and for this reason, only the two frequency methodology is tested here.

The assumption that the bubble size distribution possesses a dominant size R_{0_d} limits the range of bubble size distributions that can be studied using a two frequency approach. Especially, distributions of bubble sizes can be diverse and do not necessarily present a dominant size R_{0_d} [54]. In contrast to the two frequency methodology, the multi-frequency inverse approach (three or more frequencies, subsection 6.2.4) provides an estimate of the bubble size distribution.

The simulations consist of 100 trials for 6 different bubble size distributions (see subsection 6.3.1). The bubble size distributions (Figure 6.4) are taken to be representative of distributions presenting a strongly dominant bubble size or of more complex form. For each simulation, a reference volume V_ref is generated by adding each individual bubble volume (Equation 6.14) and this is the quantity that is sought. The performances of the two methods are addressed by comparing V_est to V_ref. The robustness to noise is also tested.

6.4.1. Two frequency approach

Dominant radius For each of the six bubble size distributions (subsection 6.3.1, Figure 6.4), 500 bubbles are generated and combined to produce in each case two measurements $s_\mathrm{v}^{f_1}$ and $s_\mathrm{v}^{f_2}$ at two frequencies $f_1 = 38\mathrm{kHz}$ and $f_2 = 120\mathrm{kHz}$. The first step of the two frequency approach is to determine the dominant size of the bubble size distribution R_{0_d} . To that purpose, Equation 6.7 is optimized numerically. Results for R_{0_d} are shown in Figure 6.6. The estimates for R_{0_d} are found to fluctuate and the spikiness varies between being less pronounced in Leifer minor 2 distribution (Figure 6.6(f)) and more pronounced in the Chi distribution (Figure 6.6(b)) and Leifer major distribution (Figure 6.6(d)). Summarizing results in Table 6.2, the standard deviation for R_{0_d} over the 100 simulations is found to be lowest for the Leifer minor 2 distribution and highest for the chi distribution. From Figure 6.4, it is interesting to note that the Leifer minor 2 is the distribution with the lowest spreading in bubble size with a large peak at $R_0 = 2.3\,\mathrm{mm}$. For each distribution, Table 6.2 details the modes of the probability density functions R_mode (value of R_0 for which the probability is the highest). The quantity R_mode is an indicator of the performance of the algorithm as one would ideally want R_{0_d} to predict R_mode. Final results in Table 6.2 are presented as the deviation of $\bar{R}_{0_\mathrm{d}}$ from R_mode: $\left|\bar{R}_{0_\mathrm{d}} - R_\mathrm{mode}\right| / R_\mathrm{mode}$. In the case of the Leifer major distribution (Figure 6.4(b), solid black line), no peak value is clearly identifiable and consequently, no value

	Chi	Leifer major	Leifer minor 1	Leifer minor 2	Leifer mixed	Lognormal
mean value $\bar{R}_{0_\mathrm{d}}$ (mm)	6.6	3.3	2.5	2.4	3.9	4.6
R_{0_d} standard deviation (mm)	1.4	0.6	0.5	0.3	0.4	0.8
R_{0_d} standard deviation (% of $\bar{R}_{0_\mathrm{d}}$)	21.2	18.2	20	12.5	10.3	17.4
pdf mode R_mode (mm)	5.2	-	1.9	2.3	3.8	3.2
pdf standard deviation (mm)	1.3×10^{-4}	-	3.9×10^{-5}	9.8×10^{-6}	5.7×10^{-5}	1.7×10^{-4}
difference with $\bar{R}_{0_\mathrm{d}}$ (%)	26.9	-	24	4.3	2.6	43.8

Table 6.2.: Results from the two frequency approach for the six bubble size distributions considered. For each case, over the 100 simulations, the mean of the dominant radius R_{0_d} is given together with the standard deviation (in mm and as a percentage of $\bar{R}_{0_\mathrm{d}}$). The accuracy of the results is addressed by comparing $\bar{R}_{0_\mathrm{d}}$ to R_mode, the value of R_0 for which the probability density function is largest (called "mode").

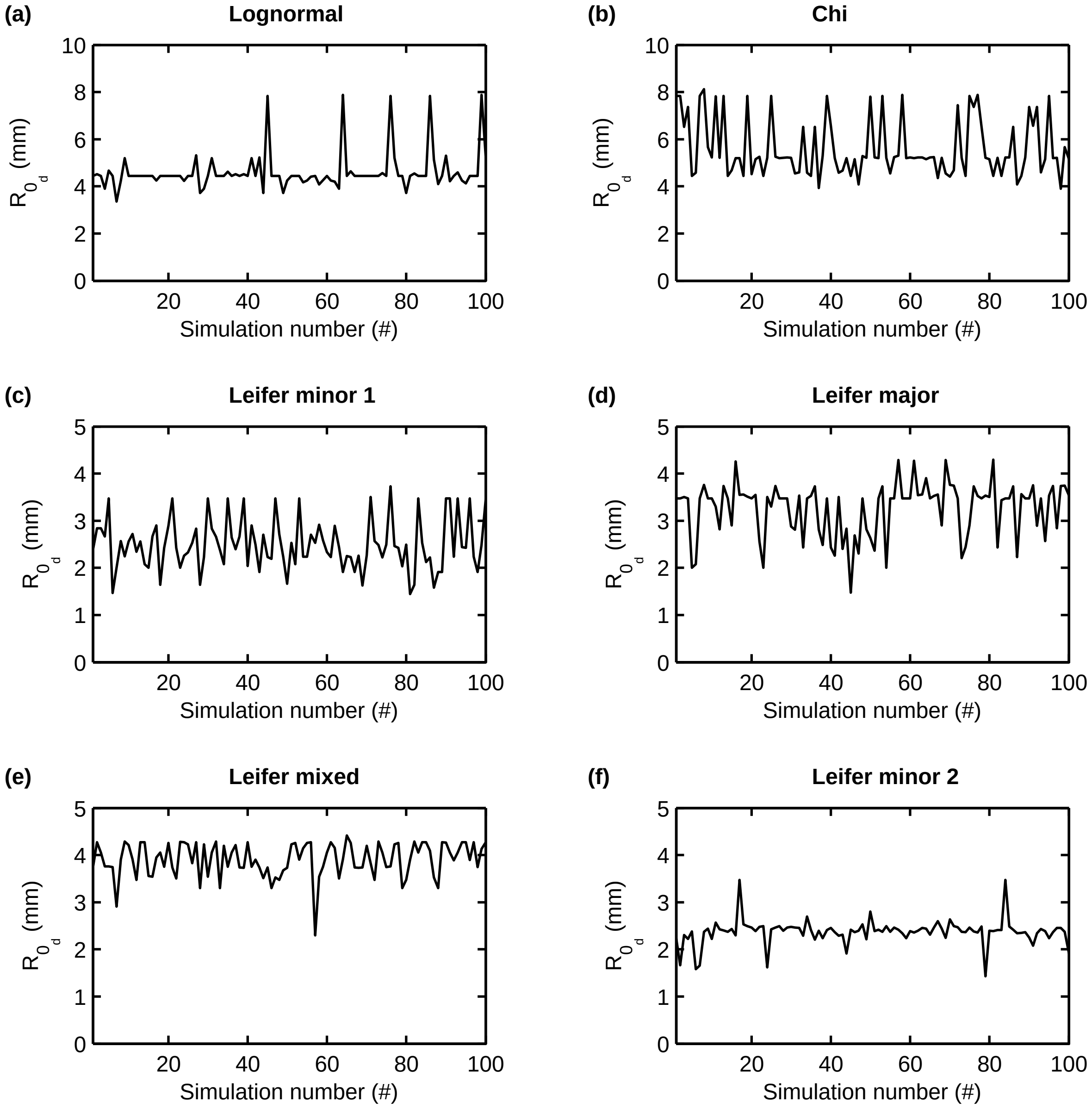

Figure 6.6.: Dominant bubble radius R_{0_d} (mm) estimated for each simulation trial. For each bubble size distributions (six distributions considered, Figure 6.4), 100 simulations are computed and analysed.

is given in Table 6.2. For the Leifer minor 2 distribution, over the 100 trials, the mean value for the dominant radius is $\bar{R}_{0_\mathrm{d}} = 2.4\,\mathrm{mm}$ (Table 6.2), and is in good agreement with the initial distribution ($R_\mathrm{mode} = 2.3\,\mathrm{mm}$, deviation of 4.3%). Conversely the lognormal and chi distributions perform poorly due to their larger spread (Table 6.2, shown as the standard deviation of the probability density functions). Note that while these two distributions are limited to an interval from $R_0 = 1\,\mathrm{mm}$ to $R_0 = 10\,\mathrm{mm}$, the 4 other distributions span bubble radii from $R_0 = 1\,\mathrm{mm}$ to $R_0 = 5\,\mathrm{mm}$. Although the lognormal and chi distributions present clear peaks in their probability density functions (Figure 6.4(a)), their large spread in bubble sizes degrades the performance of the two frequency algorithm. Conversely, the method performs best in the case of the Leifer minor 2 distribution, probability density function that presents the smallest standard deviation. In light of these results, it is clear that the two frequency approach performs best at recovering the dominant radius R_{0_d} when the bubble size distribution is of a simple form with a strongly dominant bubble size (i.e. with a spreading in bubble size which is minimal).

Performance against gas volume The two frequency method consist on a two step algorithm. First, the dominant radius R_{0_d} is estimated by optimizing Equation 6.7 numerically. Then, the abundance N_0 is determined through Equation 6.6. The simulated measurements $s_\mathrm{v}^{f_1}$ and $s_\mathrm{v}^{f_2}$ are generated using the bubble size distributions in Figure 6.4 and assuming a single abundance N_0 associated to a single radius R_{0_d} is an approximation. For this reason, no exact solution can be obtained when solving the two frequency inversion. As a result, Equation 6.7 is optimized and the value of R_{0_d} is then replaced in the two equations in Equation 6.6 that produce two solutions for N_0 (one for each equation). From R_{0_d} and the two abundances N_0, gas volumes are computed using Equation 6.9. Because two values of N_0 are calculated as a result of the two frequency inversion, two gas volumes V_est are computed. For each of the six bubble size distributions, the results from the 100 trials are first presented as a scatter plot in Figure 6.7. Black and white dot markers represent the two solutions for each simulation. The reference volumes V_ref are plotted against the estimated volumes V_est and the diagonal line represents $V_\mathrm{est} = V_\mathrm{ref}$ (i.e. the perfectly accurate estimate). Of interest is the closeness of the two solutions (black and grey dots overlapping each other), varying from distant (e.g. Leifer mixed, Figure 6.7(e)) to near (i.e. Leifer minor 2, Figure 6.7(f)). This is an indicator of the consistency between the two solutions for V_est. Results suggest a better consistency between

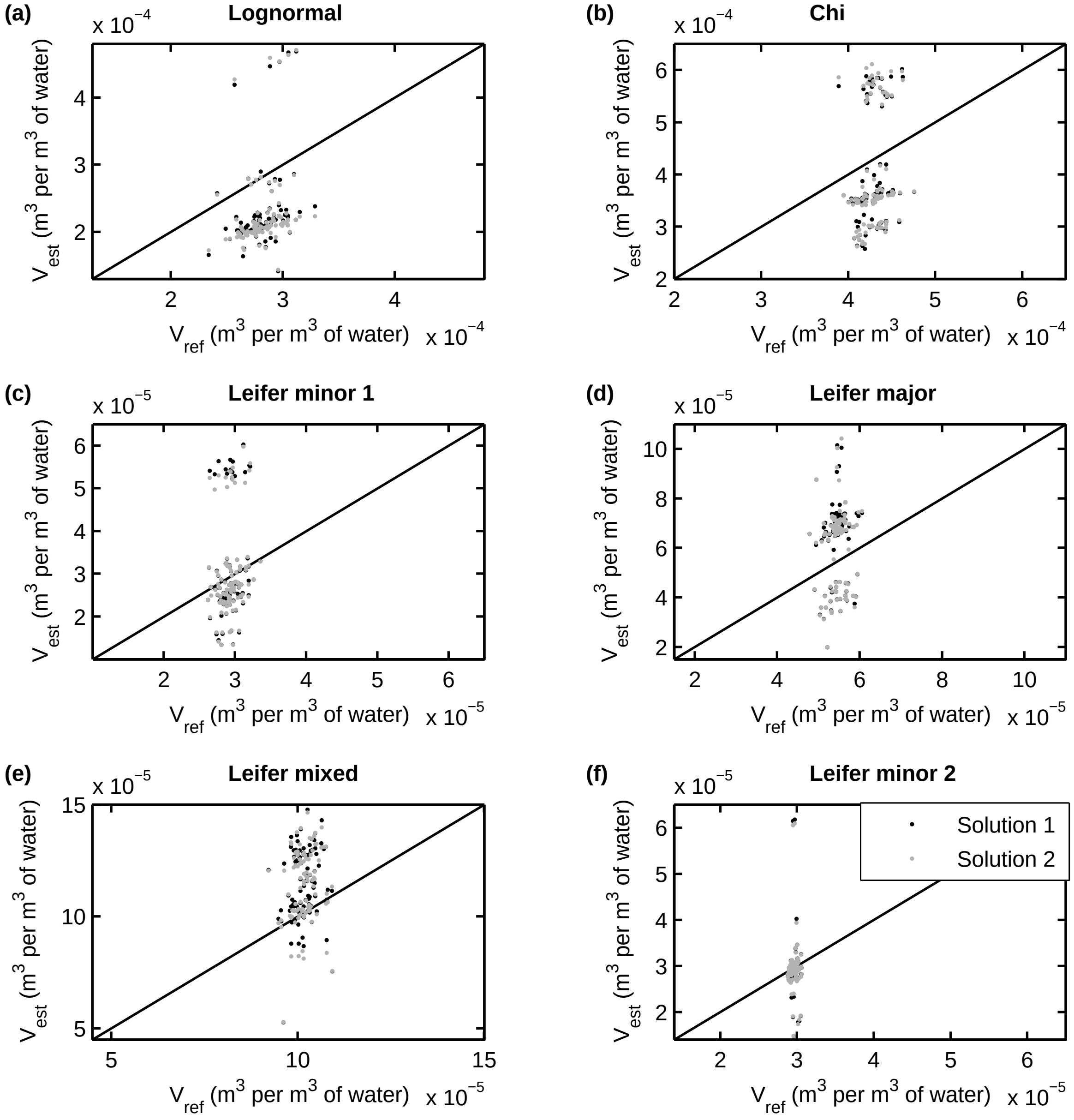

Figure 6.7.: Scatter plot of the results from the inversion of the simulated data using the two frequency approach (subsection 6.2.3). For each bubble size distribution (six distributions, Figure 6.4), 100 simulations are computed, each presenting a reference gas volume V_{ref} that is sought (V_{est}). In each graph, the diagonal line represents the exact estimate $V_{\mathrm{ref}} = V_{\mathrm{est}}$. There is two solutions for V_{est} because no exact solution can be obtained through the two frequency inversion. The two solutions are represented by black and grey dot markers.

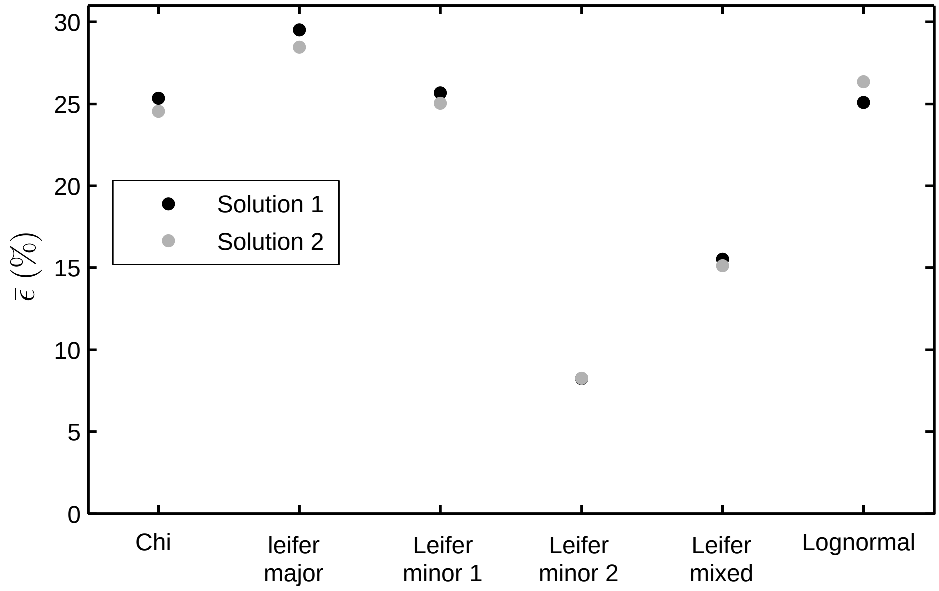

Figure 6.8.: Performance of the two frequency inversion against estimated volumes. Results are shown for the six different bubble size distributions. The quantity $\bar{\epsilon}$ (Equation 6.15) is computed over the 100 simulations in each case and is expressed in %. There is two solutions for V_{est} because no exact solution can be obtained through the two frequency inversion. The two solutions are represented by black and grey dot markers.

the two solutions with distribution presenting a strongly dominant bubble size (e.g. Leifer minor 2 distribution, Figure 6.7(f)). As the range of the size distribution of bubbles increases, the agreement between these two solutions is less (e.g. Leifer mixed, Figure 6.7(e)).

For each simulation, the deviation of V_{est} compared to V_{ref} can be calculated and represents the error in estimated gas volumes ($\bar{\epsilon}$, Equation 6.15, expressed in %). In each case, two results are shown representing the two solutions to Equation 6.6. Results are presented in Figure 6.8. Similarly to Figure 6.7, the closeness of the two solutions are representative of the robustness of the two frequency inversions. When estimating volumes generated using a Leifer minor 2 distribution, results are consistent (Figure 6.8(a), 0.02% difference in volume estimate error between the two solutions). The difference between the two solutions is larger with the other bubble size distributions considered. For example, the lognormal distribution exemplifies the highest difference in error between the two solutions with 1.2% difference (Figure 6.8(a)). Though, the difference between the two solutions for V_{est} for the six bubble size distributions remains within an acceptable level. As for the estimation of R_{0_d}, the error in gas volume (Figure 6.8(a)) is found to be minimized for the Leifer minor 2 distribution with a mean error of $\bar{\epsilon} = 8.2\%$. Chi, Leifer major, Leifer minor 1 and lognormal distributions present errors in excess of 25%. The two frequency approach seems to perform best with bubble distributions presenting a highly dominant bubble radius (e.g. Leifer minor 2 distribution). For bubble size distributions of a more complicated form, the method remains limited in terms of accuracy.

Performance against different spreading in the bubble size distribution Results in Figure 6.8 suggest that the performance of the two frequency inversion is best for bubble size distributions have a strongly dominant bubble radius. Results in Figure 6.8 are only suggestive because results are from six distributions that present different characteristics (Figure 6.4). In order to further the investigation of the effect of the spreading in bubble sizes on the performance of the two frequency approach, a lognormal distribution with different standard deviation is used to simulate $s_\mathrm{v}^{f_1}$ and $s_\mathrm{v}^{f_2}$. The expression for the lognormal distribution is given in Appendix C and the spreading of the distribution is controlled by the variance of $\ln(\mathrm{X})$, σ_X, with X representing the random variable (bubble radii R_0 here). Measurements are simulated from five lognormal distributions with σ_X ranging from 0.5 to 0.1 in 0.1 steps. The distributions are presented in Figure 6.9(a). Figure 6.9(b) shows results for the estimation of R_{0_d} similarly to Table 6.2. The absolute deviation between $\bar{R}_{0_\mathrm{d}}$ and R_mode is calculated as $\left|\bar{R}_{0_\mathrm{d}} - R_\mathrm{mode}\right| / R_\mathrm{mode}$. This quantity decreases with decreasing σ_X. This shows that the two frequency method becomes more accurate at determining mode of the pdf as the spreading in bubble sizes in reduced. In term of accuracy for V_est, results are presented in Figure 6.9(c). Again, two solutions result from the two frequency approach and it is clear that the algorithm performs best with reduced spreading in bubble sizes.

Impact of noise For the six bubble size distributions, various amounts of noise are added to $s_\mathrm{v}^{f_1}$ and $s_\mathrm{v}^{f_2}$ before solving the two frequency inversion. The error in gas estimate $\bar{\epsilon}$ is calculated for these scenarios. Results are shown in Figure 6.10. This displays $\bar{\epsilon}$ against the relative noise level E (Equation 6.16). It can be observed that the effect of noise differ between the different bubble size distributions. Leifer minor 1 and Leifer minor 2 are very sensitive to the added noise with 80% error reached with only ~15% of relative noise level. In contrast, lognormal and chi distributions

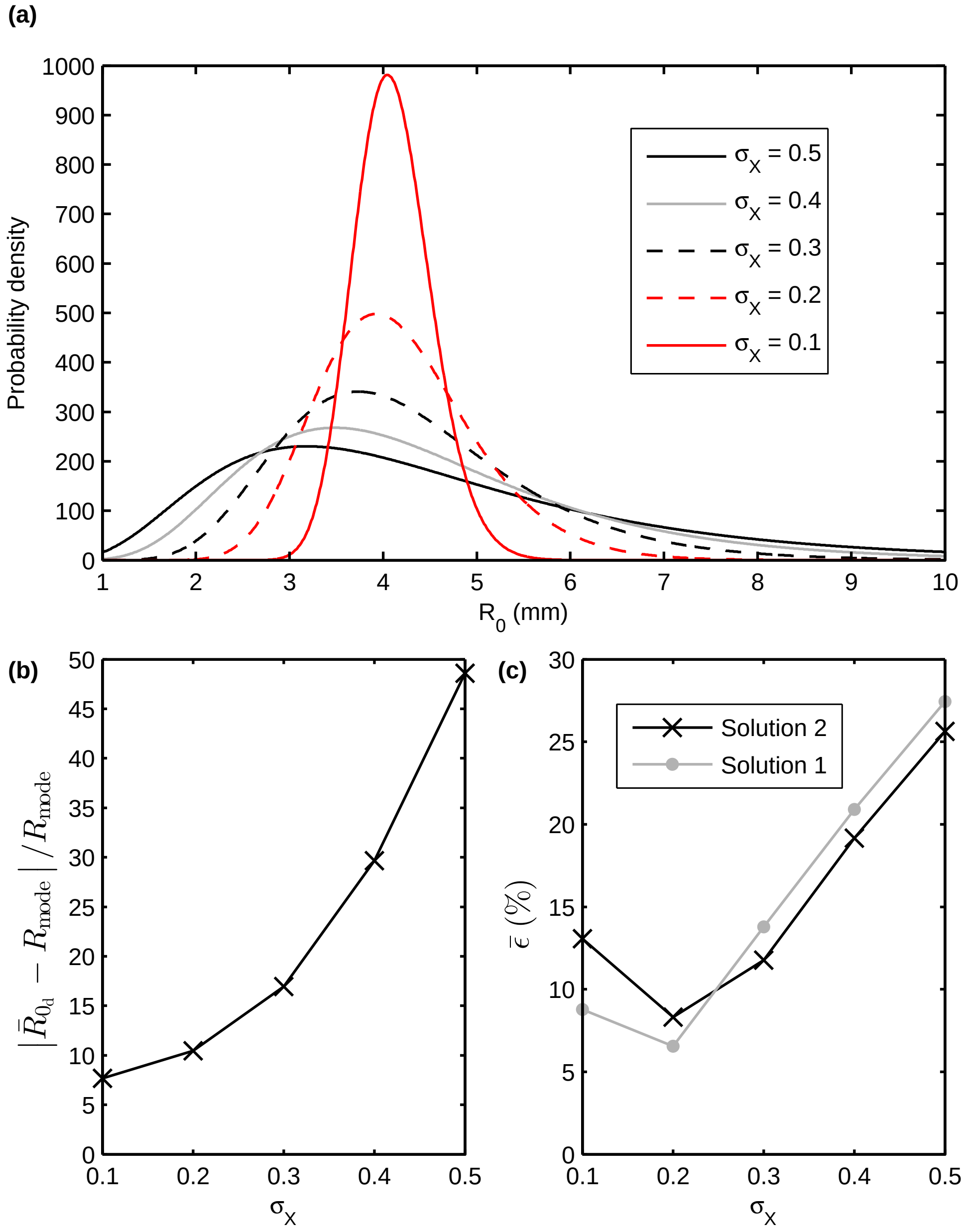

Figure 6.9.: Results of the two frequency inversion on data generated using lognormal distributions with different spreading. The spreading of the lognormal distribution is controlled by the quantity σ_X in Equation C.2. Five cases for σ_X are considered for the probability density function: $\sigma_\mathrm{X} = 0.1$ (low spreading) to $\sigma_\mathrm{X} = 0.5$ (high spreading) in 0.1 steps. (a): Probability density function computed with different values σ_X (i.e. different spreading). (b): Dominant radius R_{0_d} estimates using a two frequency inversion on data sets generated with lognormal distributions with different σ_X. The results are presented as the percentage error of R_{0_d}averaged over each 100 simulations relative to R_mode (the value of R_0 for which the probability density function is largest): $\left|\bar{R}_{0_\mathrm{d}} - R_\mathrm{mode}\right| / R_\mathrm{mode}$. (c): Error in volume estimates $\bar{\epsilon}$ using a two frequency inversion on data sets generated with lognormal distributions with different σ_X. The two lines represent the two solutions deduced from the two frequency method.

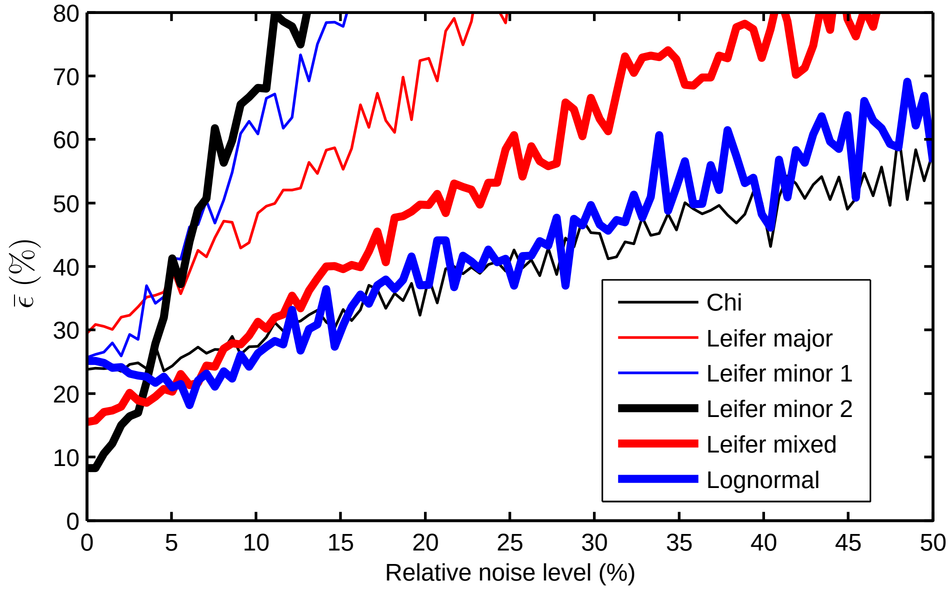

Figure 6.10.: Impact of noise on the estimated volumes V_{est} computed using a two frequency acoustic inversion. Results $\bar{\epsilon}$ (Equation 6.15) are plotted against the relative noise level E (Equation 6.16).

are found to be the most robust.

6.4.2. Multi-frequency approach

Results presented in subsection 6.4.1 suggest the two frequency approach can be suited for bubble size distributions that present a strongly dominant bubble size. However, with bubble size distributions of more complex form, the accuracy is poor. In order to deal with these issues, and if the data set allows it (s_{v} measurements at three or more frequencies), a multi-frequency inverse approach can be employed. Similarly to the two frequency approach, the inverse method is tested against simulated data (subsection 6.3.1) and the ability of the method to predict accurately the bubble size distributions and the gas volumes is investigated.

Recovering BSD Using measurements at N_ω frequencies $s_{\text{v}}^{f_1} \dots s_{\text{v}}^{f_{N_\omega}}$, the inverse problem is built following the procedures in subsection 6.3.2. The number of bubble radius bins is $N_R = \text{UND} \times N_\omega$ with UND the under-determination factor (section 2.2). The direct result of the inverse problem is the bubble size distribution vector $\mathbf{N}$, containing the abundances $N_1 \dots N_{N_R}$ in each bubble size bin. These are origin-

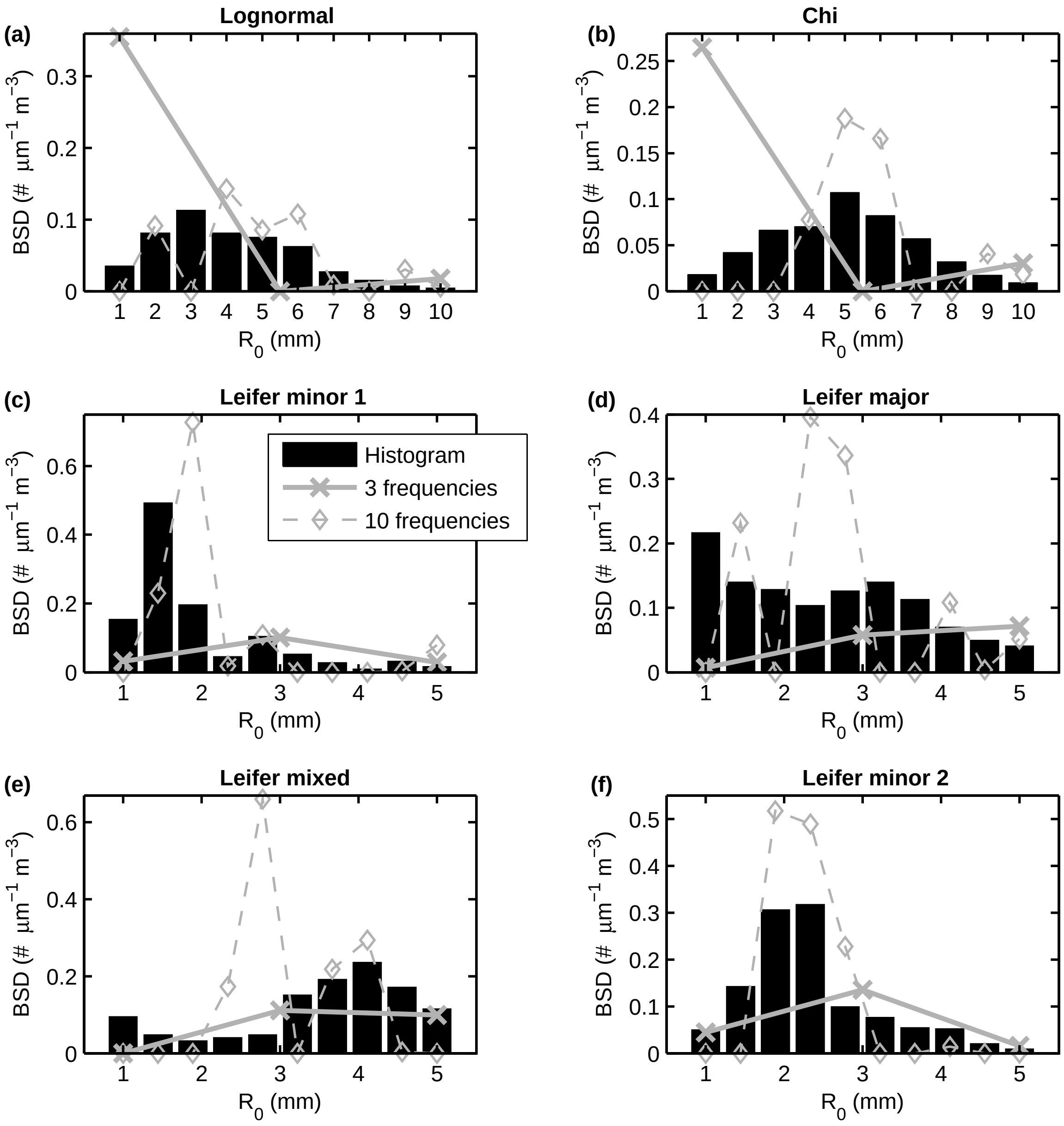

Figure 6.11.: Example of bubble size distributions inferred from simulated measurements using a three frequency inversion (solid grey line with cross markers) and a ten frequencies inversion (dashed grey line with diamond markers). The black bars represent the reference distributions.

ally expressed in number of bubbles relative to 1 m^3 of water. By scaling $\mathbf{N}$ as $\mathbf{N}/\Delta R_0 \times 10^{-6}$, the abundances are normalized to number of bubbles $\mu\mathrm{m}^{-1}\mathrm{m}^{-3}$. Considering first UND = 1 (i.e. $N_R = N_\omega$), result examples for $\mathbf{N}$ for the six probability density functions are shown in Figure 6.11. In each case, one result (out of 100 simulations) is presented. Cases with a data set containing three and ten frequencies are compared to the reference distributions. Data sets obtained using three and ten frequencies represent cases with extremely sparse and relatively large number of frequencies respectively. The limiting case of using only three frequencies (solid grey lines with cross markers) is exhibited here with a limited resolution in bubble radius (only three data points defining the bubble size distribution). Most distributions are poorly recovered with only three frequencies (e.g. chi and Leifer major distributions, Figure 6.11(b) and (d)). The results for the three frequency inversion in the case of the chi distribution (Figure 6.11(b)) is misleading. The reference distribution has a peak at $R_0 = 5.2$ mm but the inversion produces the lowest abundance around this bubble radius. Using ten frequencies (dashed lines with diamond markers) enhances the results. It can be observed that features in the distributions are identified with greater accuracy. For example, considering the chi distribution, $\mathbf{N}$ inferred from measurements at ten frequencies now exhibits a peak value at $R_0 = 5$ mm, similarly to the reference distribution. Though, in some cases agreement remains poor with a 10 frequency inversion, e.g. for Leifer mixed and Leifer major distributions (Figure 6.11(d) and Figure 6.11(e)).

Performance against gas volume While comparing bubble size distributions can help addressing the efficiency of the inversion, the final quantity of interest here is the estimated gas volume V_{est} compared to the reference volumes V_{ref}. Estimated volumes V_{est} are computed by integrating $\mathbf{N}$ across bubble radii. Reference volumes V_{ref} is the summation of the volumes of each single bubble generated (Equation 6.14). The accuracy of V_{est} is measured using the quantity $\bar{\epsilon}$ (Equation 6.15) which is the mean across all the simulations of the absolute difference between V_{est} and V_{ref}. Figure 6.11 only shows 1 case study out of 100 simulations for each trial. In order to present results from an entire set of 100 simulations, a scatter plot is used and the results are displayed in Figure 6.12. Results in the case of inversions performed with three and ten frequencies are presented. Similarly to Figure 6.7, the diagonal line represents the exact volume estimate ($V_{\mathrm{est}} = V_{\mathrm{ref}}$). Each data point is a result from a simulation trial. The more a data point deviates from the diagonal line the

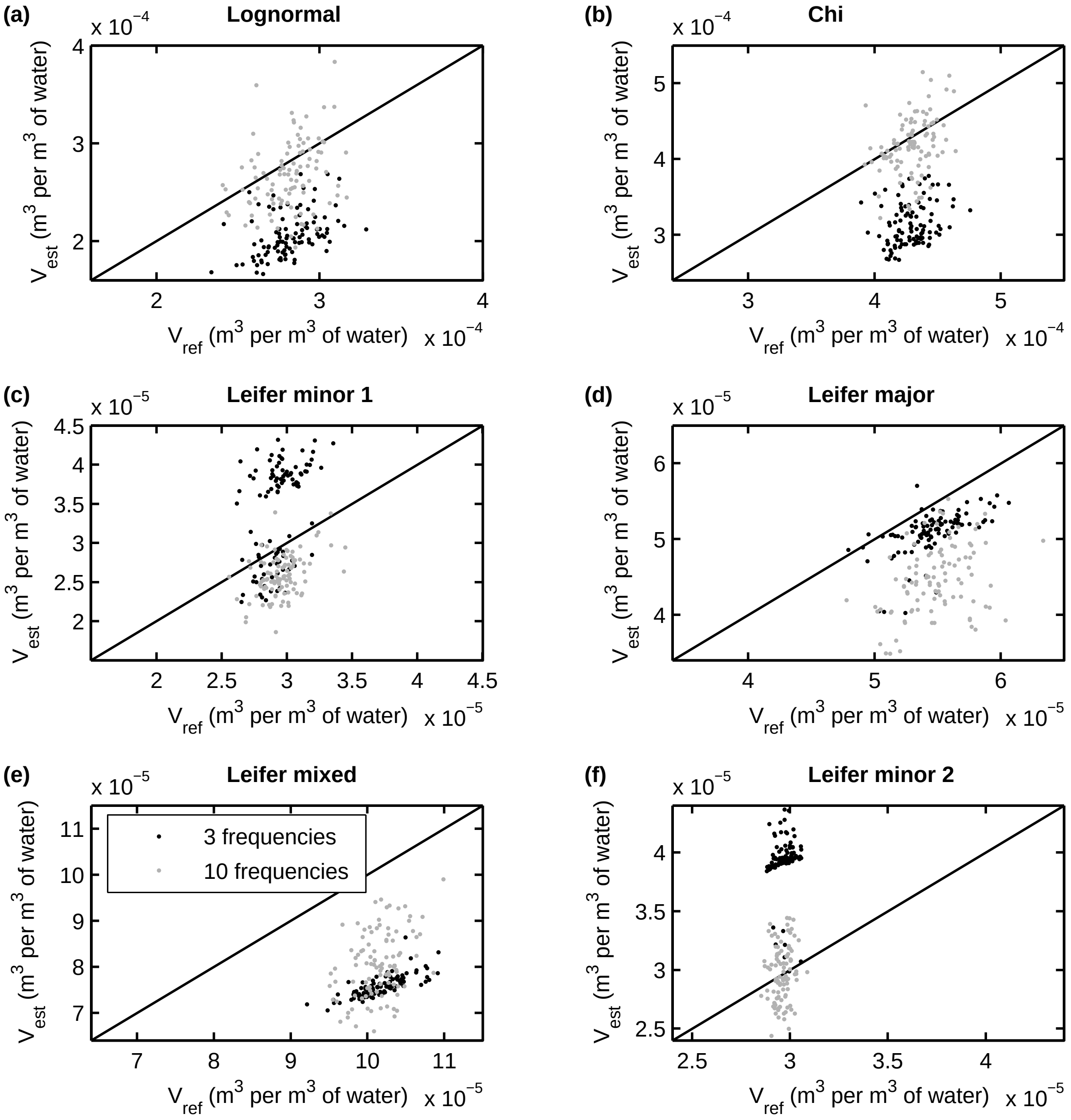

Figure 6.12.: Scatter plot of the results from the inversion of the simulated data using three and ten frequencies. For each bubble size distribution (six distributions, Figure 6.4), 100 simulations are computed, each presenting a reference volumes V_{ref} that is sought (V_{est}). In each graph, the diagonal line represents the exact estimate $V_{\text{ref}} = V_{\text{est}}$. Black dots are the results from the three frequencies inversion and grey dots the results from the ten frequencies inversion

more inaccurate the volume estimate is for this particular trial. For all distributions except Leifer major (Figure 6.12(d)), the increase in number of frequencies results in better estimates with grey dot markers being brought closer to the $V_{\text{est}} = V_{\text{ref}}$ line. This graph demonstrates that the accuracy is highly dependent on the bubble size distribution.

As described in subsection 6.3.1, simulations are performed for 13 scenarios (13 different number of frequencies). Figure 6.12 only shows the 3 and 10 frequencies cases and Figure 6.13 shows the results in a form that allows to observe the accuracy of the inverse method for the 13 scenarios. Similarly to Figure 6.8, the performance of each inversion is addressed through the quantity $\bar{\epsilon}$ (Equation 6.15) which represented the percentage error of V_{est} relative to V_{ref}. Results are presented in Figure 6.13 and this compares two methods for solving the inverse problem (section 2.2): Tikhonov regularization (using the GCV criterion for the optimization of α); Levenberg-Marquardt least squares (using the L-curve criterion for the optimization of Λ). So far, results are computed using the Levenberg-Marquardt least squares (Figure 6.11 and Figure 6.12) but comparing Tikhonov regularization and Levenberg-Marquardt least squares could demonstrate the usefulness of one of the technique over the other for a given scenario. With solid thick lines representing results from Levenberg-Marquardt least squares and dashed thin lines results from Tikhonov regularization, Figure 6.13 clearly shows that the Levenberg-Marquardt least squares method is in general more suited for the inverse problem considered here. Both methods are found to perform similarly in most cases with a reduced number of frequencies (e.g. Leifer major and Leifer mixed distribution for N_ω between 3 and 10, Figure 6.13(d), (e)). However, with an increased number of frequencies, $\bar{\epsilon}$ increases significantly for results computed using Tikhonov regularization (e.g. Leifer minor 2 distribution with an error of more than 60% for $N_\omega = 20$, Figure 6.13(f)). The Leifer mixed distribution (Figure 6.13(e)) is the only case where results from both methods are comparable (with Tikhonov regularization performing slightly better). Though, in all other cases, the results computed using Levenberg-Marquardt least squares produces volumes estimates that are more accurate as N_ω is increased. This suggests a better robustness of the Levenberg-Marquardt algorithm for the particular problem considered here. The main difference between regularization and least squares methods is that regularization assumes a smooth solution. This could explain that the Levenberg-Marquardt performs best for this particular inverse problem. These results clearly show that the Levenberg-Marquardt least squares is more suited for

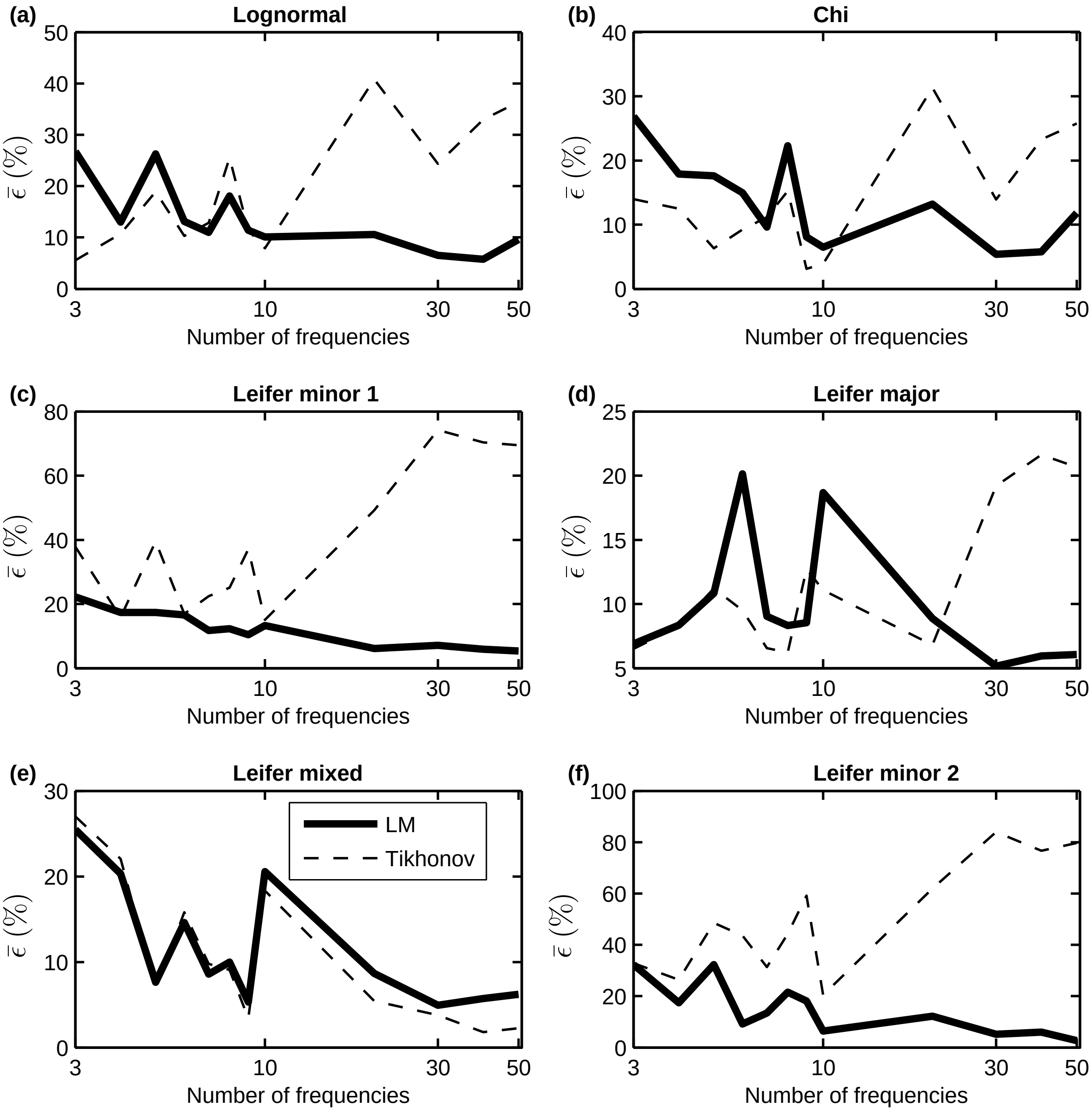

Figure 6.13.: Performance of the acoustic inversion of simulated data using different number of frequencies (from 3 frequencies to 50 frequencies). Two methods are used for solving the inverse problem (Tikhonov regularization and Levenberg-Marquardt least squares, section 2.2). Results are shown for the six different bubble size distributions in term of $\bar{\epsilon}$ (Equation 6.15). Results using a Tikhonov regularization are shown as dashed thin black lines. Results computed using Levenberg-Marquardt least squares are shown as thick solid thick black.

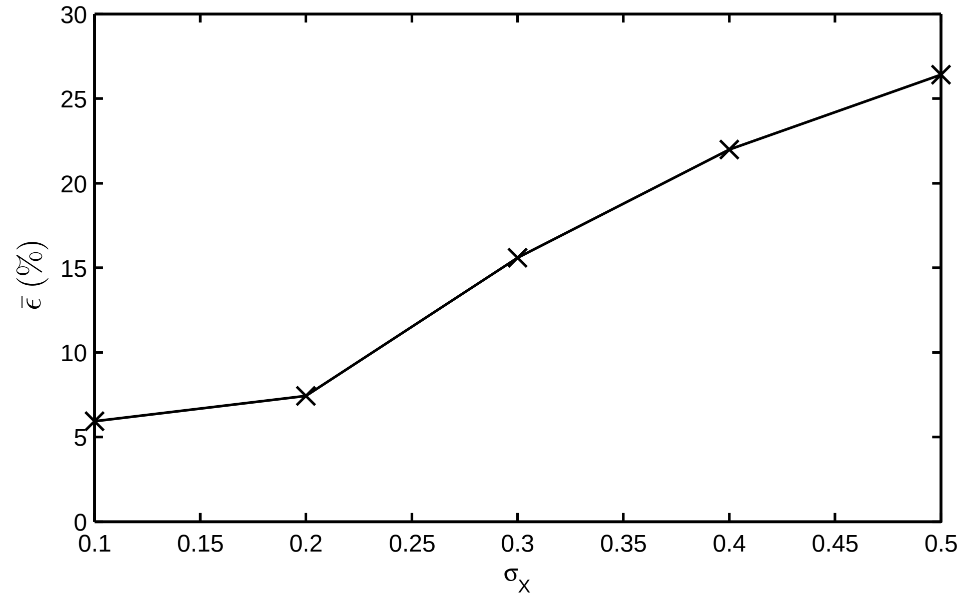

Figure 6.14.: Results of a three frequency inversion on data generated using lognormal distributions with different spreading. The quantity $\bar{\epsilon}$ is plotted against different spreading (parameter σ_{X}). The spreading of the lognormal distribution is controlled by the quantity σ_{X} in Equation C.2. Five cases for σ_{X} are considered for the probability density function: $\sigma_{\mathrm{X}} = 0.1$ (low spreading) to $\sigma_{\mathrm{X}} = 0.5$ (high spreading) in 0.1 steps. The probability density functions are shown in Figure 6.9(a).

solving the inverse problem considered here. As a results, this method will be used in the following sections and in chapter 7.

Figure 6.14 shows the performance of three frequency inversion applied to measurements simulated from lognormal distributions with different standard deviations (i.e. different spreading in bubble sizes). The spreading of the lognormal distribution (Equation C.2) is controlled by the parameter σ_{X}. As for the two frequency case, five cases are considered (Figure 6.9(a)). Figure 6.14 shows that a reduction in standard deviation decreases $\bar{\epsilon}$, meaning that the volume estimates V_{est} become more accurate. This trend is similar to what is observable for the two frequency approach (Figure 6.9(c)). This suggests the limiting case of the three frequency inversion performs best with bubble size distributions presenting a strongly dominant bubble size.

Impact of the number of scatterers in the sampled volume In addition to testing solving methods with different data sets, s_{v} measurements are simulated

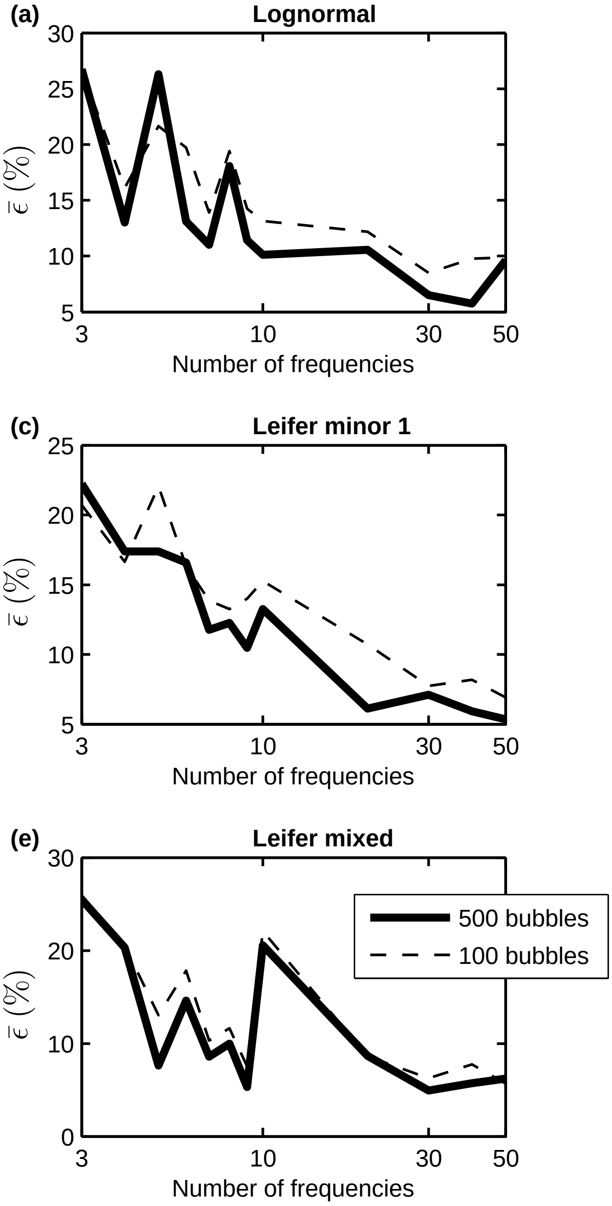

Figure 6.15.: Performance of the acoustic inversion of simulated data using different number of frequencies (from 3 frequencies to 50 frequencies) and two different number of scatterers N_b in the sampled volume V_0: $N_\mathrm{b} = 500$ (thick black lines) and $N_\mathrm{b} = 100$ (thin dashed lines). Results are shown for the six different bubble size distributions in term of $\bar{\epsilon}$ (Equation 6.15).

using different numbers of bubbles in the sampled volume ($N_\mathrm{b} = 500, 100$). This investigates the robustness of the algorithm against different bubble population sizes (and thus gas volumes). Similarly to Figure 6.13, the accuracy of V_est is addressed through the quantity$\bar{\epsilon}$ (Equation 6.15) and results are shown in Figure 6.15. Dashed thin lines represent results from the inversion using 100 bubbles in V_0 while solid thick lines are for simulations with 500 bubbles. In all cases an increase in N_b leads to volume estimates that are more accurate, notably with s_v at numerous frequencies. However, these differences in $\bar{\epsilon}$ are relatively small with a maximum difference of ~5% for the Leifer minor 2 distribution (Figure 6.15(f)) at $N_\omega = 40$ and the lognormal distribution (Figure 6.15(a)) at $N_\omega = 20$. Despite the decrease in N_b, volume estimates remain within reasonable accuracy and precision levels.

In order to further investigate the robustness against the number of scatterers in the sampled volume, inversions are employed on data generated with N_b from 10 to 1000 in 15 logarithmically spaced bins. Data are generated using four distributions: a lognormal distribution with $\sigma_\mathrm{X} = 0.5$; a chi distribution; a lognormal distribution with $\sigma_\mathrm{X} = 0.3$; a Leifer minor 2 distribution. Inversions are performed with with 3 frequencies, 10 frequencies and 20 frequencies. Results from the inversions are plotted in Figure 6.16 as $\bar{\epsilon}$ against N_b for the four case studies. In all cases, the change in $\bar{\epsilon}$ is within 10% with N_b from 10 to 1000. This shows that the performance of the inversion remains within acceptable levels. This suggests that the multi-frequency approach is robust against a change in the number of scatterers in the sampled volume.

Increasing the UND factor Considering the limiting case of s_v measured at three frequencies, the results shown in Figure 6.11 poorly resolve the bubble size distributions because of the lack of resolution in R_0. Compared to data sets with more frequencies, this results in gas volume estimates with lower accuracy and precision (Figure 6.12, Figure 6.13). As described in section 2.2, the number of radius bins at which the abundance vector $\mathbf{N}$ is determined can be increased by adding rows to the inverse problem. With the Levenberg-Marquardt least squares, this is controlled through the UND factor with UND $= 1$ defining a problem where $N_\omega = N_\mathrm{b}$ and UND > 1 defining a problem where $N_\omega < N_R$ (i.e. more outputs than measurements). For example, with a three frequency data set, using UND $= 2$, the vector of abundances $\mathbf{N}$ is defined in six radius bins to compare to three bins with UND $= 1$. Although increasing UND could potentially increase the accuracy when estimating

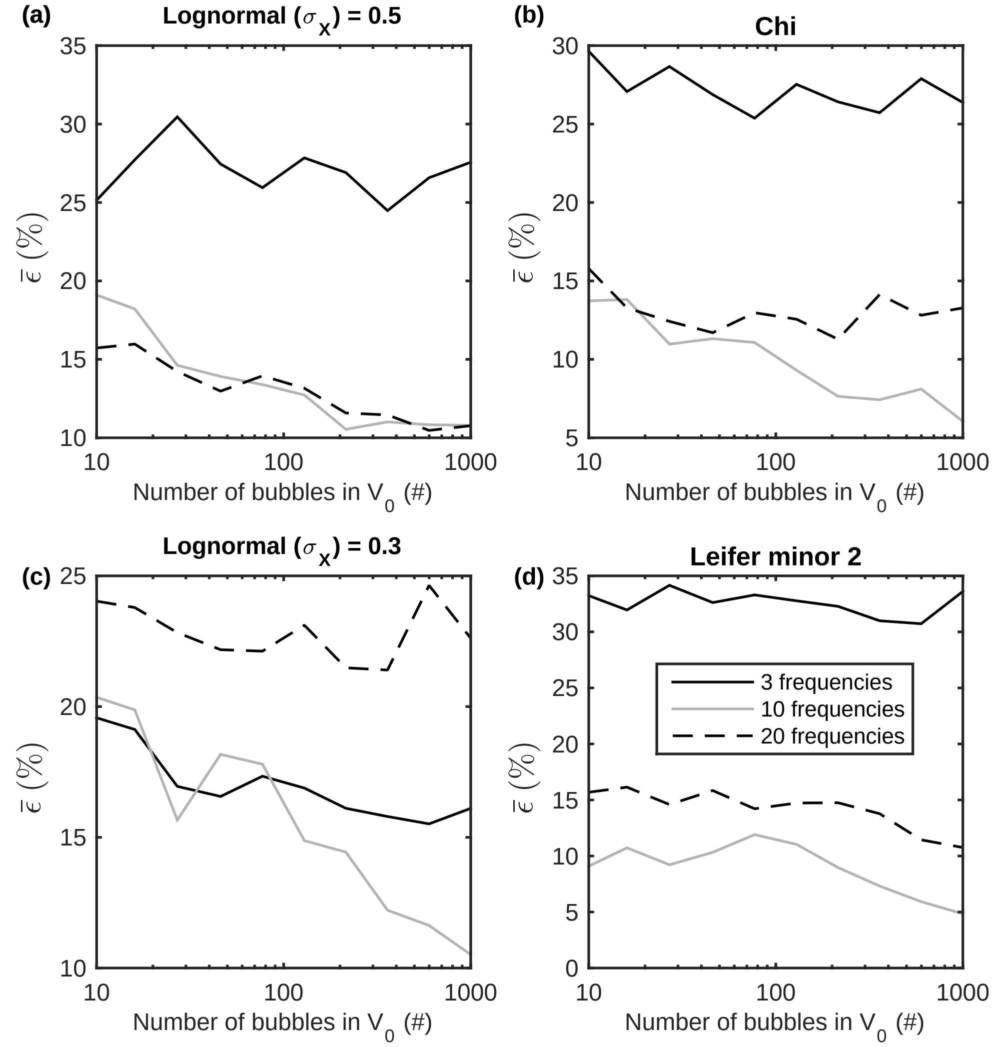

Figure 6.16.: Performance of the multi-frequency inversion for different number of bubbles $N_b$in the sampled volume V_0. The quantity N_b is varied from 10 to 1000 and inversions are performed with 3 frequencies (solid black line), 10 frequencies (solid grey line) and 20 frequencies (dashed black line). Results are shown for four different bubble size distributions in term of $\bar{\epsilon}$ (Equation 6.15): lognormal distribution with $\sigma_X = 0.5$ (a); chi distribution (b); lognormal distribution with $\sigma_X = 0.3$ (c); Leifer minor 2 distribution (a).

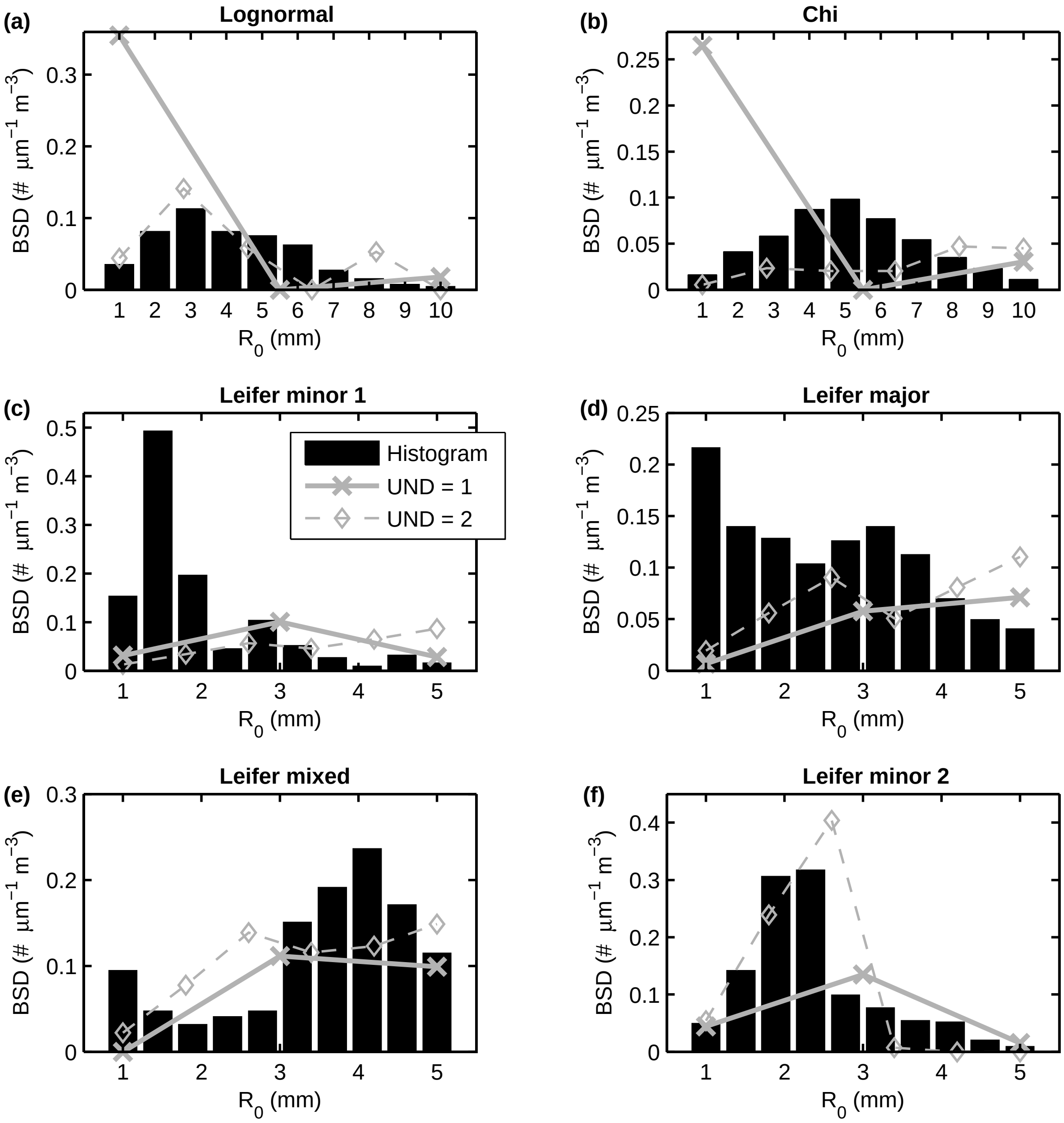

Figure 6.17.: Example of bubble size distributions computed from simulated measurements using a three frequencies inversion with UND = 1 (grey solid lines with cross markers) and UND = 2 (grey dashed lines with diamond markers). Each graph represents one of the six bubble size distribution considered in this chapter. Reference distributions are represented as black bars.

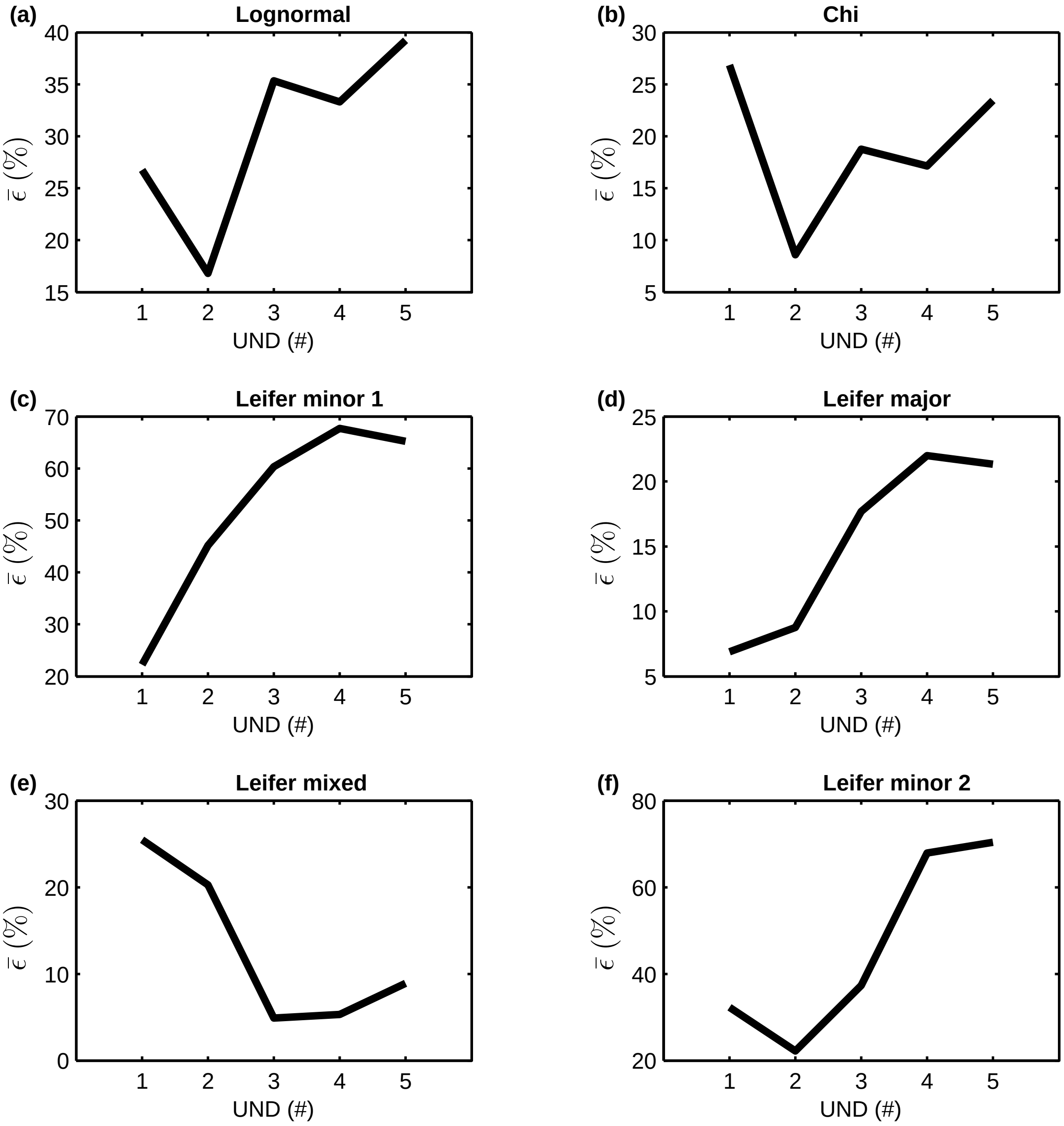

Figure 6.18.: Accuracy and precision of a three frequencies inversion of the simulated data set using different amount of under-determination. Each graph represents one of the six bubble size distribution considered in this chapter. Measures of accuracy are displayed as thick black lines and relate to the right axis (black colour). Measures of precision are displayed as thick grey lines and relate to the left axis (grey colour).

the bubble size distribution, it is important to investigate the efficiency of this resolution enhancement because the inversion remains based on the same number of frequency measurements. Considering a three frequency inversion, as in Figure 6.11, results for bubble size distributions are presented in Figure 6.17 for UND = 1 and UND = 2. For each initial size distribution, one resulting bubble size distribution out of 100 simulation trials is presented. Increasing the resolution in R_0 produces mixed results depending on the bubble size distribution. The lognormal (Figure 6.17(a)) and Leifer minor 2 (Figure 6.17(f)) distributions seem to benefit from the increased UND factor. In these two cases, the peaks in the computed bubble size distributions correlate well with the reference bubble size distributions: Figure 6.17(a), peak at $R_0 \approx 3\,\mathrm{mm}$; Figure 6.17(f), peak at $R_0 \approx 2.5\,\mathrm{mm}$. In contrast, the case of the Leifer major (Figure 6.17(d)) and Leifer minor 1 (Figure 6.17(c)) distributions, results for $\mathbf{N}$ with UND = 2 and UND = 1 are misleading. In these cases, $\mathbf{N}$ increases with increasing R_0. This is opposite to the trend in the reference bubble size distribution. In terms of recovery of the bubble size distributions, Figure 6.17 shows mixed results.

As the UND factor is increased, the resolution of abundances is refined but the inversion remains limited to a small dataset (three s_v values for one set of measurement). For each simulation trial, the inverse problem is further solved with UND = $1, \dots, 5$ to test the accuracy of the methods with various amount of under-determination. This is achieved by comparing estimated V_est to the reference volumes through $\bar{\epsilon}$ (Equation 6.15), similarly to Figure 6.13. Results are shown in Figure 6.18. In Figure 6.17, the benefits of increasing the UND factor is shown to be highly dependent on the bubble size distribution. From results in Figure 6.18, the three frequency inversion performs very efficiently in the case of the Leifer mixed distribution (Figure 6.18(e)) with an improvement of 20% in $\bar{\epsilon}$ from UND = 1 to UND = 3. Whereas for the Leifer minor 1 (Figure 6.18(c)) distribution it exhibits levels of error that increase with increasing UND factor (increase of $\bar{\epsilon}$ of 43% from UND = 1 to UND = 5). To a lesser degree, the Leifer major (Figure 6.18(c)) distribution also presents a diminishing accuracy with an increase of the UND factor (increase of 14.4% from UND = 1 to UND = 5). The lognormal (Figure 6.18(a)), chi (Figure 6.18(b)) and Leifer minor 2 (Figure 6.18(f)) distributions show a mixed level of accuracy in response to different levels of under-determination. These distributions demonstrate a decrease in $\bar{\epsilon}$ at UND = 2 followed by an increase. It is interesting to note that these three distributions are those presenting the abundances

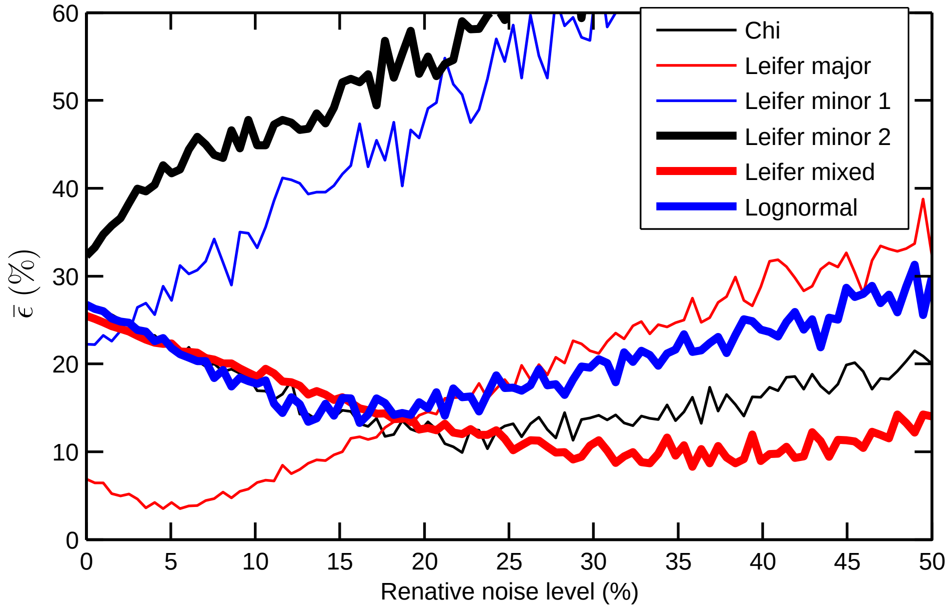

Figure 6.19.: Impact of noise on the estimated volumes V_{est} computed using a three frequencies acoustic inversion. The quantity $\bar{\epsilon}$ (Equation 6.15) is plotted against the relative noise level E (Equation 6.16).

with the simplest forms (i.e. presents a strongly dominant radius). This suggests that UND = 2 could be an optimum amount of under-determination for the three frequency inversion for bubble size distributions that are not of a complex form.

Impact of noise With UND = 1, the robustness of the method is tested against relative noise levels from $E = 0\%$ to $E = 50\%$ (Equation 6.16). Results are presented in Figure 6.19 and Figure 6.20 in the case of data sets with three and ten frequencies respectively. With both data sets, the accuracy decreases with increasing noise level. However, the various bubble size distributions are affected differently. The Leifer minor 1 (thin blue line) and the Leifer minor 2 (thick black line) distributions are the most affected by the inclusion of noise. It is interesting to note that results from the two frequency approach (Figure 6.10) also show that these two distributions are the most sensible to noise. In the case of the three frequency data set, greater disparities between the different bubble size distributions can be observed (Figure 6.19). Results from the ten frequency inversion show results that are more consistent between the six bubble size distributions. The accuracy is improved with the ten frequencies data set (comparing results from Figure 6.19 and Figure 6.20). These results suggest an increased robustness of the inversion with a larger data set.

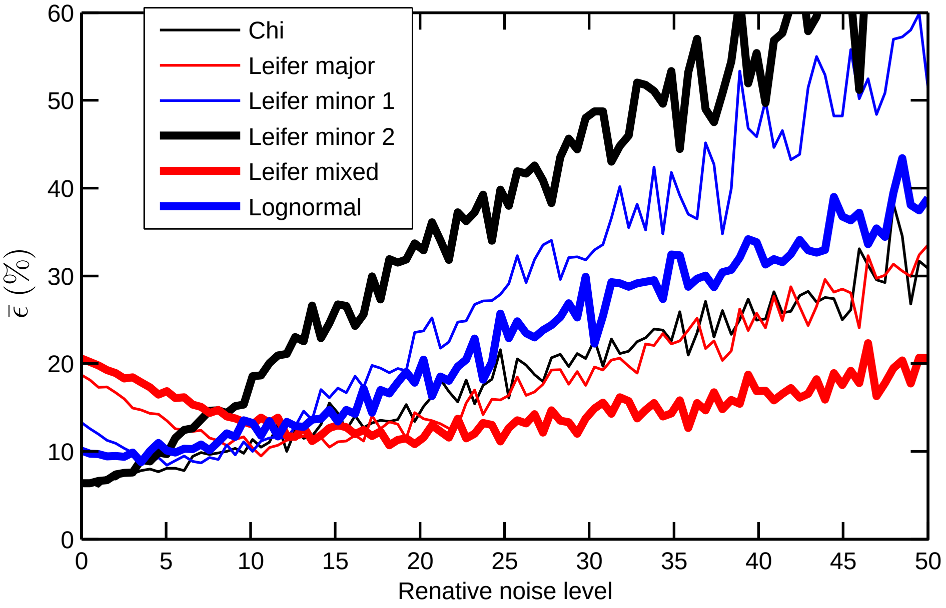

Figure 6.20.: Impact of noise on the estimated volumes V_{est} computed using a ten frequency acoustic inversion. The quantity $\bar{\epsilon}$ (Equation 6.15) is plotted against the relative noise level E (Equation 6.16).

6.5. Summary

In this chapter, inverse methods based on the acoustic backscattering from gas bubbles are described. They are aimed at quantifying gas release from echosounder data at multiple frequencies. From a cloud of bubbles insonified by an acoustic beam at different frequencies, the procedures described in section 6.2 allow to determine gas volumes. Three approaches are described here based on: measurements at a single frequency ($N_\omega = 1$); measurements at two frequencies ($N_\omega = 2$); measurements at three or more frequencies ($N_\omega \geqslant 3$). Commonly, data sets consists of three or four frequency channels. The achievable accuracy with such a limited data set is investigated here. The two frequency inversion and the multi-frequency inversions are tested against simulated data generated from six different bubble size distributions with various amount of noise.

The two frequency approach consists on determining two unknowns: the dominant bubble radius of the bubble size distribution; the abundance of this bubble size. From the solution to this inversion, gas volumes can be inferred. The applicability of this method is found to be limited to distributions with a strongly dominant bubble size. In these cases, the method performs well and the algorithm also estimates the dominant bubble radius with good agreement. More importantly, it achieves acceptable accuracies in estimating gas volumes. The robustness to noise of the method is found to be highly dependent on the bubble size distribution and disturbances from added noise can be significant. In general, for bubble size distributions that present a complex form, the performance of the method is poor. This demonstrates the need for an inverse approach based on a bigger data set ($N_\omega \geqslant 3$) to resolve the bubble size distribution.

The use of a multi-frequency inversion ($N_\omega \geqslant 3$) allows one to determine bubble size distributions from backscattering measurement from a cloud of bubbles at various frequencies. From the bubble size distribution, the volume of gas can then be estimated. Both in terms of the recovery of the bubble size distributions and the estimation of gas volumes, it is shown that the performance of the technique is enhanced with measurements at an increasing number of frequencies. The Levenberg-Marquardt least squares method (section 2.2) is found to be best suited for solving this inverse problem and is robust to different bubble population sizes. This technique is also beneficial because it allows one to add under-determination to the inverse problem in order to increase the resolution of the inferred bubble size distribution. This is shown to be advantageous with limited data sets (e.g. with measurements at only three frequency) but the performance of such a change is dependent on the type of bubble size distribution considered. The best improvements in accuracy are for the distributions presenting a simple form and results suggest the optimal under-determination is UND = 2. The multi-frequency inversion is found to be more robust to noise than the two frequency approach.

Using both methods tested in this chapter, chapter 7 draws on data collected at sea during two research cruises (JR253, HE387). These research cruises investigated methane seeps to the west of Svalbard. Many bubble releases from methane seeps were imaged from a single beam echosounder at two or three different frequencies. Using these data sets, the usefulness of the acoustic inversion described in this chapter is demonstrated.

7. Acoustical quantification of methane seeps to the west of Svalbard

7.1. Introduction

It is known that, around the world, significant amounts of methane are stored below the ocean floor in sediment layers in the form of methane hydrates. Methane hydrate (or methane clathrate) is a crystal structure of water where gas is stored [170]. These compounds are stable at low temperature and high pressure conditions, i.e. under specific water depths and bottom water temperatures. A change in either pressure or temperature can cause the hydrate to dissociate, then releasing gas in the water column either in gas or dissolved phase. In high latitude regions, because of the low bottom water temperatures, hydrates can be found at relatively shallow depths ($\approx 100 - 400$ m) [20, 47]. In addition, warming of the ocean induced by climate change occur at a faster pace in these regions, and as a consequence the potential release of methane gas is a positive feedback to global warming [24, 25, 171]. In the last decade, this has raised interest in studying methane seeps in Arctic regions [20, 36, 127, 172–175].

In 2009, gas bubble emissions were reported on the western Svalbard margin (Norway) [176] at a depth of ~390 m by Wesbrook et al. [20]. They suggest that these releases might originate from dissociation of methane hydrates and that the 1 °C increase in water temperature in the last 30 years could be the cause of the observed released of methane gas in the water column at specific depths. Furthering this hypothesis, direct collection of methane hydrates in western Svalbard is reported by Fisher et al. [174]. In addition, gas emissions are found to cluster at a depth of 396 m, and it is suggested this corresponds to the depth at which hydrates

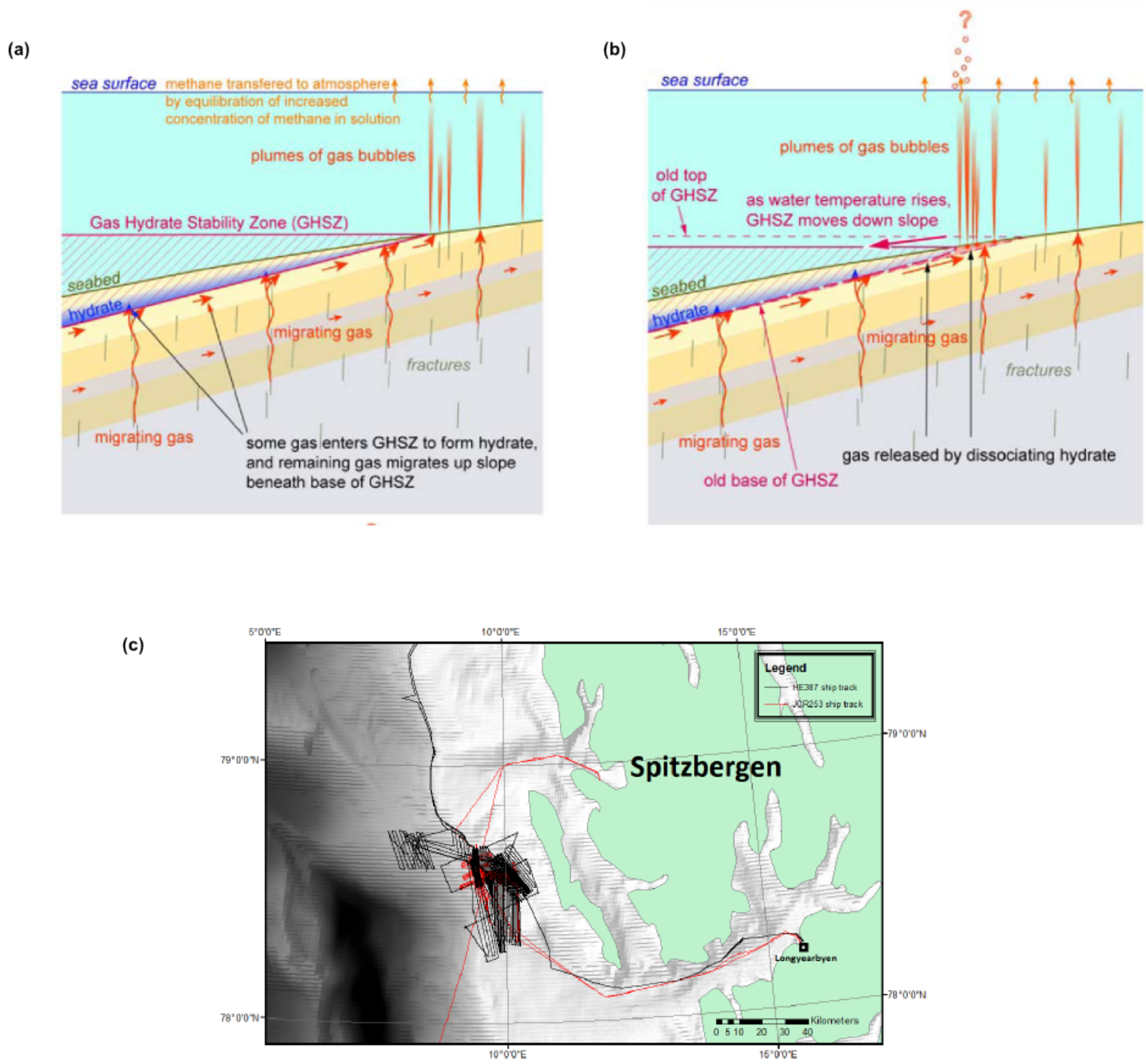

Figure 7.1.: Schematic of Westbrook et al. [20] hypothesis for concentrated methane discharges in western Svalbard at ~390 m depth. (a): Methane hydrates are stored at given temperature and pressure conditions, defining the Gas Hydrate Stability Zone (GHSZ). Thermogenic methane is seeping from the seafloor at various depths. (b): With an increase in bottom water temperature, the stability of the hydrates is disturbed and hydrates start the dissociate. This produces clustering gas release at the margin (defined by the GHSZ). (c): vessel tracks of research cruises JR253 and HE387 in western Svalbard.

dissociate [20] (based on the composition of the gas, bottom water temperature and hydrostatic pressure on site). Schematics illustrating this mechanisms are extracted from Westbrook et al. [20] and presented in Figure 7.1(a) and (b). Gas migrates through fractures in the sediments and is released in the water column, producing gas releases at various depths (Figure 7.1(a)). With increasing bottom water temperatures, the gas hydrate stability zone is moved to a lower depth because of dissociation of hydrates, producing strong discharges of gas at localised depths (Figure 7.1(b)). Recently, the study by Berndt et al. [36] suggests seasonally variation of the gas hydrate stability zone and then gas emissions. Since 2009, strong endeavour is given to study the western Svalbard region [36, 172–174] because it could prove to be one of the first sites to demonstrate global warming induced by hydrate dissolution. The data presented in this chapter are from two research cruises (JR253, HE387 [47, 48], ship tracks in Figure 7.1(c)) motivated by this context.

Considering the western Svalbard region, the survey area (where the gas releases are located) is very large and contains over 1000 flares (i.e. echosounder marks) [47, 48]. While the application of strictly local techniques can provide quantitative and qualitative insights into the mechanisms of gas release, these are restricted to a very small part of the gas escape area. Of interest for climate scientists are order of magnitude estimates for gas volumes released across the entire area. In addition, of importance for the study of gas release is the ability to produce large amount of data with relative ease. To this purpose, this study investigates the performance of the inversions described in chapter 6 to quantify gas releases.

Drawing on echosounder data from methane seeps collected during the two research cruises JR253 [47] and HE387 [48], this chapter demonstrates the usefulness of these "signal of opportunity" data sets for the study of gas seeps. Preliminary assessment of the applicability of the two frequency and the multi-frequency inversions (section 6.2) is presented.

7.2. Procedures

Research cruise JR253 was conducted from 26th July 2011 to 25th August 2011 and research cruise HE387 from 21st August 2012 to 16th September 2012. During both research campaigns, various non acoustic operations were conducted: coring, CTD (Conductivity, Temperature, Depth) of the water column, ROV video survey (including bubble counting), gas sampling, flow rate monitoring... ROV operations were performed using the HyBis (NOC) vehicle during research cruise JR253 and the Cherokee vehicle (MARUM) during research cruise HE387. In parallel, acoustic operations consisted on:

- Large scale gas plume mapping using:
    - Multi-beam echosounders: EM122 instrument during research cruise JR253; EM710 instrument during research cruise HE387.
    - Single beam echosounders (EK60): 3 frequencies available during research cruise JR253 (38 kHz, 120 kHz and 200 kHz); 4 frequencies available during research cruise HE387 (38 kHz, 70 kHz, 120 kHz and 200 kHz).
- Mapping of local gas streams during research cruise HE387 using the multi-frequency imaging sonar Imaginex 881A mounted on the Cherokee ROV from MARUM.

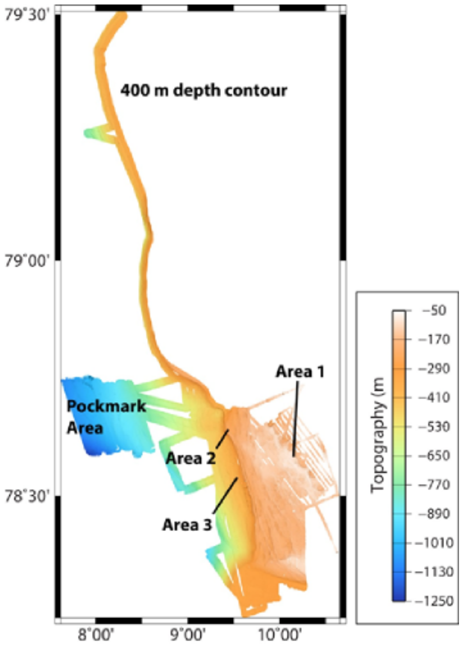

Figure 7.2.: Topography of the region surveyed during research cruise HE387 (similar to research cruise JR253). The 400 m depth contour was followed in order to investigate potential gas releases along the ~390 m depth margin. The pockmark area was investigated for potential gas releases because hydrates are reported to be found in this area by Fisher et al. [174]. Regions that were extensively covered during research cruise JR253 and research cruise HE387 are Area 1 (~90 m), Area 2 (~250 m) and Area 3 (~390 m).

From acoustic surveys, three areas presenting high intensity of gas releases at different depths were identified and are shown in Figure 7.2. Each region is labelled as follows and exhibits a specific depth: Area 1 (~90 m); Area 2 (~250 m); Area 3 (~390 m). Gas escape in Area 3 is believed to be induced by methane hydrate dissociation [20].

7.2.1. Data collection

During the two research cruises, data from the EK60 single beam echosounder were recorded using the ER60 software. Each reccord was stored as *.raw files and processed afterwards using the readEKRaw MATLAB toolkit [177]. This toolkit was used to convert the data in the *.raw files into s_v quantities in order to produce corresponding echograms. The EK60 instrument is widely used on vessels because of its robustness [178] and standardized calibration procedure against calibration spheres [43, 133, 179]. This enables this equipment to produce comparable data set between research cruises. Measurements of s_v are performed at a sampling rate of 0.5 Hz (measures every 2 seconds) and at a depth resolution of 0.1912 m. If each data point is represented by a pixel on a colour scale, a 3D plot (echogram) can be produced. Because s_v values can span large ranges on a dB scale from high (high backscatter near the surface and from seabed) to low (low backscatter from background noise), low and high thresholds are used for clarity in these graphs. Throughout this study, an upper threshold of $s_\mathrm{v} = -30$ dB and lower threshold of $s_\mathrm{v} = -90$ dB are used. An echogram example is presented in Figure 7.3(a). Over ~10 minutes, this shows the acoustic imaging of the water column while the vessel is navigating at low speed. The observed acoustic flares are the strong acoustic response produced by the gas bubbles escaping from the seabed. They show a high degree of variability in height and intensity across the entire study area [48]. Acoustic operations during the two research cruises consisted on surveying areas using three acoustic instruments: multibeam systems (water column imaging and bathymetry); single beam systems (water column imaging); sub-bottom profilers (imaging layers below the seabed). On both cruises, the single beam echosounders were EK60 systems and because of their ease of use, they were primarily used to give preliminary assessments, i.e. identifying regions of interest.

An important specification for single beam echosounders is the beam angle $\theta_{-3\mathrm{dB}}$ that represents the angle between two points at which the acoustic energy

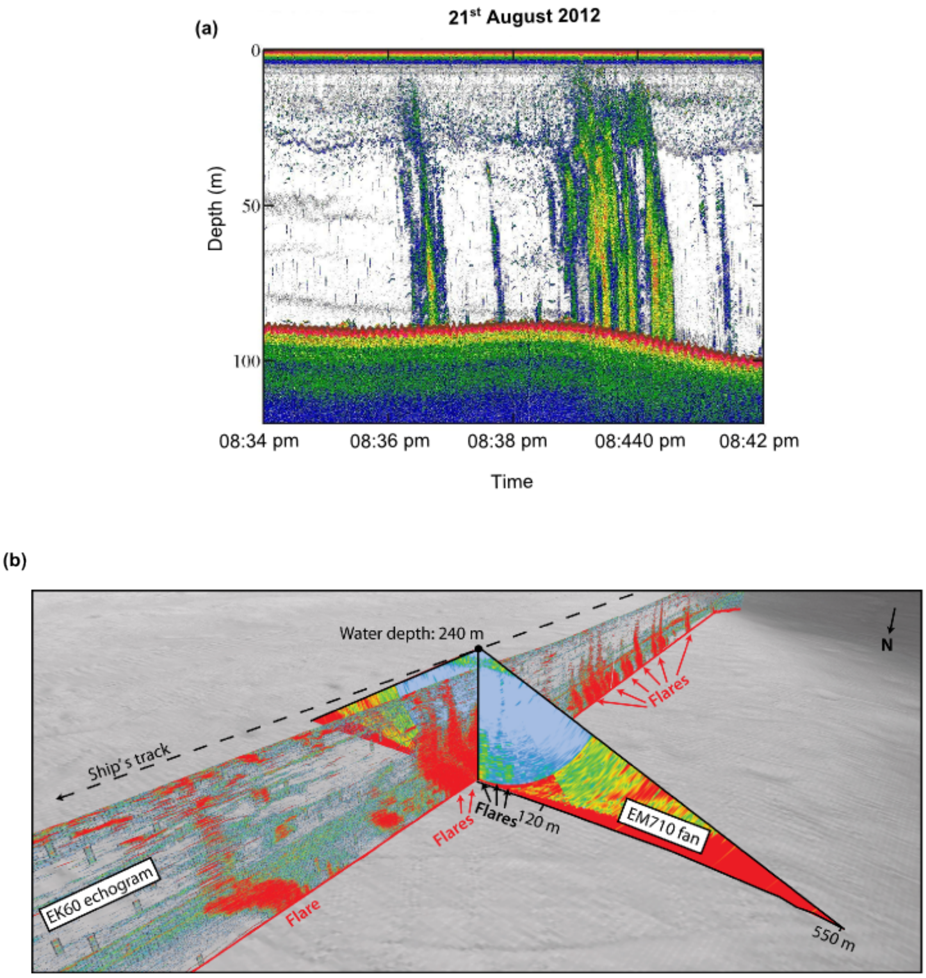

Figure 7.3.: Imaging of gas releases using single beam and multi-beam echosounders. (a): Echogram collected during research cruise HE387 from the EK60 instrument exemplifying several acoustic flares. (b): Along the same path, an EK60 echogram is superposed to a cross section of the water column from the EM710 multi-beam system. Single acoustic flares from the EK60 echogram are observed to originate several flares from the EM710.

	Area 1	Area 2	Area 3
Maximum number of streams per cluster (#)	50	15	10
Minimum number of streams per cluster (#)	3	1	2
Average number of streams per cluster (#)	15	6	8
Maximum bubble stream flow rate (mL/min)	100.1	27.9	41
Minimum bubble stream flow rate (mL/min)	4.3	5.2	3
Average bubble stream flow rate (mL/min)	27.3	15.1	20.9

Table 7.1.: Summary of research cruise HE387 data collected through various ROV dives. Flow rates were measured using a bubble catcher and video analysis. The localization of single bubble streams was performed using the 881A Imaginex sonar mounted on the ROV. Data are extracted form Sahling et al. [48].

intensity has fallen by 3 dB [180]. Of importance is that this quantity defines the insonified area $A_{-3\mathrm{dB}} = \pi\left(z \times \tan\left(\theta_{-3\mathrm{dB}}\right)\right)^2$, i.e. a circle of diameter $D_{-3\mathrm{dB}} = z \times \tan\left(\theta_{-3\mathrm{dB}}\right)$ [44, 181] at depth z. The EK60 system presents a beam angle of 7° at the frequencies of interest (38 kHz, 70 kHz, 120 kHz, 200 kHz), and the resulting footprint $D_{-3\mathrm{dB}}$ is approximately 12.3% of the water depth z. Thus, at depths considered here, the footprint is significant (e.g. at 80 m depth, $D_{-3\mathrm{dB}} = 11.1\,\mathrm{m}$ and $A_{-3\mathrm{dB}} = 383\,\mathrm{m}^2$) and the resolution of the EK60 echosounder is inadequate to allow one to localize singular features such as bubble streams. Responses obtained from the scattering of gas bubbles are the combination of several bubble streams within the sonar beam.

Whilst multi-beam systems propose enhanced resolution, their calibration is not as robust as that for the EK60 system. An example exhibiting differences in resolution between the EM710 and the EK60 can be observed in Figure 7.3(b). An EK60 echogram is displayed together with a water column cross section from the EM710 multi-beam system. With the EM710, several flares are identified (2-3 flares) through the cross section of the water column. This appears as a single mark in the EK60 records. During research cruise HE387, using the ROV vehicle, this was confirmed by mapping of individual bubble stream from visual and acoustic (using a 881A imaginex system) observations [48, 49]. It was noticed that bubble streams are clustering, and flares from the EM710 and EK60 systems are the combination of several individual gas streams [48].

When calculating an order of magnitude estimates for the gas being released in Area 2 and Area 3, Sahling et al. [49] use these ROV observations correlated to multi-beam data. They assume that each flare observed in EM710 records corresponds to a cluster of bubble streams. Then, further employing an average bubble stream flow rate and an average number of bubble streams per cluster (both inferred from ROV observations), they calculate an order of magnitude for the total flow rate of Area 2 and 3. Such an approach remains inaccurate because the average of the bubble streams flow rates and the number of bubble streams per clusters is based on very small samples over the overall area considered. These estimates are two order of magnitude higher than those of Berndt et al. [36] (seasonal observation from a lander on the seafloor). Both studies [36, 49] envision further investigation on refining order of magnitude estimates, and point out the need for increased research on the yearly variation of gas fluxes. This temporal variability could be resolved by employing for example the inverse method presented in chapter 4 and chapter 5.

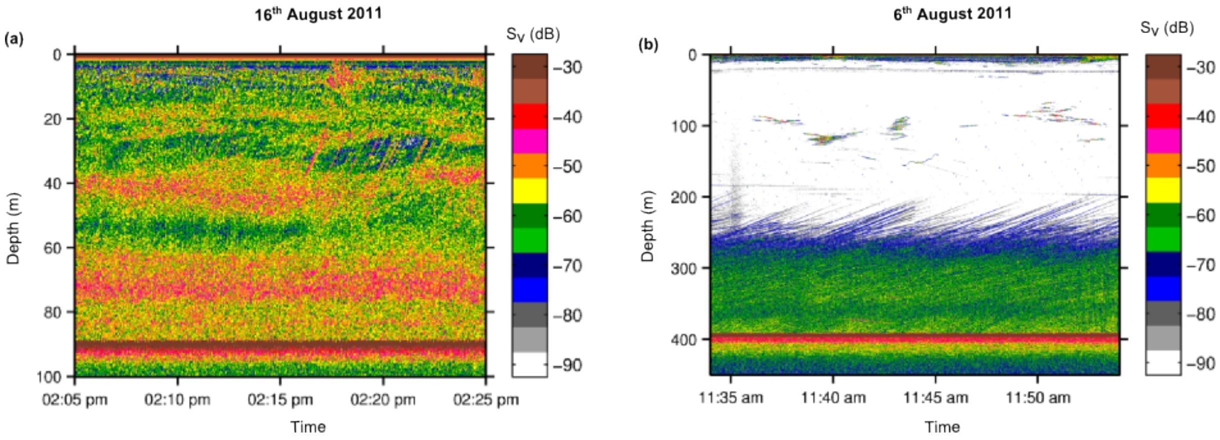

Figure 7.4.: Acoustic flares observed with the EK60 echosounder from the vessel on station. (a): Acoustic flare from Area 1. (b): Acoustic flare from Area 3.

Extracted from Sahling et al. [48], Table 7.1 summarizes various quantities for the three venting areas. Numbers in Table 7.1 are used for comparison when assessing the performance of the active acoustic inversion.

During research cruise JR253, bubble plumes were heavily studied with lengthy acoustic surveys but for the purpose of investigating their temporal variability, active acoustic data were collected while keeping the vessel on station. This was performed at Area 1 and Area 3. Echogram examples are presented in Figure 7.4.

The overall performances of the echosounder was very good during both research cruises and only disturbances due to bad weather conditions were experienced. An echogram presenting data collected under rough weather is shown in Figure 7.5(a). Such data can be used for flare mapping but for the purpose of quantification using an inverse method, these data are hardly exploitable. In addition, because of transmission losses, every frequency channel could not perform similarly at any depth. Channels that are available without significant amount of noise over the different areas are:

- Area 1 (~90 m): 38 kHz, 70 kHz (only during research cruise HE387), 120 kHz, 200 kHz
- Area 2 (~250 m): 38 kHz, 70 kHz (only during research cruise HE387), 120 kHz
- Area 3 (~380 m): 38 kHz, 70 kHz (only during research cruise HE387), 120 kHz

For Area 1, using thresholds $s_\mathrm{v} = -30$ dB and $s_\mathrm{v} = -90$ dB (e.g. in Figure 7.3(a),

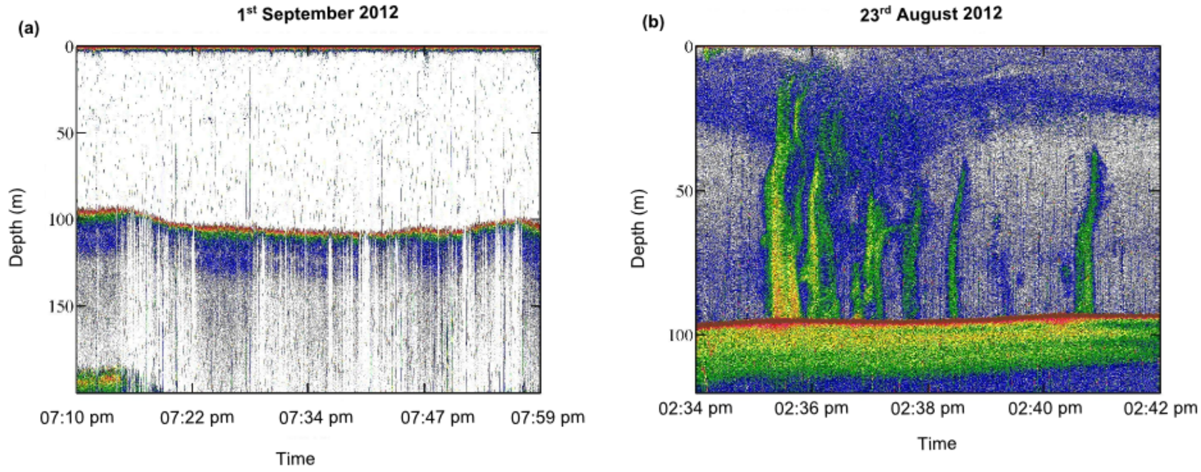

Figure 7.5.: (a): Echogram presenting disturbances produced by bad weather conditions. (b): Increased background noise level at the 200 kHz frequencies channel (induced by further attenuation at higher frequencies).

echogram at 38 kHz), Figure 7.5(b) shows the increased background noise in the 200 kHz channel.

7.2.2. Flare mapping and classification

The EK60 instrument is a powerful tool for mapping gas flares. During acoustic surveys, the time and position of appearance of each flare was recorded using the 38 kHz channel of the EK60 instrument. Also, from these records, the strongest events with heights near the water surface can be identified. During research cruise JR253, this was performed manually with an operator recording the time of appearance and comments on the intensity and height of the flare. Using the positioning system of the vessel, the position of each flare was inferred. During research cruise HE387, this process was improved by using a home made MATLAB toolbox to map gas release and give preliminary assessments of their intensity. From an EK60 echogram at 38 kHz, the MATLAB routine allows the user to select flares over a rectangle section as shown in Figure 7.6. For each selected flare, an identification number (with the format DayMonthNumbering) is given, and the following characteristics are stored:

- The date and time at which the flare is observed.
- The longitude, and latitude of the flare.
- The sum of all s_v within the rectangle area (in m^{-1}).

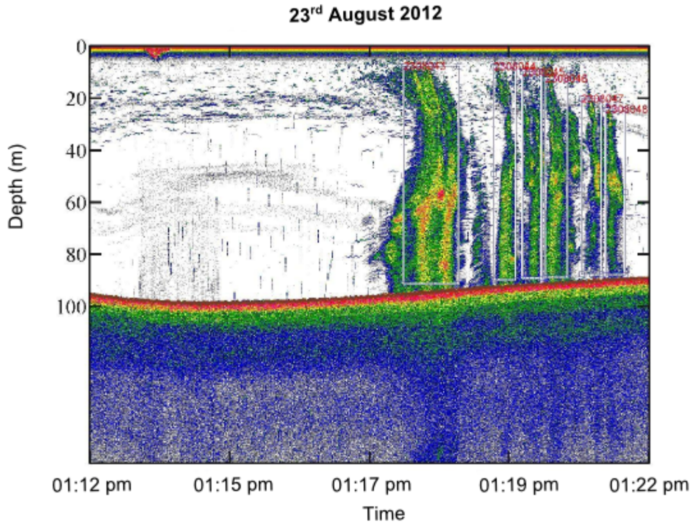

Figure 7.6.: Echogram exemplifying the use of a MATLAB toolbox designed to perform echo-integration. In this echogram, six flares were picked up manually in rectangle areas. These areas define the data set that are stored and analysed.

- The selected rectangle area (in s × m).
- The height extend (in m).

Running this procedure over the research cruise HE387 data set, this allows one to produce a map like the one shown in Figure 7.7. It is clear that flares are concentrated in three main areas (Area 1, 2 and 3). During research cruise HE387, these records helped selecting multi-beam data of interest in order to give further directions for ROV dives. It is important to note the abundance of flares could be increased artificially with the relative observation activity. If an area is surveyed several times, the number of flares observed is enhanced if care is not given to identify each single flare (e.g. discard flares occurring in position of earlier observations). During research cruise HE387, acoustic surveys were performed so that survey lines did not overlap, thus producing distributions of flares with minimal artificial enhancement of this sort.

Furthermore, dividing the summed s_v by the selected area (of dimensions s × m, time extend multiplied by height extend), a measure of the relative intensity of each flare can be determined. From these quantities, a relative classification is achieved (e.g. in Sahling et al. [49, Figure 2] where strong and weak flares are distinguished). This is easily obtained and provides useful information that helps to

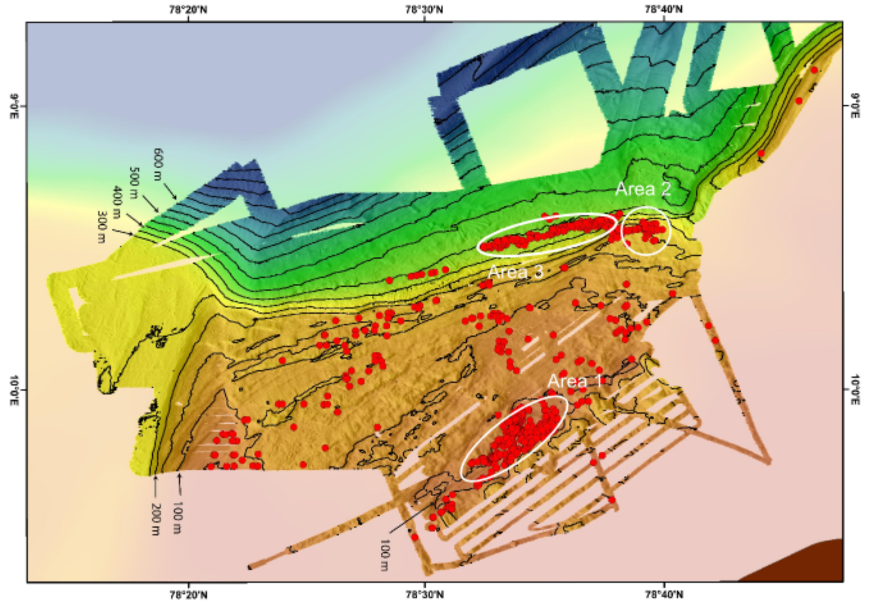

Figure 7.7.: Flare positions recorded using EK60 echosounder records. Strong gas emissions were observed in so called Area 1, Area 2 and Area 3.

refine the areas of interest. From research cruise HE387, the distribution of flares is displayed in Figure 7.8. A clear dependence of the number of flares with depth is noticeable, especially in Area 3 (Figure 7.8(a) ~390 m, zoomed view in Figure 7.8(c)) and Area 1 (Figure 7.8(a) ~90 m, zoomed view in Figure 7.8(b)). In Area 3, a very high abundance of flares is observable in the 390 m depth bin. This also corresponds to the highest intensity of flares (Figure 7.8(a) and (c), grey scale). During research cruise HE387, from the distribution of flares obtained from the multi-beam instrument, Sahling et al. [49, Figure 11] show that most of the flares in Area 3 are found between 360 m and 415 m depth. Their composition is confirmed as methane using samples collected on site and this interval in depth corresponds to a gradient in sediment temperature of 1.2 C°. This result correlates well with the hypothesis from Westbrook et al. [20] (localized depth at which flares are observed, corresponding to a 1 C° increase in the last 30 years) and the seasonal change in temperature observed by Berndt et al. [36] ($1 - 2$ C° change). Area 2 (Figure 7.8(a), $\approx$ 250 m depth) also presents a large number of flares, but there are fewer than in Area 1 and Area 3. However, a peak in intensity is noticeable for the 240 m depth bin. In comparison, Area 1 (Figure 7.8(a) $\approx$ 90 m, Figure 7.8(b)) presents much higher abundances and greater intensities. In addition, the abundance of flares is spread over a larger range of water depths.

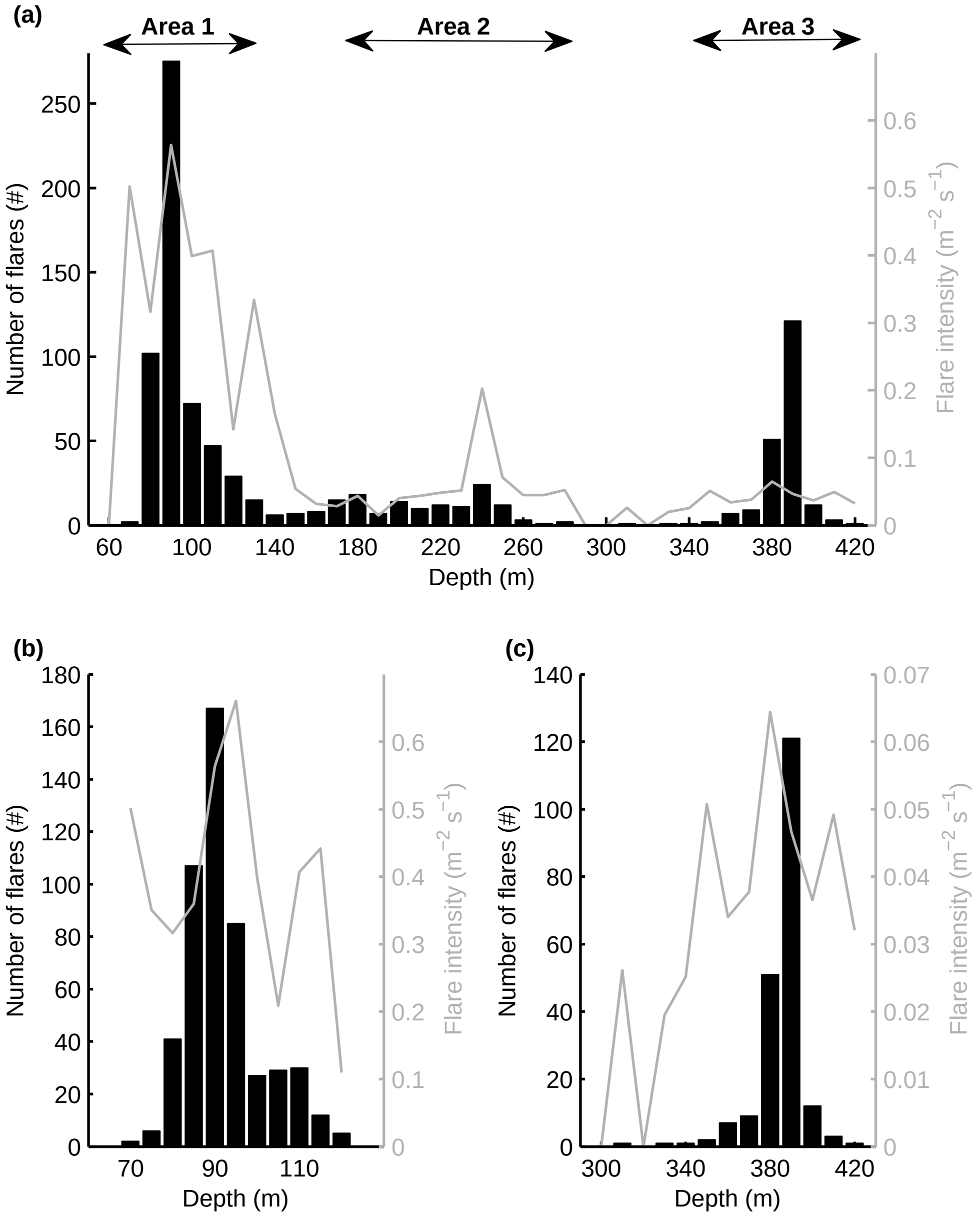

Figure 7.8.: Density and intensity of flares versus water depth. The flare abundances and intensities are computed from EK60 data at 38 kHz. (a): Overall results. (b): Zoom on Area 1 (between ~70 m and ~120 m). (c): Zoom on Area 3 (between ~300 m and ~420 m).

During research cruise HE387, video recordings of bubbles rising from the seafloor were performed during ROV dives. The cruise report of the research cruise HE387 [48] shows the methods and results. From several bubble releases, bubble radii R_0 and bubble rise speeds v are estimated. Results for Area 1 are extracted from Sahling et al. [48] and presented in Table 7.2. This shows R_0 and v with uncertainties and the number of observed bubbles these estimates are based on. Each observed stream is labelled with a different name that relates it to its area (1,2 or 3) and the corresponding cluster [48]. It is important to note that 6 streams is a very small sample and is certainly not necessarily of all gas streams in Area 1. Marine seepages have shown to span various range of bubble size. For example, Leifer [182] observed bubbles up to $R_0 = 20$ mm and Leifer and Culling [54] bubbles sizes vary from $R_0 = 1$ mm $R_0 = 8$ mm. Furthermore, [48] infers R_0 from the measure of the largest extend of each bubble object observed. Bubble sizes are then given as spherical bubble radii. However, for bubbles of relatively large sizes [102] the departure from sphericity is more likely and a direct measure of the bubble radius then introduces a bias in the estimate. On the other hand, the measure of the rise speed is performed over few frames by tracking the bubble object rising the water column and do not introduce this bias. It is suggested that equivalent spherical bubble radii R_0 could be indirectly estimated by inverting v using for example [183]. Because the buoyancy velocity v is directly related to the amount of gas in the bubble, such an inversion could provide more robust estimates for R_0 than estimating R_0 directly from the size of the object.

Stream name	R_0 (mm)	v (m/s)	number of bubbles observed
A1-C1-S2	2.1 ± 0.3	0.262 ± 0.032	2965
A1-C4-S1	1.4 ± 0.1	0.379 ± 0.035	3000
A1-C4-S4	2 ± 0.5	0.256 ± 0.061	2410
A1-C4-S1	1.8 ± 0.5	0.317 ± 0.081	3279
A1-C4-S2	1.1 ± 0.2	0.387 ± 0.034	4230
A1-C4-S6	1.9 ± 0.3	0.336 ± 0.031	1785

Table 7.2.: Results from video observations during research cruise HE387. Results show the averaged bubble radii R_0 and rise speeds v from the video analysis of several bubbles. Each estimate is deduced from different number of bubbles. Data are extracted from Sahling et al. [48].

7.2.3. Acoustic inversion

Here, the inversion procedures described in chapter 6 are applied to EK60 data collected during the research cruise JR253. With the vessel on station, gas release is observed over time (e.g. Figure 7.4(a) and (b)) in Area 1 and Area 3. These data sets are used to estimate the amount of gas released. The different parameters used when solving the inverse problem are for methane gas and correspond to environmental conditions on site (the different quantities are summarized in Appendix E). The inversion methods are described and tested in chapter 6. For data collected at Area 3, because of the relatively large depth (~390 m), two frequency channels are available (38 kHz and 120 kHz) and only the two frequency approach is applicable.

As shown in chapter 6, the results of the two frequency approach consist of the estimation of the dominant radius R_{0_d} of the bubble size distribution. However, this approach does not allow one to resolve the full bubble size distribution. Using an inverse approach with three or more frequencies, the bubble size distribution $N\left(R_0\right)$ can be determined with a resolution which is dependent on the number of frequency channels available. From the results of the two methods, gas volumes can be calculated assuming spherical bubbles (Equation 6.9 for the two frequency inversion, Equation 6.13 for the multi-frequency inversion). As shown in chapter 6, the resolution of $N\left(R_0\right)$ can be enhanced by increasing the under-determination factor UND (section 2.2). These results suggest the value of UND = 2 as a good compromise. For this reason, the inversions performed on data from Area 1 are conducted with UND = 2, in order to better resolve the bubble size distributions.

The input to the inversion is the vector containing s_v measurements at the various frequencies. The fundamental assumption of volume scattering strength s_v is that the total scattered intensity from a volume containing a random distribution of scatterers, on average, is equal to the sum of the scattered intensities from each individual target [60, 67, 68]. The quantity s_v is a random process and the measurement that relates to the abundance of scatterers is the average of s_v. Consequently, s_v needs to be time averaged over several samples in order to be meaningful. However, the average also needs to account for the stationarity of the scatterers in the insonified volume, i.e. averages need to be applied to s_v over volumes presenting the same mix of scatterers. The average values are biased if the target size distribution changes significantly over the period over which the average is computed. Computing the input measurements to the inverse problem then constitutes a trade off between converging toward the true mean value for s_v and averaging over a period time presenting a realistically stable target size distribution in V_0. Here, only data where the ship was on station are used as the variability of the signal can be investigated (e.g. Figure 7.4(a) and (b)). These data sets are best candidates for applying the inversions. Data collected during acoustic surveys present a limited number of samples over which averaging can be performed because the vessel is traversing a flare. These data are not analysed as this requires further research on the stability of s_v. Using stationary data, at each depth, s_v values at the different frequencies are averaged over 100 samples in time (corresponding to 200 seconds). Inversion is then performed on each resulting s_v quantity (at two or three frequencies). The result of the inversion can further be converted into gas volumes V_est. As a result, it provides a track of gas volumes and distribution of bubble sizes across depths and time. Because s_v quantities are relative to a volume of 1 m^3, resulting volumes from the inversion are in m^3 per 1 m^3 of water. Although these calculations of gas volumes provide insights into the amount of gas released, researchers are mainly interested in gas fluxes instead of gas volume.

From size distributions to meaningful quantities Considering a bubble generation rate $\psi_\mathrm{A}\left(R_0\right)$ per unit bubble radius, per unit area, per second, then the number of bubbles dN_b generated in an area dA , over a period dt , within a radius bin of width dR_0 is given by:

$$dN_\mathrm{b} = \psi_\mathrm{A}\left(R_0\right) dR_0 dA dt. \tag{7.1}$$

The bubble rise speed for a bubble of radius R_0 is defined by $v\left(R_0\right) = \dfrac{dh}{dt}$ where h is the vertical elevation. With $dAdt = \dfrac{dAdh}{v\left(R_0\right)} = \dfrac{dV}{v\left(R_0\right)}$, the number of bubbles per radius increment dR_0 in the increment volume dV is then:

$$dN_\mathrm{b} = \frac{\psi_\mathrm{A}\left(R_0\right)}{v\left(R_0\right)} dR_0 dV, \tag{7.2}$$

with $v\left(R_0\right)$ the bubble buoyancy velocity, i.e. solely due to buoyancy effect (not accounting for upward flow) [102]. The model used here is the one given by Fan and Tsuchiya [183] and recalled by Leifer and Patro [184]. For salt water, $v\left(R_0\right)$ is plotted in Figure 7.9. Rise speeds for clean and dirty bubbles are compared and it

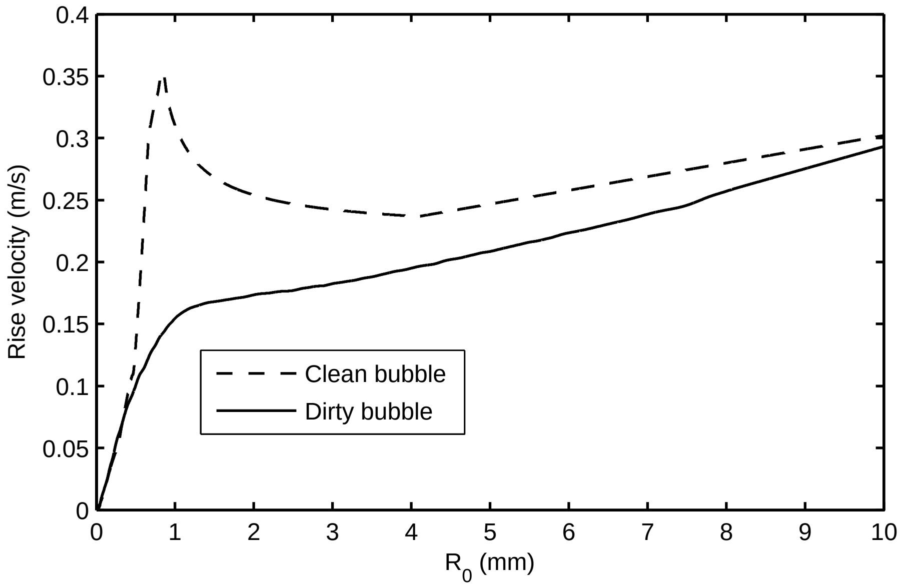

Figure 7.9.: Bubble rise speed [183] for clean (dashed line) and dirty bubbles (solid line).

can be observed that differences are significant, especially around $R_0 = 1\,\text{mm}$. This shows the importance of the contamination of the bubble wall by surfactant.

The inverse problem considered here evaluates $N\left(R_0\right)$, the number of bubbles per unit volume per µm radius increment. Using Equation 7.2, with $dV = 1\ \text{m}^3$, $N\left(R_0\right)$ then relates to $\psi_\text{A}\left(R_0\right)$ as:

$$N\left(R_0\right) = \frac{\psi_\text{A}\left(R_0\right)}{v\left(R_0\right)} dR_0, \tag{7.3}$$

and the volume gas flux per unit area per second is given by:

$$F_\text{gm} = \frac{4\pi}{3} \int\limits_{R_1}^{R_{N_R}} R_0^3 \psi_\text{A}\left(R_0\right) dR_0 = \frac{4\pi}{3} \int\limits_{R_1}^{R_{N_R}} R_0^3 N\left(R_0\right) v\left(R_0\right) dR_0. \tag{7.4}$$

It represents the volume flux per unit area.

7.3. Results and discussion

Here, drawing on data collected during research cruise JR253 from Area 1 and Area 3, results from two inversions are presented: a two frequency inversion (subsection 6.2.3); a multi-frequency inversion (subsection 6.2.4, based three frequencies). The backscattering cross coefficient per unit volume s_v is measured at three frequencies (38 kHz, 120 kHz, 200 kHz) at Area 1 (~90 m) and two frequencies (38 kHz, 120 kHz) at Area 3 (~390 m). Each data set consists on backscattering strength time series (at a sampling rate of 0.5 Hz) at various depth (linear spacing of 0.1912 m).

General considerations Considering the echogram of the acoustic flare from Area 1 presented in Figure 7.4(a), the variability of s_v values is shown in Figure 7.10(a). At each frequency and each depth, 887 time samples are analysed (approximately 25 minutes). the mean values, 75th and 25th percentiles of S_v (s_v on a dB scale) are displayed. At 86 m depth (1 m above the seabed), $S_\mathrm{v}^{38\,\mathrm{kHz}} = -62.1$ dB, $S_\mathrm{v}^{120\,\mathrm{kHz}} = -63.2$ dB, $S_\mathrm{v}^{200\,\mathrm{kHz}} = -65.8$ dB. With decreasing depth, S_v decreases, reaching a water depth (~30 m) where s_v increases with decreasing depth. This enhanced backscattered intensity near the sea surface can be the result of the interaction of the sound waves with bubbles near the surface produced by the hull of the vessel [43]. Consequently, further in this chapter, the inversions are applied to this data set between $z = 86$ m and $z = 10$ m. At $z \approx 40$ m, a large increase in S_v is noticeable (especially at 38 kHz). From the echogram (Figure 7.4(a)), the increased intensity at this depth is noticeable but is intermittent. This suggests the increase in s_v is from random scatterers in the sampled volume (e.g. fish). At all three frequencies, the difference between the mean value and the 75th and 25th percentiles is approximately of 3 dB, confirming the variability in the data and the need for averaging over several samples before applying the inversion. Similarly, mean values, 75th and 25th percentiles for a gas plume in Area 3 is presented in Figure 7.10(b) (echogram shown in Figure 7.4(b), 27 minutes). Because these data were collected at larger depths (~390 m), only two frequency channels are usable (38 kHz, 120 kHz). At $z = 390$ m (1 m from the seabed), $S_\mathrm{v}^{38\,\mathrm{kHz}} = -66.6$ dB, $S_\mathrm{v}^{120\,\mathrm{kHz}} = -65.4$ dB and S_v decreases with depth, with $S_\mathrm{v}^{38\,\mathrm{kHz}}$ becoming greater than $S_\mathrm{v}^{120\,\mathrm{kHz}}$ from ~370 m. At $z > 250$m, S_v is below the echogram threshold of -90 dB (Figure 7.4(b)). Such low S_v is near the background noise and suggests no bubbles are detected.

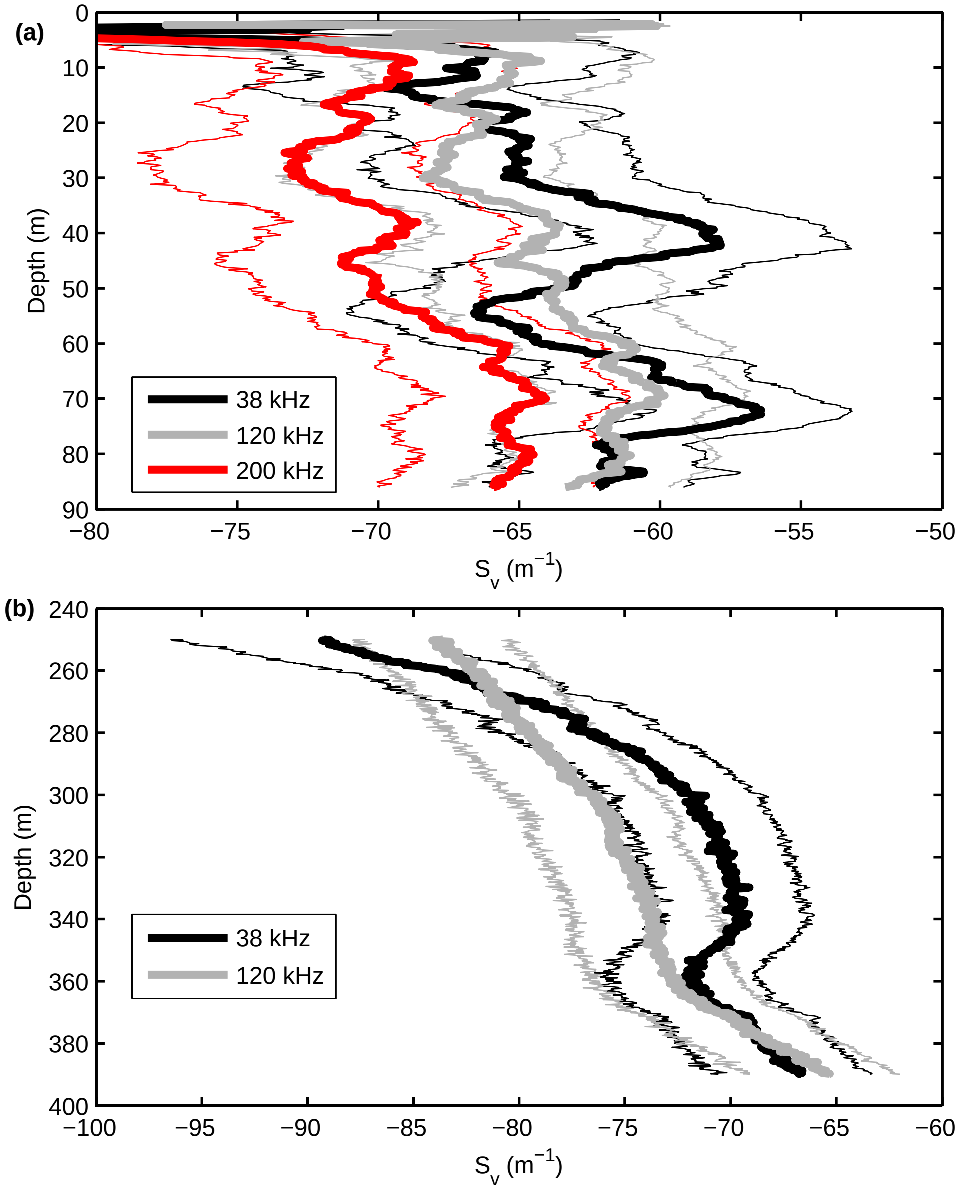

Figure 7.10.: S_{v} versus depth for the two acoustic flares shown in Figure 7.4. (a): Acoustic flare in Area 1 (Figure 7.4(a)). (b): Acoustic flare in Area 3 (Figure 7.4(a)). Thin lines are 75th and 25th percentile. Thick lines are the mean values.

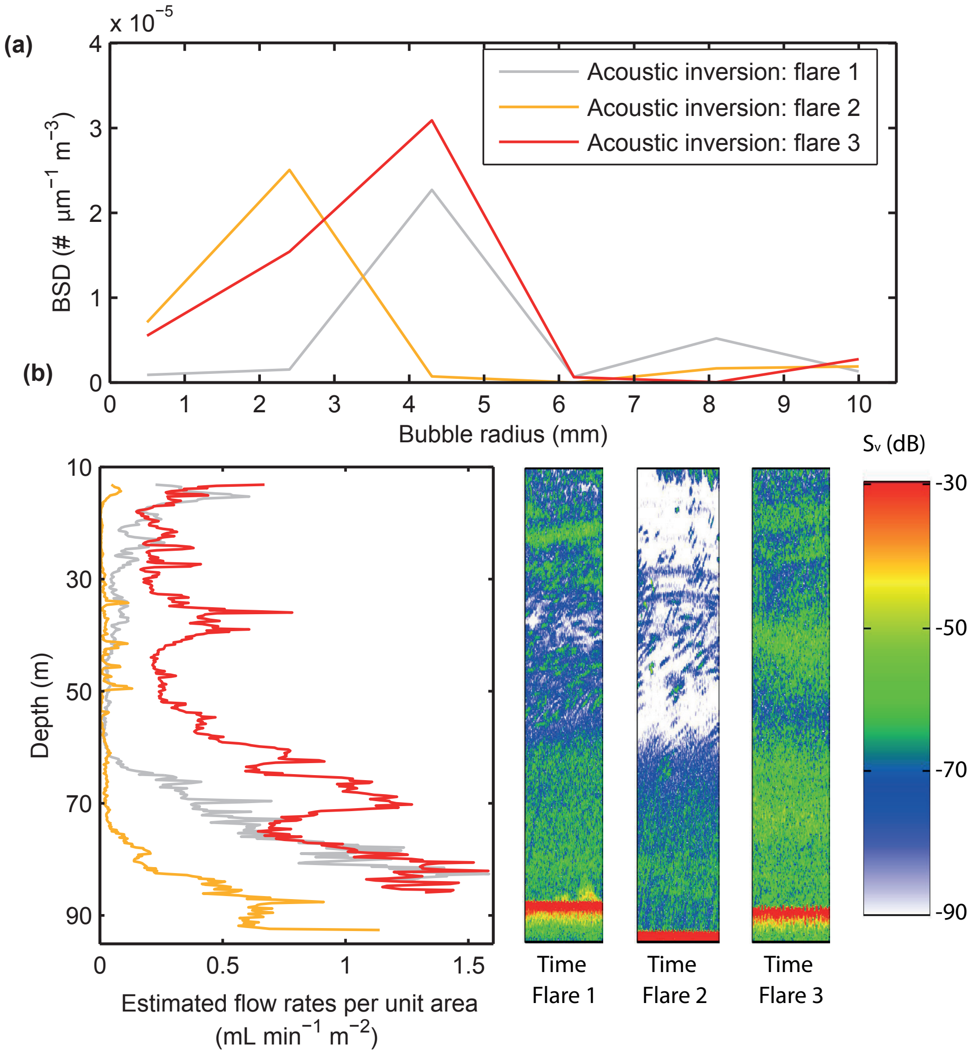

Figure 7.11.: analysis of three gas plumes through a three frequency acoustic inversion (38 kHz, 120 kHz, and 200 kHz). The bubble size distributions are computed from a bubble radius $R_0 = 0.5$ mm to $R_0 = 10$ mm. By integrating over all bubble sizes, gas volumes are determined. Following the procedure in subsection 7.2.3, they can further be converted into flow rates per unit area. For each sampled depth, this procedure is applied on times series for S_v collected with the vessel on station (e.g. Figure 7.4) for: 15 minutes for flare 1; 23 minutes for flare 2; 27 minutes for flare 3. (a): Resulting bubble size distributions near the seabed from the three different plumes (grey, yellow and red lines) and ROV video analysis of bubble release (black bars). (b): Gas volume estimates for the three gas flares from the seabed to 10 m below the water surface. (c): Sampled 5 minutes of 38 kHz EK60 echogram profiles for each individual plume.

	Area 1			Flare Area 3
	Flare 1	Flare 2	Flare 3	
Flow rate per unit area at seafloor (mL min^{-1} m^{-2})	1.3	1.1	1.3	0.7
EK60 footprint area (m^{-2})	334.2	400.9	350.3	7200
Flow rate over footprint area (mL min^{-1})	434.5	440.9	455.4	5040
Average flow rate per cluster (mL min^{-1}) [48, 49]	409.5			167.2

Table 7.3.: Summary of results from the acoustic inversion in Area 1 and Area 3. Results are first presented as flow rates per unit area. Using the footprint area at the operating depth, total flow rate can be calculated. This is further compared to flow rates inferred by Sahling et al. [48, 49] from ROV observations.

Inversion of data from Area 1 At each frequency and depth, s_v is averaged over 100 samples and an inversion is applied following the procedure in subsection 6.3.2. For each averaged time sample, at each depth, this gives a bubble size distribution $\mathbf{N}$ in six size bins (UND = 2). This can be integrated through Equation 6.13 to compute V_est. Following the procedure in subsection 7.2.3, using the model of Fan and Tsuchiya [183] for the buoyancy bubble velocity, this can further be converted into flow rates per unit area (expressed in mL min^{-1} m^{-2} for comparison with the data from Sahling et al. [48, 49], summary of results in Table 7.3). In Area 1, this method is applied to 3 gas plumes presenting different profiles (Figure 7.11(c)): "flare 1", observed on 15th August from 09:35 pm to 09:49 pm, 14 minutes, 84 m water depth; "flare 2", observed on 15th August from 10:01 pm to 10:23 pm, 23 minutes, 92 m water depth; "flare 3", observed on 16th August from 02:05 pm to 02:32 pm, 27 minutes, 86 m water depth, acoustic flare shown in Figure 7.4(a) and analysed in Figure 7.10(a)). The size distributions $\mathbf{N}$ (1 m above the seabed) and flow rates per unit area F_gm are averaged over the time period that the flares are observed. Results are presented in Figure 7.11. Figure 7.11(a) first compares the different bubble size distributions from the inversion of the three gas flares in Area 1 (Figure 7.11(a)). The result of the inversion consists of $\mathbf{N}$ resolved in six size bins. Through the three cases considered, various bubble size distributions are obtained. Flare 1 and 3 (Figure 7.11(a), grey and red curves) have their highest abundance in the size bin $R_0 = 4.3$ mm while the distribution computed for flare 2 has a peak in the size bin $R_0 = 2.4$ mm. With a peak at $R_0 = 2.4$ mm, results of the inversion of flare 2 are the closest to the video observations performed during research cruise HE387 [48] (Table 7.2). The bubble size distributions for flare 1 and 3 show larger bubble sizes that are larger than what was observed using the video analysis [48]. However, this analysis is based on 6 streams and this is only a small samples of bubble releases in Area 1. Several studies suggest that the range of bubble sizes can vary [33, 40, 42, 54, 75, 182] and the results obtained here from the inversion remain within in a physically viable range of R_0.

For the three flares of interest, integrating $\mathbf{N}$ through Equation 7.4 allows to estimate the flow rates relative to $1\,\mathrm{m}^2$, F_{gm}. Results are presented in Figure 7.11(b). It can be observed that F_{gm} decreases with depth. Similarly, s_{v} decreases with decreasing depth (echogram profiles shown in Figure 7.11(c)). Considering flare 1, $F_{\mathrm{gm}} = 1.3\,\mathrm{mL\,min^{-1}\,m^2}$ and at $z = 84$ m, the footprint is $A_{-3\mathrm{dB}} = 334.2\,\mathrm{m}^2$. Consequently, over the footprint area, flare 1 exhibits a flow rate of 434.5 mL min^{-1}. Similarly, flow rates for flare 2 and 3 over their respective footprint areas are 440.9 mL min^{-1} and 455.4 mL min^{-1}. In Area 1, Sahling et al. [48] report an average bubble stream flow rate of 27.3 mL min^{-1} and an average number of 15 bubble streams per cluster (Table 7.1). This gives an approximate flow rate of 409.5 mL min^{-1} per cluster. This suggests the footprint area of the EK60 at depths in Area 1 is approximately the size of one cluster of bubble streams.

Two frequency inversion and quantification of flares in Area 3 If two frequencies (38 kHz and 120 kHz) are available instead of three, the inverse approach is not applied. However, using the two frequency approach described in subsection 6.2.3, gas volumes can still be estimated. In order to compare results presented in Figure 7.11, a two frequency inversion is employed on the data of flare 3. First, computation of the dominant bubble radius $R_{0_{\mathrm{d}}}$ is performed through a numerical optimization of Equation 6.7. If the computed values for $R_{0_{\mathrm{d}}}$ are used in Equation 6.7, two solutions for the abundance of $R_{0_{\mathrm{d}}}$ are found and through Equation 6.9 volumes are estimated. Similarly to the inverse approach, these can be converted into flow rates per unit area (subsection 7.2.3). In Figure 7.12(a) (Area 1), the two solutions (black and grey solid lines) are compared to the results from the three frequency inversion (dashed red line). Across all depths, the solutions for F_{gm} computed with two frequencies vary significantly with depth, with large spikes. Flow rates F_{gm} computed through a

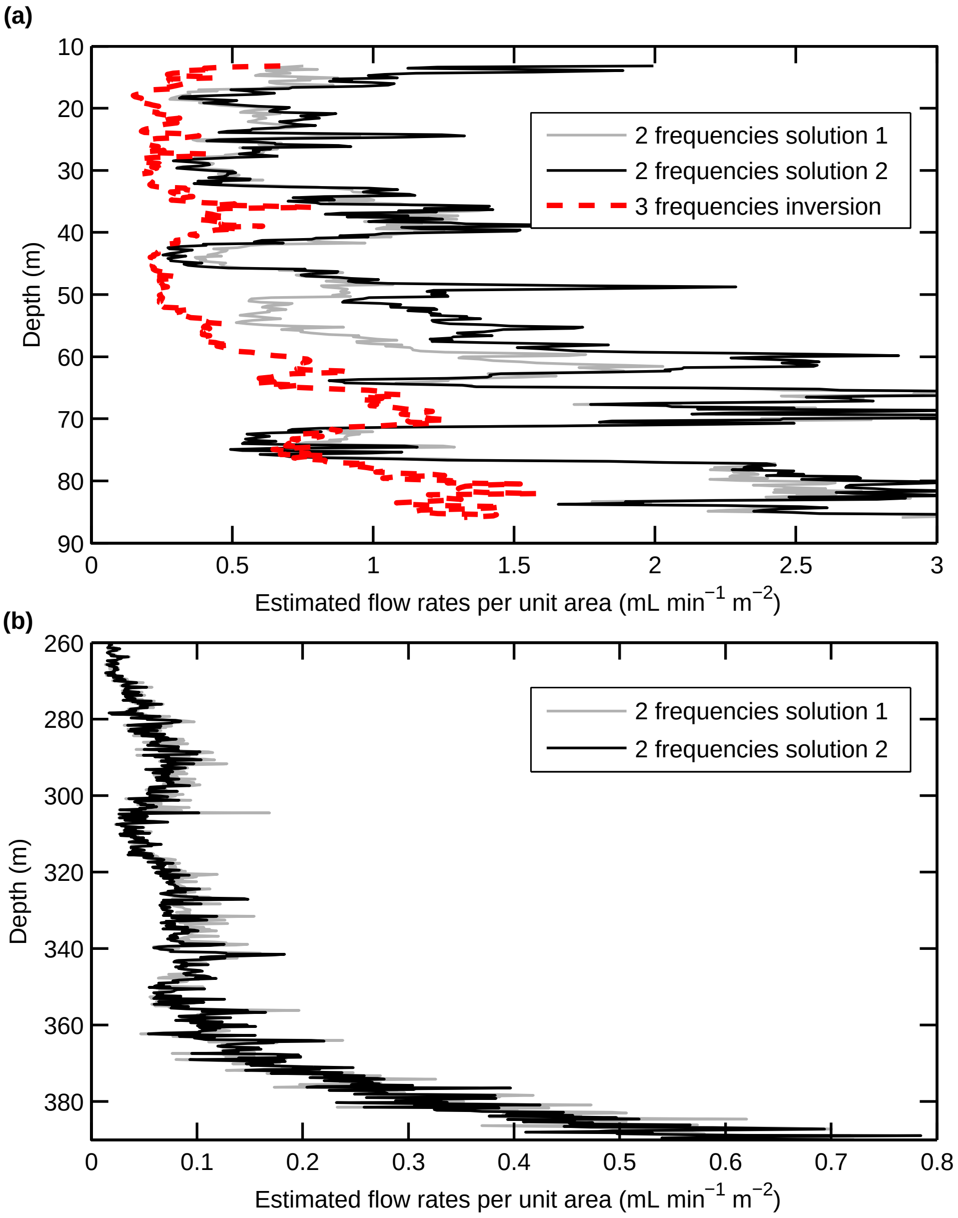

Figure 7.12.: Flow rate per unit area F_{gm} versus depth. (a): Gas flow rates inferred from the time series of a flare in Area 1 (Figure 7.4(a), flare 3 in Figure 7.12) using two frequency and three frequency inversions. (b): Gas flow rates inferred from the time series of an acoustic flare in Area 3 (Figure 7.4(b)).

two frequency inversion are within one order of magnitude to F_{gm} computed through a three frequency inversion. Near the bottom (z = 86 m), $F_{\mathrm{gm}} \approx 3$ mL min^{-1} m^{-2} (two frequency approach), ~2 times higher than those from the three frequency inversion. It is important to note that the solution using a three frequency inversion is less spiky than the two frequency inversion, suggesting the multi-frequency inversion method is more robust. In Area 3, the acoustic flare presented in Figure 7.4(b) is analysed using the two frequency approach and results are shown in Figure 7.12(b). The two solutions for F_{gm} are close, exemplifying good robustness of the algorithm. Near the seabed (z = 390 m) $F_{\mathrm{gm}} \approx 0.7$ mL min^{-1} m^{-2}, ~38% lower than F_{gm} for the flares analysed in Area 1 (Table 7.3). At z = 390 m, the footprint area is of $A_{-3\mathrm{dB}} = 7200\,\mathrm{m}^2$ and the flow rate is then of 5040 mL min^{-1}. Sahling et al. [48, 49] observed an averaged bubble stream flow rate of 20.9 mL min^{-1} with an average number of 8 bubble streams per cluster. This suggests the footprint area of the EK60 at depths in Area 3 is produced by a combination of several clusters.

7.4. Summary

During two research cruises (JR253, HE387) to the west of Svalbard, single beam echosounder data of methane seeps were collected. Bubbles released from the seafloor strongly scatter sound and emissions of methane are identified by strong acoustic flares during acoustic surveys from single beam echosounder instruments. Here, these data are used to investigate the spatial variability of the gas emissions by recording each acoustic flare position. This allows to determine the strong dependence of gas release with water depth. In addition, in order to quantify these releases, the inverse methods described in chapter 6 are applied to data collected when the vessel was on station over a gas flare. These data are collected for Area 1 (~90 m depth) and Area 3 (~390 m depth).

In order to quantify gas emissions, the two methods of chapter 6 are used in this chapter. These methods predict gas volumes that can be converted into flow rates per unit area (subsection 7.2.3). First, based on a two frequency data set, the method described in subsection 6.2.3 allows to determine the dominant bubble size and then the amount of gas in the insonified volume. Second, the multi-frequency inversion described in subsection 6.4.2 is based on echosoudner data set at three or more frequencies. With this technique, the bubble size distribution can be resolved. Results from chapter 6 suggest the volume of gas estimated are more precise than with the two frequency method. While it is preferable to use the inverse method because it resolves the bubble size distribution, the operating depth limits the number of frequency channels that are usable. For this reason, the acoustic flare from Area 3 is analysed using the two frequency method. In Area 1, the inversion method is applied on echosounder data from three gas release of different intensity.

Results from the inversion of data in Area 1 show different bubble size distributions. Highest abundances are found at sizes $R_0 = 4.3$ mm or $R_0 = 2.4$ mm. The amount of gas released it is found to decrease with decreasing depth with an estimated flow rate per unit area near the seafloor varying from $F_{\mathrm{gm}} = 1.1\,\mathrm{mL\,min^{-1}\,m^2}$ to $F_{\mathrm{gm}} = 1.3\,\mathrm{mL\,min^{-1}\,m^2}$. Results from the two frequency inversion on data from Area 3 also exhibit a clear decay of estimated flow rates with decreasing depth. Near the seafloor, $F_{\mathrm{gm}} = 0.7\,\mathrm{mL\,min^{-1}\,m^2}$, ~38% less than in Area 1.

The results presented here are only based on data collected with vessel on station and are preliminary assessments for the inversion methods described in chapter 6. The aim is to apply the inversion to data collected with vessel cruising in order to obtain estimates for the amount of gas released over the whole studied area.

In the next chapter, concluding remarks will be addressed on the use of the inversion methods (using passive and active acoustics) described in this thesis. Also, leads for further work will be given.

8. Conclusions and future work

8.1. Summary of main findings

In this study, quantification of gas escape from the seafloor using passive and active acoustics is described. It has application to the monitoring of anthropogenic (e.g. leak from pipelines...) and natural (e.g. methane seeps) gas releases. Two acoustic inversions are described and are based on models of: the passive acoustic emissions of gas bubbles; the acoustics backscattering of gas bubbles at multiple frequencies. These methods are applicable to the monitoring of gas leaks in the form of bubbles and are therefore unable to detect gas released in dissolved phase. For the detection of gas release in dissolved phase, chemical sensors can be used [185].

In chapter 4 the passive acoustic inversion was successfully implemented in laboratory conditions and validated the methodology for further at sea deployment (chapter 5). Metered amount of gas are released with two different bubble generation systems (an arrangement of needles and a bubbling stone) in a large enclosure and the sound from the bubbles are recorded and used to infer flow rates. Acoustically inferred flow rates are given as a spread of acoustic estimates and gas estimates span one order of magnitude. This large spreads is due to the unknown parameter $R_{\epsilon 0\mathrm{i}}/R_0$, which accounts for the strength of the acoustic emission when the bubble is released. The absolute level for flow rates then rely on accurate prediction for this parameter. However, results show good accuracy at tracking the relative changes in flow rate, this for both bubble generation systems. In light of the current knowledge [61, 82], $R_{\epsilon 0\mathrm{i}}/R_0$ is dependent upon the bubble size, the type of bubble generation system (e.g. solid orifice, sediments...) and potential the depth of the bubble release. The results from the laboratory measurements suggest $R_{\epsilon 0\mathrm{i}}/R_0 = 3.5 \times 10^{-4}$ for the arrangement of needles (1.2 mm diameter) and $R_{\epsilon 0\mathrm{i}}/R_0 = 1.6 \times 10^{-4}$ for the bubbling stone. The ratio $R_{\epsilon 0\mathrm{i}}/R_0$ is key in order to quantify precisely with the passive acoustic inversion and although the understanding to date of $R_{\epsilon 0\mathrm{i}}/R_0$ remains limited, knowledge will increased with further experimental and theoretical work.

In chapter 5, the deployment of a passive acoustic recorder during an experimental release of CO_2 gas at sea [50] is described. From a container positioned onshore, gas was injected through a bore hole and gas migrated through the sediments and seeped into the water column. An hydrophone was deployed and was able to measure the sound from bubble releases. The passive acoustic method can then be employed to monitor the amount of gas released in the form of bubbles in the water column every ten seconds. In comparison, diver measurements provided a single data point at expensive cost by measuring individual streams over a one hour window. Strong correlation with tide is found with a decrease of 15.1 kg d^{-1} in flow rate for each meter of tide increase. This shows that tide effects are significant in the amount of gas release from say gas seeps. It is important to account for them when addressing the amount of gas released from gas seeps [36, 175]. In addition, the acoustically inferred flow rates correlate well with the various changes in the rate of gas injection.

Models for predicting the scattering strength of a single gas bubble are described in chapter 3 and are of two types: analytical breathing mode solutions; modal solutions. They are used to compute the backscattering cross section matrix, kernel matrix of the active acoustic inversion (chapter 6, chapter 7). The modelling of the backscattering cross section via the analytical model (Equation 3.31) for the breathing mode assumes the wavelength of the driving acoustic field is large compared to the size of the bubble ($kR_0 \ll 1$). An analytical expression by Thuraisingham (Equation 3.32) [96] expands its applicability to all kR_0. At $kR_0 \approx 1$ and $kR_0 \gg 1$, the contribution of the breathing mode is shown to becomes negligible and it is then important to account for the contribution of other modes. In that context, the modal solution described in subsection 3.6.2 is best suited to work at regimes $kR_0 \approx 1$ and $kR_0 \gg 1$. These regimes are the one considered in Chapter 6 and 7. It is interesting to note that in many studies [37, 42, 152, 153], the analytical breathing mode solution (e.g. Equation 3.31) is used while considering kR_0 regimes that are not fulfilling $kR_0 \ll 1$, thus making the use of the backscattering models improper. Here, this issue is addressed prior to the formulation of the inverse problem. The methodology for solving the inversion problem is inspired from the estimation of zookplankton populations [60, 62, 65].

The active acoustic inversion is based on the backscattering strength levels from clouds of bubbles at different frequencies. Two inversion approaches are considered: using two frequency data sets; using three or more frequency data sets. While the two frequency approach provides the dominant radius of the bubble size distribution, the inversion based on more numerous frequencies is able to resolve the bubble size distribution. In chapter 6, each methodology is described and then tested against simulated data. Various bubble size distributions are used for the simulations. Simulated measurements are used to run inversions with different number of frequencies. The performance of the methods are addressed from the accuracy of the estimation of the gas volumes. The two frequency approach is found to perform well under the constraint that the bubble size distribution considered present a strongly dominant size. However, using an approach with three or more frequencies exemplifies an increased accuracy and robustness to noise.

The methods described and tested in chapter 6 is applied to at sea data in chapter 7. From two research cruises, single beam echosounder data from methane seeps were collected. Each gas release consists on a strong acoustic flare and using the position of each flare, the depths at which seepage occur are identified. Strong abundance of gas releases is found at a depth of ~390 m. This correlates well with previous studies that hypothesise that these releases are induced by methane hydrate dissociation [20]. The active acoustic inversion methodologies are applied to data collected with vessel on station. Preliminary quantitative estimates of gas volumes are presented. For shallow gas escapes (~90 m), the inversion can be carried out using three frequencies. The bubble populations are obtained and exemplify the peaks in abundances varying from $R_0 = 4.3$ mm to $R_0 = 2.4$ mm depending on the acoustic flare considered. For these flares observed at shallow water, the amount of gas is also predicted and they are shown to decrease significantly with decreasing depth. For deeper gas escape (~390 m), only two frequencies are usable and only the two frequency methodology is applicable. This does not allow to resolve bubble size populations. However, estimates for gas flow rates are computed. At seafloor level, these are less than for the shallow seeps, correlating well with ROV observations on the field [48]. Along the water column, the deep gas escapes show a decrease in amount of gas with decreasing depth.

To summarize, this study has yielded a number of results that might be considered an advancement in the field of acoustic quantification of gas leaks. These include:

1. Addressing the accuracy and applicability of the passive acoustic method described by Leighton and White [61].
2. Performing indirect measure of the initial bubble wall amplitude ($R_{\epsilon 0\mathrm{i}}/R_0$) for two bubble generation systems and for bubble release from a sediment layer:
    - Needle array (1.2 mm needle orifice): $R_{\epsilon 0\mathrm{i}}/R_0 = 3.5 \times 10^{-4}$.
    - Bubbling stone: $R_{\epsilon 0\mathrm{i}}/R_0 = 1.6 \times 10^{-4}$.
    - Sediment layer: $R_{\epsilon 0\mathrm{i}}/R_0 = 1.2 \times 10^{-4} \pm 6.8 \times 10^{-6}$.
3. Measurements of the temporal variability of gas release at sea. The effect of tide and injection flow rate is clearly resolved.
4. A formulation for the backscattering strength from a cloud of bubbles.
5. A systematic method for determining the optimisation of the Levenberg-Marquardt least squares parameter Λ through the L-curve criterion.
6. Development of two inversion methods based on single beam echosounder data at multiple frequencies for the quantification of gas leaks.
7. Addressing the precision and accuracy of the two active acoustic inversion methods.
8. Estimation of bubble populations for methane seeps to the west of Svalbard.
9. Estimation of gas volumes for methane seeps to the west of Svalbard. This include tracking the fate of free gas in the water column.

8.2. Suggested future work

The following points are suggested for furthering the research undertaken in this thesis:

- Measuring the initial bubble wall amplitude ($R_{\epsilon 0\mathrm{i}}/R_0$) for different type of rigid bubble injection systems (e.g. using bubble generation systems with different orifice sizes). This would help understanding the dependency of $R_{\epsilon 0\mathrm{i}}/R_0$ with the type of gas injection. This would improve the accuracy of the passive acoustic method.

- Measuring the initial bubble wall amplitude ($R_{\epsilon 0\mathrm{i}}/R_0$) for bubbles emitted from sediments beds with different types of sediments. This would improve the accuracy of the passive acoustic method.
- Comparison of independent measurements of bubble size distributions with bubble size distributions inferred from passive acoustic measurements. This would further the understanding of the dependency of $R_{\epsilon 0\mathrm{i}}/R_0$ with bubble size.
- Comparison of bubble populations at different tidal height levels using the passive acoustic inversion. This would further the understanding of the dependency of $R_{\epsilon 0\mathrm{i}}/R_0$ with depth.
- Implementation of the passive acoustic inversion with increased number of hydrophones. This would improve the operating range of the passive acoustic method.
- Experimental implementation of the active acoustic technique with more numerous frequency channels.
- Study of the effect of non-spherical bubbles and various incidence angles on the active acoustic inversion methods.
- Analysis of acoustic flares with vessel cruising using the active acoustic inversion methods.
- Analysis of an entire research cruise data set using the active acoustic inversion methods.

A. Sound field in test tank

In chapter 4, passive acoustic emissions of gas bubbles are investigated under laboratory conditions in a large water tank (8 m x 8 m x 5 m, i.e. of volume $V = 320\,\mathrm{m}^3$). Of importance is the effect of reverberation on the measurements because the passive acoustic inversion scheme described in section 4.2 requires to invert the acoustic contribution to the spectrum from bubbles only. Any enhancement from say noise floor or reverberation would enhance the bubble count artificially, thus leading to systematic errors in gas flow rate estimates. For that purpose, under laboratory conditions, measurements were performed at different distances from the bubble emissions in order to determine the uncertainties induced by working in a reverberant environment. The results for various gas flow rate regimes are shown in Figure 4.2. This chapter first describes the theory used to assess the impact of reverberation. This describes the correlation between the sound emission in free field and in a test tank. Second, procedures for the measurements of reverberation time T_{60} is presented. These are used in chapter 4. Finally, an experimental procedure for the acoustic power of underwater loudspeakers is described and exemplified with measurements in a small test tank.

A.1. Theoretical considerations

With a steady state sound field, the total acoustic pressure p_t in an enclosure is the combination of the direct field (p_d) and the reverberant field (p_r), and $p_\mathrm{t}^2 = p_\mathrm{r}^2 + p_\mathrm{d}^2$. With the source output $S_\mathrm{o} = p_\mathrm{d} \times r$, measure of the source efficiency in free field, the averaged total rms pressure as a function of range r is [113, 114]:

$$\overline{p_\mathrm{t}^2}\,(r) = S_\mathrm{o}^2 \left[\frac{1}{r^2} + \frac{16\pi}{A_\mathrm{s} Q_\theta} \right], \tag{A.1}$$

with the symbol $^-$ denoting spatial average. For an omnidirectional source, the

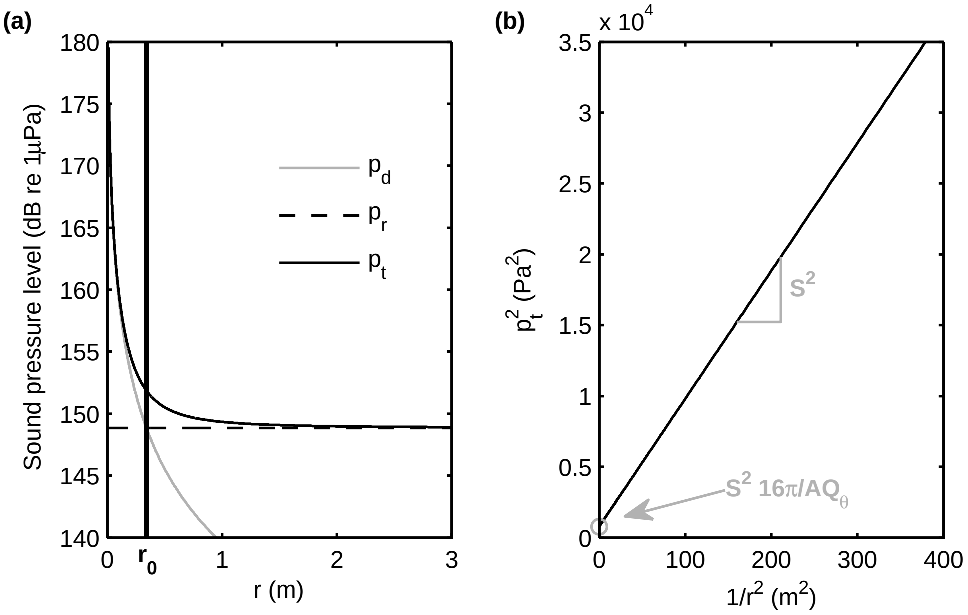

Figure A.1.: Illustrating example of the pressure field in an enclosure as function of range r and $1/r^2$. Values used here are those from Hazelwood and Robinson [114]: $S_\mathrm{o} = 9.5\,\mathrm{Pa\,m}$; $A_\mathrm{s} = 5.9\,\mathrm{m}^2$; $Q_\theta = 1$. (a): Sound pressure level against r for the direct (solid grey line), reverberant (dashed black line) and total (solid black line) pressure fields. The vertical thick black line represents the radius of reverberation r_0 as defined by Equation A.3. (b): Total pressure p_t^2 versus $1/r^2$. The linear rate of increase of p_t^2 represents the square of the source output S_o^2 and the y-intercept of the curve is $S_\mathrm{o}^2 16\pi/A_\mathrm{s}Q_\theta$.

directivity factor Q_θ is $Q_\theta = 1$ when the source is suspended and $Q_\theta = 2$ when lying on a reflective flat surface. The quantity A_s is the Sabine coefficient defined as [113, 186]:

$$A_\mathrm{s} = 55.3 \times \frac{V}{T_{60} c_\mathrm{l}}. \tag{A.2}$$

Equation A.1 exemplifies a balance between the direct field pressure $p_\mathrm{d}^2(r) = S_\mathrm{o}^2/r^2$ and the reverberant field pressure $p_\mathrm{r}^2 = S_\mathrm{o}^2 16\pi/A_\mathrm{s}Q_\theta$. The range at which both fields are equal r_0 is called the radius of reverberation (or critical radius), and is given by:

$$r_0 = \sqrt{\frac{A_\mathrm{s}Q_\theta}{16\pi}}. \tag{A.3}$$

An example of a pressure field in an enclosure is given in Figure A.1. In Figure A.1(a), the acoustic pressure due to the reverberant field and the direct field, and the total acoustic pressure are plotted against the distance from the source r. It can be observed that at large r, the reverberant field dominates, giving a total pressure field converging toward $\overline{p_\mathrm{t}^2}\,(r) = \dfrac{S_\mathrm{o}^2 16\pi}{A_\mathrm{s} Q_\theta}$. Near the source, p_t converges toward the direct field p_d. At the radius of reverberation r_0, both fields contribute equally and p_t^2 is 3 dB higher than expected from either alone [113]. Figure A.1(b) shows that p_t^2 linearly increases with $1/r^2$. Of importance here is the linear rate of increase. This relates directly to S_o^2. The y-intercept of p_t^2 is equal to $S_\mathrm{o}^2 16\pi / A_\mathrm{s} Q_\theta$. Then, the source output S_o can be measured by plotting p_t^2 versus $1/r^2$. This requires measurements at different distances from a source emitting a steady state acoustic field. The acoustic source power W can be computed from S_o[187]:

$$W = \frac{S_\mathrm{o}^2}{4\rho_\mathrm{l} c_\mathrm{l}}. \tag{A.4}$$

Combining the reading of S_o to the y-intercept value with the directivity factor Q_θ, A_s can be determined. Furthermore, using Equation A.2, the reverberation time can also be inferred.

An important limitation of measurements in enclosure is the mode mixing, i.e. working at frequencies where there is enough mode overlap to give an acoustic field that is isotropic and homogeneous[113, 187]. This condition can be fulfilled by working at frequencies higher than the Schroeder frequency[113]

$$f_\mathrm{min} = c_\mathrm{l} \times \sqrt{6/A_\mathrm{s}} \tag{A.5}$$

A.2. Reverberation time

Measurements of reverberation times T_{60} were performed in two water tanks of different sizes: 1.82 m x 1.24 m x 0.82 m, $V = 1.85\,\mathrm{m}^3$ (Figure A.4(a)); 8 m x 8 m x 5 m, $V = 320\,\mathrm{m}^3$. Both enclosures had a body of fresh water of 10 °C.

The reverberation time were measured using an underwater loudspeaker (Neptune sonar T143). This acoustic source was placed 2 m below the water surface and was driven by white noise generated by a signal generator (Stanford research DS345). Using a B&K T8105 hydrophone, the acoustic emissions were recorded for ten seconds. Over the acquisition period, the signal generator was switched off. The decay of the acoustic energy is then used to measure T_{60}. In the large test

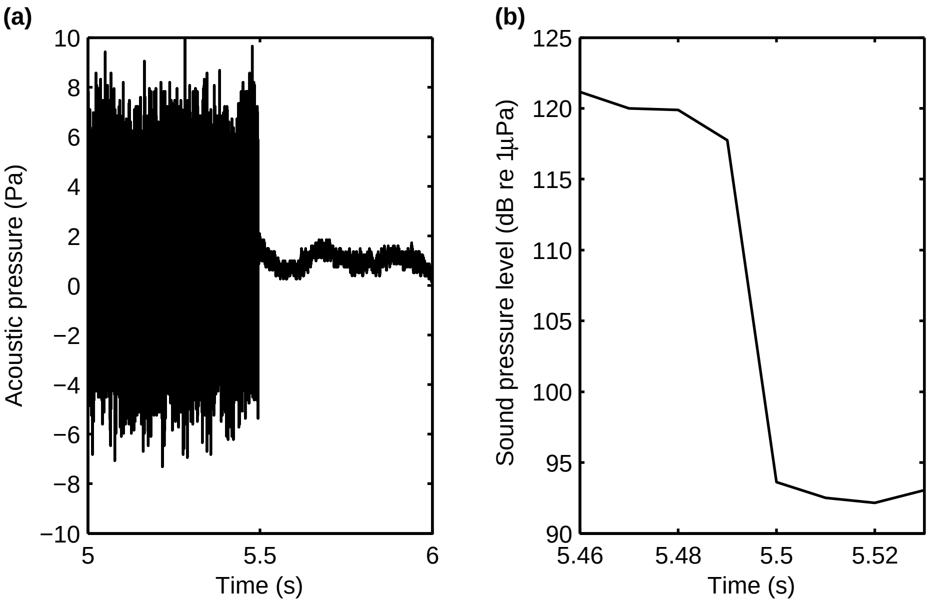

Figure A.2.: Example of T_{60} measurements in the large test tank. (a): Time series recorded by the hydrophone exemplifying the acoustic source being turned off at $t \approx 5.5$ s. (b): Sound pressure level calculated every 0.01 second. The decay rate is used to infer T_{60} in third octave bands.

tank, measurements at 36 different locations were performed and 24 measurements at different locations for the small test tank. An example of time series is plotted in Figure A.2(a). This shows the signal generator being switched off at ≈ 5.5 s.

Reverberation time T_{60} is the time required for the acoustic energy to decay by 60 dB. In order to determine this quantity, each time series is divided into 1000 windows of 0.01 seconds. Over each segment of the data, rms pressure is computed in third octave frequency bands. In each frequency band, sound pressure levels are calculated. The decay time is then determined from the decrease of the sound pressure level when the source is turned off. An example of sound pressure levels recorded in the large test tank are shown in Figure A.2(b). Here, a decay of ≈ 25 dB is observable at $t \approx 5.5$ s when the source is turned off. This relatively small decay is due to the limited power delivered by the signal generator. The decay rate is used to infer the 60 dB reverberation time T_{60}. If the sound pressure level decays at a rate γ_{d}, T_{60} is:

$$T_{60} = \frac{-60}{\gamma_{\mathrm{d}}}. \tag{A.6}$$

	0.7-22.3 kHz			0.8-8 kHz		
	T_{60} (ms)	std (ms)	r_0 (m)	T_{60} (ms)	std (ms)	r_0 (m)
large tank	177.7	28.9	1.64	181.2	30.3	1.64
small tank	113.4	39.2	0.12	-	-	-

Table A.1.: Summary of values for T_{60} in the two test tanks considered here. Results are shown in different frequency bands.

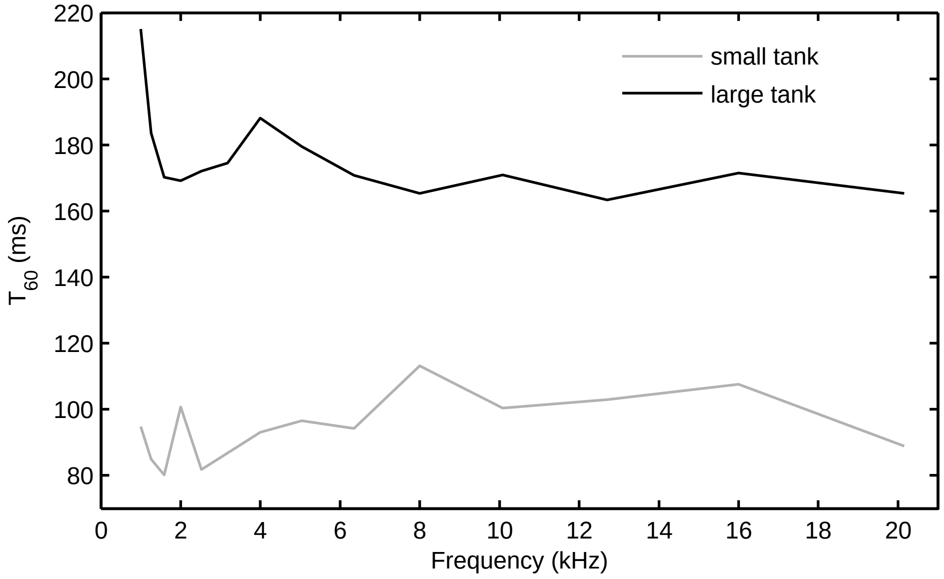

Figure A.3.: Comparison of T_{60} measurements for two enclosures of different size.

In each frequency bands, T_{60} is then measured for two test tank. In chapter 4, T_{60} measurements in the large enclosure are used in a frequency band between 0.8 kHz and 8 kHz. Results are summarized in Table A.1 for the two enclosures. Considering a large frequency band (0.7 to 22.3 kHz), it can be observed that T_{60} is smaller for the smallest enclosure considered. The radius of reverberation r_0 is also significantly smaller for this test tank ($r_0 = 0.12$ m compared to $r_0 = 1.64$ m). In third octave bands, T_{60} for these two test tanks is plotted in Figure A.3. The small enclosure presents a smaller reverberation in all frequency bands.

A.3. Acoustic sources power

In this section, the model described in section A.1 is used to measure the acoustic power of two sources. In a small water tank (1.82 m x 1.24 m x 0.82 m, $V = 1.85\,\mathrm{m}^3$,

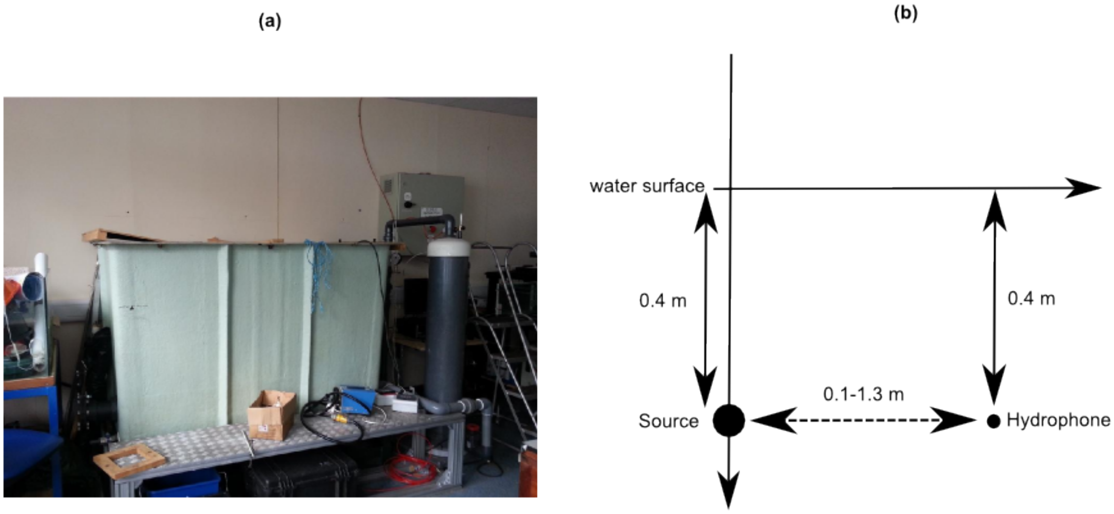

Figure A.4.: (a): Photograph of the ISVR 1013 laboratory test tank. (b): schematic of the experimental set up to measure pressure levels at different horizontal distances from the source.

Figure A.4(a)), two acoustic sources are tested: a B&K T8105 hydrophone used as projector; a circular baffle (15 cm in diameter, unknown model). Each projector was driven by a signal generator (Stanford research DS345). Acoustic emissions at different locations in the tank were acquired using a B&K hydrophone T8103 connected to a charge amplifier (B&K T2635). Acoustic signals were acquired at a sampling rate of 50 kHz with a data acquisition system (NI BNC-2110) installed on a desktop computer using MATLAB. The sensors and the acoustic sources were suspended using metal bars and were immersed at a depth of 0.4 m. Sources were driven with white noise and measurements were taken at 26 different ranges r. Each distance from the source to the sensors was measured precisely and it varied from 0.1 m to 1.3 m. A schematic of the experiment is presented in Figure A.4(b).

For each locations, over 10 seconds, the power spectral density is determined and in each third octave band, the squared rms acoustic pressure p_{t}^2 is computed. In each frequency band, if sound pressure level is plotted against r the contribution of the direct and reverberant fields can be observed. In Figure A.5(a) and (b), this is shown for the 0.9-1.1 kHz and 17.9-22.6 kHz frequency bands. This exemplifies a similar trend to Figure A.1. The acoustic field is dominated by the direct field near and source and further away, the reverberant field dominates and the pres-

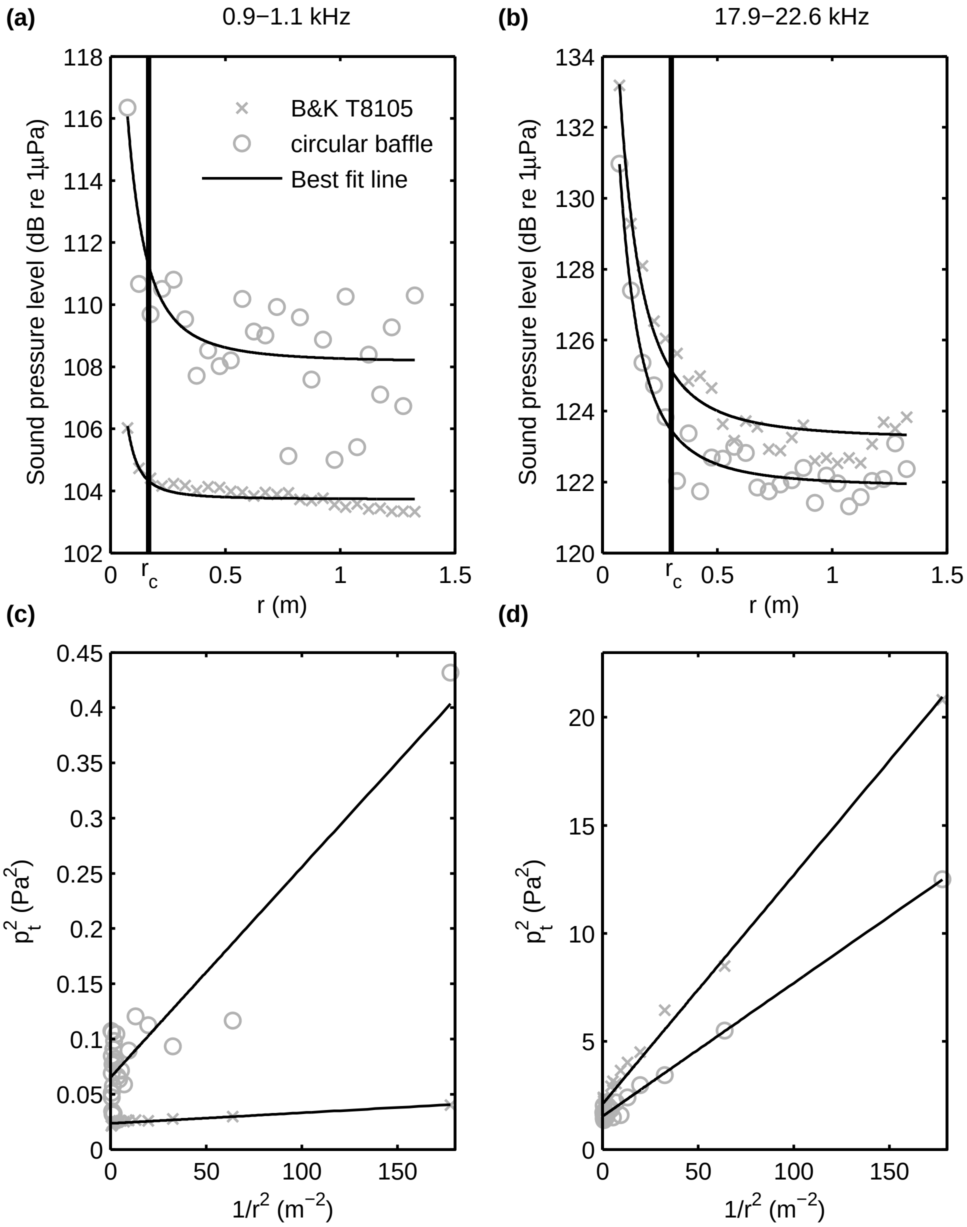

Figure A.5.: Examples of measured sound pressure field in a small enclosure for two sources. (a) and (b): Sound pressure level versus range r in two third octave frequency bands: between 0.9 and 1.1 kHz (a); between 17.9 and 22.6 kHz (b). Cross and circle markers are the measurements at 26 different ranges respectively for the B&K T8105 and circular baffle sources. The solid black lines are the best fits based on Equation A.1 for the measurements. These are computed from the linear fitting between p_{t}^2 and $1/r^2$ (c) and (d). (c) and (d): p_{t}^2 versus $1/r^2$ in two third octave frequency bands: between 0.9 and 1.1 kHz (c); between 17.9 and 22.6 kHz (d). Cross and circle markers are the measurements at 26 different ranges respectively for the B&K T8105 and circular baffle sources. Black solid lines are the linear relationships determined by polynomial fitting based on Equation A.1.

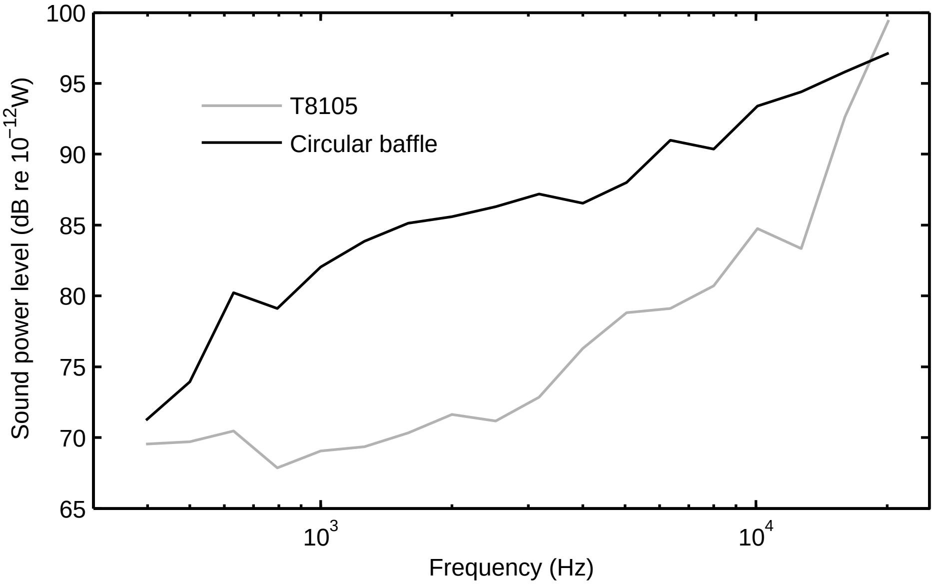

Figure A.6.: Source power in third octave bands. This compares the two sources considered: B&K T8105 hydrophone used as a projector (grey solid line); a circular baffle (15 mm diameter, solid black line).

sure levels off. Furthermore, as explained in section A.1, p_t^2 linearly increases with increasing $1/r^2$ (Equation A.1, see Figure A.1(b)). The gradient of this linear relationship is the squared source output S_o^2 and the y-intercept represent the quantity $S_\mathrm{o}^2 16\pi/A_\mathrm{s}Q_\theta$. Here, measurements in Figure A.5(a) and (b) are plotted against $1/r^2$ in Figure A.5(c) and (d) (in frequency bands 0.9-1.1 kHz and 17.9-22.6 kHz). A linear regression is performed and is represented by the solid black line. This same line is transposed in Figure A.5(a) and (b) with p_t^2 (expressed in sound pressure level) plotted versus r. In Figure A.5(c) and (d), it can be observed that most data points are located around $1/r^2 = 0$. In order to have a good resolution, it is important to have many measurements near the source in order to resolve the linear regression at large $1/r^2$. However, this requires precise measurement of the range r. In the experimental set up, because of technical limitations, good precision of the measurement of distances could not be achieved, especially very near the source. As a result, there is only few data points at large $1/r^2$ (e.g. only one data point at $1/r^2 > 100\,\mathrm{m}^{-2}$).

From the polynomial fitting of the measurements in each frequency band, the source output S_o is determined. This can be used to calculate the acoustic source power in free field W using Equation A.4. For the two sources considered here, W is computed in third octave bands and results are presented in Figure A.6. The quantity W is comparable to the transmitting response to voltage of the projectors. Here, for both sources, the acoustic power emitted increases significantly with frequency.

B. L-curve criterion for Tikhonov and Levenberg-Marquardt methods

In this section, expressions for $\rho^{'}$, $\rho^{''}$, $\xi^{'}$, $\xi^{''}$ as a function of Λ and α (chapter 2) are derived. These are used for the optimization of Λ and α through the L-curve criterion. The matrix problem depicted in Equation 2.2 is considered. The Singular Value Decomposition (SVD) [51] of matrix $\mathbf{A}$ is as:

$$\mathbf{A} = \mathbf{UMV}^t = \sum_{l=1}^{n} \mathbf{u}_l \sigma_l \mathbf{v}_l^t. \tag{B.1}$$

The matrix $\mathbf{M}$ of size $n \times n$ contains the singular values $\sigma_l \; l = 1, \ldots, n$ on its diagonal: $\mathbf{M} = \operatorname{diag}(\sigma_1, \ldots, \sigma_n)$, $\sigma_1 \geq \ldots \geq \sigma_n \geq 0$. The matrices $\mathbf{U}$ and $\mathbf{V}$ of size $n \times n$ contain the left and right singular vectors $\mathbf{u}_l$ and $\mathbf{v}_l$: $\mathbf{U} = (\mathbf{u}_1, \ldots, \mathbf{u}_n)$, $\mathbf{V} = (\mathbf{v}_1, \ldots, \mathbf{v}_n)$.

B.1. Tikhonov regularization

From the SVD formulation, regularization methods can be expressed as a filtered expansion [51, Chap. 4] and for a Tikhonov regularization:

$$\begin{aligned} \mathbf{x}_\alpha &= \sum_{l=1}^{n} \varphi_i^{[\alpha]} \frac{\mathbf{u}_l^t \mathbf{b}}{\sigma_l} \mathbf{v}_l \\ \varphi_l^{[\alpha]} &= \frac{\sigma_l^2}{\sigma_l^2 + \alpha^2} \end{aligned} . \tag{B.2}$$

Using the last formulation, ρ and ξ are as [51]:

$$\begin{aligned}\xi &= \sum_{l=1}^{n}\left(\varphi_l^{[\alpha]}\frac{\mathbf{u}_l^t\mathbf{b}}{\sigma_l}\mathbf{v}_l\right)^2 \\ \rho &= \sum_{l=1}^{n}\left(\left(1-\varphi_l^{[\alpha]}\right)\mathbf{u}_l^t\mathbf{b}\right)^2 + \left\|\mathbf{I}_n - \mathbf{U}\mathbf{U}^t\right\|^2\end{aligned}, \tag{B.3}$$

and the first derivatives with respect to α can be derived:

$$\begin{aligned}\xi^{'} &= -\frac{4}{\alpha}\sum_{l=1}^{n}\left(1-\varphi_l^{[\alpha]}\right)\varphi_l^{[\alpha]2}\frac{\left(\mathbf{u}_l^t\mathbf{b}\right)^2}{\sigma_l^2} \\ \rho^{'} &= -\alpha^2\xi^{'}\end{aligned}. \tag{B.4}$$

The second derivatives are then:

$$\begin{aligned}\xi^{''} &= -\frac{4}{\alpha^2}\sum_{l=1}^{n}\left(1-\varphi_l^{[\alpha]}\right)\left(6\varphi_l^{[\alpha]}-5\right)\varphi_l^{[\alpha]2}\frac{\left(\mathbf{u}_l^t\mathbf{b}\right)^2}{\sigma_l^2} \\ \rho^{''} &= -2\alpha\xi^{'} - \alpha^2\xi^{''}\end{aligned}. \tag{B.5}$$

B.2. Levenberg-Marquardt least square

The Levenberg-Marquardt method depicted in section 2.2 and the SVD of the problem is considered here. Defining the vector $\mathbf{g} = \mathbf{U}^t\hat{\mathbf{b}}$ containing elements g_l, the norm of the solution vector and of the residual (ρ and ξ with Λ) are defined by Lawnson and Hansen [52, Chap. 25]:

$$\begin{aligned}\xi &= \sum_{l=1}^{n}\left(\frac{g_l\sigma_l}{\sigma_l^2+\Lambda^2}\right)^2 \\ \rho &= \sum_{l=1}^{n}\left(\frac{g_l\Lambda^2}{\sigma_l^2+\Lambda^2}\right)^2\end{aligned}, \tag{B.6}$$

and the first and second derivatives are then given by:

$$\begin{aligned} \xi^{'} &= -4 \times \sum_{l=1}^{n} \left(\frac{g_l}{\sigma_l}\right)^2 \times \frac{\Lambda\sigma_l^2}{\left(\sigma_l^2 + \Lambda^2\right)^2} \\ \rho^{'} &= 4 \times \sum_{l=1}^{n} g_l^2 \times \frac{\Lambda\sigma_l^2}{\left(\sigma_l^2 + \Lambda^2\right)^2} \end{aligned} , \tag{B.7}$$

$$\begin{aligned} \xi^{''} &= -4 \times \sum_{l=1}^{n} \left(\frac{g_l}{\sigma_l}\right)^2 \times \sigma_l^2 \times \frac{\left(\sigma_l^2 + \Lambda^2\right)^2 - 4\Lambda^2}{\left(\sigma_l^2 + \Lambda^2\right)^4} \\ \rho^{''} &= 4 \times \sum_{l=1}^{n} g_l^2 \times \sigma_l^2 \times \frac{\left(\sigma_l^2 + \Lambda^2\right)^2 - 4\Lambda^2}{\left(\sigma_l^2 + \Lambda^2\right)^4} \end{aligned} \tag{B.8}$$

C. Probability density functions typical of bubble releases

In this section, expressions for probability density functions used throughout the different chapters are given. These pdf are representative of various bubble releases.

Chi distribution The chi distribution is defined as:

$$P_{\text{chi}}\left(R_0\right) = \frac{R_0^{a_{\text{chi}}-1} e^{R_0/\theta_{\text{chi}}}}{\theta_{\text{chi}}^{a_{\text{chi}}} \Gamma\left(a_{\text{chi}}\right)}, \tag{C.1}$$

with Γ the gamma function. Considering the distribution in Sauter et al. [55], $\theta_{\text{chi}} = 1 \times 10^{-5}$ and $a_{\text{chi}} = 6$.

Lognormal distribution The lognormal distribution is a distribution that only takes positive real values and is controlled by the mean μ_X and the variance σ_X of $\ln\left(X\right)$. Here, the random variable is the bubble equilibrium bubble radius and the probability density function is expressed as:

$$P_{\text{lognormal}}\left(R_0\right) = \frac{1}{R_0 \sigma_X \sqrt{2\pi}} \times e^{-\dfrac{\left(\ln\left(R_0\right) - \mu_X\right)^2}{2\sigma_X^2}}, \tag{C.2}$$

with $\mu_X = -5.5$ and $\sigma_X = 0.5$ in order to build a realistic distribution with a dominant bubble size of 4.1 mm.

Leifer minor 1 distribution The Leifer minor 1[54, Figure 5(a)] is a distribution of bubbles observed from a minor methane seep. The distribution is given by:

$$P_{\text{Leifer minor 1}}\left(R_0\right) = \begin{array}{l} 0.01 \times e^{-\left(\frac{R_0\times 10^6-1878}{344}\right)^2} \\ +0.0019 \times e^{-\left(\frac{R_0\times 10^6-2979}{436}\right)^2} \\ +0.0004 \times e^{-\left(\frac{R_0\times 10^6-4149}{596}\right)^2} \end{array} . \tag{C.3}$$

In order to obtain a probability density function, $P_{\text{Leifer minor 1}}$ is normalised by its area.

Leifer minor 2 distribution The Leifer minor 2[54, Figure 6(a)] is a distribution of bubbles observed from a minor seep. The distribution is given by:

$$P_{\text{Leifer minor 2}}\left(R_0\right) = \begin{array}{l} 0.0046 \times e^{-\left(\frac{R_0\times 10^6-2062}{109}\right)^2} \\ +0.0151 \times e^{-\left(\frac{R_0\times 10^6-2313}{137}\right)^2} \\ +0.0031 \times e^{-\left(\frac{R_0\times 10^6-2735}{303}\right)^2} \end{array} . \tag{C.4}$$

In order to obtain a probability density function, $P_{\text{Leifer minor 2}}$ is normalised by its area.

Leifer mixed distribution The Leifer mixed[54, Figure 7(a)] is a distribution of bubbles observed from a minor methane seep. The distribution is given by:

$$P_{\text{Leifer mixed}}\left(R_0\right) = \begin{array}{l} 0.0027 \times e^{-\left(\frac{R_0\times 10^6-969}{62}\right)^2} \\ +1.63 \times \left(R_0 \times 10^6\right)^{-1.05} \\ +0.0026 \times e^{-\left(\frac{R_0\times 10^6-3889}{860}\right)^2} \end{array} . \tag{C.5}$$

In order to obtain a probability density function, $P_{\text{Leifer mixed}}$ is normalised by its area.

Leifer major distribution The Leifer major[54, Figure 5(b)] is a distribution of bubbles observed from a major methane seep. The distribution is given by:

$$\begin{aligned} P_{\text{Leifer major}}\left(R_0\right) = \quad & 0.05 \times 1000^{2.22} \times \left(R_0 \times 10^6\right)^{-2.22} \\ & +0.02 \times 2000^{0.21} \times \left(R_0 \times 10^6\right)^{-0.21} \\ & +0.0248 \times e^{-\left(\frac{R_0 \times 10^6 - 3262}{329}\right)^2} \\ & +0.006 \times 5000^{2.83} \times \left(R_0 \times 10^6\right)^{-2.83} \end{aligned} \quad . \tag{C.6}$$

In order to obtain a probability density function, $P_{\text{Leifer major}}$ is normalised by its area.

D. Acoustic scattering from rigid spheres

For a sphere, the spherical scattering cross section σ_{sp} (isotropic cross section, no directional dependence) can be defined as $\sigma_{\mathrm{sp}} = 4\pi\sigma_{\mathrm{bs}}$. For a sphere of radius a, in terms of the form function f_∞, the spherical scattering cross section is given by:

$$\sigma_{\mathrm{sp}} = \pi a^2 \left| f_\infty \left(ka \right) \right|^2 . \tag{D.1}$$

In this study, the form function $f_\infty \left(ka \right)$ in the far field ($kr \gg 1$) is resolved using the modal solution [94]:

$$f_\infty(ka) = -\frac{2}{ka} \sum_{l=0}^{\infty} \left(-1 \right)^l \left(2l + 1 \right) \sin\left(\eta_l \right) e^{i\eta_l}, \tag{D.2}$$

with the term η_l being determined as follows:

$$\begin{cases} q_1 = ka\dfrac{c_{\mathrm{l}}}{c_{\mathrm{s_l}}} \\[2ex] q_2 = ka\dfrac{c_{\mathrm{l}}}{c_{\mathrm{s_t}}} \\[2ex] A_2 = \left(l^2 + l - 2\right) j_l\left(q_2\right) + q_2^2\, j_l^{''}\left(q_2\right) \\[2ex] A_1 = 2l\left(l+1\right)\left[q_1\, j_l^{'}\left(q_1\right) - j_l\left(q_1\right)\right] \\[2ex] B_1 = 2\left(\dfrac{\rho_{\mathrm{s}}}{\rho_{\mathrm{l}}}\right)\left(\dfrac{c_{\mathrm{s_t}}}{c_{\mathrm{l}}}\right)^2 \\[2ex] B_2 = 2\left(\dfrac{\rho_{\mathrm{s}}}{\rho_{\mathrm{l}}}\right)\left(\dfrac{c_{\mathrm{s_l}}}{c_{\mathrm{l}}}\right)^2 - B_1 \\[2ex] C_2 = A_2 q_1^2\left[B_2\, j_l\left(q_1\right) - B_1\, j_l^{''}\left(q_1\right)\right] - A_1 B_1\left[j_l\left(q_2\right) - q_2 j_l^{'}\left(q_2\right)\right] \\[2ex] C_1 = ka\left[A_2\, q_1\, j_l^{'}\left(q_1\right) - A_1 j_l\left(q_2\right)\right] \\[2ex] \tan\left(\eta_l\right) = -\dfrac{C_2\, j_l^{'}\left(ka\right) - C_1\, j_l\left(ka\right)}{C_2\, y_l^{'}\left(ka\right) - C_1\, y_l\left(ka\right)} \end{cases} . \tag{D.3}$$

The terms c_{lon} and c_{trans} denote respectively the longitudinal and transverse wave velocities within the sphere and ρ_{s} is the density of the material of the sphere. The quantities j_l and y_l are defined as follow and the $'$and $''$ denote their first and second derivative:

$$\begin{cases} j_l\left(ka\right) = J_{l+1/2}\left(ka\right)\sqrt{\dfrac{\pi}{2ka}} \\[2ex] y_l\left(ka\right) = Y_{l+1/2}\left(ka\right)\sqrt{\dfrac{\pi}{2ka}} \end{cases} , \tag{D.4}$$

where $J_{\mathrm{l+1/2}}$ and $Y_{\mathrm{l+1/2}}$ are Bessel functions of the first and second kind respectively. In terms of the form function described above, the target strength of a rigid sphere TS of radius a is then:

$$\mathrm{TS} = 10\log\left(\frac{\mathrm{a}^2\left|\mathrm{f}_\infty\left(\mathrm{ka}\right)\right|^2}{4}\right) \tag{D.5}$$

E. Table of parameters

Density of free gas at sea level for air ρ_{gA} (kg $\times$ m^{-3})	1.29
Water heat capacity at constant pressure $C_{\mathrm{p,l}}$ (J $\times$ kg^{-1} $\times$ K^{-1})	4.19×10^3
Gas heat capacity at constant pressure $C_{\mathrm{p,g}}$ (J $\times$ kg^{-1} $\times$ K^{-1})	1.01×10^3
Water thermal conductivity λ_{l} (W $\times$ m^{-1} $\times$ K^{-1})	56.3×10^{-2}
Gas thermal conductivity λ_{g} (W $\times$ m^{-1} $\times$ K^{-1})	2.57×10^{-2}
ratio of specific heat of a gas at constant pressure to that at constant volume γ	1.4
Gas molecular weight (g $\times$ mol^{-1})	28.97
Gas sound speed c_{g} (m $\times$ s)	353
Water salinity S_{l} (parts per thousand)	35
Temperature T_{l} (°C)	10

Table E.1.: Summary of parameters used for the computation of the various examples presented in chapter 3.

Water heat capacity at constant pressure $C_{\mathrm{p,l}}$ (J $\times$ kg^{-1} $\times$ K^{-1})	4.19×10^3
Gas heat capacity at constant pressure $C_{\mathrm{p,g}}$ (J $\times$ kg^{-1} $\times$ K^{-1})	1.01×10^3
Water thermal conductivity λ_{l} (W $\times$ m^{-1} $\times$ K^{-1})	56.3×10^{-2}
Gas thermal conductivity λ_{g} (W $\times$ m^{-1} $\times$ K^{-1})	2.57×10^{-2}
ratio of specific heat of a gas at constant pressure to that at constant volume γ	1.4
Gas molecular weight (g $\times$ mol^{-1})	14.01
Gas sound speed c_{g} (m $\times$ s)	349
Water salinity S_{l} (parts per thousand)	0
Temperature T_{l} (°C)	10

Table E.2.: Summary of parameters used for the calculations in chapter 4

Water heat capacity at constant pressure $C_{\mathrm{p,l}}$ (J $\times$ kg^{-1} $\times$ K^{-1})	4.19×10^3
Gas heat capacity at constant pressure $C_{\mathrm{p,g}}$ (J $\times$ kg^{-1} $\times$ K^{-1})	0.83×10^3
Water thermal conductivity λ_{l} (W $\times$ m^{-1} $\times$ K^{-1})	56.3×10^{-2}
Gas thermal conductivity λ_{g} (W $\times$ m^{-1} $\times$ K^{-1})	1.59×10^{-2}
ratio of specific heat of a gas at constant pressure to that at constant volume γ	1.4
Gas molecular weight (g $\times$ mol^{-1})	44.01
Gas sound speed c_{g} (m $\times$ s)	259
Water salinity S_{l} (parts per thousand)	34
Temperature T_{l} (°C)	11

Table E.3.: Summary of parameters used for the calculations in chapter 5

Gas sound speed c_{g} (m × s)	353
Gas density ρ_{g} (kg × m^{-3})	1.2
Water salinity S_{l} (parts per thousand)	35
Temperature T_{l} (°C)	10
depth z (m)	80

Table E.4.: Summary of parameters used for the calculations in chapter 6

Gas sound speed c_{g} (m × s)	446
Gas density ρ_{g} (kg × m^{-3})	1.2
Water salinity S_{l} (parts per thousand)	35
Temperature T_{l} (°C)	5

Table E.5.: Summary of parameters used for the calculations in chapter 7

Bibliography

[1] T. G. Leighton, *The acoustic bubble.* London: Academic Press, 1994.

[2] M. A. Ainslie and T. G. Leighton, "Near resonant bubble acoustic cross-section corrections, including examples from oceanography, volcanology, and biomedical ultrasound.," *The Journal of the Acoustical Society of America*, vol. 126, pp. 2163–75, Nov. 2009.

[3] M. A. Ainslie and T. G. Leighton, "Review of scattering and extinction cross-sections, damping factors, and resonance frequencies of a spherical gas bubble," *Journal of the Acoustical Society of America*, vol. 130, no. 5, pp. 3184–3208, 2011.

[4] Det Norske Veritas, "Selection and use of subsea leak detection systems," tech. rep., Recommended Practice DNV-RP-F302, 2010.

[5] IPCC, *Working group I. Climate Change 2013: The Physical Science Basis. Contribution of the Fifth Assessment Report of the Intergovernmental Panel on Climate Change.* Cambridge, United Kingdom and New York, NY, USA: Cambridge University Press, 2013.

[6] T. Stocker, D. Qin, G.-K. Plattner, L. Alexander, S. Allen, N. Bindoff, F.-M. Bréon, J. Church, U. Cubasch, S. Emori, P. Forster, P. Friedlingstein, N. Gillett, J. Gregory, D. Hartmann, E. Jansen, B. Kirtman, R. Knutti, K. Krishna Kumar, P. Lemke, J. Marotzke, V. Masson-Delmotte, G. Meehl, I. Mokhov, S. Piao, V. Ramaswamy, D. Randall, M. Rhein, M. Rojas, C. Sabine, D. Shindell, L. Talley, D. Vaughan, and S.-P. Xie, "2013: Technical summary," in *Climate Change 2013: The Physical Science Basis. Contribution of Working Group I to the Fifth Assessment Report of the Intergovernmental Panel on Climate Change* (T. Stocker, D. Qin, G.-K. Plattner, M. Tignor, S. Allen, J. Boschung, A. Nauels, Y. Xia, V. Bex, and P. Midgley, eds.), pp. 33–115, Cambridge, United Kingdom and New York, NY, USA: Cambridge University Press, 2013.

[7] M. Collins, R. Knutti, J. Arblaster, J.-L. Dufresne, T. Fichefet, P. Friedlingstein, X. Gao, W. Gutowski, T. Johns, G. Krinner, M. Shongwe, C. Tebaldi, A. Weaver, and M. Wehner, “2013: Long-term climate change: projections, commitments and irreversibility,” in *Climate Change 2013: The Physical Science Basis. Contribution of Working Group I to the Fifth Assessment Report of the Intergovernmental Panel on Climate Change* (T. Stocker, D. Qin, G.-K. Plattner, M. Tignor, S. Allen, J. Boschung, A. Nauels, Y. Xia, V. Bex, and P. Midgley, eds.), pp. 1029–1136, Cambridge, United Kingdom and New York, NY, USA: Cambridge University Press, 2013.

[8] IPCC, *Working Group III. Climate Change 2014: Mitigation of Climate Change. Contribution of the Fifth Assessment Report of the Intergovernmental Panel on Climate Change.* Cambridge, United Kingdom and New York, NY, USA: Cambridge University Press, 2014.

[9] T. Bruckner, A. B. Igor, Y. Mulugetta, H. Chum, A. de la Vega Navarro, J. Edmonds, A. Faaij, B. Fungtammasan, A. Garg, E. Hertwich, D. Honnery, D. Infield, M. Kainuma, S. Khennas, S. Kim, H. Nimir, K. Riahi, N. Strachan, R. Wiser, and X. Zhang, “Energy systems,” in *Climate change 2014: mitigation of climate change* (O. Edenhofer, R. Pichs-Madruga, Y. Sokona, E. Arahani, S. Kadner, K. Seyboth, A. Adler, I. Baum, S. Brunner, P. Eickemeier, B. Kriemann, J. Savolainen, S. Schlömer, C. Von, T. Z. Stechow, and J. Minx, eds.), ch. 7, pp. 1–137, Cambridge, United Kingdom and New York, NY, USA: Cambridge University Press, 2014.

[10] IPCC, *2005: IPCC Special Report on Carbon Dioxide Capture and Storage. Prepared by Working Group III of the Intergovernmental Panel on Climate Change.* Cambridge, United Kingdom and New York, NY, USA: Cambridge University Press, 2005.

[11] R. Monastersky, “Seabed scars raise questions over carbon-storage plan.,” *Nature*, vol. 504, pp. 339–40, Dec. 2013.

[12] R. Van Noorden, “Carbon sequestration: Buried trouble.,” *Nature*, vol. 463, pp. 871–3, Feb. 2010.

[13] UK CCS Policies, *Increasing the use of low-carbon technologies: Carbon capture and storage (CCS).* date accessed: 28 August 2014, https://www.gov.uk/government/policies/increasing-the-use-of-low-carbon-technologies/supporting-pages/carbon-capture-and-storage-ccs, 2014.

[14] O. Eiken, P. Ringrose, C. Hermanrud, B. Nazarian, T. A. Torp, and L. Hø ier, "Lessons learned from 14 years of CCS operations: Sleipner, In Salah and Snøhvit," *Energy Procedia*, vol. 4, pp. 5541–5548, Jan. 2011.

[15] R. Sugisaki, "Deep-seated gas emission induced by the Earth tide: a basic observation for geochemical earthquake prediction.," *Science*, vol. 212, pp. 1264–6, June 1981.

[16] J. Hartmann and J. K. Levy, "Hydrogeological and Gasgeochemical Earthquake Precursors ? A Review for Application," *Natural Hazards*, vol. 34, pp. 279–304, Mar. 2005.

[17] L. F. Khilyuk, G. V. Chilingarian, B. Endres, and J. O. R. Jr., *Gas Migration: Events Preceding Earthquakes (Petroleum Engineering)*. Gulf Publishing, 2000.

[18] K. M. Lee, P. S. Wilson, and E. C. Pettit, "Underwater sound radiated by bubbles released by melting glacier ice," in *Proceedings of Meetings on Acoustics*, vol. 20, pp. 1–11, Acoustical Society of America, Feb. 2014.

[19] J. Tegowski, G. B. Deane, P. Blondel, O. Glowacki, and M. Moskalik, "An Acoustical Study of Gas Bubbles Escaping from Melting Growlers," in *UA2014 - 2nd International Conference and Exhibition on Underwater Acoustics*, (23-27 June 2014, Rhodes, Greece), pp. 137–142, 2014.

[20] G. K. Westbrook, K. E. Thatcher, E. J. Rohling, A. M. Piotrowski, H. Pälike, A. H. Osborne, E. G. Nisbet, T. a. Minshull, M. Lanoisellé, R. H. James, V. Hühnerbach, D. Green, R. E. Fisher, A. J. Crocker, A. Chabert, C. Bolton, A. Beszczynska-Möller, C. Berndt, and A. Aquilina, "Escape of methane gas from the seabed along the West Spitsbergen continental margin," *Geophysical Research Letters*, vol. 36, p. L15608, Aug. 2009.

[21] A. G. Judd, "The global importance and context of methane escape from the seabed," *Geo-Marine Letters*, vol. 23, no. 3-4, pp. 147–154, 2003.

[22] D. K. Woolf and S. Thorpe, "Bubbles and the air-sea exchange of gases in near-saturation conditions," *Journal of Marine Research*, vol. 49, no. 3, pp. 435–466, 1991.

[23] I. M. Brooks, M. J. Yelland, R. C. Upstill-Goddard, P. D. Nightingale, S. Archer, E. D'Asaro, R. Beale, C. Beattie, B. Blomquist, A. A. Bloom, B. J. Brooks, J. Cluderay, D. Coles, J. Dacey, M. DeGrandpre, J. Dixon,

W. M. Drennan, J. Gabriele, L. Goldsen, N. Hardman-Mountford, M. K. Hill, M. Horn, P.-C. Hsueh, B. Huebert, G. de Leeuw, T. G. Leighton, M. Liddicot, J. J. N. Lingard, C. McNeil, J. B. McQuaid, B. I. Moat, G. Moore, C. Neill, S. J. Norris, S. O'Doherty, R. W. Pascal, J. Prytherch, M. Rebozo, E. Sahlee, M. Salter, U. Schuster, I. Skjelvan, H. Slagter, M. H. Smith, P. D. Smith, M. Srokosz, J. A. Stephens, P. K. Taylor, M. Telszewski, R. Walsh, B. Ward, D. K. Woolf, D. Young, and H. Zemmelink, "Physical exchanges at the air-sea interface: UK-SOLAS Field Measurements," *Bulletin of the American Meteorological Society*, vol. 90, pp. 629–644, May 2009.

[24] D. Archer, "Methane hydrate stability and anthropogenic climate change," *Biogeosciences*, vol. 4, pp. 521–544, July 2007.

[25] A. D. McGuire, F. Chapin, J. E. Walsh, and C. Wirth, "Integrated Regional Changes in Arctic Climate Feedbacks: Implications for the Global Climate System," *Annual Review of Environment and Resources*, vol. 31, pp. 61–91, Nov. 2006.

[26] M. Rhein, S. Rintoul, S. Aoki, E. Campos, D. Chambers, R. Feely, S. Gulev, G. Johnson, S. Josey, A. Kostianoy, C. Mauritzen, D. Roemmich, L. Talley, and F. Wang, "2013: Observations: Ocean," in *Climate Change 2013: The Physical Science Basis. Contribution of Working Group I to the Fifth Assessment Report of the Intergovernmental Panel on Climate Change* (T. Stocker, D. Qin, G.-K. Plattner, M. Tignor, S. Allen, J. Boschung, A. Nauels, Y. Xia, V. Bex, and P. Midgley, eds.), pp. 255–315, Cambridge, United Kingdom and New York, NY, USA: Cambridge University Press, 2013.

[27] P. Ciais, C. Sabine, G. Bala, L. Bopp, V. Brovkin, J. Canadell, A. Chhabra, R. DeFries, J. Galloway, M. Heimann, C. Jones, C. Le Quéré, R. Myneni, S. Piao, and P. Thornton, "2013: Carbon and Other Biogeochemical Cycles," in *Climate Change 2013: The Physical Science Basis. Contribution of Working Group I to the Fifth Assessment Report of the Intergovernmental Panel on Climate Change* (T. Stocker, D. Qin, G.-K. Plattner, M. Tignor, S. Allen, J. Boschung, A. Nauels, Y. Xia, V. Bex, and P. Midgley, eds.), pp. 465–570, Cambridge, United Kingdom and New York, NY, USA: Cambridge University Press, 2013.

[28] J. Schneider von Deimling, J. Greinert, N. R. Chapman, W. Rabbel, and P. Linke, "Acoustic imaging of natural gas seepage in the North Sea: Sensing

bubbles under control of variable currents," *Limnology and Oceanography: Methods*, vol. 8, pp. 155–171, June 2010.

[29] I. Leifer and J. Boles, "Turbine tent measurements of marine hydrocarbon seeps on subhourly timescales," *Journal of Geophysical Research*, vol. 110, no. C1, p. C01006, 2005.

[30] M. Torres, J. McManus, D. Hammond, M. de Angelis, K. Heeschen, S. Colbert, M. Tryon, K. Brown, and E. Suess, "Fluid and chemical fluxes in and out of sediments hosting methane hydrate deposits on Hydrate Ridge, OR, I: Hydrological provinces," *Earth and Planetary Science Letters*, vol. 201, pp. 525–540, Aug. 2002.

[31] K. Heeschen, R. Collier, M. de Angelis, P. Linke, E. Suess, and G. Klinkhammer, "Methane sources, distributions, and fluxes from cold vent sites at Hydrate Ridge, Cascadia Margin," *Global Biogeochemical Cycles*, vol. 19, p. GB2016, July 2005.

[32] S.-K. Hsu, S.-Y. Wang, Y.-C. Liao, T. F. Yang, S. Jan, J.-Y. Lin, and S.-C. Chen, "Tide-modulated gas emissions and tremors off SW Taiwan," *Earth and Planetary Science Letters*, vol. 369-370, pp. 98–107, May 2013.

[33] J. Greinert, "Monitoring temporal variability of bubble release at seeps : The hydroacoustic swath system GasQuant," *Journal of geophysical research*, vol. 113, no. C7, pp. 1–20, 2008.

[34] J. R. Boles, J. F. Clark, I. Leifer, and L. Washburn, "Temporal variation in natural methane seep rate due to tides, Coal Oil Point area, California," *Journal of Geophysical Research*, vol. 106, no. C11, p. 27077, 2001.

[35] K. Heeschen, A. Trehu, R. Collier, E. Suess, and G. Rehder, "Distribution and height of methane bubble plumes on the Cascadia Margin characterized by acoustic imaging," *Geophysical Research Letters*, vol. 30, p. 1643, June 2003.

[36] C. Berndt, T. Feseker, T. Treude, S. Krastel, V. Liebetrau, H. Niemann, V. J. Bertics, I. Dumke, K. Dünnbier, B. Ferré, C. Graves, F. Gross, K. Hissmann, V. Hühnerbach, S. Krause, K. Lieser, J. Schauer, and L. Steinle, "Temporal constraints on hydrate-controlled methane seepage off Svalbard.," *Science*, vol. 343, pp. 284–287, Jan. 2014.

[37] J. S. Hornafius, D. Quigley, and B. P. Luyendyk, “The world’s most spectacular marine hydrocarbon seeps (Coal Oil Point, Santa Barbara Channel, California): Quantification of emissions,” *Journal of Geophysical Research-Oceans*, vol. 104, no. C9, pp. 20703–20711, 1999.

[38] A. Nikolovska and J. J. Schanze, “Acoustic methane seepage quantification model design, experiments and deep-sea application,” in *OCEANS 2007-Europe*, (Aberdeen, 18-21 June 2007), pp. 1–6, IEEE-Institute of Electrical and Electronic Engineers.

[39] I. Ostrovsky, “Methane bubbles in Lake Kinneret: Quantification and temporal and spatial heterogeneity,” *Limnology and oceanography*, vol. 48, no. 3, pp. 1030–1036, 2003.

[40] I. Ostrovsky, D. F. Mcginnis, L. Lapidus, and W. Eckert, “Quantifying gas ebullition with echosounder: the role of methane transport by bubbles in a medium-sized lake,” *Limnology and Oceanography: Methods*, vol. 6, pp. 105–118, 2008.

[41] C. Caudron, A. Mazot, and A. Bernard, “Carbon dioxide dynamics in Kelud volcanic lake,” *Journal of Geophysical Research*, vol. 117, p. B05102, May 2012.

[42] J. Greinert and B. Nutzel, “Hydroacoustic experiments to establish a method for the determination of methane bubble fluxes at cold seeps,” *Geo-Marine Letters*, vol. 24, pp. 75–85, May 2004.

[43] E. J. Simmonds and D. N. MacLennan, *Fisheries acoustics : theory and practice*. No. 10, Oxford ; Ames, Iowa: Blackwell Science, 2nd ed., 2005.

[44] X. Lurton, *An Introduction to Underwater Acoustics: Principles and Applications*. Springer, 2010.

[45] G. Bayrakci, C. Scalabrin, S. Dupré, I. Leblond, J.-B. Tary, N. Lanteri, J.-M. Augustin, L. Berger, E. Cros, A. Ogor, C. Tsabaris, M. Lescanne, and L. Géli, “Acoustic monitoring of gas emissions from the seafloor. Part II: a case study from the Sea of Marmara,” *Marine Geophysical Research*, vol. 35, pp. 211–229, June 2014.

[46] I. Leblond, C. Scalabrin, and L. Berger, “Acoustic monitoring of gas emissions from the seafloor. Part I: quantifying the volumetric flow of bubbles,” *Marine Geophysical Research*, vol. 35, pp. 191–210, June 2014.

[47] I. C. Wright, “Cruise report No. 13, RRS james Clark Ross Cruise 253, Arctic methane hydrates,” tech. rep., 2012.

[48] H. Sahling, B. Bergès, J. Boelmann, W. Dimmler, P. Geprägs, M. Glockzin, S. Kaboth, N. Nowald, T. Pape, M. Römer, C. dos Santos Fereirra, L. Schroedter, and M. Tomczyk, “R/V Heincke cruise report HE-387, Gas emissions at the Svalbard continental margin. Longyearbyen - Bremerhaven, 20 August - 16 September 2012,” tech. rep., Zentrum für Marine Umweltwissenschaften, Fachbereich Geowissenschaften, Universität Bremen, Bremen, 2012.

[49] H. Sahling, M. Römer, T. Pape, B. Bergès, C. dos Santos Fereirra, J. Boelmann, P. Geprägs, M. Tomczyk, N. Nowald, W. Dimmler, L. Schroedter, M. Glockzin, and G. Bohrmann, “Gas emissions at the continental margin west off Svalbard: mapping, sampling, and quantification,” *Biogeosciences*, vol. 11, pp. 6029–6046, May 2014.

[50] J. Blackford and J. Kita, “A Novel Experimental Release of CO2 in the Marine Environment to Aid Monitoring and Impact Assessment,” *Energy Procedia*, vol. 37, pp. 3387–3393, 2013.

[51] P. C. Hansen, *Discrete Inverse Problems: Insight and Algorithms (Fundamentals of Algorithms)*. SIAM-Society for Industrial and Applied Mathematics, 2010.

[52] C. L. Lawson and R. J. Hanson, *Solving Least Squares Problems (Classics in Applied Mathematics)*. Society for Industrial and Applied Mathematics, 1987.

[53] P. C. Hansen and D. P. O Leary, “The Use of the L-Curve in the Regularization of Discrete Ill-Posed Problems,” *SIAM Journal on Scientific Computing*, vol. 14, pp. 1487–1503, Nov. 1993.

[54] I. Leifer and D. Culling, “Formation of seep bubble plumes in the Coal Oil Point seep field,” *Geo-Marine Letters*, vol. 30, pp. 339–353, Feb. 2010.

[55] E. J. Sauter, S. I. Muyakshin, J.-L. Charlou, M. Schlüter, A. Boetius, K. Jerosch, E. Damm, J.-P. Foucher, and M. Klages, “Methane discharge from a deep-sea submarine mud volcano into the upper water column by gas hydrate-coated methane bubbles,” *Earth and Planetary Science Letters*, vol. 243, pp. 354–365, Mar. 2006.

[56] A. Doicu, T. R. Trautmann, and F. Schreier, *Numerical regularization for atmospheric inverse problems*. Springer, 2010.

[57] N. R. Chapman, “Inverse Problems in Underwater Acoustics,” in *Handbook of Signal Processing in Acoustics*, pp. 1723–1735, Springer New York, 2008.

[58] M. I. Taroudakis and G. Makrakis, *Inverse Problems in Underwater Acoustics*. Springer New York, 2001.

[59] P. C. Hansen, *Rank-Deficient and Discrete Ill-Posed Problems: Numerical Aspects of Linear Inversion*. SIAM-Society for Industrial and Applied Mathematics, 1999.

[60] C. F. Greenlaw and R. K. Johnson, “Multiple-frequency Acoustical Estimation,” *Biological Oceanography*, vol. 2, pp. 227–252, 1983.

[61] T. G. Leighton and P. R. White, “Quantification of undersea gas leaks from carbon capture and storage facilities, from pipelines and from methane seeps, by their acoustic emissions,” *Proceedings of the Royal Society a-Mathematical Physical and Engineering Sciences*, vol. 468, no. 2138, pp. 485–510, 2012.

[62] A. Lebourges-Dhaussy and J. Ballé-Béganton, “Multifrequency multimodel zooplankton classification,” *ICES CM*, vol. 22, no. R:22, 2004.

[63] D. Holliday and R. Pieper, “Bioacoustical oceanography at high frequencies,” *ICES Journal of Marine Science*, vol. 52, pp. 279–296, Aug. 1995.

[64] J. Horne and J. M. Jech, “Multi-frequency estimates of fish abundance: constraints of rather high frequencies,” *ICES Journal of Marine Science*, vol. 56, pp. 184–199, Apr. 1999.

[65] A. Lebourges-Dhaussy, “Caractérisation des populations planctoniques par acoustique multifréquence,” *Océnis*, vol. 22, no. 1, pp. 71–92, 1996.

[66] D. V. Holliday, “Extracting bio-physical information from the acoustic signatures of marine organisms,” in *Oceanic sound scattering prediction*, pp. 619–624, Plenum Press, 1977.

[67] C. Greenlaw, “Acoustical estimation of zooplankton populations,” *Limnol. Oceanogr.*, vol. 24, no. 2, pp. 226–242, 1979.

[68] C. F. Greenlaw, “TAPS web page.”

[69] J. R. Lovett, “Merged seawater sound-speed equations,” *The Journal of the Acoustical Society of America*, vol. 63, p. 1713, June 1978.

[70] G. Siedler and H. Peters, "Physical properties of sea water," in *Numerical Data and Functional Relationships in Science and Technology* (J. Sündermann, ed.), vol. 3a of *Landolt-Börnstein - Group V Geophysics*, pp. 237–259, Springer Berlin Heidelberg, 1986.

[71] C. S. Clay and H. Medwin, *Acoustical Oceanography: Principles and Applications*. New York: John Wiley & Sons, 1977.

[72] T. G. Leighton and A. J. Walton, "An experimental study of the sound emitted from gas bubbles in a liquid," *European Journal of Physics*, vol. 8, pp. 98–104, 1987.

[73] G. E. Updegraff and V. C. Anderson, "Bubble noise and wavelet spills recorded 1 m below the ocean surface," *The Journal of the Acoustical Society of America*, vol. 89, no. 5, pp. 2264–2279, 1991.

[74] T. G. Leighton, P. R. White, and M. F. Schneider, "The detection and dimension of bubble entrainment and comminution," *Journal of the Acoustical Society of America*, vol. 103, no. 4, pp. 1825–35, 1998.

[75] I. Leifer and D. Tang, "The acoustic signature of marine seep bubbles," *The Journal of the Acoustical Society of America*, vol. 121, no. 1, pp. EL35–EL40, 2007.

[76] M. Minnaert, "On musical air-bubbles and the sounds of running water," *Philosophical Magazine Series 7*, vol. 16, no. 104, pp. 235–248, 1933.

[77] A. Prosperetti, "Thermal effects and damping mechanisms in the forced radial oscillations of gas bubbles in liquids," *The Journal of the Acoustical Society of America*, vol. 61, no. 1, pp. 17–27, 1977.

[78] H. Medwin, "Counting bubbles acoustically: a review," *Ultrasonics*, vol. 15, pp. 7–13, Jan. 1977.

[79] S. Vagle and D. M. Farmer, "The Measurement of Bubble-Size Distributions by Acoustical Backscatter," *Journal of Atmospheric and Oceanic Technology*, vol. 9, no. 5, pp. 630–644, 1992.

[80] H. Medwin, "Acoustical determinations of bubble-size spectra," *The Journal of the Acoustical Society of America*, vol. 62, p. 1041, Oct. 1977.

[81] Y. Zhang and S. C. Li, "Notes on radial oscillations of gas bubbles in liquids: thermal effects.," *The Journal of the Acoustical Society of America*, vol. 128, pp. EL306–EL309, Nov. 2010.

[82] G. B. Deane and M. D. Stokes, “The acoustic excitation of air bubbles fragmenting in sheared flow,” *Journal of the Acoustical Society of America*, vol. 124, no. 6, pp. 3450–3463, 2008.

[83] H. C. Pumphrey and A. J. Walton, “Experimental study of the sound emitted by water drops impacting on a water surface,” *European Journal of Physics*, vol. 9, pp. 225–231, July 1988.

[84] H. Medwin and M. M. Beaky, “Bubble sources of the Knudsen sea noise spectra,” *The Journal of the Acoustical Society of America*, vol. 86, p. 1124, Sept. 1989.

[85] H. C. Pumphrey and L. A. Crum, “Free oscillations of near-surface bubbles as a source of the underwater noise of rain,” *The Journal of the Acoustical Society of America*, vol. 87, p. 142, Jan. 1990.

[86] G. B. Deane and M. Dale Stokes, “The acoustic signature of bubbles fragmenting in sheared flow,” *The Journal of the Acoustical Society of America*, vol. 120, p. EL84, Nov. 2006.

[87] T. G. Leighton, K. J. Fagan, and J. E. Field, “Acoustic and photographic studies of injected bubbles,” *European Journal of Physics*, vol. 12, pp. 77–85, 1991.

[88] M. R. Loewen and W. K. Melville, “A model of the sound generated by breaking waves,” *The Journal of the Acoustical Society of America*, vol. 90, no. 4, pp. 2075–2080, 1991.

[89] G. B. Deane and H. Czerski, “A mechanism stimulating sound production from air bubbles released from a nozzle,” *Journal of the Acoustical Society of America*, vol. 123, no. 6, pp. EL126–EL132, 2008.

[90] T. G. Leighton, “How can humans, in air, hear sound generated underwater (and can goldfish hear their owners talking)?,” *The Journal of the Acoustical Society of America*, vol. 131, pp. 2539–42, Mar. 2012.

[91] H. Medwin and C. S. Clay, *Fundamentals of Acoustical Oceanography.* Boston: Academic Press Inc, 1998.

[92] T. K. Stanton, “Simple Approximate Formulas for Backscattering of Sound by Spherical and Elongated Objects,” *Journal of the Acoustical Society of America*, vol. 86, no. 4, pp. 1499–1510, 1989.

[93] R. J. Urick, *Principles of Underwater Sound 3rd Edition.* Peninsula Pub, 1996.

[94] D. MacLennan, “The Theory of Solid Spheres as Sonar Calibration Targets,” *Scottish Fisheries Research Report*, no. 22, 1981.

[95] T. K. Stanton, “Sound Scattering by Spherical and Elongated Shelled Bodies,” *Journal of the Acoustical Society of America*, vol. 88, no. 3, pp. 1619–1633, 1990.

[96] R. Thuraisingham, “New expressions of acoustic cross-sections of a single bubble in the monopole bubble theory,” *Ultrasonics*, vol. 35, pp. 407–409, Aug. 1997.

[97] R. K. Johnson, “Sound scattering from a fluid sphere revisited,” *The Journal of the Acoustical Society of America*, vol. 61, p. 375, Feb. 1977.

[98] J. J. Faran, “Sound Scattering by Solid Cylinders and Spheres,” *The Journal of the Acoustical Society of America*, vol. 23, p. 405, July 1951.

[99] V. C. Anderson, “Sound Scattering from a Fluid Sphere,” *The Journal of the Acoustical Society of America*, vol. 22, p. 426, July 1950.

[100] C. Feuillade and C. S. Clay, “Anderson (1950) revisited,” *The Journal of the Acoustical Society of America*, vol. 106, p. 553, Aug. 1999.

[101] C. Feuillade, “Animations for visualizing and teaching acoustic impulse scattering from spheres,” *The Journal of the Acoustical Society of America*, vol. 115, p. 1893, May 2004.

[102] R. Clift, J. R. Grace, and M. E. Weber, *Bubbles, Drops, and Particles.* Academic Press, 1978.

[103] Z. Ye, “Low-frequency acoustic scattering by gas-filled prolate spheroids in liquids,” *The Journal of the Acoustical Society of America*, vol. 101, p. 1945, Apr. 1997.

[104] Z. Ye, “Low-frequency acoustic scattering by gas-filled prolate spheroids in liquids. II. Comparison with the exact solution,” *The Journal of the Acoustical Society of America*, vol. 103, p. 822, Feb. 1998.

[105] C. Feuillade, “Resonances of deformed gas bubbles in liquids,” *The Journal of the Acoustical Society of America*, vol. 96, p. 3684, Dec. 1994.

[106] T. Okumura, T. Masaya, T. Yoshimi, and S. Kouichi, “Acoustic scattering by an arbitrarily shaped body: an application of the boundary-element method,” *ICES Journal of Marine Science*, vol. 60, pp. 563–570, June 2003.

[107] C. A. Greene and P. S. Wilson, “Laboratory investigation of a passive acoustic method for measurement of underwater gas seep ebullition,” *Journal of the Acoustical Society of America*, vol. 131, no. 1, pp. EL61–EL66, 2012.

[108] C. A. Greene and P. S. Wilson, *Low-Frequency Acoustic Classification of Methane Hydrates.* PhD thesis, 2010.

[109] A. Nikolovska and C. Waldmann, “Passive acoustic quantification of underwater gas seepage,” in *OCEANS 2006*, (Boston, 18-21 Sept. 2006), pp. 1–6, IEEE-Institute of Electrical and Electronic Engineers.

[110] T. G. Leighton, D. G. Ramble, and A. D. Phelps, “The detection of tethered and rising bubbles using multiple acoustic techniques,” *The Journal of the Acoustical Society of America*, vol. 101, pp. 2626–2635, May 1997.

[111] H. Czerski, “A candidate mechanism for exciting sound during bubble coalescence,” *Journal of the Acoustical Society of America*, vol. 129, no. 3, pp. EL83–EL88, 2011.

[112] H. Czerski and G. B. Deane, “The effect of coupling on bubble fragmentation acoustics,” *Journal of the Acoustical Society of America*, vol. 129, no. 1, pp. 74–84, 2011.

[113] A. D. Pierce, *Acoustics: an Introduction to Its Physical Principles and Applications.* American Institute of Physics, 1989.

[114] R. A. Hazelwood and S. P. Robinson, “Underwater acoustic power measurements in reverberant fields,” in *OCEANS 2007 - Europe*, (Aberdeen, 18-21 June 2007), pp. 1–6, IEEE-Institute of Electrical and Electronic Engineers.

[115] T. G. Leighton, P. R. White, C. L. Morfey, J. W. L. Clarke, G. J. Heald, H. A. Dumbrell, and K. R. Holland, “The effect of reverberation on the damping of bubbles,” *Journal of the Acoustical Society of America*, vol. 112, no. 4, pp. 1366–1376, 2002.

[116] T. G. Leighton, D. G. Ramble, A. D. Phelps, C. L. Morfey, and P. P. Harris, “Acoustic detection of gas bubbles in a pipe,” *Acta Acustica united with Acustica*, vol. 84, no. 5, pp. 801–814, 1998.

[117] T. G. Leighton, K. Baik, and J. Jiang, “The use of acoustic inversion to estimate the bubble size distribution in pipelines,” *Proceedings of The Royal Society A Mathematical Physical and Engineering Sciences*, vol. 468, pp. 2461–2484, Sept. 2012.

[118] T. G. Leighton, P. R. White, and D. C. Finfer, “The sounds of seas in space,” in *Proceedings of the International Conference on Underwater Acoustic Measurements, Technologies and Results*, (Heraklion, Crete, Greece, 28 June-1 July 2005), pp. 833–40.

[119] T. G. Leighton and G. B. N. Robb, “Preliminary mapping of void fractions and sound speeds in gassy marine sediments from subbottom profiles,” *Journal of the Acoustical Society of America*, vol. 124, no. 5, pp. EL313–EL320, 2008.

[120] T. Leighton, “A method for estimating sound speed and the void fraction of bubbles from sub-bottom sonar images of gassy seabeds,” *ISVR technical report*, vol. 320, pp. 1–21, Dec. 2007.

[121] T. G. Leighton, “Theory for acoustic propagation in marine sediment containing gas bubbles which may pulsate in a non-stationary nonlinear manner,” *Geophys. Res. Lett.*, vol. 34, no. 17, p. L17607, 2007.

[122] *QICS webpage.* date accessed: 29 August 2014, http://www.bgs.ac.uk/qics/.

[123] J. Blackford, H. Stahl, J. M. Bull, B. J. P. Bergès, M. Cevatoglu, A. Lichtschlag, D. Connelly, R. H. James, J. Kita, D. Long, M. Naylor, K. Shitashima, D. Smith, P. Taylor, I. Wright, M. Akhurst, B. Chen, T. M. Gernon, C. Hauton, M. Hayashi, H. Kaieda, T. G. Leighton, T. Sato, M. D. J. Sayer, M. Suzumura, K. Tait, M. E. Vardy, P. R. White, and S. Widdicombe, “Detection and impacts of leakage from sub-seafloor deep geological carbon dioxide storage,” *Nature Climate Change*, vol. 4, pp. 1011–1016, Sept. 2014.

[124] P. Taylor, H. Stahl, M. E. Vardy, J. M. Bull, M. Akhurst, C. Hauton, R. H. James, A. Lichtschlag, D. Long, D. Aleynik, M. Toberman, M. Naylor, D. Connelly, D. Smith, M. D. Sayer, S. Widdicombe, I. C. Wright, and J. Blackford, “A novel sub-seabed CO2 release experiment informing monitoring and impact assessment for geological carbon storage,” *International Journal of Greenhouse Gas Control*, vol. in press, Oct. 2014.

[125] J. Gordon and S. Northridge, “Potential impacts of Acoustic Deterrent Devices

on Scottish Marine Wildlife," tech. rep., Scottish Natural Heritage Commissioned Report F01AA404, 2002.

[126] M. Cevatoglu, J. M. Bull, M. E. Vardy, T. M. Gernon, I. C. Wright, and D. Long, "Gas migration pathways, controlling mechanisms and changes in sediment physical properties observed in a controlled sub-seabed CO2 release experiment," *International Journal of Greenhouse Gas Control.*

[127] N. Shakhova, I. Semiletov, I. Leifer, V. Sergienko, A. Salyuk, D. Kosmach, D. Chernykh, C. Stubbs, D. Nicolsky, V. Tumskoy, and O. Gustafsson, "Ebullition and storm-induced methane release from the East Siberian Arctic Shelf," *Nature Geoscience*, vol. 7, pp. 64–70, Nov. 2014.

[128] L. Berger, C. Poncelet, and V. M. Trenkel, "A method for reducing uncertainty in estimates of fish-school frequency response using data from multifrequency and multibeam echosounders," *ICES Journal of Marine Science*, vol. 66, pp. 1155–1161, May 2009.

[129] S. Mau, H. Sahling, G. Rehder, E. Suess, P. Linke, and E. Soeding, "Estimates of methane output from mud extrusions at the erosive convergent margin off Costa Rica," *Marine Geology*, vol. 225, pp. 129–144, Jan. 2006.

[130] K. Wallmann, M. Drews, G. Aloisi, and G. Bohrmann, "Methane discharge into the Black Sea and the global ocean via fluid flow through submarine mud volcanoes," *Earth and Planetary Science Letters*, vol. 248, pp. 545–560, Aug. 2006.

[131] I. Klaucke, W. Weinrebe, P. Linke, D. Kläschen, and J. Bialas, "Sidescan sonar imagery of widespread fossil and active cold seeps along the central Chilean continental margin," *Geo-Marine Letters*, vol. 32, pp. 489–499, Mar. 2012.

[132] S. M. De Beukelaer, I. R. MacDonald, N. L. Guinnasso, and J. A. Murray, "Distinct side-scan sonar, RADARSAT SAR, and acoustic profiler signatures of gas and oil seeps on the Gulf of Mexico slope," *Geo-Marine Letters*, vol. 23, pp. 177–186, Dec. 2003.

[133] K. G. Foote, H. P. Knudsen, G. Vestnes, D. N. MacLennan, and E. J. Simmonds, *Calibration of acoustic instruments for fish density estimation : a practical guide.* Copenhagen Denmark: International Council for the Exploration of the Sea, 1987.

[134] V. M. Trenkel, V. Mazauric, and L. Berger, “The new fisheries multibeam echosounder ME70: description and expected contribution to fisheries research,” *ICES Journal of Marine Science*, vol. 65, pp. 645–655, Feb. 2008.

[135] K. G. Foote, D. Chu, T. R. Hammar, K. C. Baldwin, L. A. Mayer, L. C. Hufnagle, and J. M. Jech, “Protocols for calibrating multibeam sonar,” *The Journal of the Acoustical Society of America*, vol. 117, p. 2013, Apr. 2005.

[136] S. Thorpe, “On the Clouds of Bubbles Formed by Breaking Wind-Waves in Deep Water, and their Role in Air – Sea Gas Transfer,” *Philosophical Transactions of the Royal Society of London. Series A, Mathematical and Physical Sciences*, vol. 304, no. 1483, pp. 155–210, 1982.

[137] K. Commander and E. Moritz, “Off-resonance contributions to acoustical bubble spectra,” *The Journal of the Acoustical Society of America*, vol. 85, p. 2665, June 1989.

[138] K. W. Commander and R. J. McDonald, “Finite-element solution of the inverse problem in bubble swarm acoustics,” *The Journal of the Acoustical Society of America*, vol. 89, p. 592, Feb. 1991.

[139] R. Duraiswami, S. Prabhukumar, and G. L. Chahine, “Bubble counting using an inverse acoustic scattering method,” *The Journal of the Acoustical Society of America*, vol. 104, p. 2699, Nov. 1998.

[140] T. G. Leighton, S. D. Meers, and P. R. White, “Propagation through nonlinear time-dependent bubble clouds and the estimation of bubble populations from measured acoustic characteristics,” *Proceedings of the Royal Society of London. Series A: Mathematical, Physical and Engineering Sciences*, vol. 460, no. 2049, pp. 2521–2550, 2004.

[141] A. Mallock, “The Damping of Sound by Frothy Liquids,” *Proceedings of the Royal Society a-Mathematical Physical and Engineering Sciences*, vol. 84, no. 572, pp. 391–395, 1910.

[142] A. B. Wood, *A Textbook of Sound.* Macmillan, New York, 1941, 2nd ed. ed., 1941.

[143] P. S. Wilson, A. H. Reed, W. T. Wood, and R. A. Roy, “The low-frequency sound speed of fluid-like gas-bearing sediments.,” *The Journal of the Acoustical Society of America*, vol. 123, pp. EL99–104, Apr. 2008.

[144] T. G. Leighton, "What is ultrasound?," *Progress in biophysics and molecular biology*, vol. 93, no. 1-3, pp. 3–83.

[145] J. H. Costello, R. E. Pieper, and D. Holliday, "Comparison of acoustic and pump sampling techniques for the analysis of zooplankton distributions," *Journal of Plankton Research*, vol. 11, pp. 703–709, Jan. 1989.

[146] S. M. Fässler, R. Santos, N. García-Núñez, and P. G. Fernandes, "Multifrequency backscattering properties of Atlantic herring (Clupea harengus) and Norway pout (Trisopterus esmarkii)," *Canadian Journal of Fisheries and Aquatic Sciences*, vol. 64, pp. 362–374, Feb. 2007.

[147] R. J. Kloser, T. Ryan, P. Sakov, A. Williams, and J. A. Koslow, "Species identification in deep water using multiple acoustic frequencies," *Canadian Journal of Fisheries and Aquatic Sciences*, vol. 59, pp. 1065–1077, June 2002.

[148] D. Maclennan, P. G. Fernandes, and J. Dalen, "A consistent approach to definitions and symbols in fisheries acoustics," *ICES Journal of Marine Science*, vol. 59, pp. 365–369, Apr. 2002.

[149] R. J. Korneliussen, N. Diner, E. Ona, L. Berger, and P. G. Fernandes, "Proposals for the collection of multifrequency acoustic data," *ICES Journal of Marine Science*, vol. 65, pp. 982–994, Apr. 2008.

[150] V. M. Trenkel and L. Berger, "A fisheries acoustic multi-frequency indicator to inform on large scale spatial patterns of aquatic pelagic ecosystems," *Ecological Indicators*, vol. 30, pp. 72–79.

[151] T. K. Stanton and D. Chu, "Calibration of broadband active acoustic systems using a single standard spherical target.," *The Journal of the Acoustical Society of America*, vol. 124, pp. 128–36, July 2008.

[152] A. Nikolovska, H. Sahling, and G. Bohrmann, "Hydroacoustic methodology for detection, localization, and quantification of gas bubbles rising from the seafloor at gas seeps from the eastern Black Sea," *Geochemistry Geophysics Geosystems*, vol. 9, pp. 1–13, Oct. 2008.

[153] S. I. Muyakshin and E. Sauter, "The hydroacoustic method for the quantification of the gas flux from a submersed bubble plume," *Oceanology*, vol. 50, pp. 995–1001, Dec. 2010.

[154] T. G. Leighton, D. C. Finfer, P. R. White, G. H. Chua, and J. K. Dix, "Clutter suppression and classification using twin inverted pulse sonar (TWIPS),"

Proceedings of the Royal Society A: Mathematical, Physical and Engineering Science, vol. 466, no. 2124, pp. 3453–78, 2010.

[155] T. G. Leighton, J. Jiang, and K. Baik, “Demonstration comparing sound wave attenuation inside pipes containing bubbly water and water droplet fog,” *The Journal of the Acoustical Society of America*, vol. 131, pp. 2413–21, Mar. 2012.

[156] N. G. Granin, S. I. Muyakshin, M. M. Makarov, K. M. Kucher, I. A. Aslamov, L. Z. Granina, and I. B. Mizandrontsev, “Estimation of methane fluxes from bottom sediments of Lake Baikal,” *Geo-Marine Letters*, vol. 32, pp. 427–436, July 2012.

[157] Y. G. Artemov, V. N. Egorov, G. G. Polikarpov, and S. B. Gulin, “Methane emission to the hydro- and atmosphere by gas bubble streams in the Dnieper paleo-delta, the Black Sea,” *Marine ecological journal*, vol. 6, no. 3, pp. 5–26, 2007.

[158] M. Haeckel, B. P. Boudreau, and K. Wallmann, “Bubble-induced porewater mixing: A 3-D model for deep porewater irrigation,” *Geochimica et Cosmochimica Acta*, vol. 71, pp. 5135–5154, Nov. 2007.

[159] M. Bettelini and T. Fannelø p, “Underwater plume from an instantaneously started source,” *Applied Ocean Research*, vol. 15, pp. 195–206, Jan. 1993.

[160] P. J. Rew, P. Gallagher, and D. M. Deaves, *Dispersion of subsea releases. Review of Prediction Methodologies (Offshore Technology Report)*. Health and Safety Executive books, oth95 465 ed., 1995.

[161] A. O. Maksimov, “Car-jam effect and concentration anomalies in rising bubble plume,” in *PICES Scientific Report Series. Proceedings of the 3rd Okhotsk SeaWorkshop*, (Vladivostok , Victoria), pp. 67–70, 2004.

[162] J. F. Clark, L. Washburn, and K. Schwager Emery, “Variability of gas composition and flux intensity in natural marine hydrocarbon seeps,” *Geo-Marine Letters*, vol. 30, pp. 379–388, Oct. 2009.

[163] J. Schneider von Deimling and C. Papenberg, “Technical Note: Detection of gas bubble leakage via correlation of water column multibeam images,” *Ocean Science*, vol. 8, pp. 175–181, Mar. 2012.

[164] A. S. Salomatin and V. I. Yusupov, “Quantitative estimation of gas plume parameters by echo-sounder,” in *XVI Session of the Russian Acoustical Society*, pp. 455–458, 2005.

[165] D. V. Holliday, “Zooplankton acoustics,” in *Oceanography of the Indian Ocean* (B. N. Desai, ed.), pp. 733–740, 1992.

[166] T. Stanton, “On acoustic estimates of zooplankton biomass,” *ICES Journal of Marine Science*, vol. 51, pp. 505–512, Nov. 1994.

[167] R. B. Mitson, Y. Simard, and C. Goss, “Use of a two-frequency algorithm to determine size and abundance of plankton in three widely spaced locations,” *ICES Journal of Marine Science*, vol. 53, pp. 209–215, Apr. 1996.

[168] D. V. Holliday, R. E. Pieper, and G. S. Kleppel, “Determination of zooplankton size and distribution with multifrequency acoustic technology,” *ICES Journal of Marine Science*, vol. 46, pp. 52–61, Jan. 1989.

[169] J. M. Jech and W. L. Michaels, “A multifrequency method to classify and evaluate fisheries acoustics data,” *Canadian Journal of Fisheries and Aquatic Sciences*, vol. 63, pp. 2225–2235, Oct. 2006.

[170] E. D. Sloan, Jr., and C. Koh, *Clathrate Hydrates of Natural Gases, Third Edition.* CRC Press, 2007.

[171] D. Archer and B. Buffett, “Time-dependent response of the global ocean clathrate reservoir to climatic and anthropogenic forcing,” *Geochemistry, Geophysics, Geosystems*, vol. 6, pp. 1–13, Mar. 2005.

[172] A. Rajan, J. Mienert, and S. Bünz, “Acoustic evidence for a gas migration and release system in Arctic glaciated continental margins offshore NW-Svalbard,” *Marine and Petroleum Geology*, vol. 32, pp. 36–49, Apr. 2012.

[173] S. Sarkar, C. Berndt, T. A. Minshull, G. K. Westbrook, D. Klaeschen, D. G. Masson, A. Chabert, and K. E. Thatcher, “Seismic evidence for shallow gas-escape features associated with a retreating gas hydrate zone offshore west Svalbard,” *Journal of Geophysical Research*, vol. 117, p. B09102, Sept. 2012.

[174] R. E. Fisher, S. Sriskantharajah, D. Lowry, M. Lanoisellé, C. M. R. Fowler, R. H. James, O. Hermansen, C. Lund Myhre, A. Stohl, J. Greinert, P. B. R. Nisbet-Jones, J. Mienert, and E. G. Nisbet, “Arctic methane sources: Isotopic evidence for atmospheric inputs,” *Geophysical Research Letters*, vol. 38, pp. 2–6, Nov. 2011.

[175] H. Marín-Moreno, T. A. Minshull, G. K. Westbrook, B. Sinha, and S. Sarkar, “The response of methane hydrate beneath the seabed offshore Svalbard to

ocean warming during the next three centuries," *Geophysical Research Letters*, vol. 40, pp. 5159–5163, Oct. 2013.

[176] A. M. Myhre and O. Eldholm, "The western Svalbard margin (74-80N)," *Marine and Petroleum Geology*, vol. 5, pp. 134–156, May 1988.

[177] R. Towler, *readEKRaw MATLAB toolkit.* date accessed: 17 December 2014, http://hydroacoustics.net/viewtopic.php?f=36&t=131.

[178] J. M. Jech, K. G. Foote, D. Chu, and L. C. Hufnagle Jr., "Comparing two 38-kHz scientific echosounders," *ICES Journal of Marine Science*, vol. 62, pp. 1168–1179, Sept. 2005.

[179] K. G. Foote, "Optimizing copper spheres for precision calibration of hydroacoustic equipment," *The Journal of the Acoustical Society of America*, vol. 71, p. 742, Mar. 1982.

[180] C. D. de Jong, G. Lachapelle, I. A. Elema, and S. Skone, *Hydrography.* VSSD, 2006.

[181] J. L. Heaton, T. C. Weber, G. Rice, and X. Lurton, "Testing of an extended target for use in high frequency sonar calibration," *The Journal of the Acoustical Society of America*, vol. 133, p. 3537, May 2013.

[182] I. Leifer, "Characteristics and scaling of bubble plumes from marine hydrocarbon seepage in the Coal Oil Point seep field," *Journal of Geophysical Research*, vol. 115, p. C11014, Nov. 2010.

[183] L.-S. Fan and K. Tsuchiya, *Bubble wake dynamics in liquids and liquid-solid suspensions.* Stoneham, MA, USA: Butterworth-Heinemann, 1990.

[184] I. Leifer and R. K. Patro, "The bubble mechanism for methane transport from the shallow sea bed to the surface: A review and sensitivity study," *Continental Shelf Research*, vol. 22, pp. 2409–2428, Nov. 2002.

[185] S. De Gregorio, S. Gurrieri, and M. Valenza, "A PTFE membrane for the in situ extraction of dissolved gases in natural waters: Theory and applications," *Geochemistry, Geophysics, Geosystems*, vol. 6, pp. 1–13, Sept. 2005.

[186] R. W. Young, "Sabine Reverberation Equation and Sound Power Calculations," *The Journal of the Acoustical Society of America*, vol. 31, p. 912, July 1959.

[187] N. Cochard, J. L. Lacoume, P. Arzelies, and Y. Gabillet, "Underwater acoustic noise measurement in test tanks," *Ieee Journal of Oceanic Engineering*, vol. 25, no. 4, pp. 516–522, 2000.